CATALYTIC GRAPHITIZATION BY LIGHT METALS

by

Leyi Zhao

Submitted in partial fulfilment of the requirements
for the degree of Doctor of Philosophy

at

Dalhousie University
Halifax, Nova Scotia
March 2019

TABLE OF CONTENTS

LIST OF TABLES

LIST OF FIGURES

ABSTRACT

The catalytic effects of light metals (Mg and Li) on the graphitization process and the effects of precursors, blending conditions, heating conditions, and additives on the graphitization rate and the final graphite morphology were studied using a variety of techniques. Many interesting chemistries were discovered and discussed. These findings could guide to further understanding of the catalytic graphitization process and the resulting products. In general, Mg is a much better graphitization catalyst than Li. Both Mg and Li catalysts were easily removed, resulting in highly pure graphite products. Graphite with various morphologies were discovered, including Voronoi tessellated graphite and hexagonal platelet graphite made from glucose, spherical graphites made from C-Mg-$MgCl_2$ melts, and graphitic dendrites made from cellulose and C-Mg-Al melts, etc. Different morphologies suggested different graphitization mechanisms. The basic mechanism of Mg-catalytic graphite growth might be a combination of carbon dissolution-precipitation and carbide formation-decomposition. Many catalytic graphites are highly graphitized. When cycled in Li half-cells, these graphites displayed good cycling stability and high reversible capacity. The electrochemical performance of some graphites is comparable to battery grade commercial graphites.

LIST OF ABBREVIATIONS AND SYMBOLS USED

2H	Hexagonal graphite structure
3R	Rhombohedral graphite structure
ABAB	Layer positions in hexagonal close-packed notation
ABCABC	Layer positions in hexagonal close-packed notation
a-C	Amorphous carbon
AC	Activated carbon
a	Lattice constant
at. %	Atomic percent
B	Width of X-ray diffraction peaks
BET	Brunauer-Emmett-Teller
BSEs	Backscattered electrons
C-C	Carbon-carbon covalent bond
CCCV	Constant current, constant voltage
CCHPG	Carbon coated hexagonal platelet graphites
CE	Coulombic efficiency
CVD	Chemical vapor deposition
c	Speed of light (2.998 × 108 m s-1)
d	Lattice plane spacing
EDS	Energy dispersive X-ray spectroscopy
e	Charge of an electron
FWHM	Full width at half maximum
FIB	Focused ion beam
HEMM	High energy mechanical milling
HPGs	Hexagonal platelet graphites
h	Planck constant (6.626 × 10-34 m2 kg s-1)
I_G, I_D	Intensity of Raman peaks
IC	Irreversible capacity
ICDD	The International Centre for Diffraction Data

ICP	Inductively coupled plasma
K	Scale constant in Scherrer equations
L_a	Average lateral extent of graphite crystallites
L_c	Average vertical extent of graphite crystallites
LCGs	Lithium catalyzed graphites
LIBs	Lithium-ion batteries
LMIS	Liquid metal ion source
M	Average layer number of graphite crystallites
m	Mass
mAh	Milliampere-hours
o-G	Ordered graphite
OES	Optical emission spectrometry
P_i, P_f	Pressure
$\mathrm{P_r}$	Probability of random stacking
$\mathrm{P_{3R}}$	Probability of rhombohedral structure
PAA	Polyacrylic acid
PAN	Polyacrylonitrile
PDF	Powder Diffraction File
PFR	Phenol formaldehyde resin
PR	Phenolic resin
PVdF	Polyvinylidene difluoride
PVA	Polyvinyl alcohol
PVC	Polyvinyl chloride
PVP	Polyvinyl pyrrolidone
Q	Gravimetric/specific capacity
SA	Surface area
SAED	Selected area electron diffraction
SBR	Styrene butadiene rubber
SC	Sugar (glucose) carbon

SEM	Scanning electron microscopy
SEs	Secondary electrons
TEM	Transmission electron microscopy
t-G	Turbostratic graphite
V_{Solid}, V_s, V_r	Volume
V	Potential
VTGs	Voronoi-Tessellated Graphites
wt.%	Weight percent
XRD	X-ray diffraction
λ	Wavelength
θ	Incident X-ray angle
ζ	In-plane strain
ρ	Density
μ	Chemical potential
χ^2	Goodness of fit
$<\delta^2>^{1/2}$	Interlayer distance fluctuation

ACKNOWLEDGEMENTS

I am very grateful to a great number of people for their kind help and constant support throughout these past years. Particularly, I would like to thank my supervisor Mark Obrovac for his support, guidance, and patience. I would like to thank my committee members, Peng Zhang, Josef Zwanziger, and Mita Dasog for their advice and help. I would like to thank Jeff Dahn, Andy George, Alicia Oickle, and Patricia Scallion for their kind help in running instruments. I would like to thank Timothy Hatchard for his endeavored work in maintaining the lab. Specially, I would like to thank Xiuyun Zhao and Craig Bennett for their inspiring suggestions. I acknowledge funding from NSERC and 3M (IRCPJ 407487-09), Co. under the auspices of the Industrial Research Chair Program.

Most importantly I would like to give special thanks to my wife and parents for their loving support throughout the long journey of Ph.D. and M.Sc.

I would also like to thank everyone in Obrovac lab. Thanks for the awesome experience in and out of the lab.

Chapter 1 Introduction

1.1 Graphite

Graphite is one of carbon's allotropes. Each carbon allotrope (*e.g.* diamond, fullerene, and amorphous carbon) has unique properties because the way carbon atoms form bonds with each other is diverse. Specifically, graphite is a crystalline form of carbon consisting of successive planar graphene layers parallel to each other. The most common structure of graphite is hexagonal, usually labeled as 2H, with a stacking order of ABAB.[1–5] The 2H structure is shown in Figure 1.1(a). In Figure 1.1 and subsequent figures showing material structures, the circles showing atom positions do not represent actual atomic sizes. Here, "2" represents the smallest repeating layer-number, and "H" represents hexagonal. Within a layer, carbon atoms are arranged in a honeycomb lattice and each carbon atom connects with three neighboring carbon atoms by strong covalent bonds (σ-bonds), while adjacent layers are connected to each other by weak van der Waals forces. This difference in bonding leads to the great anisotropy in mechanical, thermal, electrical, and electronic properties of graphite. [1–5] In an ideal graphite lattice, the nearest neighbor interatomic distance is 1.418 Å, and the interlayer distance is 3.348 Å.[6] For a 2H graphite unit cell (outlined by red lines in Figure 1.1(a)), the lattice constant a is 2.456 Å, and c is 6.696 Å. Another type of graphite structure is rhombohedral (Figure 1.1(b)), usually labeled as 3R, with a stacking order of ABCABC. Here, "3" indicates the smallest repeating layer-number, and "R" indicates rhombohedral. Red lines in Figure 1.1(b) outline a unit cell in 3R graphite.

Figure 1.1 shows an ideal structure of graphite with no defects whatsoever. However, in real cases, graphite always contains crystalline imperfections such as vacancies, stacking faults, layer-disclination, *etc.*[1–5] Pure graphite is very chemically stable and is resistant to most base, acids and corrosive gases. However, impurities (such as hydrogen, oxygen, *etc.*) are always present in graphite to some degree. These impurities often have an important catalytic effect which increases the chemical reactivity of graphite.[3]

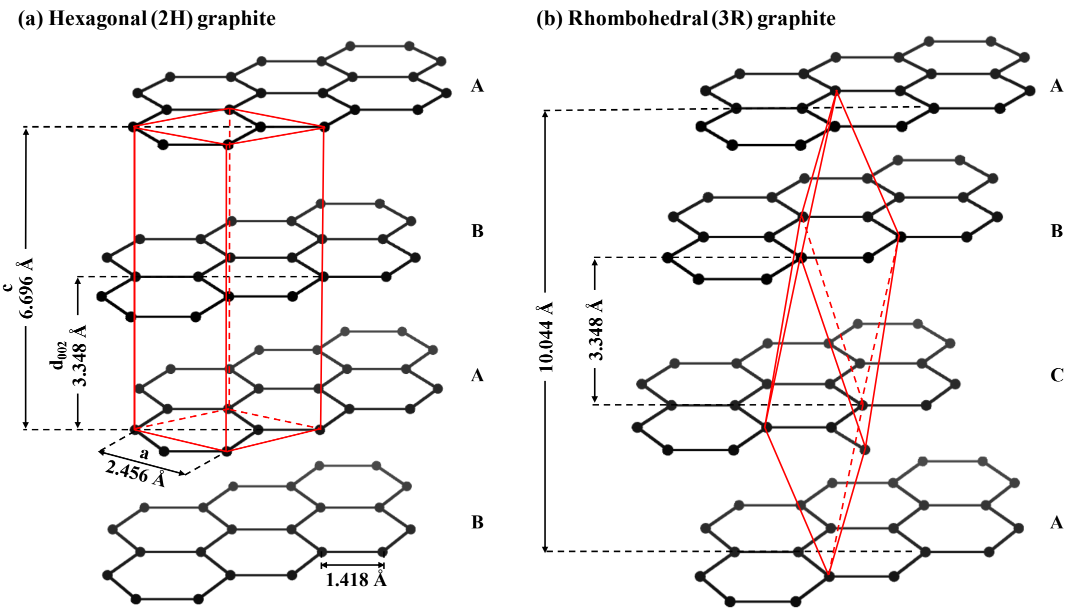

Figure 1.1 Diagrams of (a) hexagonal (2H) graphite and (b) rhombohedral (3R) graphite.

There are two sources of graphite: natural graphite and synthetic graphite. Natural graphite is found in abundance on earth. Though it has been known to people for centuries, natural graphite was not identified as an allotrope of carbon until 1855.[3] In application, natural graphite only accounts for a minority of graphite products and its utilizations are limited because it often does not have the properties required for specialty applications where the purity, particle size, shape and crystallinity of graphite must be tightly controlled. More than 120 years ago, people started using synthetic graphite.[7–9] In the last century, the application scope of synthetic graphite has considerably increased. Most of graphite products are now synthetic and these products are constantly being upgraded.[1–5,10]

The word "graphite" originated from the Greek word "graphein", which means to write. Indeed, back to 16th century, pencils had been manufactured by using graphite in Europe.[3] Nowadays, graphite has become indispensable to our technological society due to its unique physical and chemical properties, and is widely applied in Li-ion batteries, catalyst supports, specialty lubricants, powder metallurgy, nuclear reactors, friction/braking products, conductive coatings, carbon additives, paints, crucibles, *etc.*[1–5,10]

1.1.1 Carbonization and conventional graphitization

Synthetic graphite materials are derived from organic precursors, such as petroleum coke, coal-tar, natural gas, polymers, hydrocarbons, wood, plants, *etc.*[3–5,11] The transformation of organic precursors into graphite materials includes two steps: carbonization and graphitization. Carbonization can be defined as the procedure in which the organic precursor is pyrolyzed or destructively distilled, losing much of its non-carbon elements as gases and changing to forms of carbon through complex reactions such as condensation, dehydrogenation, and isomerization, *etc.*[12–14] During carbonization, the organic precursor is slowly heated in an inert atmosphere over a range of temperatures up to 1300 °C, and decomposes into a non-organized carbon with volatile substances diffusing out.[3–5] The resulting non-organized carbon materials contain small groups of 2 - 5 parallel graphite-like layers with limited extent (<25 Å) (a "parallel-layer group").[14] Graphitization can be defined as the formation of graphite from non-organized or less ordered carbon materials.

Precursors of carbonization and graphitization can be roughly divided into two types: aromatic materials and non-aromatic materials.[3–5] Most aromatic materials go through an intermediate liquid stage (mesophase) at low temperatures (~300 - 500 °C), and transform into graphitizable carbons after carbonization.[12–14] Graphitizable carbons are usually anisotropic and less porous than non-graphitizable carbons, with a graphite-like structure (Figure 1.2(a)).[3–5,14,15] On the other hand, most non-aromatic materials do not go through the mesophase stage at low temperatures, and transform into non-graphitizable carbons after carbonization.[3–5,15] Non-graphitizable carbons are usually isotropic and more porous than graphitizable carbons (Figure 1.2(b)).[14–16] Here, graphitizable carbons are defined as non-organized carbon materials that are readily converted into well-ordered graphite structure under high temperature heat-treatment, and non-graphitizable carbons are defined as non-organized carbon materials that do not graphitize upon heat-treatment to graphitizing temperatures (~2600 - 3300 °C).[14,15] Graphitizable carbon is also called soft carbon, which softens sufficiently for easy machineability upon heating to ~2700 °C, while non-graphitizable carbon is also called hard carbon, which does not soften sufficiently for easy machineability upon heating to ~2700 °C.[12]

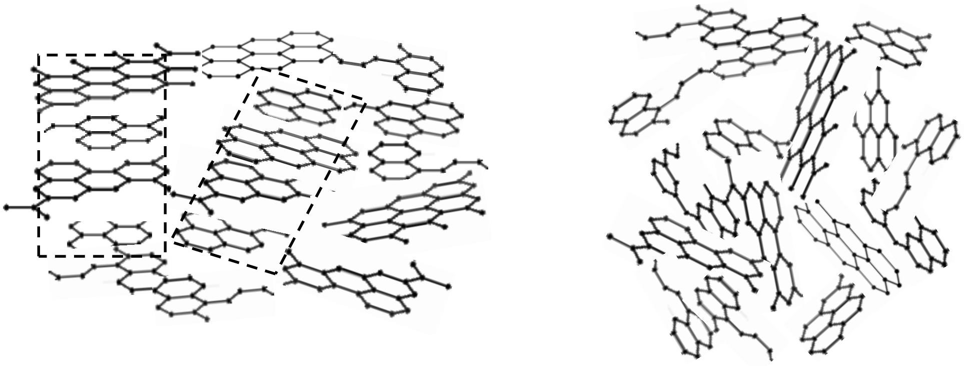
(a) Graphitizable carbon **(b) Non-graphitizable carbon**

Figure 1.2 Diagrams of (a) graphitizable carbon and (b) non-graphitizable carbon. Dashed lines show some short-ranged crystallographic order in graphitizable carbon.

In the 1950s, R.E. Franklin proposed a 2-dimentional structural model to describe graphitizable and non-graphitizable carbons.[14] Based on this model, it was pointed out that the difference in graphitizability between graphitizable and non-graphitizable carbons is that they have different types of cross-linking (bonds between parallel-layer groups). Non-graphitizable carbon contains strong cross-linking between the parallel-layer groups, which hold crystallites in a random orientation and hinder the coalescence of these groups.[14] In comparison, graphitizable carbon contains much weaker cross-linking, and thus coalescence of parallel-layer groups can easily take place.[14]

Conventional graphitization is a process in which high temperature (~3000 °C) heat-treatment is applied to a graphitizable precursor under an inert atmosphere. This process occurs in a series of steps. As the increasing temperature passes the carbonization temperature (~1200 - 1300 °C), hydrogen, sulfur, and other non-carbon elements, if any, are gradually removed, and virtually none remain at ~2000 °C.[3–5,14]

As the temperature reaches ~1800 - 2000 °C, turbostratic graphite forms after continuous coalescence of parallel-layer groups and the growth of crystallites.[3–5] Similar to ordered graphite, turbostratic graphite is composed of stacked graphene layers. However, ordered graphite has an organized stacking structure, while the graphene layers of turbostratic graphite may randomly rotate about the normal of graphene layers (Figure 1.3).[17] As a result, in an ordered graphite structure, a carbon atom locates in the center of each hexagonal unit of adjacent layers from the top view of the planar graphene layer, while the top view of turbostratic graphite looks less ordered (Figure 1.3). Furthermore, turbostratic graphite usually has smaller crystallites compared to ordered graphite. Above 2000 °C, turbostratic graphite starts to be converted into ordered graphite.[3–5] In the conversion, crystallite growth is dependent on the migration of parallel-layer groups, which involves the breaking of strong C-C

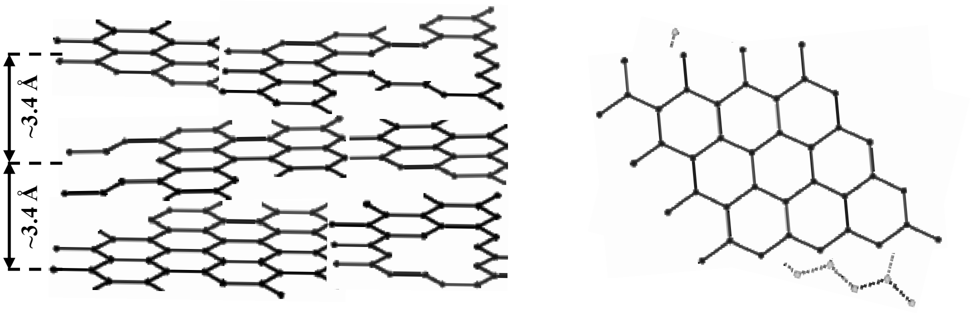

(a) Turbostratic graphite

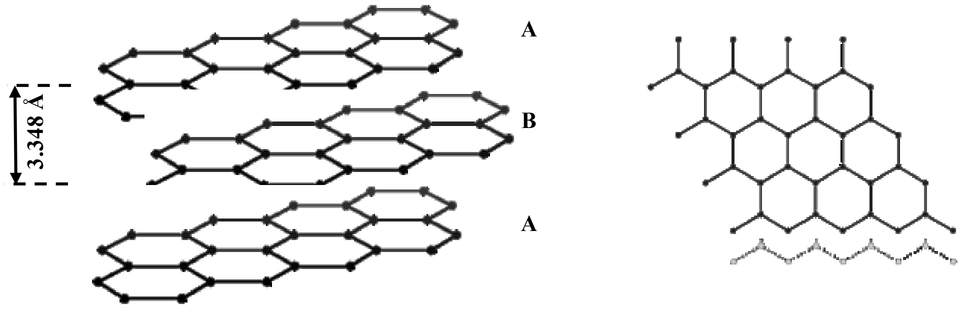

(b) Ordered (2H) graphite

Figure 1.3 Diagrams of (a) turbostratic graphite and (b) ordered 2H graphite showing perspective views roughly parallel to the basal planes, and views perpendicular to the basal planes.

bonds. Higher temperature provides higher energy to overcome activation barriers and therefore results in larger crystallites and a higher level of graphitization.[14] Most graphitizable materials require a temperature of ~3000 °C to reach full graphitization.[3–5] In industry, synthetic graphite is made commercially by electrical resistive heating at 2600 - 3300 °C for weeks.[3–5] The heating process accounts for a significant proportion of the total manufacturing cost.[15]

Non-graphitizable carbon, on the other hand, does not graphitize readily in the conventional graphitization process. In other words, non-graphitizable carbon cannot be converted into graphite by conventional graphitization methods regardless of the duration or the temperature of the heat-treatment process.[3–5] The structural change of the non-graphitizable carbon in the heat-treatment process can be explained by a "Falling Card Model".[16] According to the model, some cross-linking in non-graphitizable carbon may break when sufficient thermal energy is provided at high temperature, allowing some parallel-layer groups to rotate into parallel orientation. This action causes a slight increase in the number of organized regions, and an increase in the average pore size. However, significant amounts of cross-linking still exist in the material even being heated at 3000 °C. After high temperature heat-treatment, non-graphitizable carbon usually transforms into a microporous material and its random arrangements of crystallites mostly remain unchanged. A reduction in interlayer spacing is observed in non-graphitizable carbon during high temperature heat-treatment. However, the interlayer spacing does not decrease below 3.44 Å for most non-graphitizable carbons.[3]

1.1.2 Catalytic graphitization

Narrowly speaking, catalytic graphitization can be defined as the enhancement of the crystallinity of graphitic materials via graphitization processes that involve chemical reactions between disordered carbons and catalysts.[15,18] That is to say, adding catalysts can lower the graphitization temperature, speed up the graphitization process of graphitizable (soft) carbons, and enable the graphitization of non-graphitizable (hard) carbons.[15,18]

1.1.2.1 Catalytic graphitization by heat-treatment with catalysts

In their seminal review, Ōya and Marsh classified catalytic graphitization phenomena into three categories: the G-effect, A-effect, and T-effect.[15] The G-effect results in ordered graphites with a sharp X-ray diffraction (XRD) 002 peak at ~26.5°, corresponding to an interlayer spacing close to the theoretical value of the ideal graphite structure (Figure 1.4(a)). The T-effect results in graphites with an XRD 002 peak at ~26°, corresponding to turbostratic graphites (Figure 1.4(b)). The A-effect results in a broad XRD 002 peak at ~26°, indicating the failure of graphite structure formation, though the carbon crystallite size increases compared to the precursor (Figure 1.4 (c)). As will be seen in following chapters, it is more exact to classify these catalytic phenomena into different stages. By slightly changing the catalytic graphitization conditions (*e.g.* increasing the temperature by 100 °C, or extending the heating time by several hours), the graphitization level of the final graphite might be greatly improved, and T-effect graphite may thereby be upgraded to G-effect graphite.

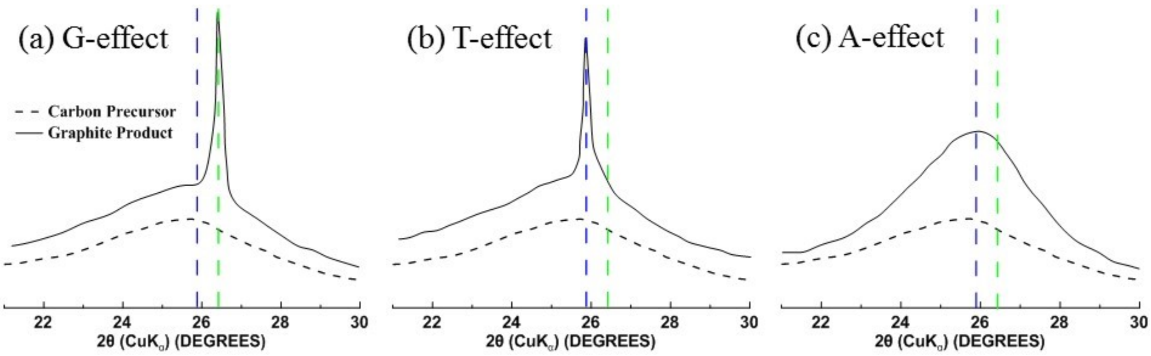

Figure 1.4 Different categories of catalytic graphitization as described in Reference [15]. Dashed and solid lines indicate carbon before and after catalytic graphitization, respectively, in XRD patterns of 002 peak regions. The blue and green lines indicate the positions of turbostratic and ordered graphite 002 peaks, respectively.

Three mechanisms have been proposed to explain catalytic graphitization. The first is the well-known dissolution-precipitation mechanism, whereby the carbon precursor dissolves into the catalyst, followed by its precipitation as a graphitic carbon. This is the most widely accepted mechanism for catalytic graphitization and was first proposed by Fitzer and Kegel.[19] Group VIII metals (Fe, Co, Ni) usually catalyze the graphitization according to this mechanism.[20,21] The second mechanism is the formation-decomposition of carbide intermediates, whereby the carbon precursor forms carbides with the catalyst, which subsequently decomposes, leaving behind a graphitic carbon. For example, Si catalyst follows this mechanism: Si reacts with C, forming SiC, which decomposes into Si and graphite.[22] The third mechanism is a combination of the first and second mechanisms, whereby the dissolution-precipitation sequence occurs concurrently with carbide formation. For example, Ti follows the third mechanism: some graphite forms by the dissolution-precipitation mechanism, while other graphite forms from the decomposition of TiC.[23] Figure 1.5 (adapted from Figure 5 in Reference [15]) illustrates how the dissolution-precipitation mechanism works. The driving force for catalytic graphitization is the excess free energy of the disordered carbon structure,[19] which leads to a greater affinity for the catalyst in the amorphous carbon compared to graphite. As a result, the catalyst does not react with graphite, but preferentially dissolves or reacts with disordered carbon. Therefore, the maximum metal concentration occurs at the reaction front.[24] During the precipitation of carbon and the decomposition of carbide, graphite is preferentially formed due to its lower free enthalpy compared to other carbon forms (*e.g.* disordered carbon).[25]

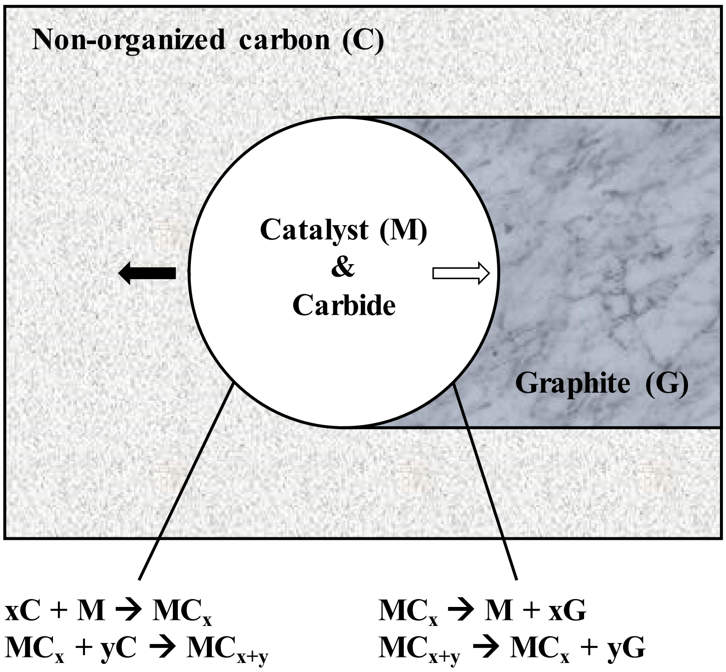

Figure 1.5 Diagram of the dissolution-precipitation mechanism for catalytic graphitization, adapted from Figure 5 in Reference [15]. The solid arrow indicates the moving direction of the catalyst, leaving graphite behind as indicated by the hollow arrow. Reactions at the leading and trailing edges of the catalyst are also given.

1.1.2.2 Improving graphitization efficiency by other methods

Besides graphitization with catalysts, many other methods can improve the efficiency of graphitization. For example, increasing pressure is an effective method in accelerating graphitization: a greater degree of graphitization can be achieved at a given temperature at high pressure (GPa level).[26–28] Other methods include using chemical vapor deposition (CVD),[29,30] applying microwave irradiation[31,32] or cathodic polarization[33] to carbon precursors.

1.1.2.3 Catalyst types

Graphitization catalysts include elements, oxides, and salts. Elemental graphitization catalysts have been intensively studied during the last decades. Research results before 1982 have been summarized by Ōya *et al.*,[15,34] Ishikawa *et al.*,[35] and Marsh *et al.*[18] Since these studies, there has been not an updated review of graphitization catalysts. To obtain an overall understanding of the advancements made in graphitic catalyzation, an up-to-date summary is necessary. Table 1.1 is a list of some of the advancements made in graphitization catalysts in the last 36 years, shown in the form of a periodic table. In this table, references in yellow correspond to research in elemental catalysts and those in blue correspond to research in compound catalysts, such as oxides, carbides, acetates, sulfates, *etc*.

Excluding transition metals, most catalysts in Table 1.1 only enhance the graphitization process to a small degree, while some of them have no graphitization catalysis effect at all. However, Na metal,[36] and compounds of B,[37] Si,[38] Al,[39] and Ca[40] can be categorized as good catalysts which can greatly accelerate the graphitization process. Transition metals (and their compounds) have much better graphitization efficiency than other catalysts, especially group VIII elements (*i.e.* Fe, Co, Ni) and their compounds. As a result, transition metal-based catalysts have been more intensively studied. These studies have shown that Fe, Co and Ni-based catalysts can effectively catalyze graphitization at much lower temperatures (800 - 1800 °C) than that of conventional methods, resulting in T-effect or G-effect graphites.

Table 1.1 An updated summary of graphitization catalysts since 1982, in the form of an incomplete periodic table. References in yellow correspond research in elemental catalysts, and those in blue correspond to research in compound catalysts (oxides, salts, carbides, *etc.* containing each specific element).

IA	**IIA**											**IIIA**	**IVA**	**VA**	**VIA**
Li	Be											B	C	N	O
	🟨 41											🟨 42			
												🟦 37,43			
Na	Mg											Al	Si	P	S
🟨 36,44	🟨 45–47											🟨 41	🟨 23,48	🟨 49	🟨 50
	🟦 51	**IIIB**	**IVB**	**VB**	**VIB**	**VIIB**	**VIII**			**IB**	**IIB**	🟦 39,52	🟦 38		
K	Ca	Sc	Ti	V	Cr	Mn	Fe	Co	Ni	Cu	Zn	Ga	Ge	As	Sn
			🟨 53	🟨 54	🟨 55	🟨 56	🟨 57–63	🟨 64–66	🟨 66–69	🟨 55	🟨 70				
	🟦 40		🟦 71	🟦 72	🟦 73		🟦 74–79	🟦 80–82	🟦 81–83		🟦 84	🟦 51			
Rb	Sr	Y	Zr	Nb	Mo	Tc	Ru	Rh	Pd	Ag	Cd	In	Sn	Sb	Te
			🟨 85							🟨 86					
			🟦 52,87		🟦 71,88										
Cs	Ba	La-Lu	Hf	Ta	W	Re	Os	Iy	Pa	Au	Hg	Tl	Pb	Bi	Po
					🟦 71										

La	Ce	Pr
🟨 89	🟨 89	🟨 89,90
🟦 91		🟦 21

1.1.2.4 Combinations of Catalysts

Catalyst combinations (two or more types of elemental and compound catalysts) have been intensively studied in graphitization, such as Fe-Ni,[92] Fe-NaCl,[93] Na-Mn(CH_3COO)$_2$,[94] $NiCl_2$-$ZnCl_2$,[95] Ni-Cu-Al_2O_3,[96] *etc*. One advantage of using a catalyst combination is that the lower melting point (eutectic) of alloys contributes to lower graphitization temperatures.[15,97] Another advantage is that the catalysts may have synergic catalytic functions, showing better catalytic effects than using any one alone.[92] In some cases, all additives have catalytic effect in graphitization: Zhou *et al.* graphitized polyacrylonitrile-based carbon fiber with Fe-Ni alloys, in which both Fe and Ni are effective catalysts.[92] While in other cases, only one additive works effectively: Tzeng investigated the catalytic graphitization of electroless Ni-P-coated polyacrylonitrile-based carbon fibers. In his study, only Ni is responsible for the catalytic graphitization.[97]

1.1.2.5 Factors influencing catalytic graphitization

Catalytic graphitization is a complex process. Besides catalyst types, catalytic graphitization is influenced by various other factors, such as temperature, precursor type, catalyst amount, catalyst particle size, the method used to combine precursors and catalysts, ambient atmosphere, *etc.*[15] For example: 6 wt.% Mn(CH_3COO)$_2$ works better as a graphitization catalyst than 1 wt.% under the same conditions;[94] and more finely-dispersed Ni catalysts tends to result in T-effect rather than G-effect graphite.[15] Some of these factors are discussed in following chapters regarding their influence on the Mg catalyzed graphitization process.

1.1.2.6 Applications of catalytic graphitization

Although various catalysts have been studied, only some transition metals (*i.e.* Fe, Co, Ni) catalysts have been successfully used to convert disordered carbon precursors into highly crystalline graphite at relatively low temperatures (800 – 1800 °C).[35,64,66] However, transition metal catalysts are difficult to remove after graphitization, resulting in the graphite products containing significant amounts of residual catalyst materials, and, therefore, reducing the practicality of this method, especially in applications where high purity graphite is desired.[15]

1.2 Li-ion batteries

LIBs are widely applied in mobile electronics (cell phones, tablets, and laptops, *etc*.), power tools, wearable devices, and electric vehicles, *etc*. [98,99] In its conventional format, a LIB consists of a negative electrode, a positive electrode, and an electrolyte comprising a solution of a lithium salt in a mixed organic solvent. The electrode coating is a mixture of active materials, a binder, and an optional conductive diluent, adhering to metal foil current collectors. Within a Li-ion battery, the positive and negative electrodes are electrically isolated by membrane separators.

Figure 1.6 shows a brief scheme of a conventional LIB. During charge/discharge, graphite and lithium metal oxide ($LiMO_2$) reversibly intercalate/de-intercalate Li ions. During charge, Li ions are de-intercalated from $LiMO_2$ and intercalated into graphite through the electrolyte, while electrons travel from $LiMO_2$ to graphite via the external circuit. The two half reactions at the positive and negative electrodes and the overall reaction are given by:

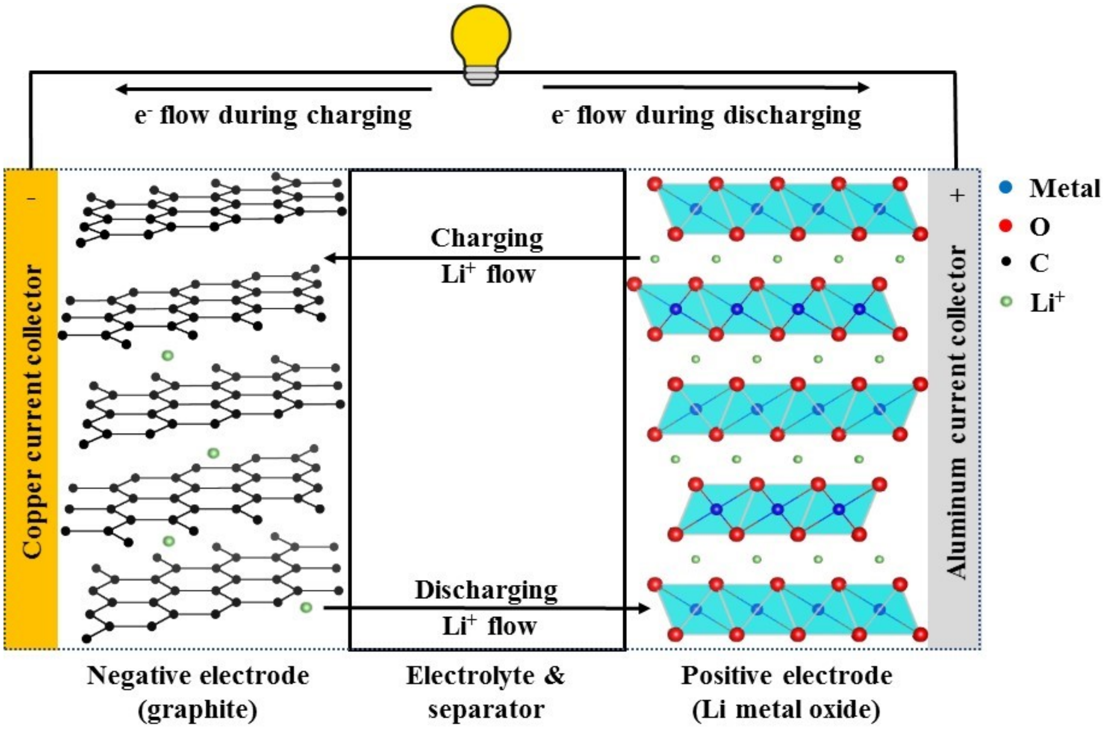

Figure 1.6 Scheme of a Li-ion cell with lithium metal oxide positive electrode (right) and graphite negative electrode (left).

Negative: $C + xLi^+ + xe^- \rightarrow Li_xC$ (1.1)

Positive: $LiMO_2 \rightarrow Li_{1-x}MO_2 + xLi^+ + xe^-$ (1.2)

Overall: $C + LiMO_2 \rightarrow Li_xC + Li_{1-x}MO_2$ (1.3)

During discharge, the reactions proceed in the opposite direction spontaneously.

1.2.1 Graphite negative electrodes

Graphite is now the most widely applied LIB negative electrode (anode) material. It is a miraculous material for LIB considering its combination of so many merits: high specific capacity (372 mAh g^{-1}), high volumetric capacity (719 Ah L^{-1}), low average voltage (~0.2 V *vs.* Li/Li^+), small hysteresis, low irreversible capacity, good thermal stability, good electronic conductivity, low volume expansion during lithiation (~10% in full lithiation), good rate capability, good cycle life, high Coulombic efficiency (CE), and low price, *etc.*[100]

As mentioned above, graphite electrodes reversibly intercalate/de-intercalate Li ions during charge/discharge. In this process, graphite undergoes staging phenomena, in which the staged phases are characterized by graphite and Li layers periodically arranged depending on the content of intercalated Li.[3,101,102] Each staged phase is identified with an integer denoting the number of graphite layers between adjacent Li layers (Figure 1.7). The first stage is the most dilute stage (or stage 1') having a small amount of intercalated Li ($x < 0.04$ in Li_xC_6,), in which the intercalated Li is randomly distributed throughout the whole graphite host.[103] As x in Li_xC_6 increases past 0.04, the stage 1' phase transforms into a stage 4 phase. As x increases further, the stage 4 phase converts to a stage 3 phase, then to a "liquid-like" stage 2 phase (stage 2L).[103] As more Li intercalates into graphite, a stage 2 phase forms, which finally converts to a stage 1 phase. In stage 1 lithiated graphite, the amount of intercalated Li reaches a maximum and the material formed is LiC_6.[3,101,102] The theoretical capacity of graphite, 372 mAh g^{-1}, is determined according to the formation of LiC_6.

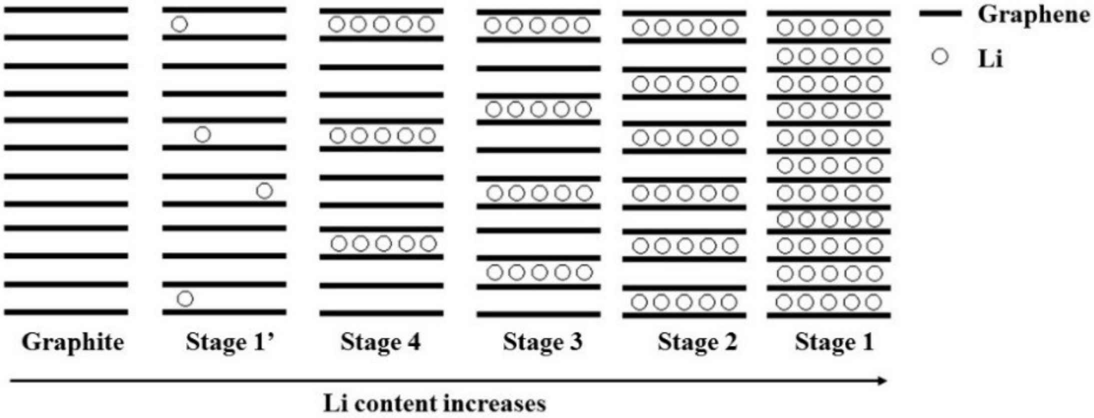

Figure 1.7 Staging phenomenon of graphite during Li intercalation.

The crystallinity level of graphite is essential for its application in LIB because a low graphitization level (*i.e.* containing significant amounts of turbostratic components) leads to a low reversible capacity, since Li cannot be intercalated effectively into turbostratic regions of graphite.[104,105]

1.2.2 Catalytically-derived graphite negative electrodes

Among previous studies of catalyzed graphite LIB anodes, most researchers used Fe-based catalysts due to their high catalysis efficiency.[57–62,74] Fe catalysts are effective at low temperatures (900 - 2000 °C), and more importantly, the resulting graphite products can have a high graphitization level.[57,58] When used in LIBs, Fe-catalyzed graphites perform well, similar to some battery grade commercial graphites.[57–62] However, Fe catalysts are difficult to remove. If the Fe is included in the specific capacity calculation, the resulting specific capacities are very low.

1.3 Motivation

As mentioned above, although transition metal catalysts (especially Fe) have proven to be good in improving graphitization efficiency, it is problematic that they are difficult to remove after graphitization, which greatly hinders their application. Considering the good performance of low temperature Fe-catalyzed graphite, it would be desirable to find a catalyst that works equally well, but that could be easily removed and even recovered from the graphite product. Therefore, the main motivation of the thesis work is to catalytically synthesize graphites of high crystallinity and of high purity, and, in doing so, to obtain a profound understanding of the catalyzation process and the resulting products.

After a comprehensive survey of the elements, it was found that Mg could be used as an effective graphitization catalyst which could be easily removed or even recovered after graphitization. Attempts to use Mg as a graphitization catalyst have been reported previously; however promising results have not been shown.[34,45–47,106] For instance, Weiswerler *et al.* heated glass-like carbon in a crucible filled with Mg at 800 °C.[106] In this early trial, Mg did not work effectively as a graphitization catalyst. Okamoto *et al.* heated Mg with cast iron, and they only found that Mg could change the morphology of graphite particles.[46] Ōya *et al.* showed that a phenol-formaldehyde resin can be effectively graphitized in the presence of 10 wt.% Mg.[34] However, the pyrolysis was conducted at very high temperatures (2600 °C for one hour and 3000 °C for ten minutes). At such high temperatures, such a soft carbon precursor can graphitize without the use of a catalyst. In all these previous studies, a detailed analysis of the characteristics of the graphite produced with an Mg catalyst was not reported.

The main focus of this thesis is to study the use of Mg as a graphitization catalyst in detail. Specifically, Chapter 3 and 4 introduce how graphite can be produced from amorphous carbon by combining carbon and Mg in different ways. Chapter 5 discusses how different precursors influence Mg catalyzed graphitization. Chapter 6 introduces the use of Li as a graphitization catalyst. Chapter 7 discusses how additives ($MgCl_2$ and Al) influence the morphology and other properties of the graphites produced by Mg catalyzed graphitization. Chapter 8 proposes some future work for the study of Mg catalyzed graphitization.

Chapter 2 Experimental Techniques

2.1 X-ray diffraction (XRD)

2.1.1 Theory

X-ray diffraction (XRD) crystallography is widely used in the field of materials characterization to obtain information on the atomic scale structure of various substances in various states.[107–109]

In an X-ray diffractometer, X-rays are usually generated from a sealed diode vacuum tube by the interaction of a heavy metal target (*e.g.* Cu) with high-speed electrons. Specifically, electrons are usually generated from a tungsten filament (cathode), and accelerated by a high voltage towards the Cu target (anode) with high kinetic energy. Most of the kinetic energy is converted into heat, therefore the Cu target must be constantly cooled by water to prevent its melting.[107–109]

When an electron with sufficient kinetic energy strikes a Cu atom, an electron in the K shell of the Cu atom may be knocked out, leaving a vacancy behind. The vacancy can be filled immediately by an electron from any of the outer shells, but is commonly filled by electrons from the L or M shell. The transition results in the emission of an X-ray photon with a sharply defined energy. Such X-rays are known as characteristic X-rays with specific wavelength determined by Equation 2.1:[107–109]

$$\lambda = h\, c\, /\, \Delta \mathrm{E}, \qquad (2.1)$$

where h is the Planck constant, c is the speed of light in vacuum, and ΔE is the energy difference between the initial and final energy states of the transition electron. Main types of characteristic X-rays from a Cu target include Kα_1, Kα_2 (both from L shell) and Kβ (from M shell), corresponding to wavelengths of 1.54051 Å, 1.54433 Å, and ~1.39 Å, respectively.[107–109] Kβ radiation is usually removed by a monochromator or a Ni film filter and the effects from Kα_2 radiation is typically removed using software.

After being emitted, X-ray beams are collimated and sized by various slits, and strike the sample. Then the incident X-rays are scattered and create diffracted X-rays upon striking. Here, the diffraction phenomena of X-rays are attributed to certain phase relations between different waves. If two waves are completely in phase, constructive interference of X-rays occurs. The constructive interference condition can be quantitatively described by Bragg's Law:

$$n \lambda = 2 d \sin\theta, \qquad (2.2)$$

where n is an integer, λ is the X-ray wavelength, d is the interplanar spacing, and θ is the diffraction angle. Figure 2.1 illustrates a constructive condition corresponding to Bragg's law.

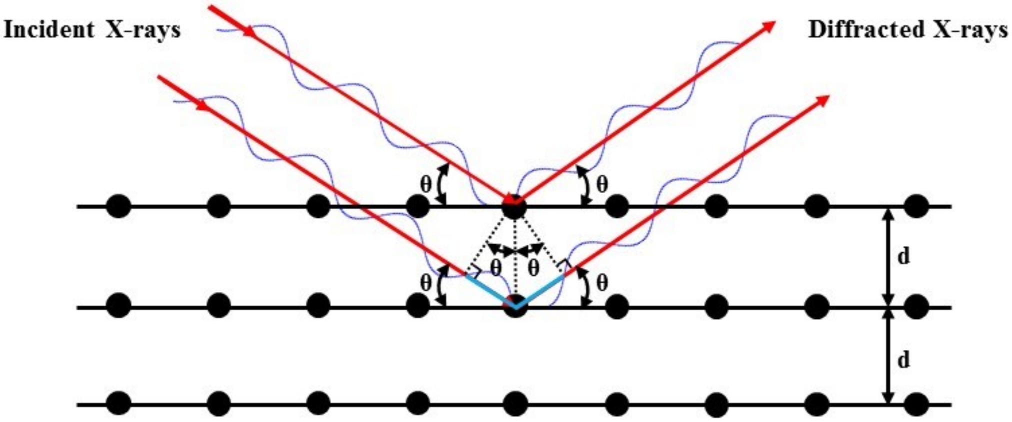

Figure 2.1 Constructive condition corresponding to Bragg's law.

In this thesis work, all XRD patterns were collected using a Rigaku Ultima IV diffractometer equipped with a Cu target, a dual position graphite diffracted beam monochromator and a scintillation counter detector. The X-ray generator accelerating voltage was set at 45 kV and the filament current was set at 40 mA. All XRD spectra were collected with a single step angle of 0.05° and a 3 second dwell time.

2.1.2 Pseudo-Voigt profile fitting

This thesis studies transitions from amorphous carbon to graphitic carbon, and, therefore, the final products may contain more than one carbon phases (*i.e.* amorphous carbon, turbostratic graphite, ordered graphite). To avoid confusion, amorphous carbon refers to non-organized carbon with broad XRD peaks, and both turbostratic and ordered graphite refers to graphitic carbons with sharp XRD peaks in this thesis. The XRD peaks of graphites were fit by using pseudo-Voigt profiles. The fit peak position was used to determine its corresponding plane spacing by using Bragg's law, which is an important factor indicating the graphitization level. The full width at half maximum FWHM of the fit peak was used to determine the extent of the crystallites (L_c and L_a) by applying the Scherrer equation:

$$L_c = (K \lambda) / (B_{002} \cos\theta_{002}), \qquad (2.3)$$

$$L_a = (K \lambda) / (B_{100} \cos\theta_{100}), \qquad (2.4)$$

where K is a scale factor (0.90 for L_c and 1.84 for L_a), B is FWHM of the 002 or 100 peak, and θ is incident angle corresponding to the 002 or the 100 peak.[110] Also, the relative area of the graphitic carbon 002 peaks or amorphous carbon 002 peak to the area of all fitted 002 peaks was used to determine the molar percent graphitic or amorphous carbon with respect to all the elemental carbon in the sample.

In addition to a polynomial background function, two or three pseudo-Voigt peaks were included in each fit depending on the graphitization level of graphite: turbostratic and ordered graphite 002 peaks with positions in the range of 26° - 27° and an amorphous carbon peak with a position of ~23°.

2.1.3 CARBONXS program

CARBONXS is a useful program developed by Shi *et al.* to fit the XRD patterns of graphites with different crystallinities.[111,112] There are two models integrated in this program: a one-layer model for less ordered graphitic carbons and a two-layer model for more graphitic carbons. Both models were used in this study depending on the graphitization level of each graphite sample. In this thesis, the model used for each fit is indicated in all figures showing CARBONXS fits. The one-layer model considers each layer as an independent entity. Starting from a layer at the "A" position, the next layer could be stacked in three ways: a random position (with a probability of P_r), or a "B" or "C" position (with equal probability of $(1-P_r)/2$; where A, B, and C refer to layer positions in hexagonal close-packed notation). Here, P_r indicates the fraction of random stacking per layer. The two-layer model considers two adjacent layers in AB stacking as the basic structure building block. AB stacking blocks could be stacked with neighboring blocks in three ways: 1), forming orderly ABAB stacking (Hexagonal 2H stacking, with a probability of $(1-2P_r-2P_{3R})/2$ per layer), 2) forming turbostratic disorder due to a random shift (with a probability of $2P_r$), or 3) forming ABCA stacking (Rhombohedral 3R stacking, with a probability of $2P_{3R}$). Here, P_r indicates the fraction of turbostratic disorder per layer and P_{3R} indicates the fraction of 3R stacking per layer. The fitting results from CARBONXS also contain other important structural parameters, such as the in-plane cell constant (a), the lateral extent of graphite layers (L_a), the in-plane strain (ζ), and the interlayer distance fluctuation ($<\delta^2>^{1/2}$). CARBONXS only can fit an average of the two sharp 002-peaks arising from ordered and turbostratic graphite. Therefore, the values of L_c and d_{002} obtained by CARBONXS for some graphites having overlapped ordered and turbostratic 002 peaks are not reliable. In this case, L_c and d_{002} were determined by the pseudo-Voigt method, as described above.

For each CARBONXS fit, a parabolic background polynomial was used, with variable scale factor between 20° (or 30°) and 80° 2θ. The fraction of low-strain regions (0) was fixed during fitting (values in parentheses). Variable parameters were: a, (2.46 Å), d_{002} (3.35 Å), average graphite crystallite layer numbers (M, 40), ζ (0), $<\delta^2>^{1/2}$ (0 Å), L_a (50 Å), P_r (0.5), P_{3R} (0), and preferred orientation parameter (0). Numbers in parentheses are initial values of each parameter. For different fitting, initial numbers might change. Details regarding these parameters and the CARBONXS program can be found in Reference [111,112].

2.2 Scanning electron microscopy (SEM)

Scanning electron microscopy is a technique used to investigate surface morphological information about a specimen.[113,114] SEM magnification can be adjusted from 10× to 300,000×, reaching nm level resolution.[115]

During operation, electrons are produced at an electron gun and are accelerated in a potential of 0.5 - 30 keV or thereabouts.[113] The electron beam is de-magnified by the lens system, consisting of condenser lenses and one objective lens, and is focused on the specimen surface. This process is conducted under a high vacuum environment. Among various interactions between incident electrons and atoms in the specimen, elastic and inelastic scattering of the impinging electrons are the elemental interaction processes. Elastic scattering of the electron is caused by its interaction with the electrical field of the nucleus and results in a deflection of the electron without a significant change in its energy, while the inelastic scattering of the electron is caused by its interaction with the electrical field of the specimen atoms' electrons.[113] After multiple interactions, electrons are emitted via a number of different processes, among which secondary electrons (SEs) and backscattered electrons (BSEs) are the main types. SEs are mainly ejected from the K-shell of the specimen atoms by inelastic scattering interactions with incident electrons. The ejection of

SEs occurs within several nanometers from the sample surface. SEs have a probable energy of < 50 eV, usually between 2 - 5 eV. BSEs are reflected out of the specimen by elastic scattering interactions with specimen atoms. Heavy elements reflect electrons more strongly than light elements and appear brighter in the image. BSEs have an energy between 50 eV and the primary electron energy.[114] Usually, SEs are used to describe the morphology of specimens while BSEs are used to detect contrast between areas with different chemical compositions.

By scanning the sample and collecting emitted SEs, an image displaying the morphology of the surface is created. The fraction of incident electrons transforming into BSEs strongly depends on the atomic number of the scattering atom, which directly affects the image brightness. Therefore, BSEs can be used to detect contrast between surfaces with different chemical compositions.

In this thesis work, particle size and morphology of samples were studied with a Phenom G2-pro Scanning Electron Microscope (Nanoscience, Arizona) and a Hitachi S-4700 FEG Scanning Electron Microscope in an SE mode with a working distance of 12.7 mm. All tested samples were powder samples. In preparation, a small amount of sample powder was placed on a double-sided conductive carbon tape on an aluminum stub. An air duster was used to remove the excess and loose powder on the carbon tape.

2.3 Energy dispersive X-ray spectroscopy (EDS)

Energy dispersive X-ray spectroscopy (EDS) analysis is the most common application of X-ray microanalysis.[116] As mentioned above, various interactions between incident electrons and atoms in specimen take place when high-speed electron beams strike the specimen in an SEM. Production of X-rays can take place when the electron beam has enough energy to ionize atoms.[116] For each atom, every shell has a unique energy level, determined by the atomic configuration of that element. Therefore, the emitted X-rays from different atoms are of different wavelength and energy. These characteristic X-rays can be detected and converted into a spectrum, indicating the presence of elements qualitatively and quantitatively. An element map can also be obtained if conducting EDS analysis within a chosen specimen area.

In this thesis work, EDS analysis was conducted with an Oxford Inca energy dispersive X-ray spectroscopy (EDS) analysis system equipped in a Hitachi S-4700 FEG SEM.

2.4 Focused ion beam (FIB)

Focused ion beam (FIB) is a technique that can be used for ablation of materials. The most popular ion source for FIB is a liquid metal ion source (LMIS), especially gallium. In a LMIS, Ga metal is placed in contact with a tungsten needle. Heated Ga wets the needle and flows to the tip, where the opposing forces of surface tension and electric field form the Ga into a cusp shaped tip called a Taylor-Gilbert cone.[117] Very focused ion beams (~5 nm) can be generated from the apex of the cone. When the Ga ion beams strike the specimen, various interactions take place, such as sputtering of ions and atoms, emission of secondary electrons, implantation of Ga ions, amorphization, *etc*. After sufficient ion impingement, the surface of the specimen can be eroded. This is useful for observation of the inner structure of the specimen.

In this thesis work, the ablation of graphites was conducted using a Hitachi FB-2000A FIB System with a liquid Ga source.

2.5 Transmission electron microscopy (TEM)

Transmission electron microscopy (TEM) is a technique in which a beam of electrons is transmitted through a specimen to form an image. Specifically, an ultrathin specimen is irradiated with an electron beam of uniform current density. After the interactions (elastic and inelastic scattering) between electrons and the sample, an electron-intensity distribution is imaged onto a fluorescent screen.[118] TEMs are capable of imaging at a significantly high resolution (~1 Å), due to the small de Broglie wavelength of electrons.

Besides imaging, selected area electron diffraction (SAED) is another core strength of TEM. By adjusting the magnetic lenses, a SAED pattern can be generated. This produces an image consisting of dots in the case of a single crystal, or a series of rings in the case of a polycrystalline or amorphous material. In the single crystal case, the SAED pattern is dependent on the orientation and the structure of the sample, providing information such as plane spacings and the space group symmetries in the crystal.[118]

In this thesis work, TEM images were taken using a Philips CM30 electron microscope. TEM samples were prepared by dispersing powders in methanol (ultrasonic for ~5 min) and placing a drop of the solution onto a lacey carbon film supported on a copper grid.

2.6 Raman spectroscopy

When light is scattered from a molecule, most photons are elastically scattered (Rayleigh scattering). The scattered photons have the same energy as the incident photons. However, a small fraction of photons (~ 1 in 10^7) is scattered at optical frequencies different from the frequency of the incident photons. The process leading to this inelastic scattering is termed Raman scattering, or Raman effect scattering. In quantum mechanics, Raman scattering is described as an excitation of molecules to a virtual state transition with nearly coincident de-excitation and a change in vibrational energy. Figure 2.2 shows the energy diagram of Raman scattering. At room temperature, the main initial state is the ground state, and the scattered photon will have lower energy than the incident photon. This is called Stokes scattering (Figure 2.2(a)) that is usually observed in Raman spectroscopy. A small fraction of the molecules is also in vibrationally excited states. Raman scattering from vibrationally excited molecules leaves the molecule in the ground state. This is called anti-Stokes scattering (Figure 2.2(b)). This anti-Stokes spectrum is always weaker than the Stokes spectrum, but both spectra usually contain the same information.[119]

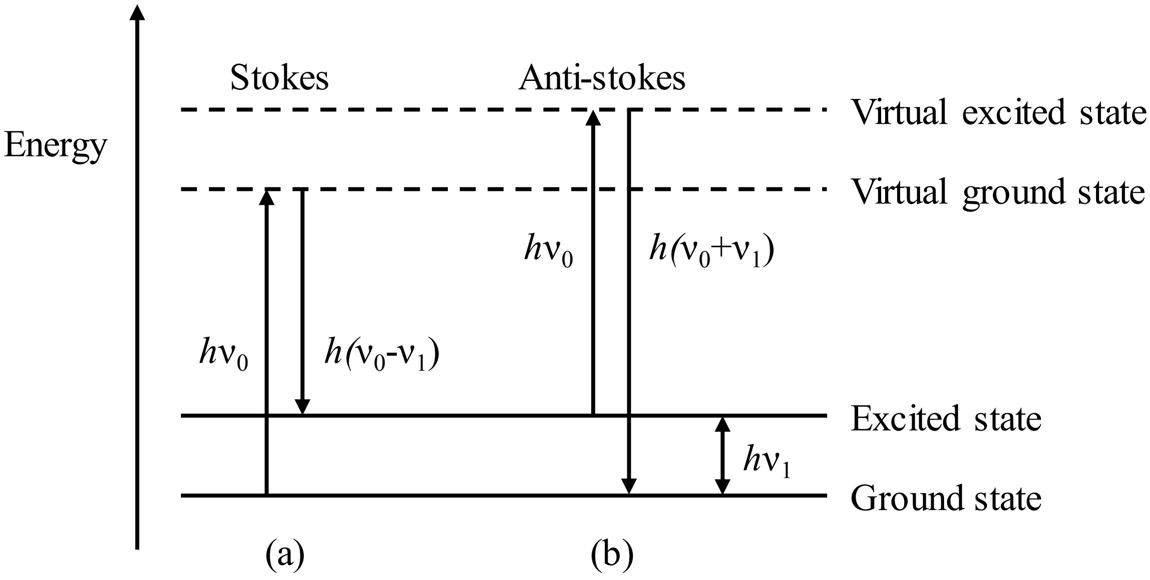

Figure 2.2 Energy level diagram of Raman scattering.

Raman spectroscopy is a powerful characterization tool to study graphite, which is non-destructive, fast, with high resolution and gives important structural and electronic information.[120] The Raman spectra of all carbon allotropes show only a few prominent features: a couple of very intense bands in the 1000 - 3000 cm^{-1} region and few other second-order modulations. Their shape, intensity and positions allow to distinguish an amorphous carbon from a graphitic carbon, and to estimate the content ratio of different carbon phases.[120]

In this thesis work, Raman measurements were performed using a HORIBA T64000 Raman spectrophotometer with a laser radiation wavelength of 532 nm and a power of 5 mW or 15 mW.

2.7 Inductively coupled plasma - optical emission spectrometry (ICP-OES)

Inductively coupled plasma optical emission spectroscopy (ICP-OES) is the most commonly used technique for determination of trace amounts of elements.[121] In an ICP-OES system, an inductively coupled plasma (ICP) is used to produce excited atoms and ions that emit electromagnetic radiation at wavelengths characteristic of specific elements, giving an optical emission spectrum.

In an ICP-OES instrument, a load coil surrounds the top end of a torch consisting of three concentric tubes, and is connected to a radio frequency (RF) generator. When RF powder is applied to the load coil, an alternation current oscillates within the coil at a rate corresponding to the frequency of the generator, causing RF electric and magnetic fields at the top of the torch. With Ar gas being directed through the torch, a spark is applied, stripping some electrons from Ar atoms. These electrons are accelerated by the RF electric and magnetic field. Then, these high-energy electrons in turn collide with other argon atoms and stripe off more electrons in a chain reaction, breaking down the Ar gas into a plasma, a co-existence of the positive ions, electrons, and neutral species.[122]

Most samples begin as liquids that are nebulized into an aerosol so as to be introduced into the ICP. The aerosol is carried into the center of the plasma by the inner argon flow. The high temperature (6000 - 10000 K) plasma first removes the solvent from the aerosol (desolvation), then decomposes the particles into a gas of individual molecules (vaporization) that are then dissociated into atoms (atomization). These molecules and atoms can be further excited and ionized. The light emitted by the excited particles is detected to obtain qualitative and quantitative information about the sample.[121,122]

In this thesis work, ICP-OES measurements were performed with a PerkinElmer Optima 8000. Each sample was placed in a 10 mL of aqua regia solution which was then diluted using 2 wt. % HNO_3 (prepared from concentrated HNO_3 (70 wt. %), Aldrich) prior to measurements.

2.8 Gas pycnometry

Gas pycnometry is a method to obtain accurate, absolute, and apparent volume of solid materials based on the Archimedes principle of displacement of an inert gas medium, such as nitrogen, argon, or helium. This method is non-destructive so that the tested samples can be retrieved. For gas pycnometry, a dry solid sample of known mass (m_s) is placed in a sample chamber (of known volume V_s). The sample chamber is connected with a reference chamber (of known volume V_r) through a valve. First, the sample chamber is isolated from the reference chamber and filled with an inert gas up to a certain pressure. The pressure decreases and reaches equilibrium (P_i) at a certain time as a result of gas penetration into the pore structure of the sample. Then the valve connecting the two chambers is opened, and the inert gas flows from the sample chamber to the reference chamber. When equilibrium is reached again, a new pressure is recorded (P_f). The solid volume of the sample V_{Solid} can be determined by:

$$V_{Solid} = V_s - \left(\frac{P_f}{P_i - P_f}\right) \times V_r. \qquad (2.5)$$

Then the density of the sample can be determined by:

$$\rho = \frac{m_s}{V_{Solid}}. \qquad (2.6)$$

In this thesis work, sample densities were measured using a helium pycnometer (AccuPyc II 1340, Micrometritics).

2.9 Brunauer-Emmett-Teller (BET) method

Surface adsorption of gas on solids occurs by two mechanisms: physisorption and chemisorption.[123] Physisorption involves relatively weak van der Waals forces, and therefore the desorption can be induced by simply increasing the temperature. In contrast, chemisorption involves stronger chemical bonding forces and it requires a great deal of energy to remove the adsorbed species. The Brunauer-Emmett-Teller (BET) method is the most popular method for surface area analysis based on the reversible physisorption of gas on a solid surface.

At the gas-solid interface, the amount of adsorbate is described by the adsorption isotherm. There are six major classifications of adsorption isotherms.[123] BET works for type II and IV isotherms (between 0.05 – 0.3 of relative pressure), which are applicable to the majority of materials.[124]

BET theory was derived by adopting the Langmuir mechanism combining some simplifying assumptions for multilayer adsorption.[123] In operation of the BET method, the solid sample must be cooled down to the boiling point of the gas (usually N_2). An equation is used to estimate the volume of the adsorbed monolayer gas molecules, from which surface area can be calculated.

In this thesis work, specific surface area was determined by the BET method using a Micromeritics Flowsorb II2300 surface area analyzer (single point).

2.10 Electrochemical techniques

The voltage (V) of a Li-ion cell is determined by:

$$V = V_{positive} - V_{negative}, \qquad (2.7)$$

where $V_{positive}$ and $V_{negative}$ are the electric potentials of the positive and negative electrodes, respectively. Capacity is defined as the total amount of electrical charge passed through a cell during charge or discharge and is measured in units of coulombs or milliampere-hours (mAh). The gravimetric or specific capacity (Q) of a material is the capacity per unit mass of the active material in units of mAh g^{-1}, while volumetric capacity is measured in units of Ah L^{-1}. The C-rate indicates the cycling current. For instance, a C/n rate corresponds to the current required to charge or discharge a cell in n hours.

When cycling Li half-cells, a constant current, constant voltage (CCCV) method is usually used to mimic the cycling protocol of commercial Li-ion cells. In this procedure, Li half-cells are first discharged (lithiation of the working electrode) at a constant current (CC) while the cell voltage keeps decreasing to a voltage limit. Then Li half-cells are discharged at this constant voltage (CV) until the current decreases to a current limit. After the CV step, cells are charged (delithiation of the working electrode) at the same constant current (CC) to a desired upper voltage limit. These form a full cycle.

Electrochemical performance of cells can be displayed in various forms. The main forms studied in this thesis work are cycling performance curves (Q *vs.* cycling number), voltage profiles (V *vs.* Q), and differential capacity curves (dQ/dV *vs.* V). From a cycling performance curve, researchers can derive information of charge/discharge capacity for each cycle, irreversible capacity, coulombic efficiency (CE), and cycling stability. Figure 2.3 shows a typical voltage profile and a differential capacity curve of a Li half-cell with a graphite working electrode. Typically, plateaus in a voltage profile and sharp peaks in a differential capacity curve are indicative of two-phase regions, while sloping regions in a voltage curve usually indicate single-phase regions. The staging phenomenon of graphite introduced in Chapter 1.2.1 can be observed in Figure 2.3. During discharge (lithiation) and charge (delithiation) of a Li half-cell, there are three plateaus in the voltage profile, indicating different phase-transitions as labelled, corresponding to sharp peaks in the differential capacity curve. If the crystallinity level of the cycled graphite is low (*i.e.* containing significant amount of turbostratic or amorphous component), these features will not be as pronounced or may be missing altogether. Therefore, these electrochemical performance graphs are significant indicators of the graphitization level. There is

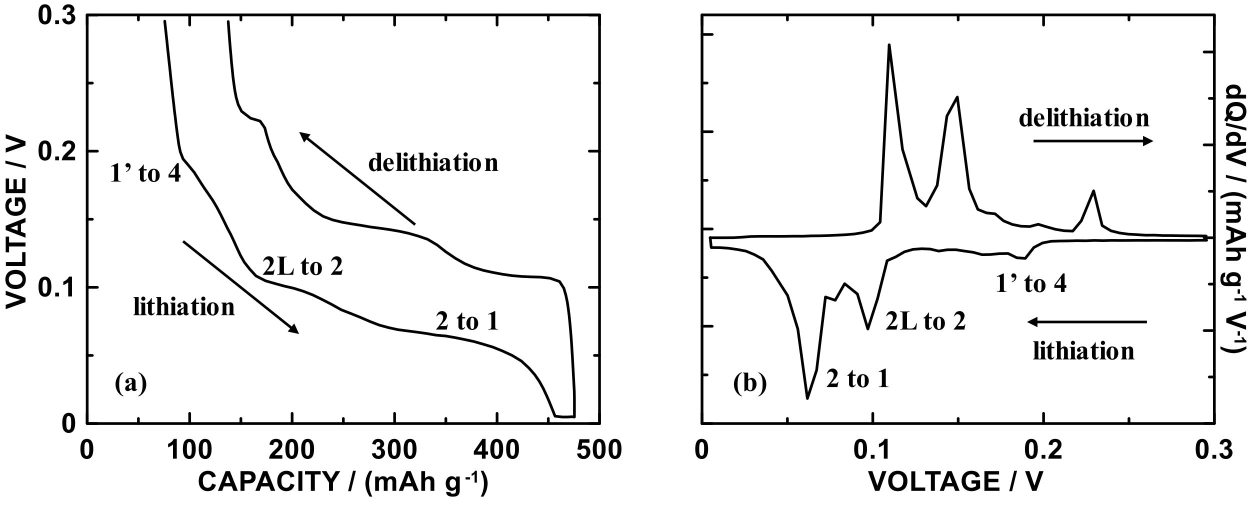

Figure 2.3 Voltage profile and differential capacity curve of graphite measured in a Li half-cell.

also a difference between the lithiation and delithiation voltages (Figure 2.3(a)), which is named hysteresis. Hysteresis is a significant factor accounting for the energy loss and low battery efficiency, and is also an indicator of battery impedance.

In this thesis work, Li-ion half-cells used to evaluate active materials were made and tested as follows. Electrode slurries containing active materials (catalyzed graphite, commercial graphite, hard carbon, *etc.*), carbon black (C-NERGY Super-C65, Imerys Graphite and Carbon), and polyvinylidene difluoride (PVdF grade 301F, KYNAR) binder in N-methyl-2-pyrrolidinone (NMP, Sigma-Aldrich, 99.5%) were mixed for 1 h using a planetary ball mill (Retsch PM 200) with four WC balls (11 mm in diameter) at 100 rpm. The weight ratio of active materials: carbon black: binder was 90: 5: 5 or 90: 2: 8. A thin layer of slurry was coated onto a Cu foil (Furukawa Electric, Japan) using a ~0.1 mm coating bar and dried in air at 120 °C for 1 h. This thesis involves different types of active materials and each material may require different electrode preparation steps. Further details regarding preparation will be introduced in following chapters. Disk electrodes (~13 mm in diameter) were punched from the coated foil and were transferred into an argon-filled glove box. Each electrode was assembled in a 2325 coin-type cell with a lithium reference/counter electrode and an electrolyte composed of 1 M $LiPF_6$ (BASF) in a solution of monofluoroethylene carbonate, ethylene carbonate, and diethyl carbonate (volume ratio 1:3:6, battery grade, all from BASF).[125] Two layers of separators (Celgard 2300) and two copper spacers were used in each Li half-cell. Figure 2.4 shows the configuration of a typical half-cell used in this thesis work. Li half-cells were cycled at 30.0 ± 0.1 °C using a CCCV method with a MACCOR Series 4000 Automated Test System at a C/10 rate and trickled discharged to C/20 for the first cycle, and a C/5 rate and trickled discharged to C/10 for all subsequent cycles, in a potential range of 0.005 - 0.9 V. In some chapters, cells were also cycled at different C-rates (*e.g.* C/5, C/2, 1C, 2C, 5C) and C-rates are labelled in all cell cycling figures. C-rates were calculated by assuming a theoretical graphite capacity of 372 mAh g^{-1} and amorphous carbon capacity of 200 mAh g^{-1}.

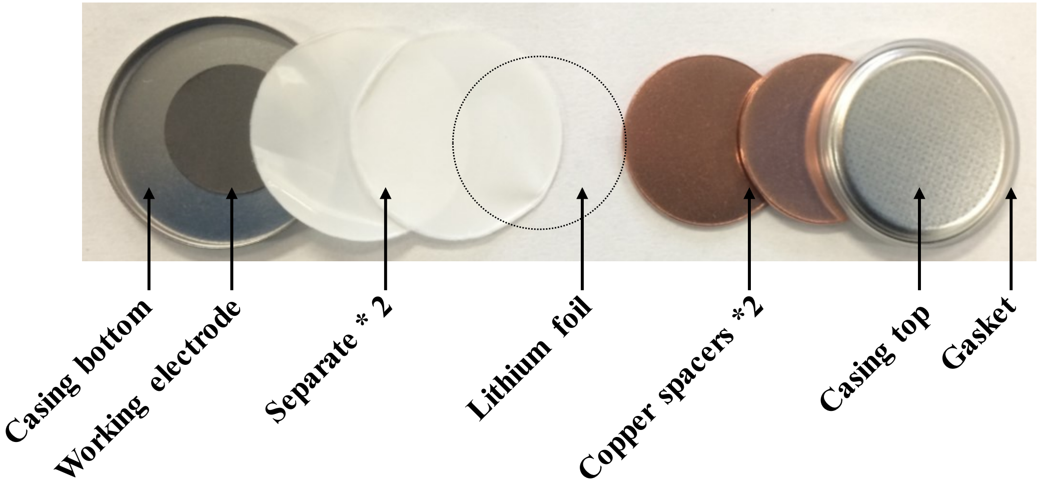

Figure 2.4 Exploded view of the 2325 coin-type cell used in this thesis work.

Chapter 3 Voronoi-Tessellated Graphites (VTGs) Grown from Ground C-Mg Mixtures

3.1 Introduction

As introduced in Chapter 1, it is desirable to find catalysts that work equally well as Fe for catalytic graphitization (effective for both graphitizable and non-graphitizable carbon at low temperature; resulting in high graphitization level), but that could be easily removed and even recovered from the graphite product. After a comprehensive survey, it was found that Mg is a promising candidate.

This chapter describes a method in which a conventionally non-graphitizable hard carbon derived from glucose can be graphitized at low temperatures with a Mg catalyst that can be easily removed. Most graphite products in this chapter are made from a ground carbon-magnesium mixture. The resulting graphite has a unique microstructure containing Voronoi-tessellations. This represents a new type of graphite microstructure. Hereafter, graphites made from the ground carbon-magnesium mixtures are termed as Voronoi-tessellated graphites (VTGs).

The majority of this work was adapted from the following peer-reviewed article and patent application:

L. Zhao, X. Zhao, L.T. Burke, C. Bennett, R.A. Dunlap, M.N. Obrovac, Voronoi-Tessellated Graphite Produced by Low-Temperature Catalytic Graphitization from Renewable Resources, ChemSusChem 10 (2017) 1–11.

Mark Obrovac, Leyi Zhao, and Xiuyun Zhao, Graphitic Materials and Methods of Making Same, U.S Patent Application No. 62/438,591, Filed December 23, 2016.

Dr. X. Zhao and M.N. Obrovac first found the graphitization effect of Mg with the help of L. T. Burke. L. Zhao (this report author) conducted most of the work of the present study, including preparation and characterization of samples and analysis of data. Prof. C. Bennett conducted the TEM measurements and TEM data analysis.

Minor changes have been made. Electrochemical measurement was re-conducted between 0.005 – 0.9V because the reactions between 0.9V and 2V are not associated with graphite lithiation/delithiation but are mainly associated with electrolyte decomposition and other side reactions. Carbon and Mg powders were also heated in a tube without mixing to test if the gas-phase Mg is effective in catalyzing graphitization.

3.2 Experimental

3.2.1 Synthesis of Voronoi-tessellated graphites (VTGs)

Glucose (96%, Aldrich) was first dewatered by heating in air for 24 h at 180 °C and then heated under an Ar flow for 3 h at 1100 °C. The resulting hard carbon was ground for five minutes with Mg powder (HART METALS, INC., -325 mesh) in a 1:1 C: Mg mole ratio using a mortar and a pestle in an Ar filled glove box. Hard carbon/Mg mixtures were heated in sealed stainless-steel tubes filled with Ar at 800, 900 or 1000 °C for 1 h or 3 h, resulting in the formation of VTG/Mg mixtures. To dissolve the Mg catalyst after heat-treatment, ~2 g of the VTG/Mg mixture was placed in a solution of 100 mL of 2 M HCl (prepared from 37 wt. % HCl, Aldrich) and ~2 mL of ethanol (98%, Aldrich) for 12 h with stirring. The ethanol reduces the surface tension of the acid solution, increasing its wetting ability. After reacting with HCl, the products were transferred into a Büchner funnel (with a Whatman circle filter paper, qualitative, 44.25 mm in diameter) and were washed with 2 M HCl five times and then washed repeatedly with distilled water until the pH of the supernatant was about seven. Finally, the products were dried in air for 3 h at 120 °C.

3.2.2 Mg vapor graphitization

Hard carbon made from glucose was ground for five minutes in an Ar-filled glovebox. Mg and carbon powders were loaded into separate ends of an argon-filled stainless-steel tube (100 mm, OD 12.70 mm, ID 9.40 mm, and sealed with Parker-A-lok caps) without mixing. Then the tube was heated at 1000 °C for 3 h. During the whole process, the tube was kept horizontal, to prevent the mixing of Mg and hard carbon.

3.2.3 Characterization

Products were characterized by using many techniques: scanning electron microscopy (SEM), energy dispersive X-ray spectroscopy (EDS), focused ion beam (FIB) technique, transition electron microscopy (TEM), X-ray diffraction (XRD), Brunauer-Emmett-Teller (BET) surface analysis, inductively coupled plasma-optical emission spectroscopy (ICP-OES), Raman spectroscopy, and pycnometry, with the equipment introduced in Chapter 2. Pseudo-Voigt profiles were used to fit some graphite XRD patterns, details of this fitting procedure have been described in Chapter 2. Electrochemical measurements in Li-half cells were performed to confirm the graphitization level of VTGs by observing staging transitions during lithium intercalation. Details of slurry making and cell assembly and cycling have been described in Chapter 2.

3.3 Results

3.3.1 Morphological Characterization

Figure 3.1(a-e) show SEM images of how the hard carbon precursor transforms during catalytic graphitization at different temperatures. The hard carbon precursor is mainly composed of carbon particles with smooth and flat surfaces (Figure 3.1(a)). After heating at 800 °C for 1 h (Figure 3.1(b)), spheroidal particles appear on the hard carbon surface. Each spheroid is surrounded by a circular region on the carbon surface, indicting a reaction front. These circular

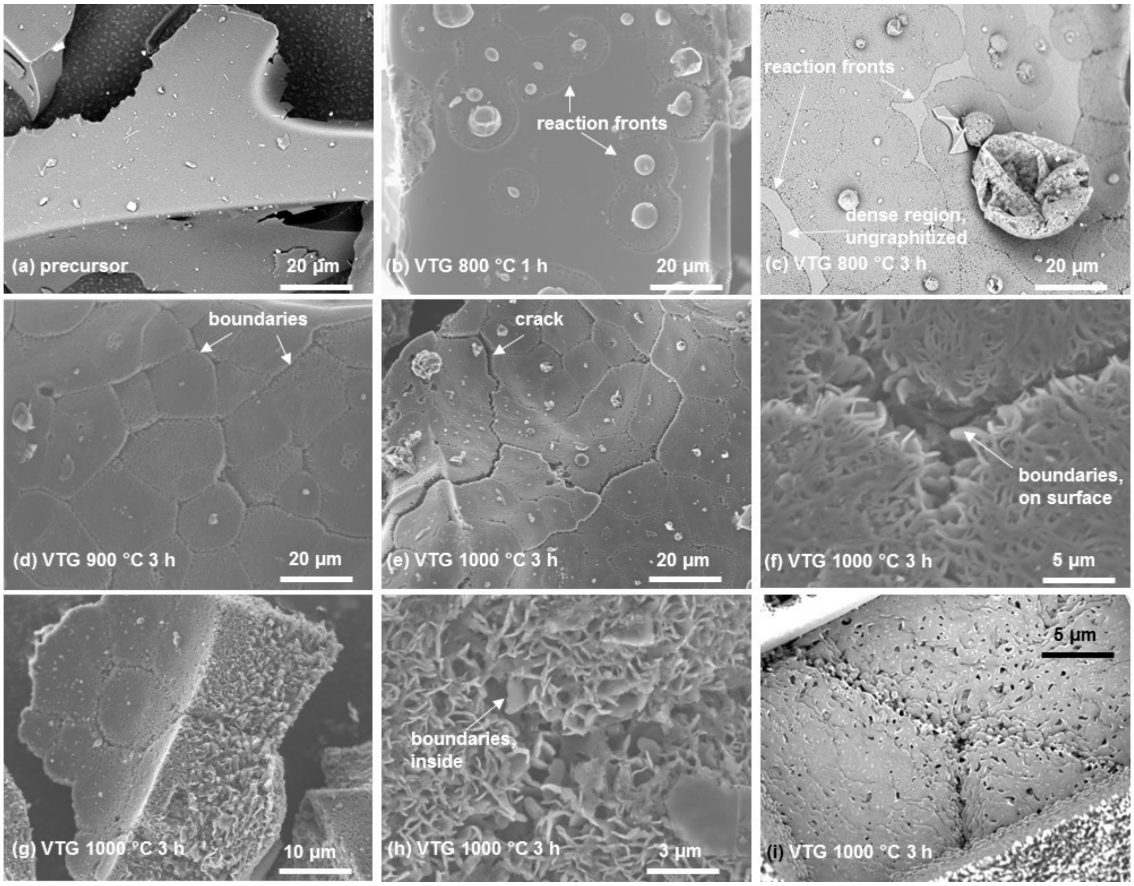

Figure 3.1 SEM images of (a) the carbon precursor, (b-e) VTGs (heat methods indicated), (f) a junction of Voronoi tessellation regions on the surface of the VTG particle made at 1000 °C for 3 h. (g-i) SEM images revealing the interior of the VTG particles made at 1000 °C for 3 h: (g) a broken particle edge, (h) a junction of Voronoi tessellation regions in the interior of a particle, and (i) a FIB cross section parallel to the particle surface at a depth of ~10 µm.

regions comprise sheets that radiate from the spheroidal particles in all directions. Outside of these regions the carbon remains similar to the starting hard carbon precursor. As the graphitization progresses (800 °C, 3 h), these reaction fronts expand in all directions, transforming most of the particle into radiating graphite sheets (Figure 3.1(c)). At higher temperatures, the process proceeds more quickly. After processing at 900 °C for 3 h (Figure 3.1(d)) the reaction has progressed to completion. All the reaction fronts meet each other, forming boundaries of a Voronoi-tessellated structure. This type of Voronoi-tessellated structure has not been previously observed during graphitization. At higher temperatures (1000 °C, 3 h, Figure 3.1(e)) the boundaries separating the tessellations expand and cracks appear. Figure 3.1(f) shows more details of the boundaries of Voronoi-tessellations, which are composed of irregular sheets aligned perpendicularly to the particle surface. Figure 3.1(g) shows an SEM image of a cross-section formed at a broken edge of a VTG particle made at 1000 °C for 3 h. The image shows that the tessellations extend from the centroid of the surface into the bulk of the particle in three dimensions. The Voronoi-tessellated regions are composed of graphite sheets that are small and compact near the particle surface and become larger and diffuse as they extend into the particle interior. All the tessellated regions observed from SEM images were nucleated from particle surfaces. No evidence of Voronoi-tessellations growing from the interior of particles was observed. Figure 3.1(h) shows the boundary region between two Voronoi-tessellations in the interior of a particle in detail, which is composed of irregular sheets. An FIB cross section of the particle to a depth of about 10 μm was imaged in order to understand the nature of the interior of the tessellated regions. Figure 3.1(i) shows the SEM image of the FIB cross section. The interior of the tessellated regions comprises graphite sheets that are terminated by hexagonal graphite platelets at each tessellation boundary.

To further understand the growth of the Voronoi-tessellated structure, EDS mapping images of Mg and C for the ground C/Mg mixtures (before graphitization) and the VTG/Mg mixtures (after graphitization and before reacting with HCl) were collected. In the ground C/Mg mixture (Figure 3.2(a-c), spherical Mg particles (< 30 μm) and platelet-like carbon particles (> ~50 μm) are mixed together with clear boundaries. On the hard carbon surface (Figure 3.2 (d-f)), there are randomly distributed small Mg particles (< 2 μm). Figure 3.2(g-i) show SEM images and EDS mapping images of the VTG/Mg mixture made by heating at 800 °C for 3 h. The reaction fronts expanding from the central spheroidal seed particles are Mg rich and C poor, while the tessellated regions themselves are composed of carbon and are essentially Mg-free. The central seed particles themselves also appear to be Mg-rich. The same Mg distribution is also apparent for the complete Voronoi-tessellated structure in the VTG (1000 °C, 3 h) sample (Figure 3.2(j-l)).

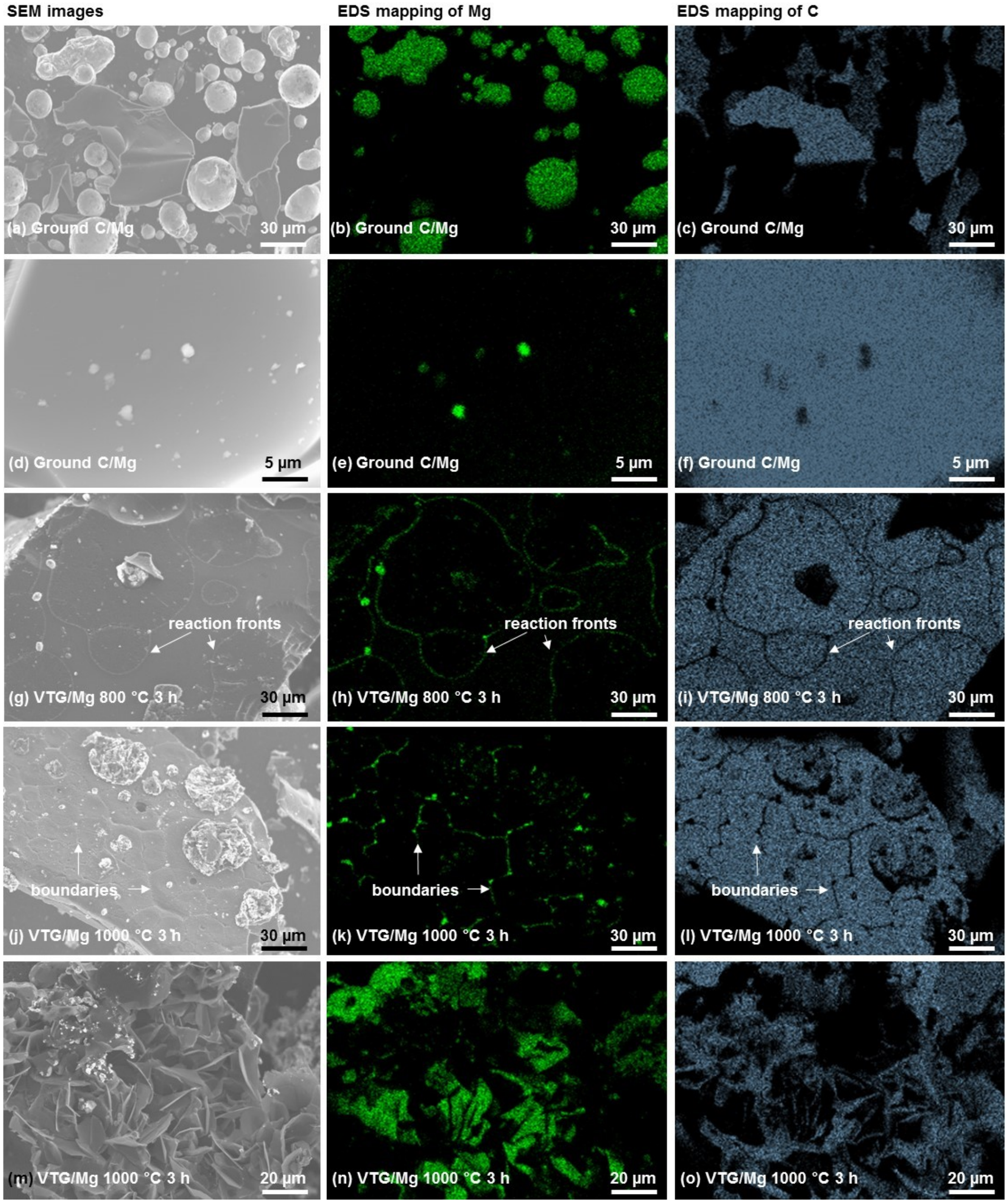

Figure 3.2 SEM images of (a, d) the ground C/Mg, (g, j, m) the VTG/Mg mixtures made by different heat-treatments as indicated and corresponding EDS mapping images of (b, e, h, k, n) magnesium (green) and (c, f, i, l, o) carbon (blue) elements.

Figure 3.3(a-e) show SEM images of spheroidal seed particles located on the surface of VTGs made with different heat-treatments. The VTG (800 °C, 1 h) sample (Figure 3.3(a)) comprises many small (<10 μm in diameter) particles, some with what appears to be graphite platelets on their surface. As the graphitization progresses, the spheroidal particles of the VTG (800 °C, 3 h) sample grow to be larger than 10 μm in diameter (Figure 3.3(b)). The surface of the spheroidal particles is made up of crystalline hexagonal graphite platelets with their basal plane being tangential to the spheroidal particle surface. After heating at 900 °C for 3 h, some broken spheroidal particles were observed (Figure 3.3(c)), and at higher temperature (1000 °C, 3 h) the broken spheroidal shells become larger (Figure 3.3(d-e)). Attached to the inner surface of the spheroidal shells are hexagonal graphite platelets arranged perpendicularly to the shell surface, but with otherwise random orientations with respect to each other (Figure 3.3(c-e)). The spheroidal shells are most common on the surface of the VTGs heat-treated at temperatures of 900 °C and1000 °C for 3 h, especially in the VTG (1000 °C, 3 h) sample. Some of these hexagonal platelets contain rotational stacking faults (Figure 3.3(f), the VTG (1000 °C, 3 h)), which is common for graphite platelets, as observed by Double *et al.*[126] Some of the platelets are perfect hexagons with no observable stacking faults.

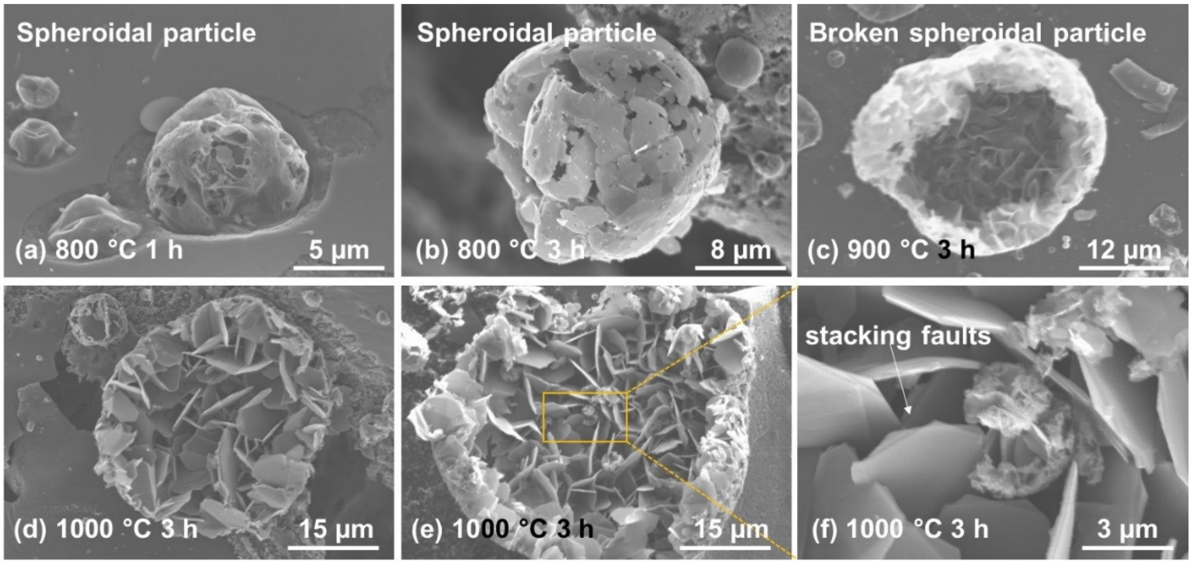

Figure 3.3 SEM images (a-e) showing the growth of spheroids found on the VTG particles made by different heat-treatments as indicated, and (f) showing the hexagonal platelets inside of spheroids found on the VTG (1000 °C, 3 h) particles.

Table 3.1 Mg content (by ICP-OES), BET specific surface areas, and pseudo-Voigt fitting results of VTGs. The error of the fitting results are calculated based on multiple measurements of the 1000 °C, 3 h sample.

Synthesis Condition	Surface Area $(m^2\ g^{-1})$	Mg Content (wt. %)	Amorphous Carbon (at. %)	Graphite (at. %)	d_{002} (Å)	L_c (Å)	χ^2
800 °C, 1 h	7.2	-	73.7(7)	26.3(7)	3.400(5)[a]	186(3)	0.5 (1)
800 °C, 3 h	24.2	0.012(1)	32.6(7)	67.4(7)	3.400(5)[a]	204(3)	0.6 (1)
900 °C, 3 h	81.9	0.009(1)	1.4(7)	98.6(7)	3.400(5)[a]	222(3)	0.9 (1)
1000 °C, 3 h	87.9	0.019(1)	0.9(7)	99.1(7)	3.400(5),[a] 3.339(2)[b]	222(3)	0.4 (1)

[a] Turbostratic graphite. [b] Ordered graphite.

The numerous sheets in the Voronoi-tessellated structures and the hexagonal platelets suggest a high surface area. Indeed, the BET surface areas of the VTGs prepared at 900 and 1000 °C for 3 h were found to be above 80 $m^2\ g^{-1}$ (Table 3.1), much higher than that of the hard carbon precursor (2.5 $m^2\ g^{-1}$). In comparison, the surface areas of VTGs made at 800 °C were 7.2 $m^2\ g^{-1}$ (1 h) and 24.2 $m^2\ g^{-1}$ (3 h). There is a clear increasing trend in surface area from the hard carbon to VTG and with higher temperature and longer heating time. Despite its high surface area, the bulk density of the VTG made at 900 °C was measured to be ~2.27 g mL^{-1}, close to a highly graphitic carbon.

Figure 3.2(m-o) show the SEM image and EDS mapping images of a spheroidal shell on the surface of the VTG/Mg (1000 °C, 3 h) sample. It comprises hexagonal graphite platelets that are uniformly covered in Mg, suggesting the shells once contained Mg. The mechanism involved creates a reaction front of Mg that emanates from the spheroidal seed particles and advances into ungraphitized carbon, leaving graphite in its wake. The distribution of elements observed by EDS suggests a mechanism consistent with that observed by Fitzer *et al.*, in which the carbon becomes solvated in the Mg catalyst followed by precipitation of the graphite.[19]

Figure 3.4(a) shows a TEM image of hexagonal platelets found within the spheroidal particles of the VTG (1000 °C, 3 h) sample. The selected area electron diffraction (SAED) patterns confirm the graphite structure for these platelets. In the central, thicker regions of the platelets such as the blue circle zone in Figure 3.4(a), complicated SAED patterns are often observed which

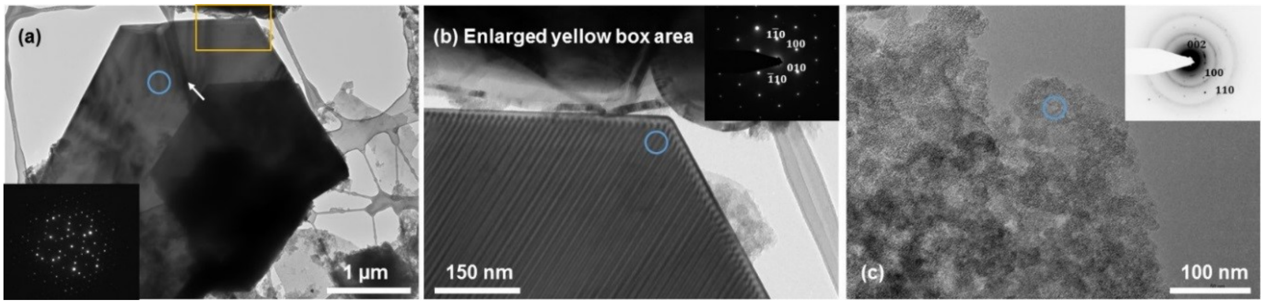

Figure 3.4 TEM images of the hexagonal platelets from the spheroidal-shell particles of the VTG (1000 °C, 3 h), and (b-c, insert) the SAED patterns of the areas indicated by blue circles.

are the result of multiple diffraction from misoriented layers (*i.e.* turbostratic disorder). As mentioned above, this type of stacking fault is common for graphite platelets.[126] In some typically thinner regions, the graphite platelets are highly ordered, as shown in Figure 3.4(b). The pattern of parallel fringes in Figure 3.4(b) and the hexagonal spot pattern of the SAED pattern (Figure 3.4(b, insert)) suggest a highly ordered crystalline graphite structure. Based on the SAED pattern, the lattice constant is determined as a = 2.46 ± 0.10 Å, typical of a highly ordered graphitic structure. The alternately dark-and-bright stripes indicated by an arrow are likely related to a Moiré pattern caused by the displacement of multiple diffracting layers or twinning defects. The VTG particles were also found to comprise nanocrystalline graphite. Figure 3.4(c) shows a region of polycrystalline carbon in the VTG (1000 °C, 3 h) sample. The SAED pattern (Figure 3.4(c, insert)) has a narrow ring pattern which has been indexed to graphite. Diffraction spots indicate the presence of larger crystallites within the aperture, while the diffuse rings are indicative of nanocrystalline graphite (15-20 nm). Here, the ring indexing is shown in an image that is greyscale-inverted for clarity.

3.3.2 Structural Characterization

An XRD pattern of pyrolyzed glucose prior to graphitization is shown in Figure 3.5(a, top panel), and is typical of a disordered non-graphitizable carbon (hard carbon). After the pyrolyzed glucose is ground with Mg and prior to heat-treatment, peaks from the Mg catalyst become dominant (Figure 3.5(a, bottom panel)). Figure 3.5(b) shows XRD patterns of the VTG/Mg samples after different heat-treatments and prior to Mg removal with HCl. After heating at 800 °C for 1 h, a peak at about 26°, corresponding to the graphite 002 peak, becomes visible. Apparently, the catalytic conversion of hard carbon has already started at this temperature in only one hour. As the heating time and temperature increase, a stronger graphite 002 peak is visible, suggesting a higher level of graphitization. Also visible in Figure 3.5(b) are peaks from the Mg catalyst. The lattice constant of the Mg phase after heat-treatment remains almost the same for all samples and is identical to that of pure Mg. No Mg-C solid solution or carbide phase was evident in these room temperature XRD patterns. MgO impurity peaks are also visible in some XRD patterns. MgO may arise from reaction of the Mg catalyst with oxygen impurity in the carbon precursor or with metal oxide on the inner surface of the stainless-steel reaction tubes.

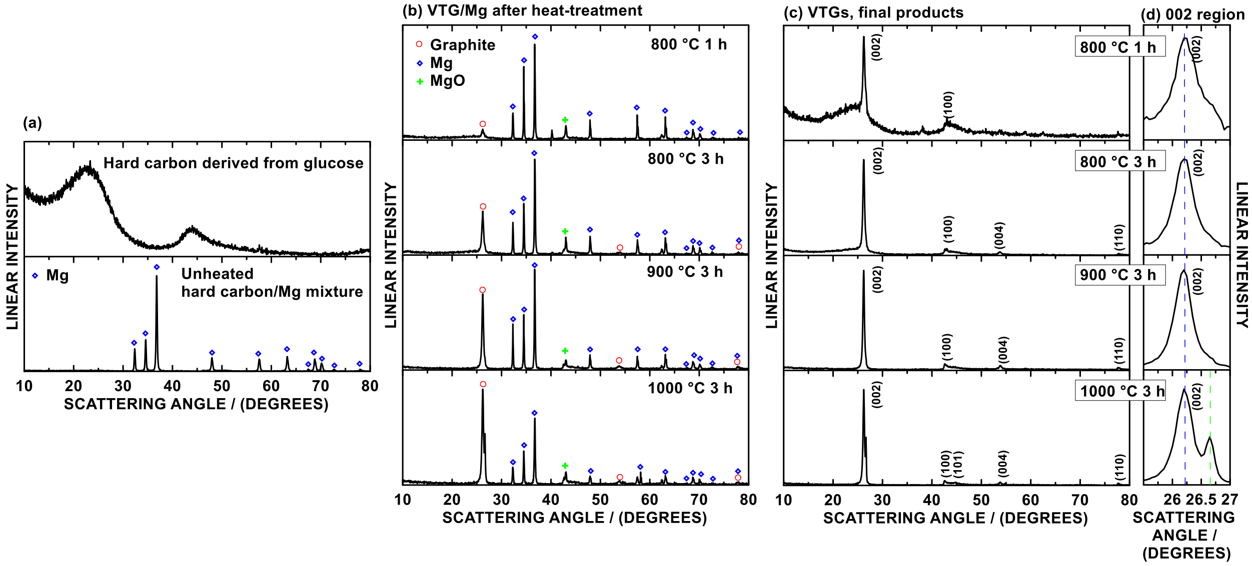

Figure 3.5 XRD patterns of (a) the hard carbon precursor and the unheated hard carbon/Mg mixture after grinding, (b) the VTG/Mg mixtures after heat-treatment and before Mg removal, (c) the VTGs and (d) 002 peak regions in (c). The 002 peak positions of turbostratic and ordered graphite are indicated by blue and green dashed lines, respectively, in (d).

Figure 3.5(c) shows XRD patterns of the final VTG products after the Mg was removed with HCl. No Mg or MgO peaks are present, suggesting that all the Mg and MgO impurities have been removed. This was also confirmed by the ICP-OES measurements. The Mg content in the VTGs was found to be 0.009-0.019 wt. % (Table 3.1). As a comparison, the Mg content in the sugar hard carbon precursor was determined to be 0.012 wt. %. Therefore, the level of residual Mg content in the VTGs is negligible. The XRD pattern of the VTG (800 °C, 1 h) in Figure 3.5(c) comprises peaks from graphite, and also a large broad peak between 10°-35°, suggesting that a significant amount of amorphous carbon exists in this sample. The broad amorphous carbon peak becomes smaller as the heat-treatment time increases from 1 h to 3 h. The XRD patterns of the VTGs synthesized above 800 °C are comprised almost completely of crystalline graphite peaks and show no other phases. Figure 3.5(d) shows an enlarged 002-peak region of each VTG XRD pattern. All VTGs have a sharp peak at around 26.25°, which has been ascribed to turbostratic graphite.[15] The VTG (1000 °C, 3 h) sample also has a clear sharp peak at ~26.7°, arising from an ordered graphitic phase.[15]

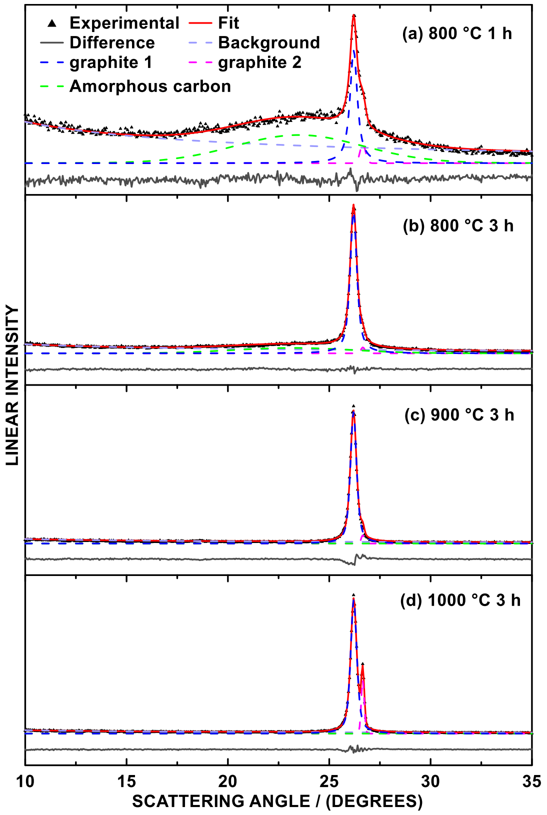

Figure 3.6 Pseudo-Voigt fitting of VTGs.

Figure 3.6 shows the XRD patterns of the VTGs fit by using pseudo-Voigt profiles between 10° - 35°. Three pseudo-Voigt peaks were included in each fit: two peaks with positions in the range of 26°-27° were used to fit the graphite 002 peaks (turbostratic and ordered graphite peaks), and one peak with a position of ~22° was used to fit the amorphous carbon peak. Table 3.1 lists quantitative values of the atomic percent of each carbon component, d_{002}, L_c, and the goodness of fit (χ^2) for each sample. The VTG (800 °C, 1 h) sample already contains a significant amount of graphitic carbon for a sample made at this temperature and for such a short period of time (26.4 at. %). Heating for only 3 h at this low temperature results in the conversion of most of the carbon into graphite (67.31 at. %). The VTG (900 °C, 3 h and 1000 °C, 3 h) samples are almost completely composed of graphitic carbon. These increasing trends of graphitization with heating time and temperature are consistent with SEM observations of the growth of the graphitization zones (Voronoi-tessellations). The d_{002} values corresponding to the turbostratic graphite are the same for all VTGs, while the d_{002} corresponding to the ordered graphite in the VTG (1000 °C, 3 h) is smaller, indicating a higher degree of crystallinity, and is consistent with d_{002} values of highly ordered graphites.[112] L_c was found to increase with heating time and temperature, indicating an increasing graphitization level. However, all values of L_c are small ($L_c \approx 186$ - 222 Å) compared to those measured by Shi *et al.* for conventionally made graphites (*e.g.* $L_c \approx 440$ - 670 Å), which reflects the thin flake morphology of the graphites made here.[112]

To determine the degree of ordering obtained in the graphitic phase, the XRD patterns of VTG samples were also fit using a one-layer model with the CARBONXS software developed by Shi *et al.*, as described in Chapter 2.[112] VTGs made at 800 °C contain significant amorphous carbon, which CARBONXS is unable to fit. Therefore, only the fitting results of VTGs made at 900 °C and 1000 °C were analyzed. Figure 3.7 shows the fit obtained for the VTG (1000 °C, 3 h) sample XRD pattern. Table 3.2 lists the probability of random stacking (P_r), in-plane cell constant (a), lateral extent of graphite layers (L_a), in-plane strain (ζ), interlayer spacing fluctuation ($<\delta^2>^{1/2}$), and the goodness of fit (χ^2) for each fit. CARBONXS only could fit an average of the two 002 peaks arising from ordered and turbostratic graphite. Therefore, L_c and d_{002} were not determined by this method, but were instead determined by fitting the 002 peaks by using pseudo Voigt functions, as described above. The VTG (1000 °C, 3 h) sample has a high degree of graphitization with a value of P_r that is close to those reported for conventional artificial graphites prepared with soft carbon precursors above 2000 °C.[111] For both VTGs made at 900 and 1000 °C, the in-plane cell constants are all close to the theoretical value. In-plane strain and interlayer spacing fluctuation of both samples are very low, characteristic of highly graphitic carbons. Both samples have high L_a values that are consistent with L_a values of conventionally made artificial graphites.[112] No rhombohedral 3R stacking peaks (*e.g.* 3R (101) at 43.5°, or 3R (012) at 46.3°) could be detected in any of the VTGs. A higher degree of graphite ordering might be achievable at higher temperatures or longer heating times.

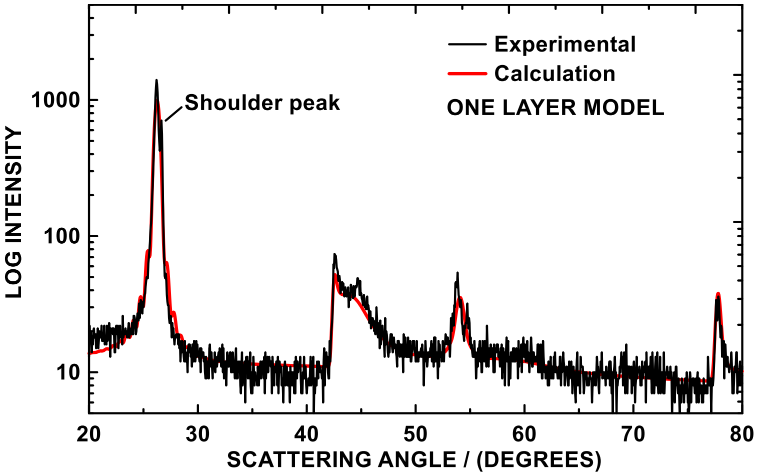

Figure 3.7 XRD pattern of VTG (1000 °C, 3 h) and its fit by CARBONXS.

Table 3.2 CARBONXS fitting results of VTGs.

Synthesis Condition	P_r at. %	a (Å)	L_a (Å)	ζ	$<\delta^2>^{1/2}$ (Å)	χ^2
900 °C, 3 h	60(9)	2.456(1)	219(3)	0.002(7)	0.113(7)	0.76(1)
1000 °C, 3 h	45(8)	2.457 (1)	235(1)	0.000(6)	0.089(7)	1.92(1)

The first-order Raman spectra of the hard carbon precursor and the VTGs prepared at different temperatures for 3 h are shown in Figure 3.8. The Raman spectrum of the unheated hard carbon precursor is typical of an amorphous carbon, with two broad peaks having about the same height. In contrast, the spectra of the VTGs have two sharp peaks: a D-band at around 1340 cm^{-1}, and a G-band at around 1580 cm^{-1}. The G-band arises from the bond stretching of all pairs of sp^2 atoms (E_{2g} mode vibration) of the ordered graphite structure.[127,128] The origin of the D-band has often been associated with disordered carbon. There is also a shoulder (D'-band) at the right side of the G-band, which might arise due to the presence of disorder.[129] The D: G peak intensity ratio (I_D: I_G) is often used as qualitative measure of the relative amount of amorphous: graphitic carbon. The D-band height in all the VTG spectra are less than half of the G-band height. As the heat-treatment temperature increases, the I_D: I_G peak ratio becomes lower, indicating an increasing graphite content, which is consistent with the XRD data. However, the difference in the I_D: I_G ratio amongst the VTGs is only slight, in comparison to the significant changes observed by XRD and SEM. As discussed above, these VTGs comprise numerous irregular graphite sheets within the Voronoi-tessellated regions and hexagonal platelets in the spheroidal particles. Therefore, the proportion of carbon at the edges of flakes is high. This is consistent with the observations of Wang *et al.*, who have pointed out that higher proportions of edge planes and smaller grain sizes result in higher D-band intensity, even in highly graphitic samples.[128] Therefore, the XRD and Raman measurements are consistent with the VTGs (900 °C, 3 h and 1000 °C, 3 h) being highly graphitic and containing a large number of edge carbons.

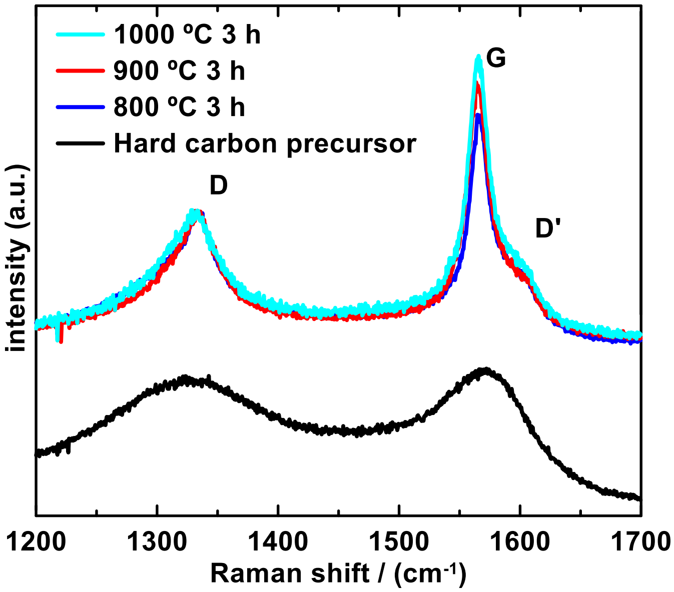

Figure 3.8 First-order Raman spectra of the sugar carbon precursor and the VTGs prepared by 3h heat-treatment at different temperatures, as indicated.

3.3.3 Electrochemical Characterization

The electrochemical characteristics of graphites in Li cells are sensitive to their surface area, degree of graphitization, and degree of turbostratic disorder. Therefore, this method is useful to verify the carbon microstructure by a direct measurement and was used to further characterize the VTG (1000 °C, 3 h) sample in comparison with the hard carbon precursor.[129] The hard carbon voltage and differential capacity curves (Figure 3.9(a, b)) show no evidence of voltage plateaus characteristic of staging and have a large voltage hysteresis, which is typical of a hydrogen containing hard carbon. In contrast, the voltage curve of the VTG (1000 °C, 3 h) shown in Figure 3.9(c) comprises staging plateaus, which correspond to peaks in the differential capacity curve

(Figure 3.9(d)), in verification of the graphitic structure of the VTG.[103] The reversible capacity of the VTG (1000 °C, 3 h) sample is about 240 mAh g^{-1}, below the theoretical graphite lithiation capacity for LiC_6 formation (372 mAh g^{-1}), and is consistent with the turbostratic disorder in this carbon, as measured by XRD.[104,105] The large irreversible capacity of the VTG (1000 °C, 3 h) sample is typical of a carbon with a high surface area. These measurements provide direct verification that a highly crystalline graphite with high surface area was obtained.

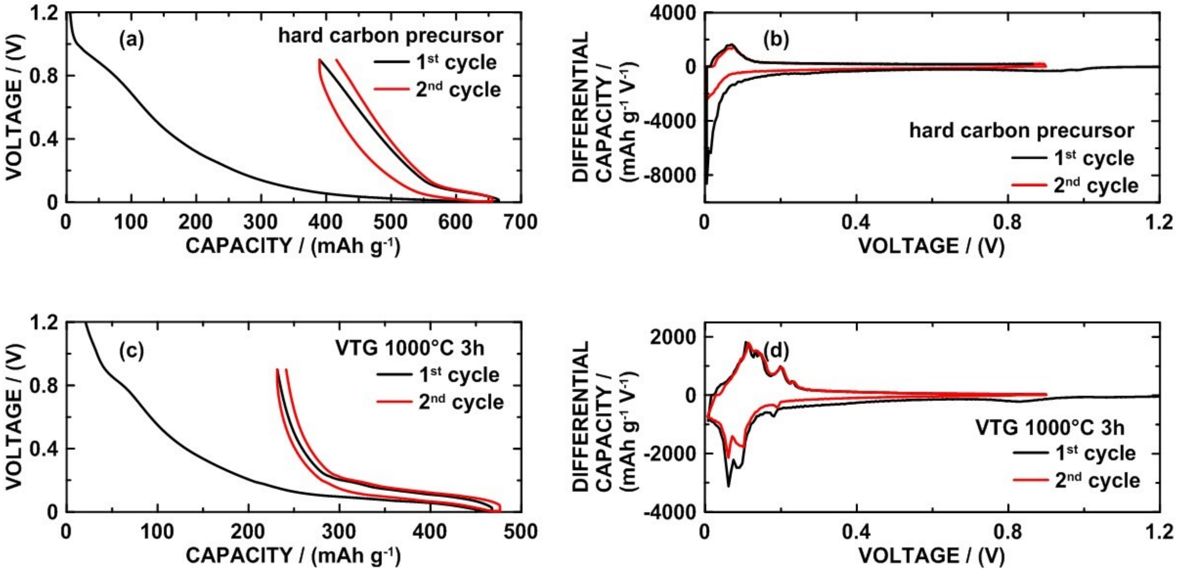

Figure 3.9 (a) Voltage and (b) differential capacity curves of the hard carbon precursor; and the (c) voltage and (d) differential capacity curves of VTG (1000 °C, 3 h).

3.3.4 Mg vapor graphitization

The XRD pattern of hard carbon after grinding has broad peaks, characteristic of highly disordered carbon (Figure 3.10(a)). The corresponding product after heating in the presence of Mg vapor at 1000 °C for 3 hours is still an amorphous carbon, suggesting the Mg vapor is not an effective graphitization catalyst.

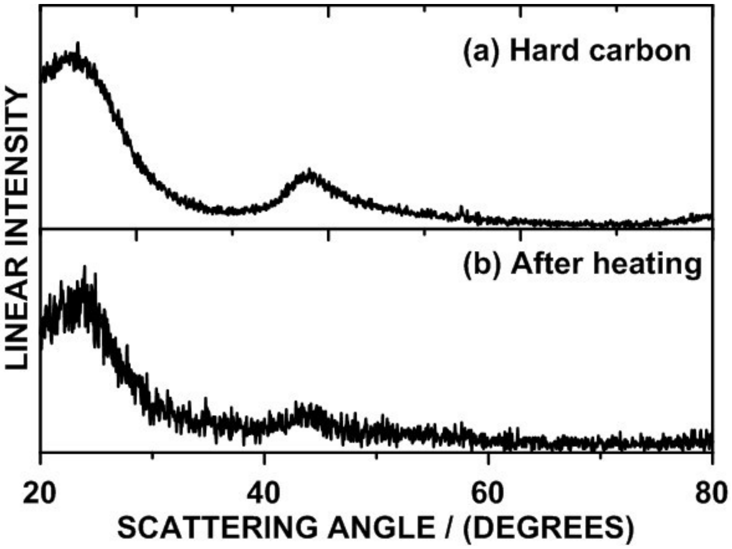

Figure 3.10 XRD patterns of (a) hard carbon after 5-min hand grinding, and (b) the carbon product after heating with Mg separately.

3.4 Discussion

Highly graphitic VTGs were successfully made at low temperatures using a Mg catalyst. The Mg catalyst could be completely removed after the graphitization process by a solution method, resulting in high purity graphites. This is a major advantage compared to the use of transition metal catalysts which can be extremely difficult to remove after graphitization and can result in high levels of catalyst impurities in the product graphites.

The VTGs themselves show a number of interesting morphological features: such as Voronoi-tessellations, and spheroidal shells containing hexagonal graphite platelets arranged perpendicularly to the shell surface. The formation of graphites from metal melts has been well studied, especially in cast irons. A number of the morphologies observed in the VTGs are similar to those previously reported in metal melts. Some of the morphologies have not been reported previously. For instance, the Voronoi-tessellated structure, shown in Figure 3.1(f, h), bears similarity to the "type B" (standardized in DIN EN ISO 945) arrangement of graphite sometimes observed in cast iron, also called "rosette graphite".[130] However, in rosette graphite, the graphite sheets emanate outward in all directions from eutectic cells in the bulk of the sample. Here the graphite sheets emanate outward from points on the surface of the particles only. At the centroid of each tessellated region on the particle surface resides a spheroidal graphite seed particle. This suggests the nucleated growth of graphite outward in all directions from spheroidal graphite particles, as mentioned earlier. Therefore, the mechanism for growth of such regions seems to be entirely different than that of rosette graphite.

The spheroidal graphites observed in the VTGs are also unique. Their surfaces are made up of crystalline hexagonal graphite platelets with their basal plane being tangential to the sphere surface. Within this spheroidal shell crystalline hexagonal graphite platelets are arranged perpendicularly to the shell surface, but otherwise have random orientations and often intersect each other. Although graphite spheres have been observed previously in metal melts, in all previous reports, the graphite making up such spheres is aligned with its basal plane tangent to the sphere surface.[59,131–133] No reports of instances of spheres containing graphite platelets that were perpendicular to the sphere surface were found as observed here. This again suggests an alternate mechanism for spheroidal graphite formation than has been previously reported.

The arrangement of the graphite platelets within the spheres is also interesting. Typically, graphite platelets arrange themselves, such that their basal planes are in alignment.[132] However, random configurations of hexagonal graphite platelets have been observed to form in cast iron melts in the presence of impurities.[134] It is thought that such impurities disrupt the crystal growth, resulting in the formation of many faceted crystal faces from which further growth can progress. A similar mechanism may be occurring here. In any case, it must be remembered that graphites prepared from cast irons represent only a small fraction of the melt composition (typically about 1.8 - 4 wt. % carbon). Consequently, the graphite yield from acid etching cast irons is tiny and the resulting graphite coexists with slag impurities. Here these microstructures are formed in high purity bulk graphite samples, which, to the author's knowledge, has not been previously reported.

In Figure 3.11, a model is proposed to explain the mechanism of the catalytic graphitization process in this study and the formation of the unique microstructures observed. During the initial stages of heating, it is speculated that magnesium (melting point 650 °C) segregates from the bulk of the hard carbon particles and coalesces into droplets on the particle surface. At high temperatures, these droplets then react with carbon to form a carbide or otherwise dissolve some of the carbon.[15] During the annealing step, the Mg diffuses into the bulk of the sample. This depletes the droplets of Mg, causing the dissolved carbon to crystallize as a spheroidal graphite shell on the droplet surface (seed particles). The Mg diffusion into the bulk may be driven by the excess free energy of the disordered carbon structure, which leads to a greater affinity for Mg in

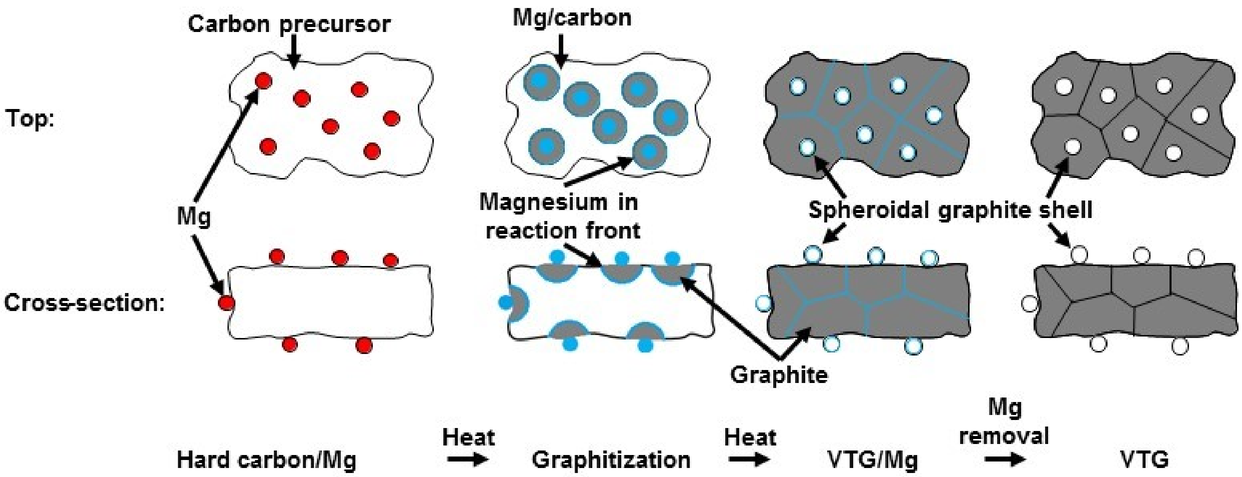

Figure 3.11 A model of how the Voronoi-tessellated structure forms, showing the top view (top row) and cross section (bottom row) of a carbon particle during the graphitization process.

the disordered carbon compared to graphite. As Mg continues to diffuse into the bulk of the particle, further Mg depletion occurs in the sphere, causing graphite platelets to crystallize out on the inside surface of the spheroidal shells. As the Mg diffusion front progresses, the Mg depletion region gets pulled into the bulk of the particle, causing graphite to crystallize in the depletion region behind the diffusion front. Eventually, expanding Mg diffusion fronts emanating from different points on the surface meet, forming fully tessellated structures with the graphite spheres located at surface centroids. It is interesting to note that according to this model, excepting for the initial formation of the spheroidal shell, the graphite basal planes are always formed in a direction perpendicular to the Mg diffusion front (or parallel to the direction of Mg diffusion).

3.5 Summary

Voronoi-tessellated graphites (VTGs) were made by heat-treatment of renewable hard carbon feedstock at 800 - 1000 °C for 1 - 3 h with a Mg catalyst. The magnesium and carbon precursor were combined together by hand grinding. The temperatures are far below that conventionally used for artificial graphites and the graphitization level of the final products is very high, suggesting that this method may lead to less energy intensive graphite synthesis methods.

A detailed and comprehensive analysis of the characteristics of VTGs was also reported. The microstructure of VTGs is quite interesting, indicating the graphite grows as sheets outwards from Mg spheroidal centers to form Voronoi-tessellated regions. Spheroidal shells comprising hexagonal graphite platelets were also observed. These microstructures result in high surface areas (> 80 m^2 g^{-1}). Such properties may be desirable for applications where highly graphitized, but high surface area graphites are needed (*e.g.* catalyst supports). These unique microstructures have not been previously reported.

It is also shown that the Mg-vapor is not an effective graphitization catalyst.

Chapter 4 Hexagonal Platelet Graphites (HPGs) Grown from Ball Milled C-Mg Alloys

4.1 Introduction

In Chapter 3, it is reported that highly ordered graphite can be made at low temperatures (800 - 1000 °C) via magnesium catalyzed graphitization of renewable hard carbon sources.[135] Using this method, the Mg catalyst can easily be removed and even recycled, resulting in a highly pure graphite product. The graphite produced by this method had a unique Voronoi tessellated structure made from sheets of graphite emanating from hollow graphite shell seed particles.

This chapter shows that by modifying the synthesis conditions of Mg catalyzation, a graphite with a completely different microstructure and higher degree of graphitization can be produced. This new graphite product comprises hexagonal platelet graphites (HPGs). When cycled in Li half-cells, HPGs display good cycling stability and high reversible capacity. After coating with a layer of carbon, its coulombic efficiency is further improved. This work shows that by altering the synthesis conditions, new highly ordered and highly pure graphites with microstructures and properties not obtainable by other methods may be produced.

The majority of this chapter was adapted from the following peer-reviewed article:

Leyi Zhao, J.C. Bennett, M.N. Obrovac, Hexagonal Platelet Graphite and its Application in Li-Ion Batteries, Carbon, 134 (2018) 507-518.

L. Zhao (this report author) conducted most of the work of the present study, including preparation and characterization of samples and analysis of data with the help of Prof. M.N. Obrovac. Prof. C. Bennett conducted the TEM measurements and TEM data analysis.

Minor changes have been made. Electrochemical measurement was re-conducted between 0.005 – 0.9V because the reactions between 0.9V and 2V are not associated with graphite lithiation/delithiation but are mainly associated with electrolyte decomposition and other side reactions. An XRD pattern was re-fit by using CARBONXS because it has two 002 peaks which could not be accommodated by the program (more details can be found in the Results section). The Mg-catalyzed graphitization mechanism was discussed in more details.

The melting point and boiling point of Mg are 650 °C and 1091 °C, respectively, at 1 atm. The vapor pressure of Mg is high at ~900 °C, being 1 atm. This makes it possible to remove Mg from graphite-Mg mixtures after graphitization by an evaporation process. A low-pressure environment can further accelerate the evaporation process. Therefore, an Mg low-pressure evaporation method was conducted to test the possibility of Mg recovery aforementioned.

4.2 Experimental

4.2.1 Synthesis of hexagonal platelet graphites (HPGs)

Glucose (96%, Aldrich) was dewatered by heating in air for 24 h at 180 °C and then heated under an argon flow for 3 h at 1100 °C to form hard carbon. The hard carbon was combined with magnesium powder (HART METALS, INC., -325 mesh) (C:Mg = 1:1 by mole) in a 65 mL hardened steel vial containing 115 g stainless-steel balls (4.76 mm in diameter) under an argon atmosphere for 2 h in a high-energy ball mill (SPEX Model 8000-D, SPEX CertiPrep, Metuchen, NJ). The resulting hard carbon/Mg mixture was heated in an argon-filled stainless-steel tube (~200 mm, OD 12.70 mm, ID 9.40 mm, sealed with Parker-A-lok caps) at 800, 900 or 1000 °C for 3 h or 20 h, resulting the formation of an HPG/Mg mixture. To remove the Mg catalyst after heat-treatment, two methods were used. Some HPG/Mg were heated under low pressure (< 20 Pa) at 900 °C for 5 h, while for other HPG/Mg, an acid wash procedure was used. For this study ~2 g of the HPG/Mg mixture was first placed in a solution of 100 mL of 2 M HCl (prepared from 37 wt. % HCl, Aldrich) and 2 mL of ethanol (98%, Aldrich) for 12 h with stirring. Here, the ethanol can reduce the surface tension of the acid solution, increasing its wetting ability. After reacting with HCl, the product was transferred to a Büchner funnel (Whatman filter paper, qualitative) and was washed with 2 M HCl five times and then washed with distilled water repeatedly until the pH of the supernatant was about 7. Finally, the products were dried in air at 120 °C for 3 h. In this chapter, the heat-treatment conditions of each HPG are indicated in parentheses.

4.2.2 Coating HPG (1000 °C) with carbon

Carbon was coated on HPGs (1000 °C) to reduce their surface area based on carbonization method 2 introduced previously.[136] In summary, 0.5 g of the HPG (1000 °C) sample was mixed with 0.7 g poly(vinyl chloride) (PVC, Sigma-Aldrich, low molecular weight, 1.4 g mL^{-1}) in a planetary ball mill (Retsch PM200) with three 11.25 mm tungsten carbide balls for 1 h at 100 rpm. The resulting graphite/PVC mixture was then heated under an argon flow at 280 °C for 0.5 h, 450 °C for 0.5 h, 900 °C for 1 h and then cooled to room temperature before exposing to air. The heating rate for all steps was 10 °C per minute. The final carbon coated HPG products are hereafter termed as CCHPG (1000 °C, 3 h) and CCHPG (1000 °C, 20 h).

4.2.3 Materials characterization

HPGs were characterized by using many techniques: scanning electron microscopy (SEM), energy dispersive X-ray spectroscopy (EDS), focused ion beam (FIB) technique, transition electron microscopy (TEM), X-ray diffraction (XRD), Brunauer-Emmett-Teller (BET) surface analysis, inductively coupled plasma-optical emission spectroscopy (ICP-OES), Raman spectroscopy, and pycnometry, with the equipment introduced in Chapter 2. Electrochemical measurements of HPGs and CCHPGs as working electrodes in Li-half cells were performed. Details of slurry making, cell assembling, and cycling have been described in Chapter 2.

The CARBONXS program developed by Shi *et al.* was used to fit the XRD patterns of HPGs and two battery-grade commercial graphites (KS 6L (Imerys Graphite and Carbon) and MAG-E (Hitachi)) to gain details about their structural order.[112] Details regarding the fitting process can be found in Chapter 2. Pseudo-Voigt profiles were also applied to fit some graphite XRD patterns, details of which have been described in Chapter 2.

4.3 Results

4.3.1 Structural and morphological characterization of HPGs

Figure 4.1 compares the morphology of the hard carbon precursor and HPGs. The hard carbon precursor prepared from glucose is mainly composed of smooth carbon particles with flat sides (Figure 4.1(a)). After heat-treatment at 800 °C for 3 h with the Mg catalyst, the particles become porous with a minor number of irregular graphite sheets that are small in size (< 1 μm) (Figure 4.1(b)). When the heat-treatment temperature increases to 900 °C or 1000 °C, the particles are composed of regions of small irregularly shaped secondary particles and regions of large hexagonal graphite platelets (up to 10 μm) (Figure 4.1(c, d)). The hexagonal platelets comprise multiple layers with well-defined edges (Figure 4.1(e)). Some of these hexagonal particles contain rotational stacking faults which is common for graphite.[126] The HPG (1000 °C, 20 h) sample, which was prepared using a longer heating time, is almost completely composed of thin hexagonal-platelets that are about 5 - 20 μm in extent (Figure 4.1(g)), while some regions of the sample

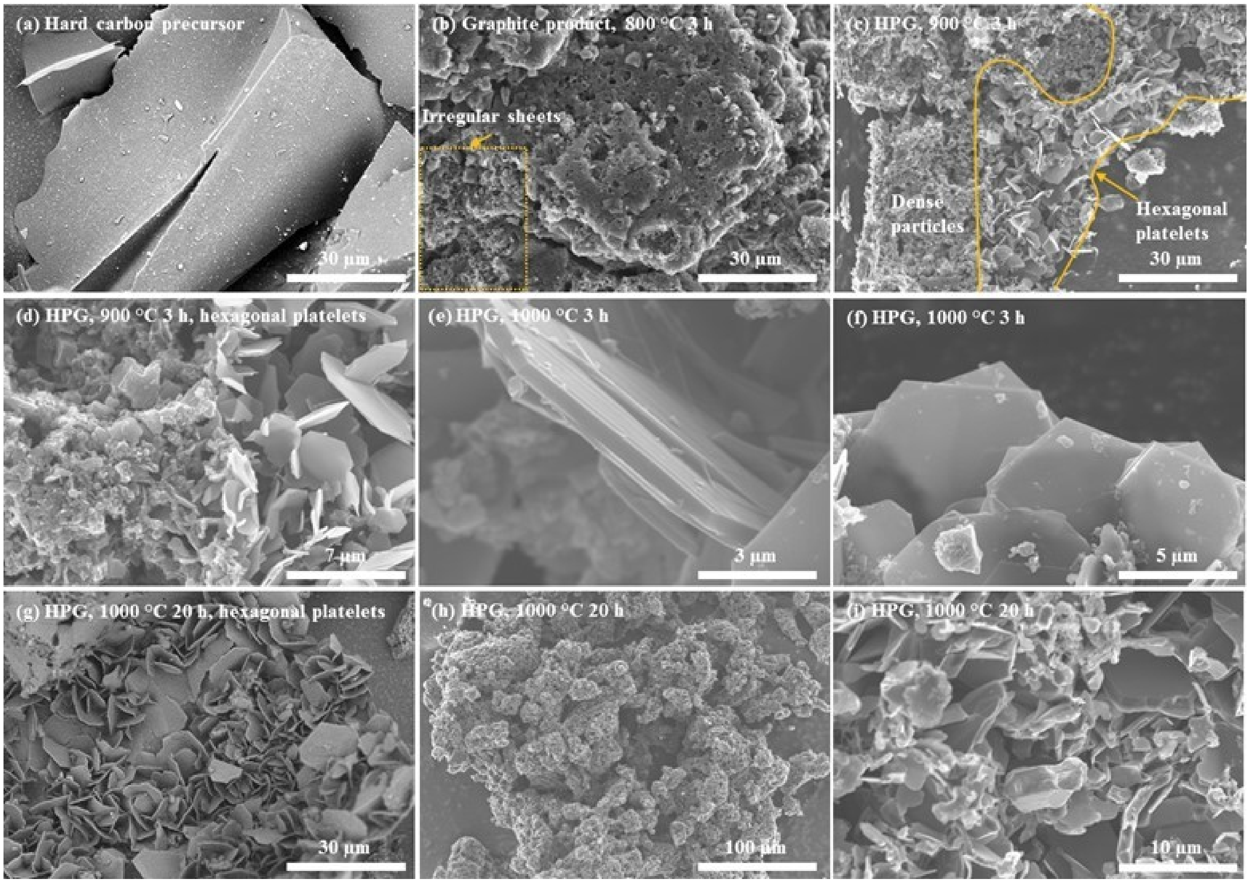

Figure 4.1 SEM images of (a) the hard carbon precursor, and (b-i) HPGs prepared under different conditions as indicated.

comprise smaller hexagonal graphite prisms (~3 - 10 μm) with substantial thickness c-direction (~1 - 7 μm) (Figure 4.1(h, i)). Based on the SEM observation, the majority of the crystal growth occurs in the basal plane, with a minority of the sample having crystal growth both in and out of the basal plane.

Similar hexagonal platelets of graphite have been observed in iron or nickel eutectic melts.[132,137] However, in such melts the carbon is a minority phase and is difficult to separate from the parent metal. In contrast, the HPG sample shown here is produced in bulk, is easily separated from the Mg catalyst and, as will be shown below, is of high purity. The special microstructure of HPGs results in a high specific surface area (55 - 82 $m^2 g^{-1}$, Table 4.1), which is not proportional

Table 4.1 Mg contents, specific surface areas, densities and structural parameters determined by pseudo-Voigt fitting of the XRD patterns of HPGs, commercial graphites, and a graphite made at 2850 °C without using Mg catalysts reported by Reference [112].

Conditions	Mg content wt. %	Surface Area $m^2\ g^{-1}$	Density $g\ mL^{-1}$	002 peak	d_{002}	L_c Å
800 °C, 3 h	0.095(3)	64	2.23	turbostratic	3.403(5)	190(5)
900 °C, 3 h	0.031(2)	55	2.26	turbostratic	3.391(4)	187(4)
				ordered	3.348(5)	302(6)
1000 °C, 3 h	0.032(2)	82	2.29	ordered	3.343(6)	357(8)
1000 °C, 20 h	0.068(3)	61	2.29	ordered	3.345(4)	508(7)
KS6L	-	20	2.24	ordered	3.346(4)	389(5)
MAGE	-	2.6	2.23	ordered	3.344(2)	511(4)
2850 °C, no Mg	-	-	-	-	3.382	250

to heating temperature or time. This is much higher than that of natural graphites (~0.6 $m^2\ g^{-1}$) and conventional artificial graphites used in Li-ion batteries (1 - 20 $m^2\ g^{-1}$).[138–140] Despite their high surface area, the bulk densities of the HPGs made at 900 °C and 1000 °C were measured to be 2.26 - 2.29 $g\ mL^{-1}$ (Table 4.1), close to that of a highly graphitic carbon.

To gain an understanding of how the graphite formed during synthesis, SEM images and EDS mapping images were taken of the milled C/Mg before heating and the HPG/Mg mixtures after heating and prior to the removal of Mg by acid. The milled C/Mg mixture contains big secondary particles composed of primary particles (Figure 4.2(a)). The Mg and C are almost evenly distributed (Figure 4.2(b-c) without obvious boundaries. Figure 4.2(d-f) show SEM images and EDS mapping images of an HPG/Mg (1000 °C, 20 h) mixture. In this sample, the hexagonal platelets are uniformly covered by Mg. The distribution of Mg and the absence of any carbide phases (confirmed by XRD below) suggests a dissolution-precipitation mechanism consistent with that observed by Fitzer *et al.*, in which the carbon becomes solvated in the catalyst, with concurrent graphite precipitation.[19] In addition, there are Mg single crystals (based on the EDS data and its hexagonal structure) that are 5 - 20 µm in extent distributed throughout the sample. Such a single Mg crystal is shown in detail in Figure 4.2(g-h). These crystals presumably grow from Mg liquid/vapor as the sample is cooled after heating.

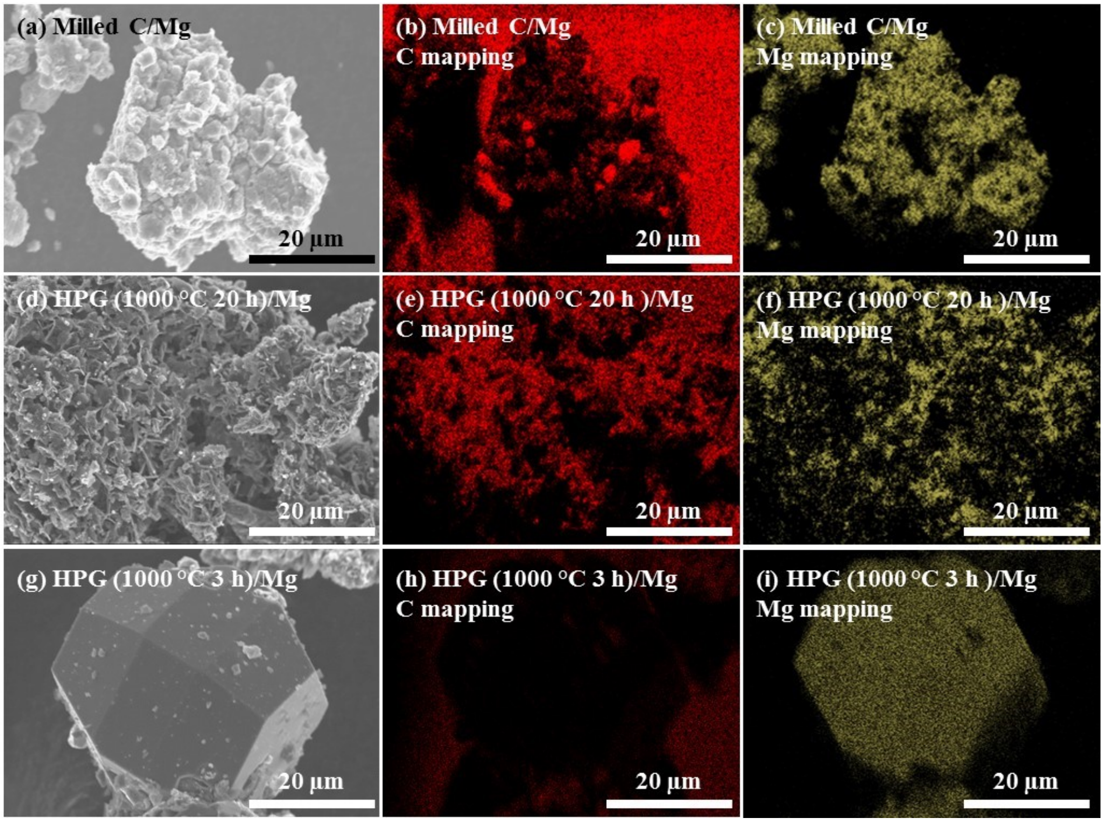

Figure 4.2 SEM images of (a) the milled C/Mg, (d, g) the HPG/Mg mixtures and corresponding EDS (b, e, h) carbon mapping images and (c, f, i) magnesium mapping images. Heat-treatment conditions are indicated in each figure.

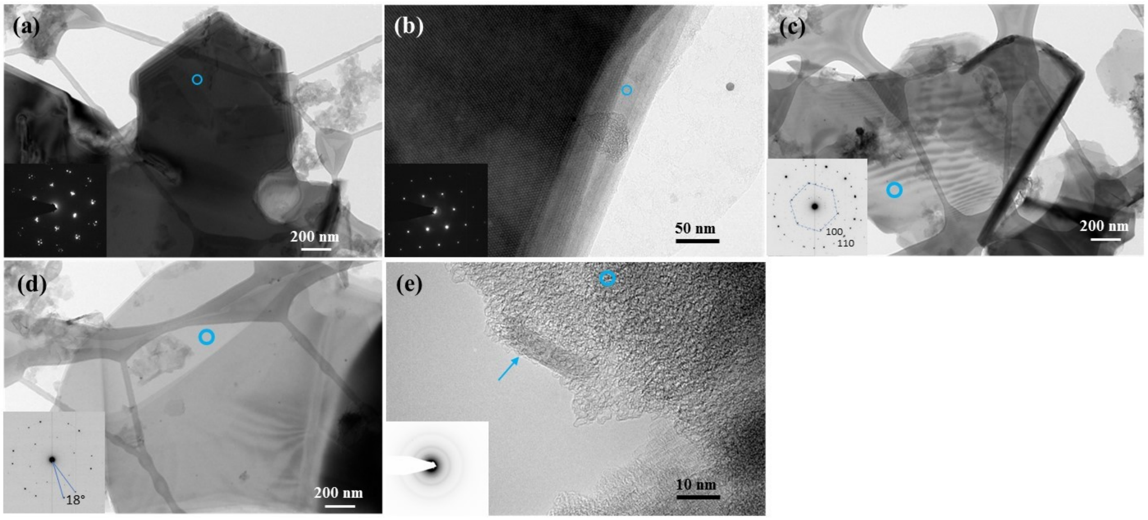

Figure 4.3 (a-e) TEM images of HPG (1000 °C, 3 h). The selected area electron diffraction patterns are taken around the blue circled areas in each figure.

TEM images were taken of the pure HPG (1000 °C, 3 h) sample to gain a better understanding of the HPG structure. Figure 4.3(a) shows a TEM image of a multilayer hexagonal platelet from this sample. The selected area electron diffraction (SAED) pattern of the near-center region confirms the graphite structure for these platelets. However, the SAED pattern is clearly more complicated, with numerous closely spaced spots around each basic spot position. This suggests slight layer stacking variants, which is common for graphite platelets.[126] In some thinner regions (*e.g.* edges), the hexagonal platelets are highly ordered (Figure 4.3(b)). The fine scale hexagonal symmetry Moiré pattern (Figure 4.3(b)) and the hexagonal spot pattern of the SAED pattern (Figure 4.3b(insert)) both suggest a high graphitization level of HPG (1000 °C, 3 h). Based on the SAED pattern, the lattice constant was determined as a = 2.46 Å, which is typical of a highly ordered graphitic structure. HPGs also contain other types of particles (*e.g.* graphene, nanocrystalline particles). The particle in Figure 4.3(c) is characteristic of thin graphite/multilayer graphene with stacking disorder consisting of AB layers rotated by ~15 degrees (indexing for graphite layer a = 2.46 Å). The SAED pattern in Figure 4.3(d) is consistent with graphene bilayer with 18 degrees rotation between layers. The region at the edges of these graphene crystallites in Figure 4.3(e) (labelled by the arrow) is composed of nano-sized parallel graphene layers (~20 layers, ~8 nm in vertical extent and ~30 nm in lateral extent). The nano-polycrystallinity of this region is consistent with the narrow rings in the SAED pattern shown in Figure 4.3(e, insert). The occasional weak diffraction spots are likely associated with the presence of the larger graphite nanoplatelets.

Figure 4.4(a) shows the XRD pattern of the hard carbon precursor prepared from glucose. It has two broad peaks near 25° and 45°, which is typical of a disordered hard carbon. After ball milling with the Mg catalyst, Mg peaks become dominant while the carbon peaks are hardly observed in comparison (Figure 4.4(b)). Figure 4.4(c) shows the XRD pattern of the HPG/Mg mixture after heat-treatment at 1000 °C for 3 h. The XRD pattern contains sharp peaks characteristic of a highly-graphitized carbon, and peaks from Mg and MgO. The MgO may have formed due to an oxygen impurity in the carbon precursor or introduced as oxides on the inner surfaces of the stainless-steel reaction tube. The Mg peaks now have different intensity ratios, which is characteristics of preferred orientation. This is consistent with the observation above of Mg single crystals in Figure 4.2(g, i). Such crystals likely become oriented during XRD sample preparation.

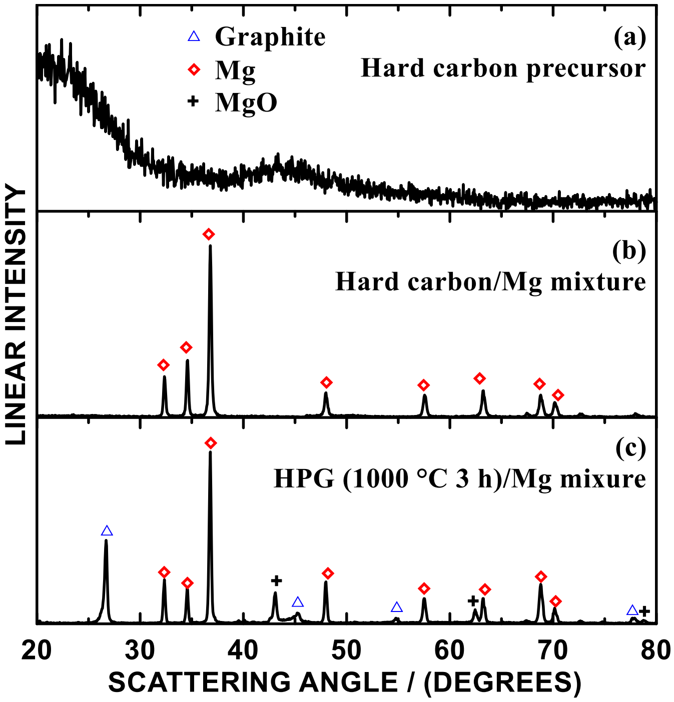

Figure 4.4 XRD patterns of (a) the hard carbon precursor, (b) the hard carbon/Mg mixture before heat-treatment, and (c) the HPG (1000 °C, 3 h)/Mg mixture before HCl treatment.

Figure 4.5(a) shows the XRD patterns of the HPG final products after washing with acid and those of two commercial graphites. No Mg or MgO peaks are present, suggesting that all the Mg and MgO impurities have been removed. This was confirmed by ICP-OES measurements. The Mg content in HPG samples was found to be negligible (0.03 - 0.09 wt. % (Table 4.1)). All XRD patterns of HPGs are characteristic of highly crystalline graphite. However, a closer look at the 002 peak of each XRD pattern suggests that HPGs prepared under different conditions have different graphitization levels (Figure 4.5(b)). The HPG (800 °C, 3 h) XRD pattern contains a 002 peak at ~26.2°, which has been ascribed to turbostratic graphite.[15] The HPG (900 °C, 3 h) XRD pattern contains two 002 peaks at ~26.2° and ~26.6°, corresponding to turbostratic graphite and ordered graphite, respectively. The ordered graphite 002 peak becomes dominant for HPG (1000 °C, 3 h) and HPG (1000 °C, 20 h). Specifically, HPG (1000 °C, 20 h) has a sharper 002 peak, similar to that of the commercial graphites, corresponding to a more ordered structure.

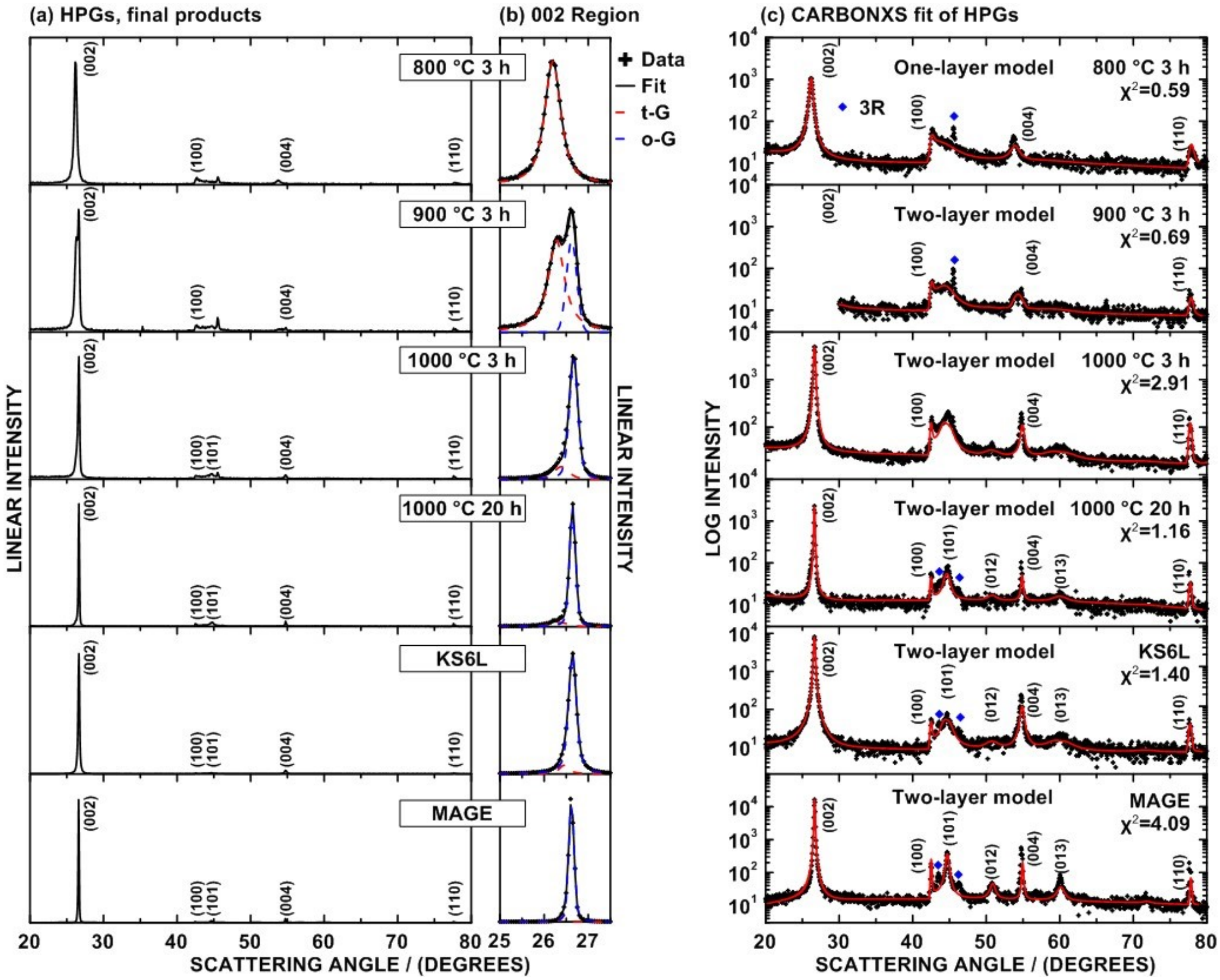

Figure 4.5 (a) XRD patterns of HPGs and commercial graphites, (b) enlarged 002 peak regions of XRD patterns with pseudo-Voigt fits, and (c) CARBONXS fits of each XRD pattern.

The 002 peaks in Figure 4.5(b) were fit using the pseudo-Voigt functions between the angles of 23° and 29°, with a combination of two pseudo-Voigt peaks with positions in the range of 26° - 27°: one for turbostratic graphite and one for ordered graphite. Based on the fitting results, the interlayer spacing (d_{002}) and the inter-plane coherent length (L_c) of HPGs and commercial graphites were determined and are shown in Table 4.1 and Figure 4.6(a, b). L_c and d_{002} values of a graphite made at 2850 °C without Mg catalysts are also given for comparison.[112] As the heat-treatment temperature and time increase, a higher graphitization level of HPGs is achieved: d_{002} decreases from 3.4019 to 3.3450 Å, and L_c increases from less than 200 Å to almost 500 Å. The

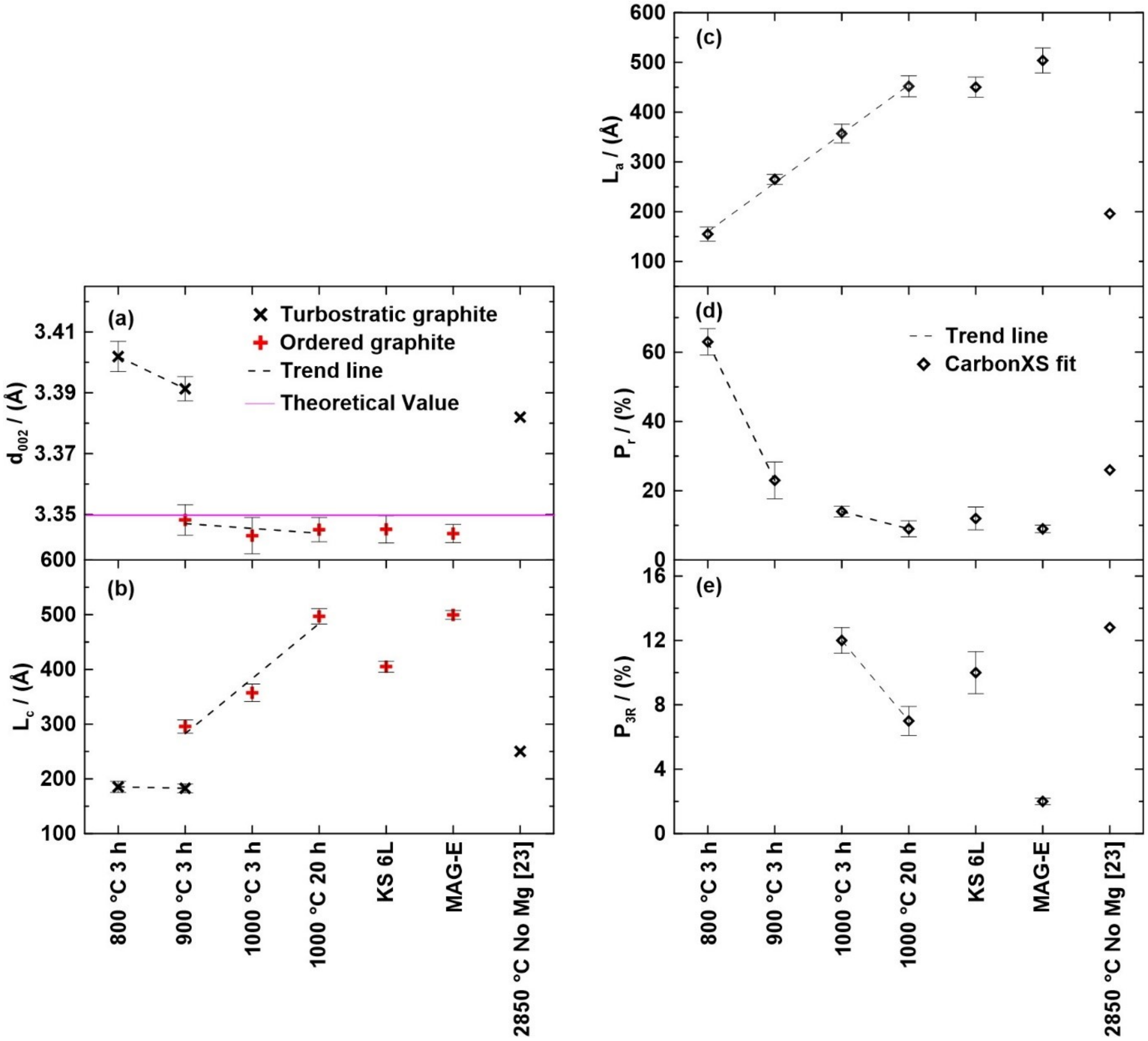

Figure 4.6 (a) The average interlayer spacing (d_{002}) and (b) the inter-plane coherent length (L_c) of HPGs and commercial graphites obtained from the pseudo-Voigt fitting of 002 peaks. (c) The in-plane coherent length (L_a), (d) the probability of random stacking per layer (P_r), and (e) the probability of 3R stacking per layer (P_{3R}) of HPGs and commercial graphites obtained from the CARBONXS fitting. The lines are guides to the eye. The data of graphite made at 2850 °C without using Mg catalysts is from a previous study.[112]

d_{002} and L_c of HPGs (1000 °C) are comparable to the commercial graphites shown in Figure 4.6. In addition, the d_{002} values of HPGs (1000 °C) are close to the theoretical value and are smaller than that of the graphite made at high temperature (2850 °C) without using an Mg catalyst.

XRD patterns were also fit using the CARBONXS program as described in Chapter 2 (Figure 4.5(c)). The fitting model used (one-layer or two-layer) is indicated in each fit. Table 4.2 lists the probability of random stacking per layer (P_r), probability of 3R stacking per layer (P_{3R}), in-plane cell constant (a), in-plane coherent length (L_a), interlayer spacing fluctuation ($<\delta^2>^{1/2}$), and the goodness of fit (χ^2) for each fit. All XRD patterns were fit well with low χ^2 values. Most XRD patterns were fit from 20° to 80°. However, patterns with two 002 peaks (*e.g.* HPG (900 °C, 3 h)) could not be accommodated by the program and thus were fit from 30° to 80°. For all HPGs, the in-plane cell constants are close to the theoretical value. In-plane strain and interlayer spacing fluctuation of all HPGs are very low, characteristic of highly graphitic carbons. Figure 4.6(c-e) compare the L_a, P_r, and P_{3R} of all HPGs, commercial graphites, and the graphite made at 2850 °C without using Mg catalysts, based on CARBONXS fitting results.[112] As the heating temperature and time increase, L_a of HPGs increases from 150 Å to 450 Å. With increasing heating temperature, P_r decreases from over 60% to about 10%, indicating an increasing graphitization level. The high L_a and low P_r values of HPGs (1000 °C) are characteristic of an extremely high degree of graphitization and are comparable to that of commercial graphites. The probability of 3R stacking per layer was determined to be ~10% for HPGs (1000 °C), also comparable to that of commercial graphites. These values from the pseudo-Voigt and CARBONXS fitting are

Table 4.2 CARBONXS fitting results of HPGs, commercial graphites, and a graphite made at 2850 °C without using Mg catalysts reported by Reference [112].

Conditions	P_r at. %	P_{3R} at. %	a Å	L_a Å	$<\delta^2>^{1/2}$ Å	χ^2
800 °C, 3 h	63(4)	-	2.454(0)	155(2)	0.133(7)	0.59(1)
900 °C, 3 h	36(5)	-	2.455(0)	260(2)	0.050(7)	0.69(1)
1000 °C, 3 h	14(2)	12(1)	2.457(1)	357(3)	0.056(1)	2.91(1)
1000 °C, 20 h	9(3)	7(1)	2.457(1)	452(3)	0.039(1)	1.16(1)
KS6L	12(3)	10(1)	2.457(1)	450(4)	0.059(1)	1.40(1)
MAGE	8(1)	2(0)	2.454(1)	504(2)	0.028(8)	4.09(1)
2850 °C, no Mg	13	6.4	2.461(1)	196(2)	0.091(5)	-

remarkable, as they indicate that a higher graphitization level is achieved here at 1000 °C than those reported for conventional artificial graphites prepared at temperatures as high as 2800 °C, and a similar graphitization level as battery grade commercial graphites.[141] It is worth noticing that the L_a value of each HPG obtained by CARBONXS fitting is similar or smaller than its L_c value obtained by the pseudo-Voigt fitting. This is contradictory to the SEM (Figure 4.1) and TEM (Figure 4.3) observation of HPG particles, which have larger horizontal extent than their vertical extent. This is because the sample also contains a number of small irregularly shaped particles. The L_c and L_a values are averages of crystallite sizes from large platelets and smaller irregularly shaped particles. Although large platelets have a higher L_a/L_c ratio, smaller irregularly shaped particles will have much smaller values of L_a. In addition, the existence of turbostratic components in graphite crystallites also contributes to the reduction of L_a values.

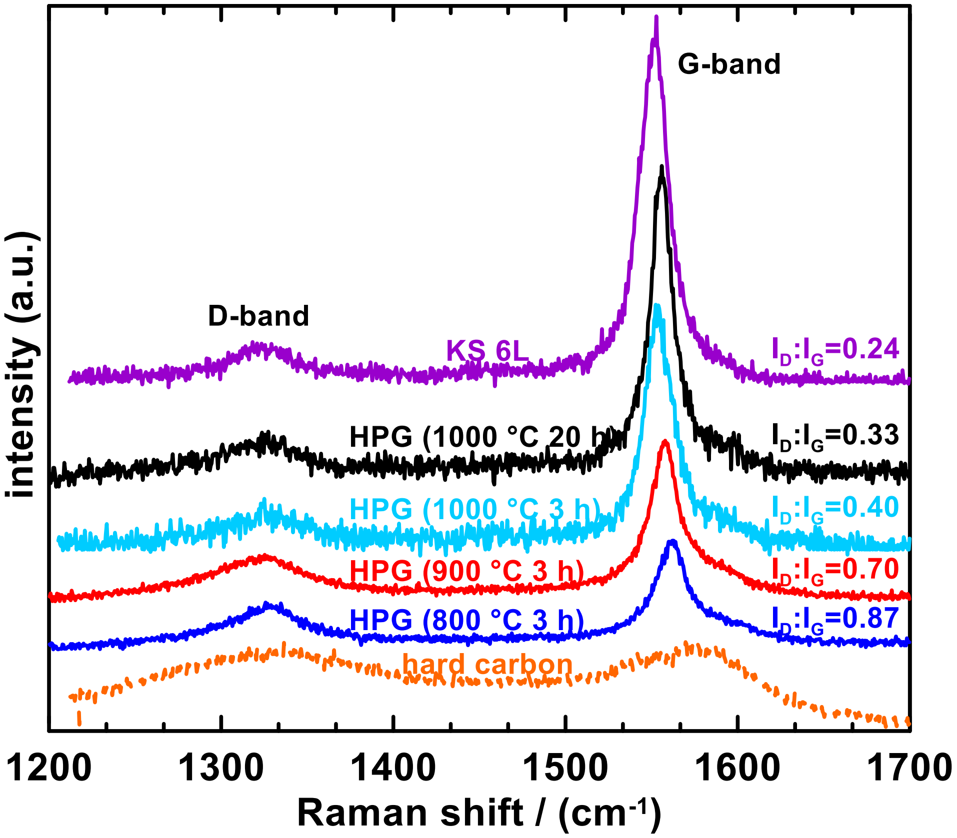

Figure 4.7 First-order Raman spectra of the hard carbon precursor, HPGs, and KS6L commercial graphite.

The first-order Raman spectra of the hard carbon precursor, HPGs, and KS 6L are shown in Figure 4.7. The hard carbon Raman spectrum has two broad peaks, consistent with its disordered composition.[142] There are two distinct main bands in the HPG and KS 6L spectra: the G-band near 1580 cm^{-1} and the D-band near 1340 cm^{-1}. The G-band arises from the bond stretching of all pairs of sp^2 atoms in the graphite structure.[128,129] The origin of the D-band has often been associated with disordered carbon. The Raman spectra of HPGs have much smaller D-bands and much sharper G-bands compared to that of the hard carbon precursor, indicating more ordered structures. There is also a very small shoulder peak at the right of the G-band in the Raman spectra of HPGs, which might arise due to the presence of structural disorder.[127] The D:G peak area ratio (I_D:I_G) is often used as a qualitative indicator for the degree of disorder in graphite. In Figure 4.7, higher temperatures and longer heating times result in lower I_D:I_G ratios, indicating decreasing disorder. This is consistent with the pseudo-Voigt and CARBONXS fitting results. HPG (1000 °C 20 h) has the lowest I_D:I_G value (0.33) among all HPGs, which is close to the value of KS 6L commercial graphite (0.24). It should be noted that the higher I_D:I_G value for HPG (1000 °C 20 h) may arise because of a large number of edge carbons in this sample, as opposed to a less degree of graphitization.[128]

4.3.2 Carbon-coated HPG

A carbon layer was coated on HPGs (1000 °C) to reduce their surface area and improve electrochemical performance. Coating with carbon greatly reduced the surface area from 82 m^2 g^{-1} to 25 m^2 g^{-1} for HPG (1000 °C, 3 h), and from 61 m^2 g^{-1} to 13 m^2 g^{-1} for HPG (1000 °C, 20 h). Figure 4.8(a, b) show SEM images of CCHPG (1000 °C, 3 h). For comparison, SEM images of HPG (1000 °C, 3 h) are also shown at the same scales in Figure 4.8(c, d). The CCHPG (1000 °C, 3 h) particles are uniformly covered with a coarse layer of carbon, making the hexagonal platelets more difficult to observe. Figure 4.9 shows XRD patterns of HPG (1000 °C, 3 h) before and after carbon coating. The XRD pattern of CCHPG (1000 °C, 3 h) has an additional broad peak near 22° compared to that of the uncoated sample, indicating more amorphous carbon content, as expected from the carbon coating process. Other than the additional broad peak, the XRD pattern of CCHPG (1000 °C, 3 h) is otherwise the same as that of HPG (1000 °C, 3 h).

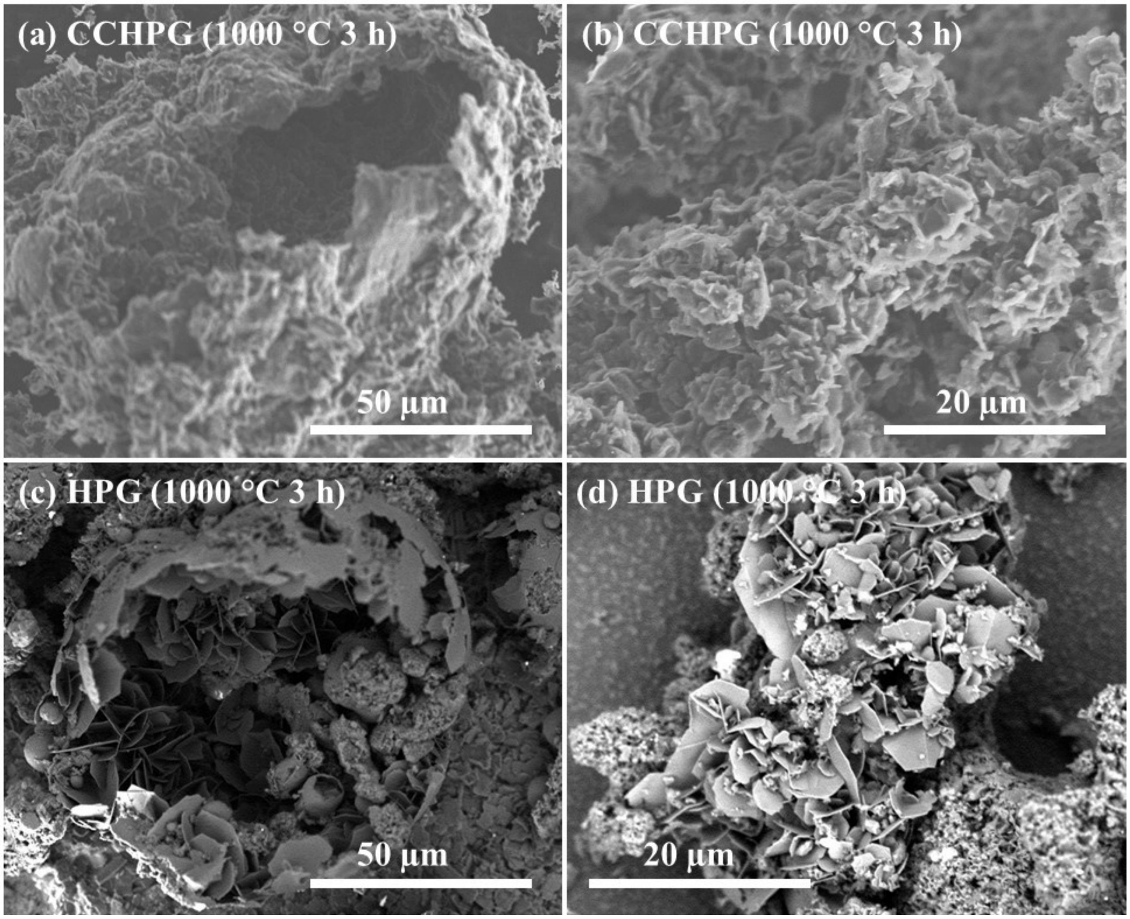

Figure 4.8 SEM images of (a, b) CCHPG (1000 °C, 3 h), and (c, d) HPG (1000 °C, 3 h).

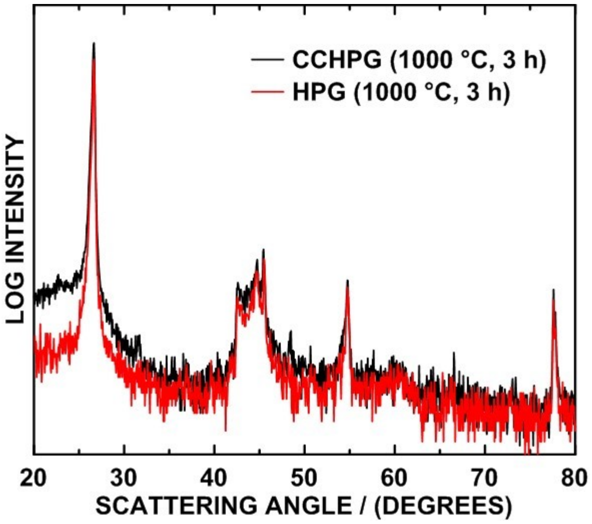

Figure 4.9 XRD patterns comparison of HPG (1000 °C, 3 h) and CCHPG (1000 °C, 3 h).

4.3.3 Electrochemical characterization

Figure 4.10 shows the voltage profiles and differential capacity curves of the hard carbon precursor, HPGs, and CCHPGs. The hard carbon voltage and differential capacity curves (Figure

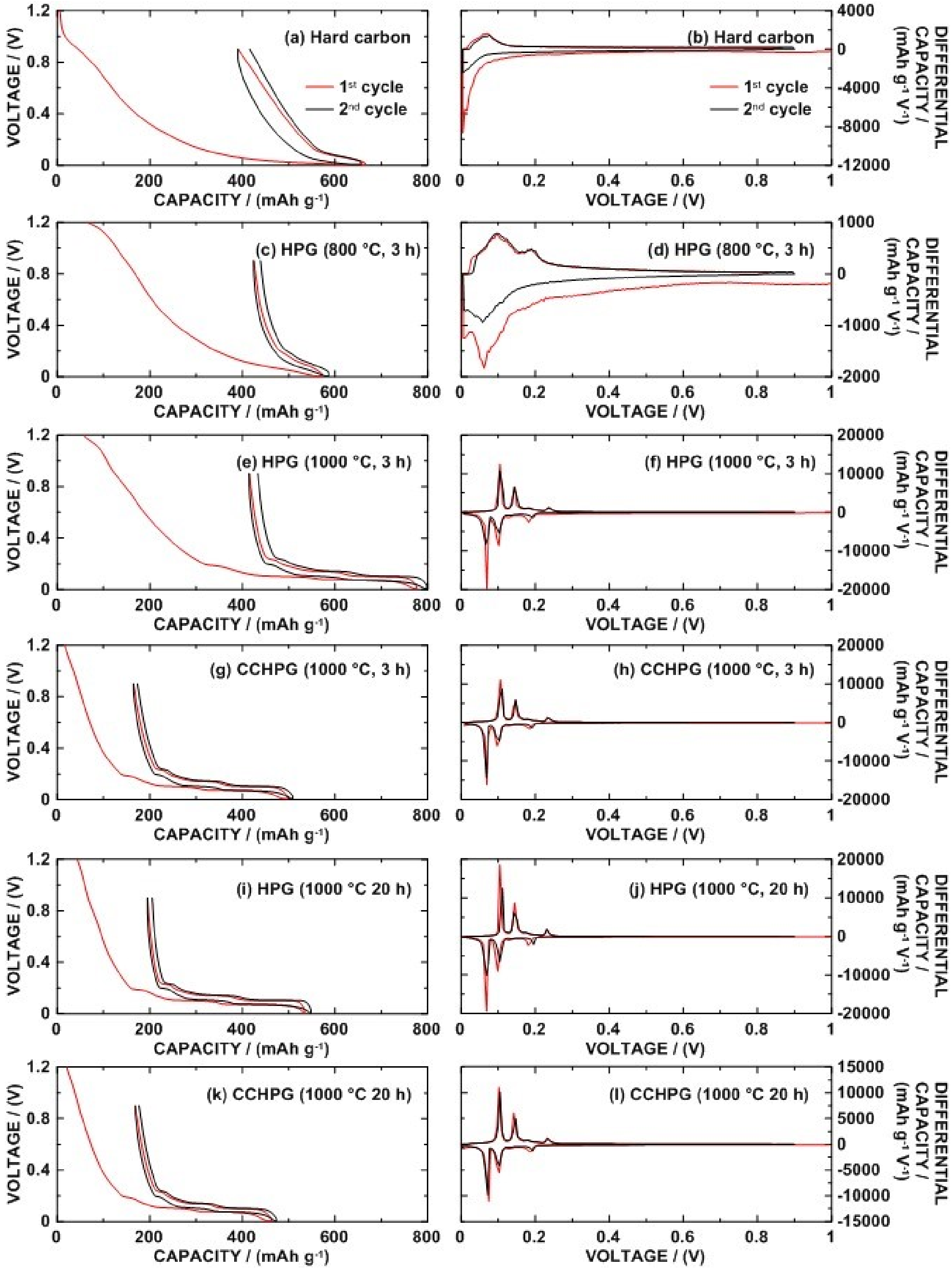

Figure 4.10 (a, c, e, g, i, k) Voltage profiles and (b, d, f, h, j, l) differential capacity curves of the hard carbon precursor, HPGs, and CCHPGs.

4.10(a, b)) show no evidence of voltage plateaus characteristic of staging, and also show large voltage hysteresis. These characteristics are typical of hydrogen containing hard carbon.[143,144] The HPG (800 °C, 3 h) sample has a reduced hysteresis (Figure 4.10(c)), and more distinguishable differential capacity peaks (Figure 4.10(d)), suggesting a more ordered structure. In contrast, the voltage curve of HPG (1000 °C, 3 h) comprises distinct staging plateaus (Figure 4.10(e)), which correspond to sharp peaks in the differential capacity curve (Figure 4.10(f)), in verification of its highly ordered graphitic structure.[103] However, the irreversible capacity (IC) of HPG (1000 °C, 3 h) is much higher than conventional graphites used in Li-ion batteries, leading to a low initial coulombic efficiency (CE) of 47%. The high IC likely results from the large specific surface area of HPG (1000 °C, 3 h) (82 m^2 g^{-1}), since IC is proportional to the specific surface area of graphite, as shown in previous studies.[138–140] Coating with carbon greatly reduces the IC of HPG (1000 °C, 3 h), resulting in an increased initial CE of ~70% (Figure 4.10(g)), presumably due to surface area reduction (to 25 m^2 g^{-1}), while the staging features remain unchanged (Figure 4.10(h)).

It is worth mentioning that the initial CE of HPG (1000 °C, 20 h) is comparable to CCHPG (1000 °C, 3 h) (Figure 4.10(i, j)). Both HPGs made at 1000 °C have high surface area (Table 4.1), but the one with a longer heating time has a much-improved initial CE. This is not fully understood yet. In following chapters, it will be shown that less-ordered tiny graphite particles exist on catalytic graphite surfaces, which are thought to reduce the initial CE. A longer heating time might reduce the content of these tiny particles and thus improve the initial CE. Carbon coating the HPG (1000 °C, 20 h) sample resulted in a surface area of 13 m^2 g^{-1}, even lower than for the HPG (1000 °C, 3 h) sample and drastic improvements in CE were observed (Figure 4.10(k, l)). However, only slight improvements in electrochemical performance were observed between CCHPG (1000 °C, 3 h) and CCHPG (1000 °C, 20 h). There seems to be a limitation in the ability of carbon coating to increase the initial CE. This may be due to the still relatively large surface area of CCHPG (1000 °C, 20 h). In addition, the carbon coating layer may contain non-negligible amounts of hydrogen, which consumes extra Li during the initial lithiation. Increasing heat-treatment temperature when coating carbon on HPGs may reduce hydrogen content and further improve initial CE.

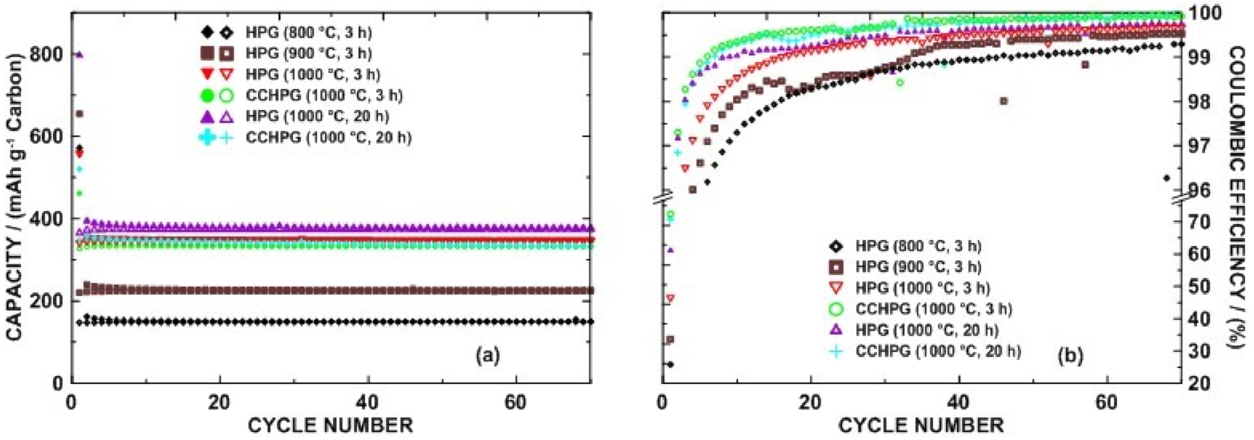

Figure 4.11(a) Cycling performance and (b) coulombic efficiency (CE) of HPGs and CCHPGs.

Figure 4.11 shows the cycling performance and CE of HPGs and CCHPGs. All samples display good cycling stability over the 70 cycles tested. As the heat-treatment temperature and time increase, the reversible capacity of HPGs increases greatly from 200 mAh g^{-1} to 370 mAh g^{-1}. This high cycling capacity is indicative of a high degree of graphitization and low turbostratic disorder,[145,146] consistent with the XRD results discussed precedingly. The initial CE of HPGs also increases with heating temperature and time, from ~30% to ~60%, while the CE of 70th cycle increases from 99.29% to 99.75%. Coating with carbon further increases 70th cycle CE to 99.99%. However, the cycling capacities of the CCHPGs are slightly lower than that of uncoated HPGs because they contain more amorphous carbon. It is remarkable that the voltage profiles and cycling performance of HPGs synthesized at only 1000 °C from a non-graphitizable precursor have characteristics comparable to that of commercial artificial graphites made at much higher temperatures (> 2800 °C)[141].

4.3.4 Mg recovery by low-pressure evaporation

After graphitization, the product is a mixture of graphite and impurities, including Mg and MgO (Figure 4.12(a)). After further heating under low pressure, Mg was completely removed (Figure 4.12(b)) while MgO remains. This is because Mg easily evaporates at 900 °C under low pressure while MgO does not.

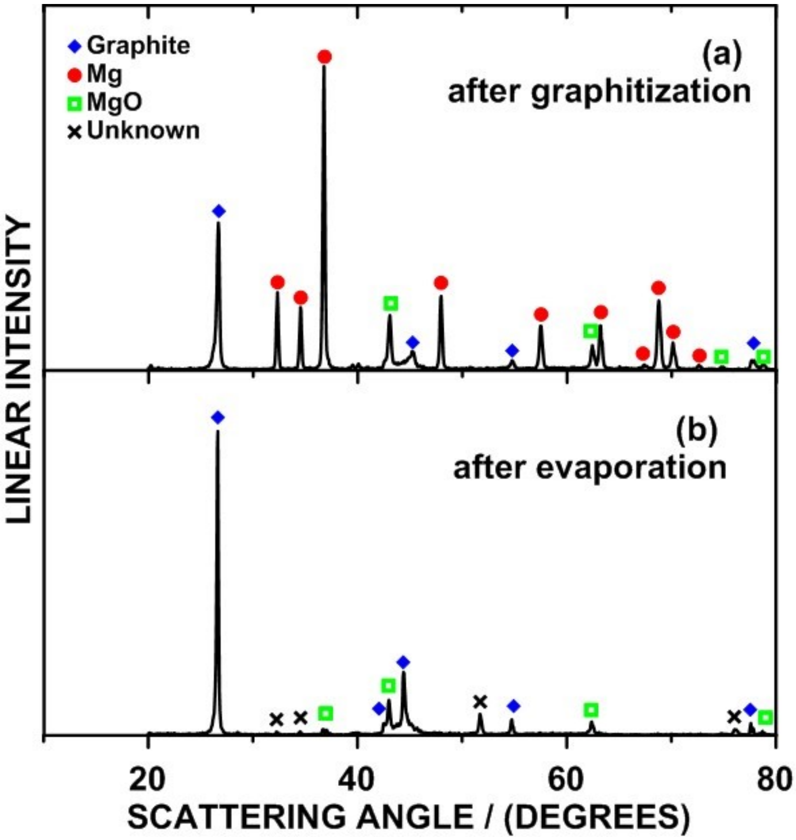

Figure 4.12 XRD patterns of an HPG/Mg sample (a) after graphitization and (b) the corresponding product after low-pressure evaporation.

4.4 Discussion

In Chapter 3, a similar method is reported to produce graphite, except the Mg and hard carbon were combined by grinding by hand.[135] After heating and removing the Mg catalyst, this resulted in a graphite comprising a Voronoi tessellated arrangement of graphite sheets emanating from central hollow graphite spheroidal seed particles. In this chapter, ball milling the precursors resulted in a completely different sample morphology, comprising mainly hexagonal graphite platelets. This change may have arisen from an improved Mg/hard carbon mixture that is dispersed on a much smaller length scale than hand grinding: most Mg particles (~5 – 30 μm) and carbon particles are separately distributed in the ground C/Mg mixtures (Figure 3.2(a-f)), while a more homogenous C-Mg distribution is observed in the milled C/Mg mixtures with much smaller Mg particles (Figure 4.2(a-c)). In addition, ball milling may have changed the precursor structure considerably, which might have also contributed to differences in the resulting graphite morphology. In any case, it is clear that modifications of the magnesium graphitization conditions can significantly change the final products. Further investigation into these processes may allow further morphologies to be produced or even designed with foresight.

In addition to sample morphology, the level of graphitization achieved by ball milling the precursors was much greater than when they were simply hand ground together. As shown in Chapter 3, hand grinding Mg and hard carbon prior to heating resulted in P_r values of about 45% being achieved at 1000 °C. By using ball milling to combine the precursors an astonishingly low value of P_r of $< 10\%$ was obtained at the same temperature (1000 °C). This value is similar to that of battery grade commercial graphites, and is higher than that reported previously for conventional artificial graphites made at 2800 °C.[141] To the author's knowledge, there is no previous report of such a highly crystalline and highly pure graphite made at such a low temperature. In addition, it is believed that this is the first report of the bulk synthesis of HPG crystals. HPG crystals reported in the past were found in iron or nickel eutectic melts where the carbon is a small minority phase that is difficult to separate from the parent metals.[62,132,137]

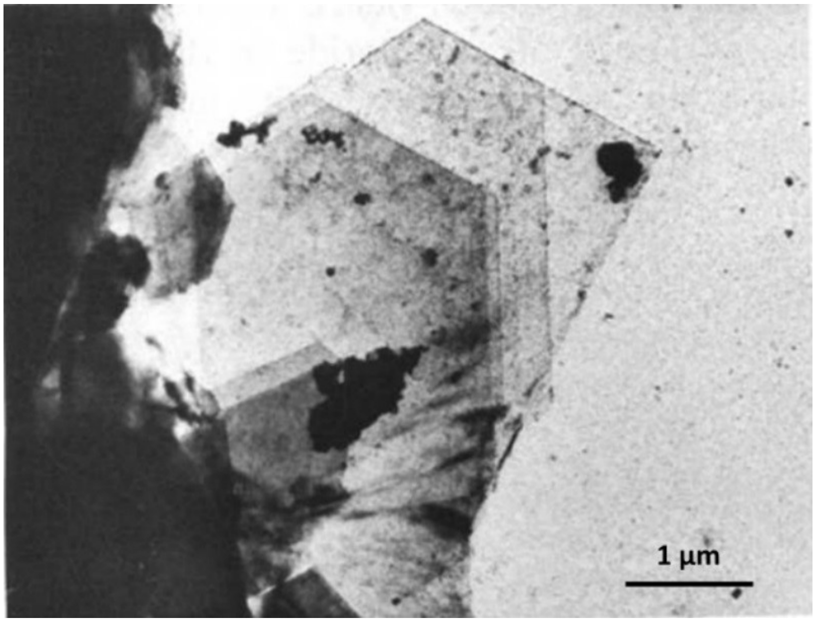

Figure 4.13 "Angular" graphite crystals found by Osetzky. Reproduced with permission from [147].

As suggested above, Mg catalyzed graphitization might follow the dissolution-precipitation mechanism proposed by Fitzer *et al*,[19] even though the solubility of carbon in magnesium is small.[148] There is no direct evidence proving the formation of magnesium carbide during graphitization. However, Osetzky found "angular" graphite crystals (Figure 4.13), which are similar to hexagonal platelets observed in this study.[147] The angular graphite crystal was obtained from the decomposition of magnesium carbide. This suggests the hexagonal platelets in HPG might also form due to the decomposition of magnesium carbide, indicating the mechanism of Mg catalyzed graphitization might be a combination of carbon dissolution-graphite precipitation and the formation-decomposition of carbides. However, it is also suggested that magnesium carbide cannot be directly made from the elements, carbon and magnesium.[149,150] Further work should be done to understand the mechanism of Mg catalyzed graphitization.

Ōya *et al.* classified catalytic graphitization into three types (G-effect, A-effect, and T-effect) as introduced in Chapter 1.1.2.1. Based on the results in Chapter 3 and 4, it is more exact to classify those catalytic phenomena into different stages in the case of using a Mg catalyst. For example, HPG (800 °C, 3 h) and VTG (900 °C, 3 h) belong to the T-effect stage while HPG (1000 °C, 3 h) and HPG (1000 °C, 20 h) belong to the G-effect stage. This maybe also true for all other catalysts.

The electrochemical properties of HPGs are exceptional for a carbon produced at this temperature. The observed high reversible capacity and staging transitions are indicative of low turbostratic disorder, consistent with XRD results. The reversible capacity of HPGs made at 1000 °C are competitive with graphites for commercial Li-ion batteries. The high degree of graphitization and high reversible capacity achieved by HPGs suggest that high performance graphites for Li-ion batteries may be made by catalyzation at temperatures as low as 1000 °C. To the author's knowledge, there is no graphite made at such low temperatures that have performance characteristics that approach those observed here. Although only Li-ion battery performance was demonstrated, considering the low temperature of the synthesis, the use of renewable organic feedstocks, the ability to form unique microstructures, and the high crystallinity and purity of the graphite produced, it is believed that this method can have enormous impact on the production of unique and specialized graphites.

The low-pressure evaporation is an effective method to remove Mg. However, the MgO impurity cannot be removed by this method. Unlike reacting with HCl, low-pressure evaporation only changes the physical state of Mg and avoids the formation of Mg compounds. It is also possible to recycle the Mg catalyst with a proper design of the heating equipment. For example, a long vacuum tube can be used in the low-pressure heating step. When the Mg vapor transits from the hot part to the cool part of the tube, Mg vapor can rapidly deposit and be recovered for subsequent use. By this means a scalable commercial process might be realized.

4.5 Summary

Hexagonal platelet graphite (HPG) crystals were grown from the milled hard carbon/Mg mixtures in 3 h at only 800 - 1000 °C. The HPGs made at 1000 °C have a high level of graphitization that is similar to battery grade commercial graphites, and higher than artificial graphites made at 2850 °C. HPGs also have an interesting microstructure, containing hexagonal platelets and some graphene particles. This results in a high specific surface area (55 - 82 m^2 g^{-1}). Mg catalyzation may be a convenient route to synthesizing high purity bulk graphite with unique microstructures. Such highly graphitized, but high surface area carbons in this study are desirable in applications such as supports for catalysts used in chemical synthesis or in fuel cells.

When cycled in Li half-cells the graphites have the best performance reported thus far for graphites made at such low temperatures, with characteristics similar to that of commercial artificial graphites made at much higher temperatures (> 2800 °C). However, the irreversible capacity of some HPGs is high, due to their high surface area. Carbon coating greatly reduced the irreversible capacity and increased the coulombic efficiency of HPGs up to 99.99% after 50 cycles. This study shows that high performance Li-ion battery graphite may be made at temperatures as low as 1000 °C from renewable materials.

By comparing this chapter to Chapter 3, it is proved that the catalytic graphitization level is greatly influenced by catalyzing conditions. The morphology of the graphite is also dependent on preparation conditions, and therefore it is believed that many other forms of graphite might be made using this method by variation of the reaction conditions.

The low-pressure evaporation method was proved to be an effective way to remove Mg, although MgO impurities remain in the product. By a proper design of the furnace and tubes, it is possible to recover the Mg catalyst.

Because of its use of renewable feedstocks, low temperature synthesis, ease of catalyst recovery, and the high purity and highly ordered graphite produced, magnesium catalyzed graphitization may have enormous impact on the production of unique and specialized carbons.

Chapter 5 Various Precursors for Mg Catalyzed Graphitization

5.1 Introduction

In Chapter 3 and 4, only glucose was used as the precursor for catalytic graphitization. However, carbon has a huge family and abundant sources can be used as graphitization precursors. In this chapter, more materials have been used as precursors for catalytic graphitization, including materials that are essentially all composed of carbon (coke and activated carbon), carbohydrates (cellulose and glucose), polymers (polyvinyl chloride (PVC), phenolic resin (PR)/phenol formaldehyde resin (PFR), polyvinyl alcohol (PVA), polyacrylic acid (PAA), and polyacrylonitrile (PAN)), and the carbon composites (tire). Among these precursors there are conventionally graphitizable materials, like coke, and non-graphitizable materials, like activated carbon; there are small molecules, like glucose, and large molecules, like polymers. There are no previous reports in the literature comparing graphites made with various precursors with one catalyst. By comparing the graphitization process and products from different precursors, the Mg-catalyzed graphitization process could be better understood.

The process of converting carbon precursors to graphites includes two main steps: carbonization and graphitization. For organic precursors and carbon composites, volatile materials and most non-carbon elements can be removed during carbonization, leaving a product that is essentially pure carbon. However, precursors have different thermal degradation properties. Specific carbonization methods should be applied accordingly. Coke and activated carbon have already been carbonized. Therefore, only degassing is required to remove adsorbed gases on material surfaces for these precursors.

One of the most commonly used graphitizable carbon precursors in industry is petroleum coke.[151] Although the process details for making artificial graphite are usually trade secrets, all conventional industry graphitization methods apply ultra-high temperature (~3000°C) heat-treatment. Coke has also been used as a precursor in catalytic graphitization.[152,153] Engle found that aluminum has a catalytic effect for coke graphitization at 2300°C.[152] Parker *et al.* also found that needle coke has a higher graphitization level by adding a Fe_2O_3 catalyst.[153]

Glucose has been intensively introduced in Chapter 3 and 4. As a non-graphitizable material, glucose precursors have been used in many catalytic graphitization studies,[154,155] besides the work done in our group.[58,135,156,157] However, in other groups' studies, the crystallinity level of the product graphite was usually not very high.[154,155]

Tires are highly complex assemblages of various components.[158] The main component of tires is rubber (*e.g.* natural rubber and styrene butadiene rubber (SBR)). Besides rubber, tires also contain different additives/fillers, such as carbon black, silica, and alumina.[158,159] In 2001 approximately 800 million tires were discarded around the globe annually.[160] This number was estimated to increase by 2% every year. Dealing with waste tires is a big issue. Most waste tires are burnt, buried, or discarded.[158] Huge efforts also have been made to recycle waste tires, including the graphitization of waste tires. Gnanaraj *et al.* tried to graphitize waste tires at 1100 °C.[161] However, the crystallinity level of the product graphite was not very high, with a huge interlayer spacing of 4.5 Å. When cycled in Li cells, the graphite electrode had a very huge irreversible capacity. The graphite electrode must also have had a huge hysteresis (low energy conversion efficiency) considering its low graphitization level.

Activated carbons are porous materials with high specific area (> 1000 m^2/g). Porous activated carbon based materials are widely applied in supercapacitors, lithium batteries, gas storage, catalytic supports, air filters, and adsorbents.[20,162] Porous graphitic carbons with a high crystallinity level are much superior in some applications due to their additional merits such as high electrical conductivity and good chemical stability.[20] Liu *et al.* converted activated carbon into a graphitic material by using a nickel nitrate catalyst at ~1000 °C.[20] However, the graphitization level of the graphite product was not very high and comprises more turbostratic graphite rather than ordered graphite, according to its XRD pattern (Fig. 2 in the Reference [20]). The surface area of the product graphite was also very high (~1600 m^2/g).

Cellulose is one of the cheapest, most abundant naturally occurring renewable organic polymers. In general, cellulose belongs to the non-graphitizable carbon class.[163] Researchers have tried to use cellulose as a precursor in catalytic graphitization in limited studies.[164–166] Sevilla *et al*. obtained a highly graphitic product by using a cellulose precursor and a Ni salt catalyst at only 900 °C.[166] However, the graphite product had a d_{002} (interlayer spacing) of 3.41 Å, characteristic of a turbostratic graphite. PVC is one of the world's most widely produced synthetic plastic polymers. Unlike most polymers, PVC is conventionally graphitizable. Inagaki *et al.* reported that graphite with a high graphitization level can be made from PVC at ~1000°C by adding metal oxide catalysts,[167] although the graphite yield is very low (< 5 wt.%). PVA is also a graphitizable polymer, with a similar structure to that of PVC. Highly ordered graphite has been made by Inagaki *et al*. from PVA with a Fe_3O_4 catalyst at 1200 °C.[81]

PAA is a conventionally non-graphitizable precursor. Inagaki *et al.* successfully converted PAA into highly ordered graphite with 50 wt. % Fe_3O_4 at 1200 °C for 5h.[78] PR is also a conventionally non-graphitizable carbon precursor.[168] Zhao *et al.* showed that highly order graphite can be made at only 1000 °C by adding a ferric nitrate catalyst.[169,170] However, the catalyst was not easily removed, with Fe_3C peaks in the graphite product XRD patterns. Ōya *et al.* also tried graphitizing PR with a tetrakis-(hydroxymethyl)-phosphonium sulfate catalyst.[49] However, a highly graphitic product was not obtained until a very high temperature was used (~3000 °C).

PAN is another conventionally non-graphitizable carbon precursor. Even when PAN was heated at 2800 °C, its 002 peak in XRD pattern is still a broad hump.[92] As an important industrial precursor for carbon fibers fabrication, PAN was intensely studied in the field of catalytic graphitization.[43,92,97,171] Highly ordered graphites were obtained at ~1000 °C from PAN by using various catalysts (Fe-Cr_2O_3,[171] Ni-P,[97] and Ni-Fe[92]). The industrial PAN-carbon fiber conversion process includes three steps: electrospinning, stabilization, and carbonization.[172,173] In the oxidative stabilization process (usually between 200 - 300°C), PAN is heated in an oxygen-containing atmosphere, cyclization and dehydrogenation occurring as shown in Figure 5.1. In this chapter, it will be shown how stabilization influences the graphitization effect.

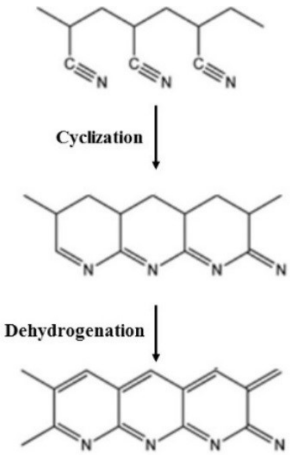

Figure 5.1 Stabilization process of PAN.

In this chapter, the effects of using various carbon materials as precursors and of using different carbonization methods on the magnesium catalyzed graphitization process are compared.

5.2 Experimental

5.2.1 Synthesis of catalytic graphites

Various precursors were pre-heated by different methods as shown in Table 5.1. Coke and activated carbon were degassed under Ar before graphitization. Carbohydrates (glucose and cellulose) were de-watered in air at low temperature (< 200°C), then carbonized at high temperature (up to 1100°C). Polymers and a carbon/polymer composite (tire powder) were carbonized using different methods based on their thermal degradation analysis. Polyacrylonitrile (PAN) was also stabilized first in air and then carbonized under Ar. Most precursors were in a solid powder state before degassing/carbonization, except phenolic resin, which was in the form of a solution (3M RPR1, resole phenol-formaldehyde resin, having phenol to formaldehyde ratio of 1.5-2.1:1, catalyzed with 2.5 percent potassium hydroxide, ~75% solution in water, 3M Co.). Tire powder was made from waste tire scrap recovered using a bench grinder.

After carbonization/degassing, the resulting carbons were combined with magnesium powder (HART METALS, INC., -325 mesh) (C:Mg = 1:1 by mole) in a 65 mL hardened steel vial containing 115 g stainless-steel balls (4.76 mm in diameter) under an argon atmosphere and milled for 2 h in a high-energy ball mill (SPEX Model 8000-D, SPEX CertiPrep, Metuchen, NJ). The resulting amorphous carbon/Mg mixture was heated in an argon-filled stainless-steel tube (~200 mm, OD 12.70 mm, ID 9.40 mm, sealed with Parker-A-lok caps) at 1000 °C for 3 h, resulting the formation of a graphite/Mg mixture. To remove the Mg catalyst after graphitization, two methods were used. Some graphite-Mg samples were heated under low pressure (< 20 Pa) at 900 °C for 5 h. For most samples, an acid wash procedure was used: ~2 g of the graphite/Mg mixture was first placed in a solution of 50 mL of 2 M HCl (prepared from 37 wt. % HCl, Aldrich) and 2 mL of ethanol (98%, Aldrich) for 12 h with stirring. Here, ethanol was used reduce the surface tension of the acid solution, increasing its wetting ability. After reacting with HCl, the product was transferred to a Büchner funnel (Whatman filter paper, qualitative) and was washed with 2 M HCl five times and then washed with distilled water repeatedly until the pH of the supernatant was about 7. Finally, the products were dried in air at 120 °C for 3 h.

Table 5.1 Sources and carbonization/degassing methods for each precursor.

Precursors	Sources	Carbonization/Degassing Methods	References
Coke	Asbury, Needle coke, Grade 4491	Ar, 600°C 5h	
Activated carbon	Nuchar WV-B 10*25 mesh	Ar, 600°C 5h	
Glucose	Sigma-Aldrich, α-D-Glucose, 96%	Air, 180°C 24h Ar, 1100°C 3h	
Tire	Goodyear Excellence	Ar, 250°C 0.5h, 380°C 0.5h, 440°C 0.5h, 1100°C 3h	174
Cellulose	Sigma-Aldrich, α-Cellulose	Air, 190°C 24h Ar, 370°C 1h, 1100°C 3h	
Polyvinyl chloride (PVC)	Sigma-Aldrich, ~48,000	Ar, 280°C 0.5h, 450°C 0.5h, 1100°C 3h	136
Phenolic resin (PR)	3M R23155	Ar, 460°C 0.5h, 550°C 0.5h, 660°C 0.5h, 1100°C 3h	175
Polyvinyl alcohol (PVA)	Sigma-Aldrich, 89,000~98,000	Ar, 425°C 0.5h, 525°C 0.5h, 1100°C 3h	176
Polyacrylic acid (PAA)	Sigma-Aldrich, ~450,000	Ar, 300°C 0.5h, 425°C 0.5h, 1100°C 3h	177
Polyacrylonitrile (PAN_1)	Sigma-Aldrich, ~150,000	Ar, 300°C 1h, 1100°C 3h	178
Polyacrylonitrile (PAN_2)	Sigma-Aldrich, ~150,000	Air, 200°C, 5h, 240°C 5h, 280°C 5h Ar, 500°C 3h, 700°C 3h, 1100°C 3h	172
Polyacrylonitrile (PAN_3)	Sigma-Aldrich, ~150,000	Air, 200°C, 5h, 240°C 5h, 280°C 5h Ar, 500°C 3h, 700°C 3h	172

5.2.2 Materials characterization

Catalytic graphites were characterized by using many techniques: scanning electron microscopy (SEM), energy dispersive X-ray spectroscopy (EDS), transition electron microscopy (TEM), X-ray diffraction (XRD), Brunauer-Emmett-Teller (BET) surface analysis, inductively coupled plasma-optical emission spectroscopy (ICP-OES), and pycnometry, with the equipment introduced in Chapter 2. Electrochemical measurements of catalytic graphites as working electrodes in Li-half cells were performed. Details of slurry making, cell assembling and cycling are described in Chapter 2.

The CARBONXS program developed by Shi *et al.* was used to fit the XRD patterns of some catalytic graphites to study their structural order.[112] Details regarding the fitting process can be found in Chapter 2. Pseudo-Voigt peak shape functions were also used to fit the 002-peak region of each XRD pattern of catalytic graphites to learn about their structural details. A description of the fitting procedure can be found in Chapter 2. The XRD pattern of MAGE commercial graphite (Hitachi) was also fit by CARBONXS and the pseudo-Voigt method for comparison.

5.3 Results

5.3.1 Structural and morphological characterization

Figure 5.2 shows SEM images of non-polymer carbon precursors after carbonization or degassing, and their corresponding graphite products. The coke precursor after degassing is composed of large needle-shaped particles (> 50 µm, Figure 5.2(a)). After graphitization (1000°C, 3h), the graphite product is mainly composed of irregular platelets (1-8 µm, Figure 5.2(b1-3)). Compared to glucose graphite shown in Figure 5.2(f1) and in Chapter 4, coke graphite platelets are more compact. The specific surface area of coke graphite is only 8.57 m^2/g, close to that of some battery grade commercial graphites, and much smaller than glucose graphite (> 80 m^2/g). The activated carbon precursor after degassing is composed of porous and much larger particles (> 300 µm, Figure 5.2(c)). After graphitization, the graphite product is composed of many dense particles (Figure 5.2(d1)), some small platelets particles (1-2 µm, Figure 5.2(d2)), and a small amount of large hexagonal platelets (up to 30 µm, Figure 5.2(d3)). Those large hexagonal platelets are very similar to those found in glucose graphite, comprising multiple layers with well-defined edges. Glucose carbon and its graphite product have been introduced in Chapter 4. In summary, most glucose graphite particles are composed of regions of small irregularly shaped secondary particles and regions of large hexagonal graphite platelets (up to 10 µm). Tire carbon after carbonization is composed of large chunks (> 75 µm). After graphitization, tire graphite is also mainly composed of irregularly shaped platelets (Figure 5.2(h1-3)), which are similar to those of coke graphite. However, the platelet size of tire graphite (1-6 µm) appears smaller than coke graphite. In addition, tire graphite comprises more tiny particles (< ~0.2 µm) on the platelet

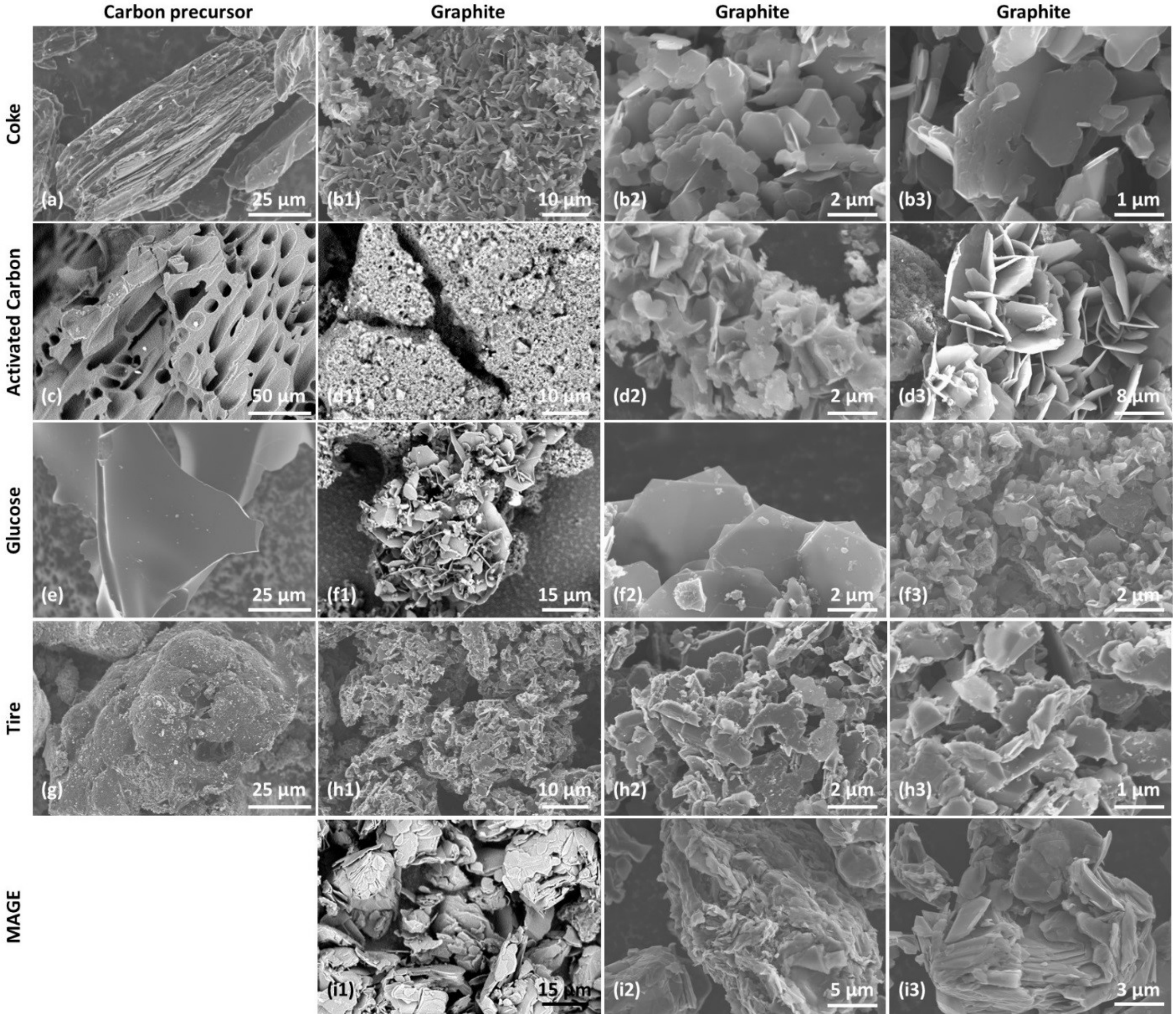

Figure 5.2 SEM images of (a, c, e, g) non-polymer and composite precursors after carbonization, and (b1-b3 ,d1-d3 ,f1-f3 ,h1-h3) corresponding catalytic graphites. (i1-i3) SEM images of MAGE.

surfaces (Figure 5.2(h2-3)), while coke graphite is essentially all composed of platelets. Tiny particles were also found in glucose graphite (Figure 5.2(f1-2)) and activated carbon graphite (Figure 5.2(d2-3)). The existence of the tiny particles might be due to incomplete graphitization.

Figure 5.3 shows SEM images of polymer precursors after carbonization, and their corresponding graphite products. Cellulose carbon has a fiber structure, composed of long threads (3-5 μm thickness, 10-20 μm width, hundreds μm length) after carbonization. Cellulose graphite is composed of relatively compact irregularly shaped platelets, similar to that of coke graphite and tire graphite. Most polymer particles after carbonization are composed of big chunks (usually > 30 μm): PVC carbon (Figure 5.3(c)), PR carbon (Figure 5.3(e)), PAA carbon (Figure 5.3(i)), and PAN_1 carbon (Figure 5.3(k)); while PVA carbon (Figure 5.3(g)) and PAN_2 carbon (Figure 5.3(m)) are composed of big secondary particles that are composed of smaller primary particles (< 2 μm for PVA carbon and < 1 μm for PAN_2 carbon). After graphitization, the graphite product made from PR is mainly composed of porous potato-shaped particles, with almost no platelets. Graphite products made from PVC and PAN_2 are essentially all composed of platelets, while graphite products made from PVA, PAA, and PAN_1 are compose of both dense particles and small platelets. The morphology of the graphite product particles is related to the graphitization level. This will be discussed later in this chapter. It is worth mentioning that the morphology of amorphous carbon and graphite made from PAN by using different pre-heating methods is very different. PAN_1 carbon is made by carbonization under Ar, while PAN_2 carbon is produced by stabilization in air and carbonization under Ar. The PAN_2 carbon particle morphology is distinct from that of PAN_1 carbon, indicating that these two amorphous carbon precursors have different structures. In addition, PAN_2 graphite is essentially all composed of platelets (graphitic structure) and PAN_1 graphite contains both dense particles (less ordered structure) and small platelets (graphitic structure).

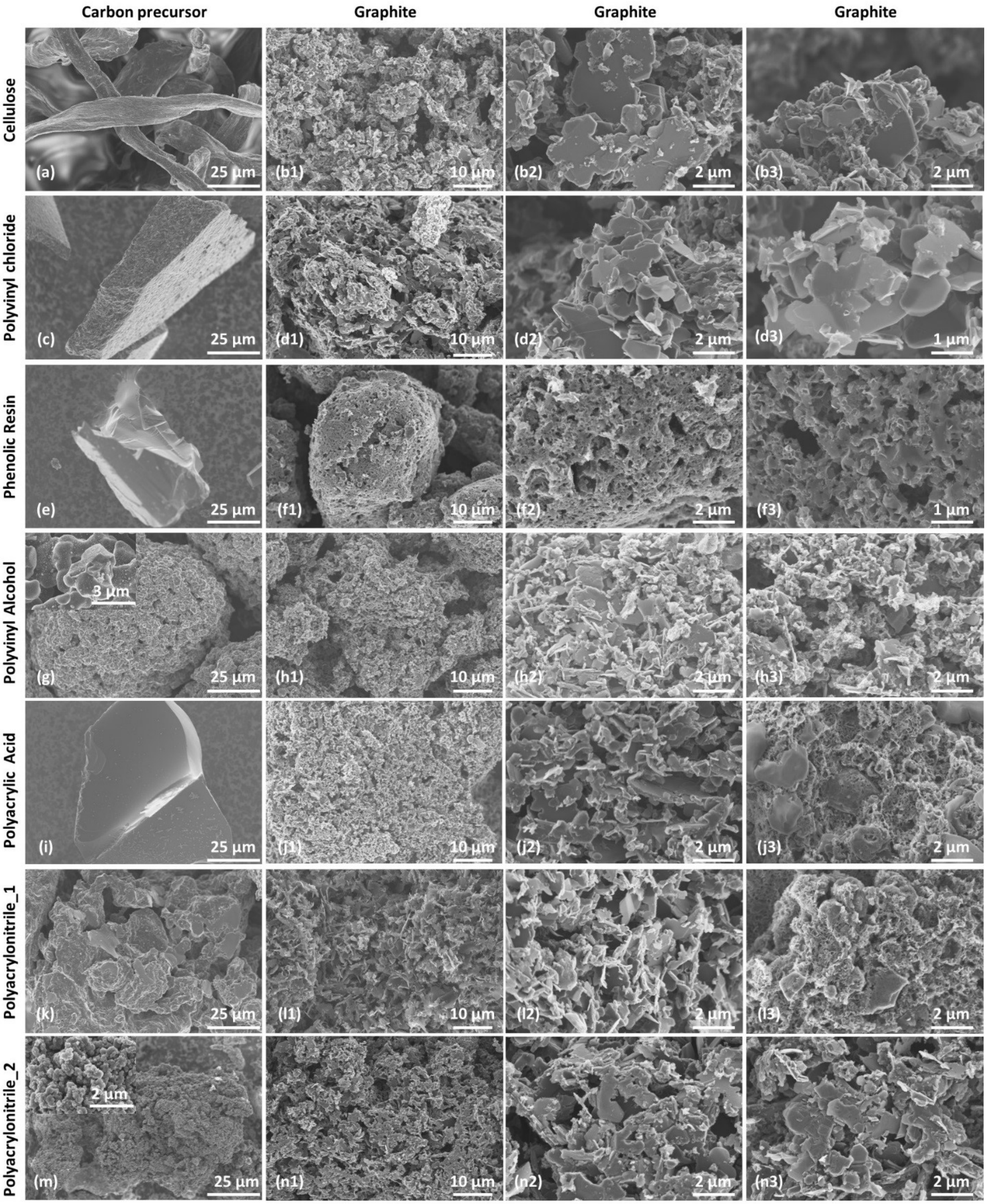

Figure 5.3 SEM images of (a, c, e, g, I, k, m) polymer precursors after carbonization, and (b1-b3, d1-d3, f1-f3, h1-h3, j1-j3, l1-l3, n1-n3) corresponding catalytic graphites.

For a better understanding of the graphitization mechanism, SEM and EDS measurements were conducted on the milled and heated carbon/Mg samples. Figure 5.4 shows SEM images of amorphous carbon/Mg materials after high energy mechanical milling. All carbon/Mg particles are composed of secondary particles comprising smaller primary particles. There is little difference among different carbon/Mg materials after milling, excepting the primary particle size. For example, activated carbon/Mg comprises the largest primary particles. The morphology of PAN_1 carbon/Mg and PAN_2 carbon/Mg look similar at this magnification (dozens of micrometers), though their corresponding graphites have very different graphitization levels.

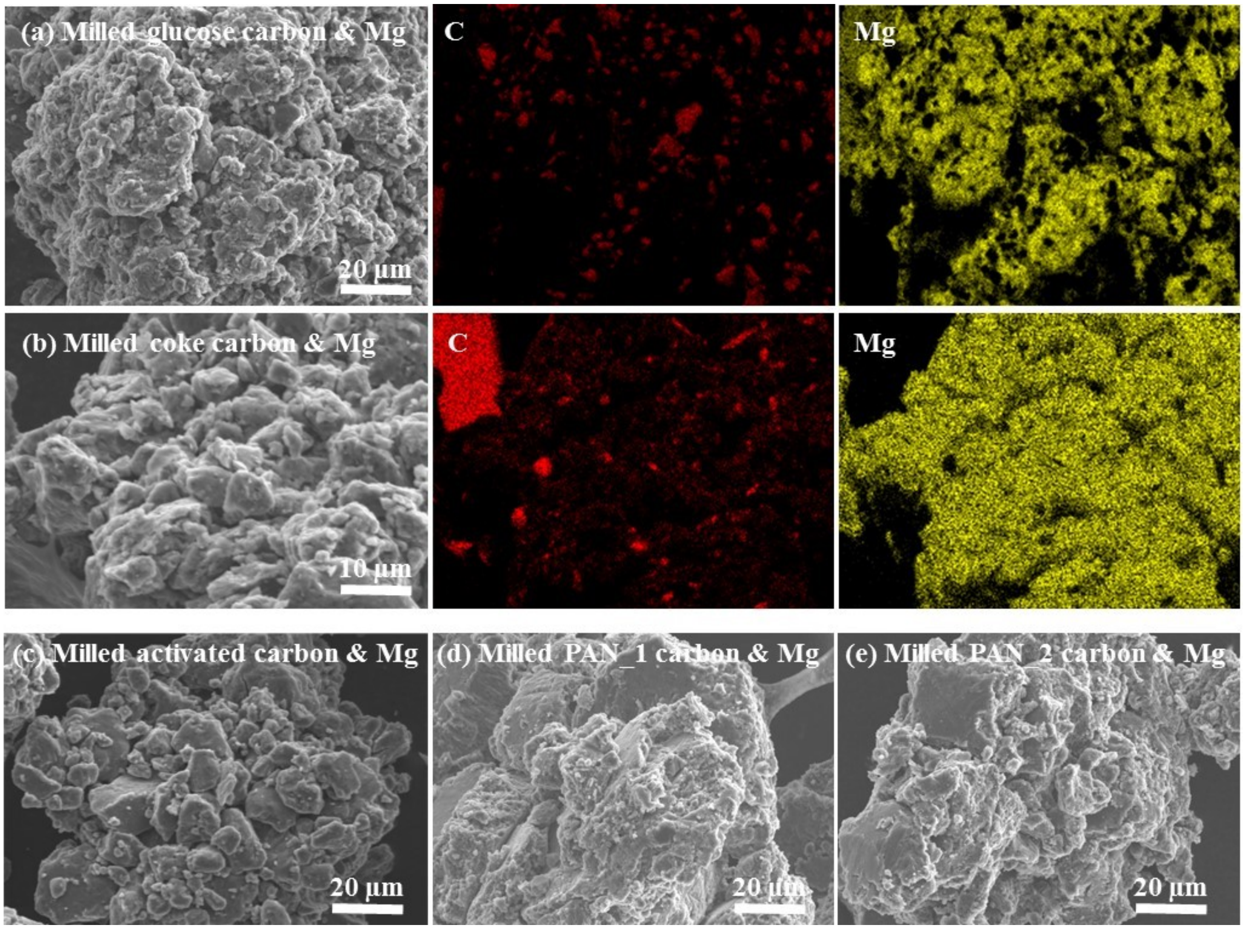

Figure 5.4 SEM images and corresponding carbon and magnesium elemental mappings of (a) SPEX milled glucose carbon/Mg and (b) SPEX milled coke carbon/Mg. SEM images of (c) SPEX milled activated carbon/Mg, (d) SPEX milled PAN_1 carbon/Mg, and (e) SPEX milled PAN_2 carbon/Mg.

After graphitization of the amorphous carbon/Mg materials, platelet graphite structures can be observed (Figure 5.5(a,b)). According to the elemental mapping images, there is more magnesium than carbon on milled carbon/Mg particles (Figure 5.4(a,b)), indicating magnesium might be covering carbon. However, magnesium and carbon are nearly evenly distributed on heated carbon/Mg particles (Figure 5.5(a,b)), indicating magnesium and carbon have re-distributed during graphitization. During the re-distribution process, carbon might become solvated in the catalyst, with concurrent graphite precipitation.[19] Carbon and magnesium elemental mapping images were also taken for other milled and heated carbon/Mg samples. They all show similar phenomenon and thus are not displayed here.

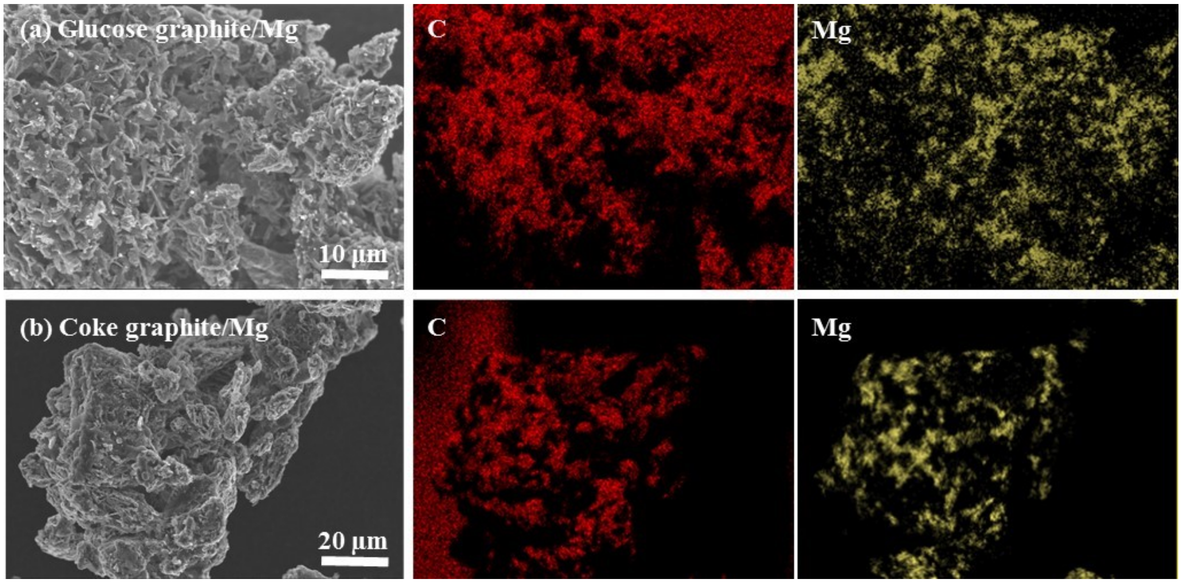

Figure 5.5 SEM images and corresponding carbon and magnesium elemental mappings of (a) glucose graphite/Mg and (b) coke graphite/Mg after graphitization and before reacting with HCl.

Figure 5.6(a) shows XRD patterns of non-polymer carbon precursors after carbonization or degassing. The XRD patterns of coke carbon and tire carbon have relatively narrow 002 peaks, indicating bigger carbon unit groups and a more anisotropic structure. In comparison, activated carbon and glucose carbon have much wider 002 peaks, indicating smaller carbon unit groups and

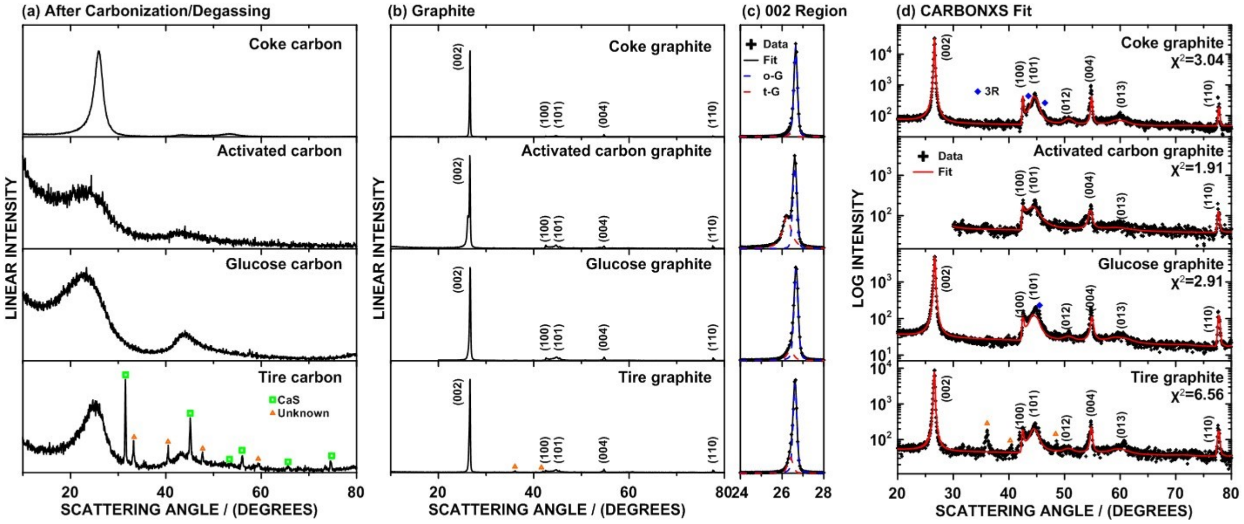

Figure 5.6 XRD patterns of (a) amorphous carbon made from composite or non-polymer precursors after carbonization/degassing. XRD patterns of (b) catalytic graphites, (c) enlarged 002 peak region, and (d) CARBONXS fits of each graphite XRD pattern.

a more isotropic structure. The tire carbon XRD pattern also contains some sharp peaks. Some peaks are consistent with CaS, which may have been formed during heating from a reaction between $CaCO_3$ (a filler commonly used in tires) and sulfur (i.e. from vulcanization). Other peaks could not be identified.

Figure 5.6(b) shows XRD patterns of the graphite products made from non-polymer precursors. All XRD patterns contain sharp and well-defined graphite peaks, indicating all non-polymer precursors were successfully graphitized. There are no Mg or MgO peaks detected, suggesting all Mg and MgO have been removed. This was also confirmed by ICP-OES measurements (Table 5.2). The Mg content in non-polymer graphites was found to be negligible (0.02 - 0.12 wt. %). However, the tire graphite XRD pattern still has the same unknown peaks as shown in the tire amorphous carbon XRD pattern. The intensity of these peaks is quite weak, suggesting this unknown impurity is of low quantity. To identify the unknown impurity, EDS spectroscopy and elemental mapping images were conducted, as shown in Figure 5.7(a). In the EDS spectrum, there is a tiny Si peak, which is almost negligible, beside carbon and oxygen peaks. In some tire graphite particles (not all), coexisting Si-rich and O-rich regions can be found (Figure 5.7(a) mapping images), suggesting that the unknown impurity might be a silicon oxide. This makes sense because silica is a common filler in tire manufacturing.[179] However, matching peaks were not found in the ICDD PDF-2 database. An oxygen peak is also obvious in the EDS spectrum because the SEM-EDS tape also contains oxygen, and there must be some oxygen containing adsorbates on the sample surface. As can be seen in the oxygen mapping image, the tire graphite particle also contains oxygen, especially in the Si rich region.

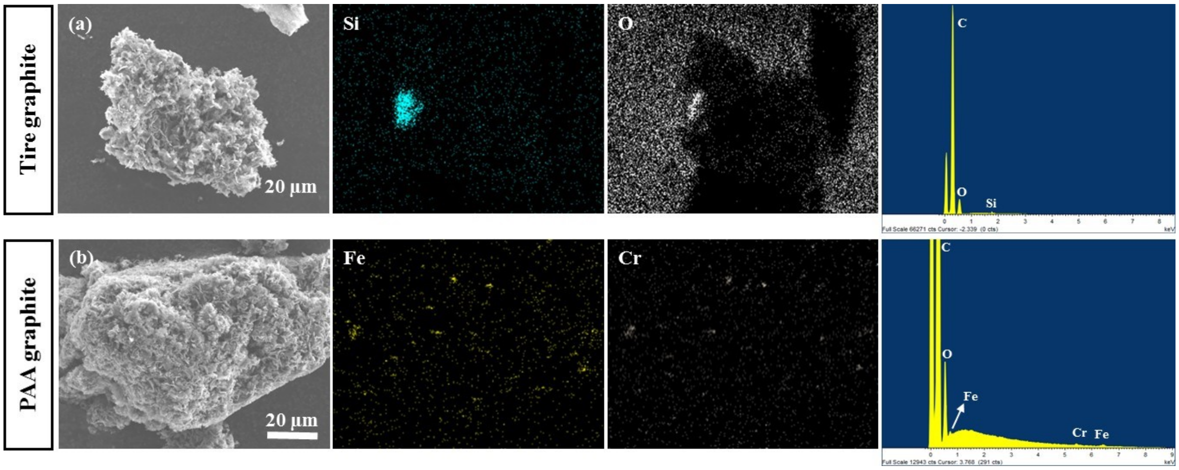

Figure 5.7 SEM-EDS of (a) tire graphite and (b) PAA graphite.

Table 5.2 Mg content, density, surface area, morphology of catalytic graphites made from different precursors.

Precursor	Mg Content wt. %	Density g/mL	Surface Area m^2/g	Morphology
Coke	-	2.2448	8.57	compact platelets
Activated	-	2.2756	142.80	porous platelets & dense particles
Glucose	0.023(1)	2.2941	82.50	porous platelets
Tire	0.120(6)	2.2318	11.90	compact platelets
Cellulose	0.019(0)	2.1946	30.00	compact platelets
PVC	0.051(2)	2.2166	13.55	compact platelets
PR	0.038(2)	2.157	87.62	porous potato-shaped particles
PVA	0.065(3)	2.1532	46.79	platelets & dense particles
PAA	0.146(8)	2.2738	28.80	platelets & dense particles
PAN_1	-	2.2217	-	platelets & dense particles
PAN_2	0.020(2)	2.1416	27.27	compact platelets

Table 5.3 Structural parameters of catalytic graphites determined by pseudo-Voigt fitting and CARBONXS. Here, “O” represents ordered graphite and “T” represents turbostratic graphite.

Precursor	pseudo-Voigt				CARBONXS				
	002	d_{002} Å	L_c Å	at. %	P_r %	P_{3R} %	a Å	L_a Å	$<\delta^2>^{1/2}$ Å
Coke	O	3.345(4)	400(5)	95.9(7)	8.1(0)	11.8(1)	2.456(1)	455(6)	0.04(2)
Activated carbon	O	3.350(4)	345(5)	47.4(7)	35.1(5)	1.2(0)	2.458(1)	340(6)	0.06(3)
	T	3.397(5)	157(5)						
Glucose	O	3.343(4)	357(5)	83.1(7)	13.7(3)	12.1(1)	2.456(1)	357(6)	0.06(2)
Tire	O	3.349(4)	374(5)	80.6(7)	16.0(5)	9.3(3)	2.458(1)	306(9)	0.04(2)
Cellulose	O	3.343(4)	393(5)	86.4(7)	13.2(4)	8.0(1)	2.456(1)	431(6)	0.04(2)
PVC	O	3.349(4)	393(5)	86.4(7)	11.4(2)	12.0(2)	2.457(1)	362(7)	0.05(2)
PR	O	3.347(4)	-	17.2(7)	62.8(8)	-	2.452(1)	101(3)	0.10(4)
	T	3.408(5)	161(5)						
PVA	O	3.350(4)	342(5)	52.7(7)	35.0(3)	1.0(0)	2.455(1)	201(4)	0.07(3)
	T	3.396(5)	192(5)						
PAA	O	3.345(4)	357(5)	66.5(7)	28.6(2)	4.1(2)	2.456(1)	281(7)	0.06(2)
	T	3.387(5)	225(5)						
PAN_1	O	3.347(4)	323(5)	45.5(7)	37.6(4)	1.1(0)	2.456(1)	210(7)	0.09(2)
	T	3.398(5)	254(5)						
PAN_2	O	3.348(4)	407(5)	87.0(7)	12.6(1)	10.6(2)	2.457(1)	422(4)	0.05(1)
PAN_3	O	3.350(4)	-	22.5(7)	45.2(5)	0.1(0)	2.457(1)	195(9)	0.07(3)
	T	3.393(5)	208(5)						

To quantitatively characterize the structure of the graphites made from different non-polymer precursors, 002 peaks of each graphite XRD pattern were fit by using pseudo-Voigt peak shape functions. Fitting results are shown in Figure 5.6(c) and data are listed in Table 5.3. According to the fitting results, coke graphite is essentially all composed of ordered graphite (95.9 at. %,), indicating a very high graphitization level. For comparison, the MAGE graphite is composed of 95.4 at. % ordered graphite. Both glucose graphite (83.1 at. %) and tire graphite (80.6 at. %) are mainly composed of ordered graphite. However, their graphitization levels are less than coke graphite. This suggests that the tiny particles observed in Figure 5.2(f1-2, h2-3)) might be less ordered graphite. Activated carbon graphite, on the other hand, only contains 45.3 at. % ordered graphite, consistent with the high turbostratic graphite peak in its XRD pattern. The interlayer spacing (d_{002}) and the inter-plane coherent length (L_c) were also determined by fitting 002 peaks (Table 5.3). These data are discussed later in the text.

The CARBONXS program was also used to fit non-polymer graphites with a two-layer model, as shown in Figure 5.6(d). For graphite XRD patterns with only one pronounced 002 peak, the CARBONXS fitting ranges were from 20° to 80°. For graphite XRD patterns with two 002 peaks (*e.g.* activated carbon graphite XRD), the fitting ranges were from 30° to 80° to avoid the 002-peak region. This is because CARBONXS cannot fit patterns with two 002 peaks and usually yields an untrustworthy fit as a result. Table 5.3 lists the probability of random stacking per layer (P_r), probability of 3R stacking per layer (P_{3R}), in-plane cell constant (a), in-plane coherent length (L_a), in-plane strain (ζ), interlayer spacing fluctuation ($<\delta^2>^{1/2}$), and the goodness of fit (χ^2) for each fit. Most XRD patterns were fit well with low χ^2 values (< 4). The relatively high χ^2 value of tire graphite (6.56) is probably due to the impurity peaks. For all non-polymer graphites, the in-plane cell constants (a) are close to the theoretical value for pristine graphite, indicating highly graphitic structures. The CARBONXS fitting results agree well with the fits using pseudo-Voigt fitting functions: the P_r value (indicating turbostratic content) by CARBONXS fitting and the atomic percent of ordered graphite by pseudo-Voigt fitting sum to nearly 100% for all graphites. Other CARBONXS fitting results of non-polymer graphites are compared with polymer graphites and are discussed later in the text.

Figure 5.8(a) shows XRD patterns of polymer carbon precursors after carbonization. The XRD patterns of carbon made from PVC and PAN have relatively narrow 002 peaks, indicating bigger carbon unit groups and a more anisotropic structure, while XRD patterns of carbon made from PVA, PAA, and especially cellulose have much wider 002 peaks, indicating smaller carbon unit groups and a more isotropic structure.

Figure 5.8(b) shows XRD patterns of graphite products made from polymer precursors. Similarly, all XRD patterns contain sharp and well-defined graphite peaks, indicating all polymer

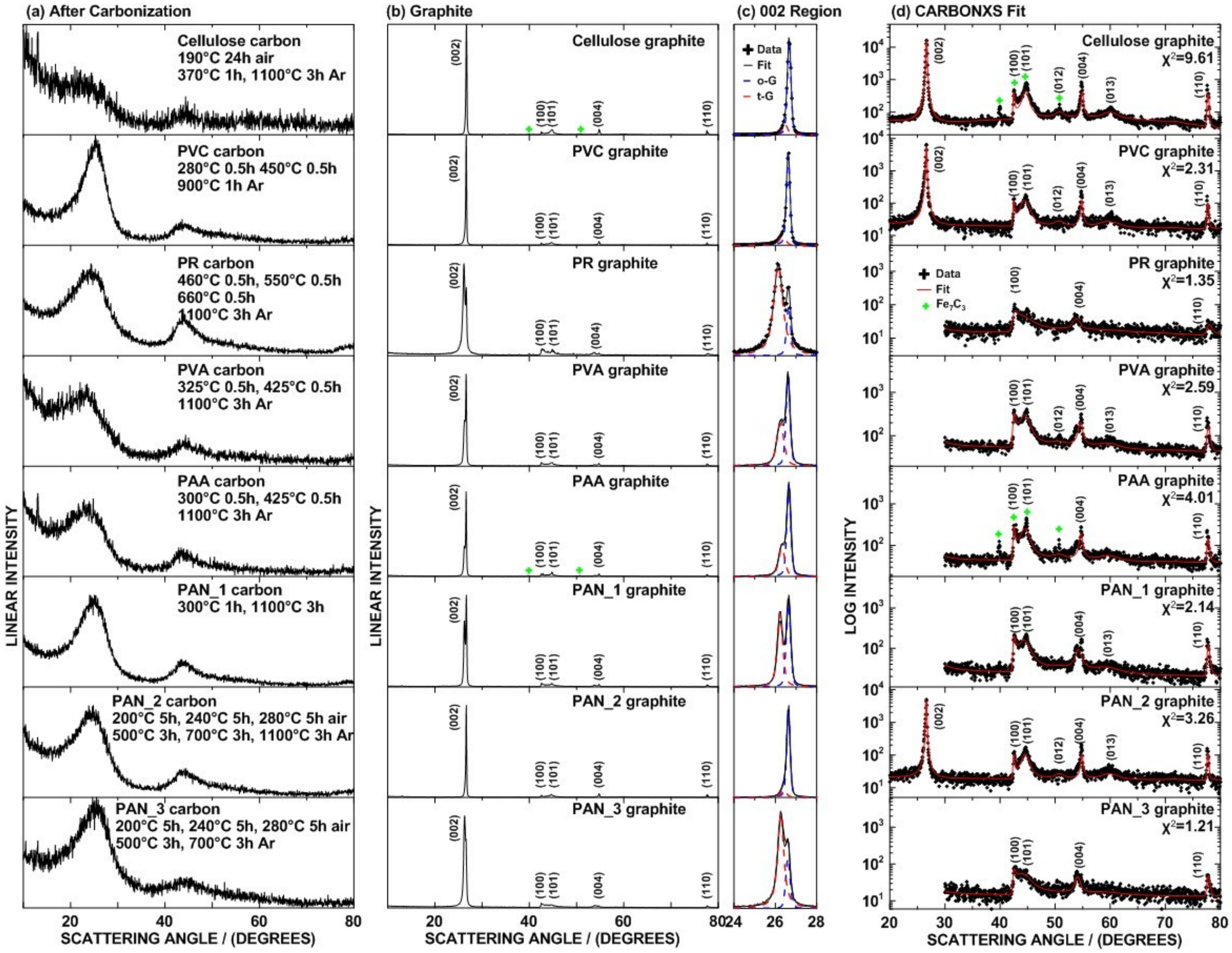

Figure 5.8 XRD patterns of (a) amorphous carbon from polymer precursors after carbonization/degassing. XRD patterns of (b) catalytic graphites, (c) enlarged 002 peak region, and (d) CARBONXS fits of each graphite XRD pattern.

precursors were successfully graphitized. Also, the Mg content in all polymer graphite products was negligible, as confirmed by ICP-OES measurements (0.02 - 0.15 wt. %, Table 5.2). However, the XRD patterns of cellulose graphite and PAA graphite also contain tiny impurity peaks. These peaks are so small that can only be observed by changing the vertical axis scale from linear to log (Figure 5.8(d)). The intensity of these peaks is so tiny that the amount of impurity must be very low. To identify the impurity, EDS spectroscopy and elemental mapping were conducted for PAA graphite, as shown in Figure 5.7(b). In the EDS spectrum, tiny iron and chromium peaks appear along with carbon and oxygen peaks. From the elemental mapping images, Fe-rich and Cr-rich regions can be observed. Usually, iron and chromium signals co-exist (Fe-rich spots are also Cr-rich spots), indicating the contamination probably comes from the high energy milling process. Stainless steel balls and hardened steel vials were used in this step, which contain both Fe and Cr. Fe/Cr contamination is inevitable as long as high energy milling with Fe/Cr containing balls are used.[180] The difference is that some graphite samples were more severely contaminated than others. Based on the contamination sources, Fe_7C_3 was identified as the impurity. Fe_7C_3 peaks were also detected by XRD in cellulose graphite/Mg and PAA graphite/Mg after graphitization and before reacting with HCl. This suggests that Fe contamination was probably induced by high energy ball milling, and then Fe reacted with carbon during heating, forming Fe_7C_3. However, no matching peaks of Cr-containing materials were found in the XRD patterns of cellulose graphite or PAA graphite. It is likely that the Cr is incorporated in the iron carbide as $(Fe,Cr)_7C_3$ carbides are well known in cast irons.[181]

All 002 peaks of polymer graphite XRD patterns were fit by using the pseudo-Voigt peak functions. Fitting results are shown in Figure 5.8(c) and fitting data are listed in Table 5.3. Both PVC graphite and cellulose graphite are composed of 86.4 at. % ordered graphite, close to that of a high-crystallinity commercial graphite. The XRD patterns of PAA graphite and PVA graphite have obvious turbostratic peaks, indicating a 66.5 at. % and 52.7 at. % content of ordered graphite, respectively. PR graphite contains only 17.2 at. % ordered graphite, with a huge turbostratic 002 peak in its XRD pattern. By applying different pre-heating methods, graphites with very different crystallinity levels were made from PAN. If PAN was simply carbonized under Ar (PAN_1), the graphite product only contains 45.5 at. % ordered graphite. If PAN was stabilized in air and then carbonized under Ar (PAN_2), the graphite product contains a high percent of ordered graphite (87.0 at. %). PAN_3 carbon was also stabilized and carbonized. However, the final carbonization temperature was 700 °C (lower than 1100°C for PAN_2 carbon). Its corresponding graphite product merely contains 22.5 at. % ordered graphite.

The CARBONXS program was also used to fit graphite products made from polymers as shown in Figure 5.8(d). Fitting data are listed in Table 5.3. For all polymer graphites, the in-plane cell constants (a) are close to the theoretical value, indicating highly graphitic structures. Most XRD patterns were fit well with low χ^2 values (≤ 4). The relatively high χ^2 values of the XRD fittings of cellulose graphite and PAA graphite are probably due to Fe_7C_3 impurity peaks. Some Fe_7C_3 peaks overlap with graphite 100 and 101 peaks, which must influence the fitting accuracy.

Structural data of all catalytic graphites and MAGE are compared in Figure 5.9. The samples are ordered according to their percent ordered graphite from left to right along the horizontal axes. Most non-polymer graphites are mainly composed of ordered graphite (>80 at. %), especially coke graphite, which is essentially all composed of ordered graphite (95.9 at. %) and is comparable to MAGE (95.4 at. %). However, activated carbon graphite, as an exceptional non-polymer graphite, is composed of a lower content of ordered graphite (47.4 at. %). Compared to non-polymer graphites, most polymer graphites are composed of a relatively lower amount of ordered graphite. Graphites made from PAA, PVA, and PAN_1 are composed of ~50 at. % ordered graphite. PR graphite has the lowest graphitization level, only containing 17.2 at. % ordered graphite. Some polymers can also be converted into highly ordered graphites, like PVC (86.4 at. % ordered graphite). It is also shown how the pre-heating step influences the graphitization result in Figure 5.9(a). PAN_1 (with only carbonization under Ar) was converted to a typical polymer-type graphite (~50 at. % ordered graphite). PAN_2 (with both stabilization and carbonization) was converted to a highly ordered graphite, with 87.0 at. % ordered graphite, which is the 2nd highest ordered graphite content among all the catalytic graphites in this study. PAN_3 (with only carbonization, and lower carbonization temperature) was converted to a turbostratic graphite.

Figure 5.9(b) shows the d_{002} (interlayer spacing) for both turbostratic and ordered graphite of all catalytic graphites. The ordered graphite d_{002} agrees well to the theoretical value, suggesting a highly graphitic structure. The turbostratic graphite d_{002} generally decreases as the graphitization level increases, with an exception of PAN_3 graphite.

Figure 5.9(c) shows the L_c (inter-plane coherent length) for both turbostratic and ordered graphite of all catalytic graphites. The ordered graphite L_c increases from ~320 Å to ~ 400 Å as the graphitization level increases. However, even the catalytic graphite of the highest graphitization level (coke graphite) has a much smaller L_c (400.3 Å) than MAGE (511 Å). In addition, the presence of tiny poorly graphitized particles in the sample might lower the L_c value. It is possible that the L_c could be higher if longer heating time was applied. As shown in Chapter 4, heating glucose carbon at 1000°C for 20 hours results in an ordered graphite with a large Lc (>

500 Å). The turbostratic graphite L_c ranges between ~150 Å and ~250 Å. There is not an obvious trend in turbostratic graphite L_c as the graphitization level increases.

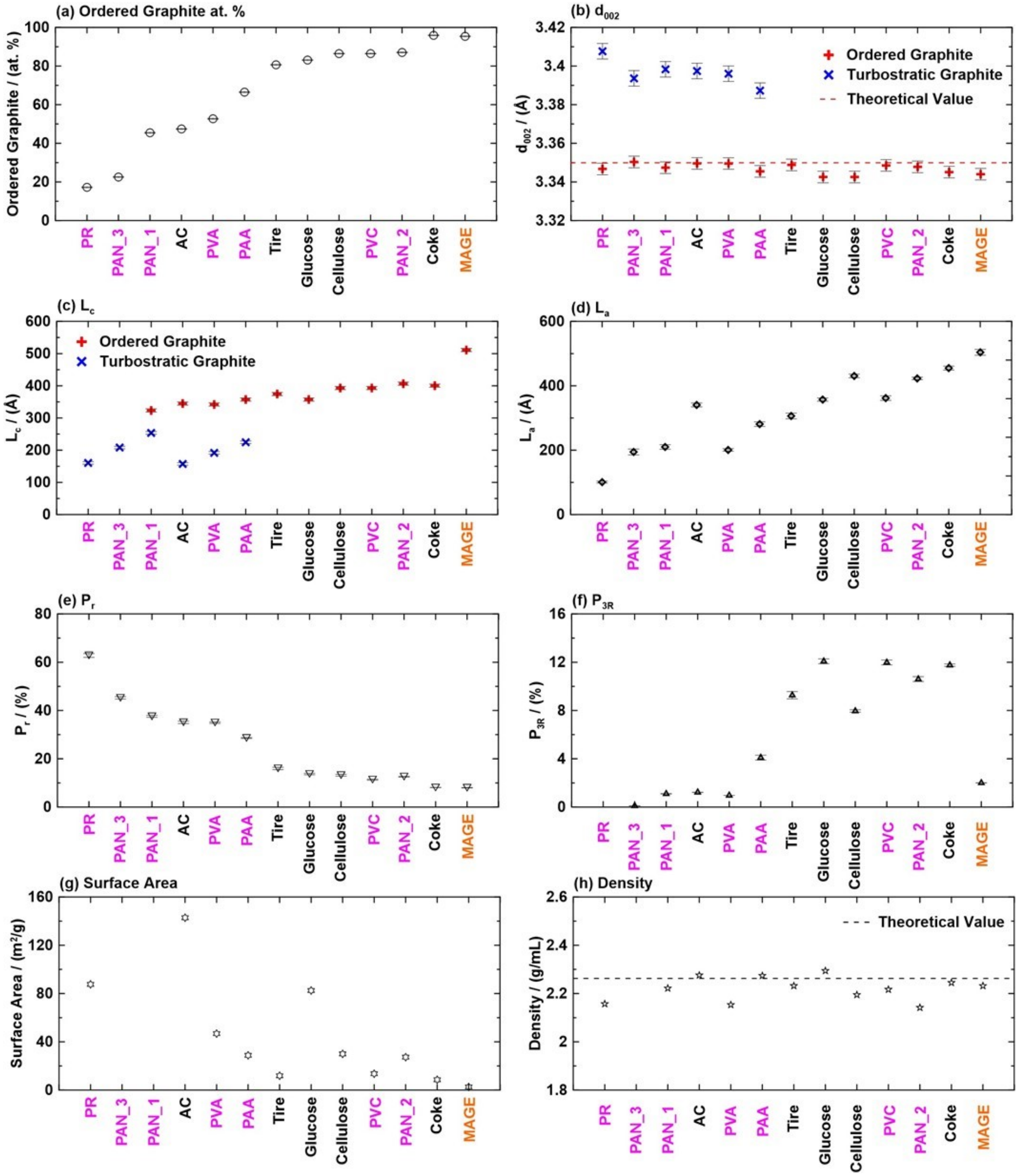

Figure 5.9 (a-f) Fitting results of all catalytic graphites and MAGE. Ordered graphite at. %, d_{002}, and L_c are obtained by using the pseudo-Voigt method. L_a, P_r, and P_{3R} are obtained by using CARBONXS. The horizontal axis is labelled by precursors: polymer precursors are in purple while non-polymer and composite precursors are in black. AC stands for activated carbon. (g) Surface area and (h) density of different graphites as labelled.

Figure 5.9(d) shows the L_a (in-plane coherent length) of all catalytic graphites. There is a rising trend in L_a as the graphitization level increases, growing from ~100 Å to ~460 Å. As a comparison, the L_a of MAGE is 504 Å. There are two outliers: L_a values of activated carbon graphite and cellulose graphite. Activated carbon graphite contains many large hexagonal platelets as shown in Figure 5.2(d3), which might increase the average L_a. In comparison, tire graphite, which contains more ordered graphite but has a lower L_a, comprises relatively small irregular-shaped platelets. Cellulose graphite also contains many wide platelets (Figure 5.3(b2)), while PAN_2 graphite contains relatively smaller platelets (Figure 5.3(g2-3)) although it is of higher graphitization level. The inconsistent changing trends between L_a and the graphitization level might be due to the different graphitization pathways of these precursors.

Figure 5.9(e-f) show the P_r (probability of random stacking per layer) and P_{3R} (probability of 3R stacking per layer) of all catalytic graphites. The changing trend in P_r is roughly mirror-symmetric to that of at. % ordered graphite. This means the two fitting methods (pseudo-Voigt and CARBONXS) yield the same or similar results in terms of graphitization level. Catalytic graphites with low crystallinity levels contain a small amount of 3R structure (~1%), while those with high crystallinity levels contain more 3R structure (8% - 13%). MAGE does not have a high P_{3R} value. The catalytic graphitization process might be more 3R-structure-formation preferred than conventional graphitization processes.

Figure 5.9(g) compares the specific surface area of catalytic graphites based on data listed in Table 5.2. There is not an obvious pattern between the surface area and graphitization level. However, the two graphites containing large hexagonal platelets (activated carbon graphite and glucose graphite) both have high surface area. This suggests that surface area is greatly influenced by graphite morphology. Specially, the surface area of activated graphite is as high as 142.8 m^2/g, presumably because the active carbon precursor has a high surface area (1760.6 m^2/g).

Figure 5.9(h) shows the density of some catalytic graphites and MAGE measured by pycnometer. The densities of most catalytic graphites are close to the theoretical value (2.266 g/mL); the largest difference being only ~5.5%, indicating highly graphitic structures.

5.3.2 Electrochemical characterization

Figure 5.10 shows the voltage profiles and differential capacity curves of the catalytic graphites with the highest ordered graphite content compared to MAGE. Voltage profiles of all catalytic graphites comprise distinct staging plateaus (Figure 5.10(a,c,e,g,I,k)), corresponding to sharp peaks in the differential capacity curves (Figure 5.10(b,d,f,h,j,l)), in verification of their highly ordered graphitic structure. For comparison, the voltage profile and differential capacity curve of MAGE are shown in Figure 5.10(m,n). All the materials also have excellent capacity retention during cycling, as shown in Figure 5.11(a). However, their reversible and irreversible capacities differ significantly as will be discussed in detail below.

Figure 5.11(b) shows the percent IC of the catalytic graphites and MAGE. All catalytic graphites have higher IC than conventional battery graphites. Glucose graphite has the highest IC (> 50%), and most other catalytic graphites have IC between 30% and 40%. Coke graphite has the lowest IC (< 30%), but still much higher than MAGE (~10%). In general, IC (in %) and IC loss (in mAh/g) of catalytic graphites decrease as specific surface area (SA) decreases (Figure 5.11(c)). As analyzed in Chapter 4, glucose graphite has a high surface area (>80 m^2/g), which is likely the main reason leading to its high IC (> 50%) and high IC loss (> 370 mAh/g. Compared to glucose graphite, cellulose graphite and PAN_2 graphite have lower surface areas (both ~ 30 m^2/g, Table 5.2), corresponding to their reduced IC (35% - 40%) and IC loss (180 – 210 mAh/g). Coke graphite, tire graphite and PVC graphite all have relatively small surface areas (all ~10 m^2/g, Table 5.2). However, their IC (30% - 37%) and IC loss (155 – 185 mAh/g) are only slightly reduced compared to cellulose graphite and PAN_2 graphite. According to previous studies, the IC of graphite almost linearly increases with surface area,[138–140] which is different from the observation in this study (Figure 5.11(c)). It is possible that a high surface area is not the only reason for the high ICs of catalytic graphites. Another reason may be that the tiny particles on big graphite particle surfaces (Figure 5.2 and Figure 5.3) also increase IC. These tiny particles are less ordered graphite and may also contain non-negligible amounts of hydrogen, which consumes extra Li during the initial lithiation.

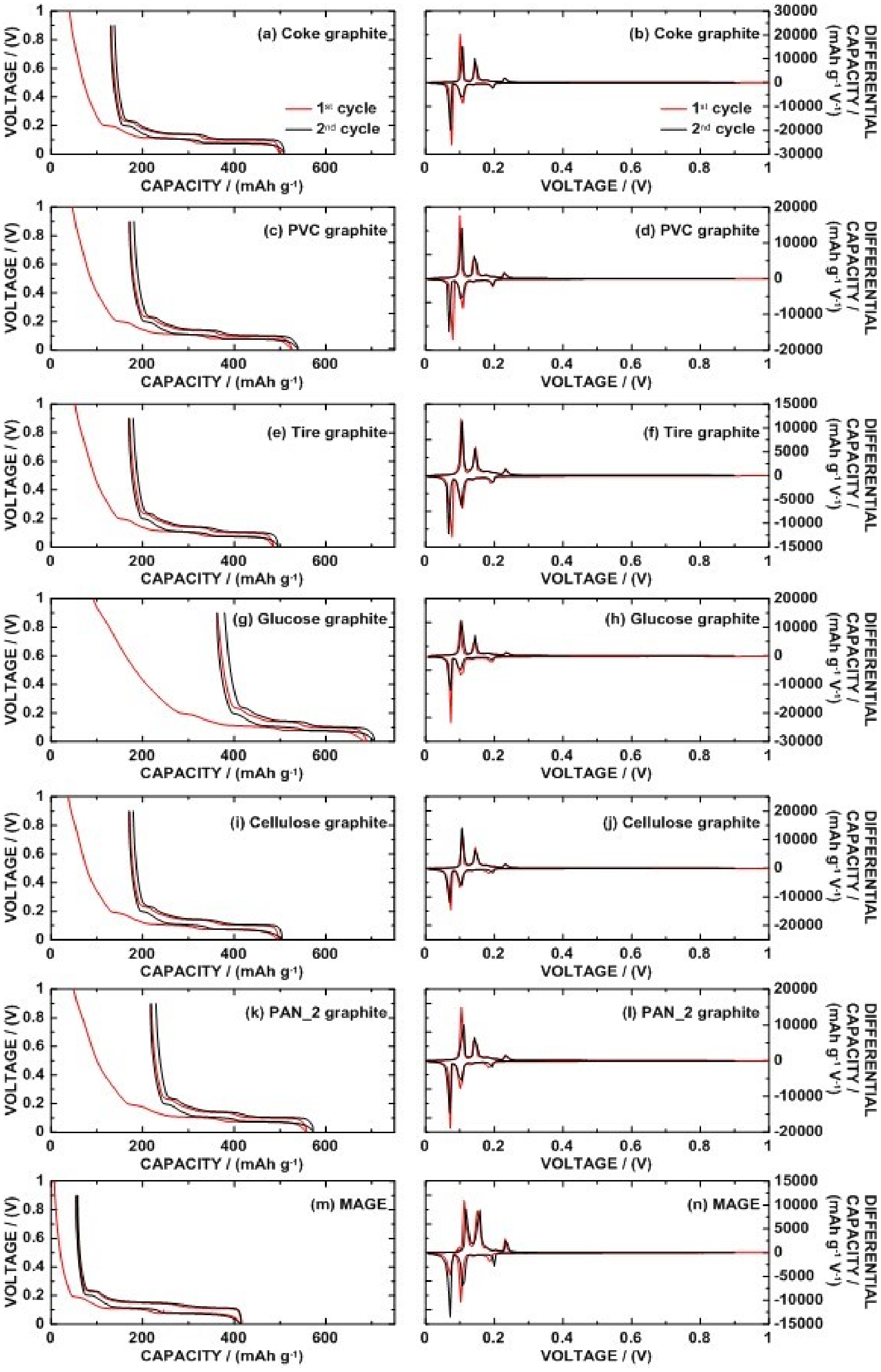

Figure 5.10 (a, c, e, g, i, k, m) Voltage profiles and (b, d, f, h, j, l, n) differential capacity curves of MAGE and catalytic graphites made from different precursors. In all figures, red lines represent 1st cycle and black lines represent 2nd cycle.

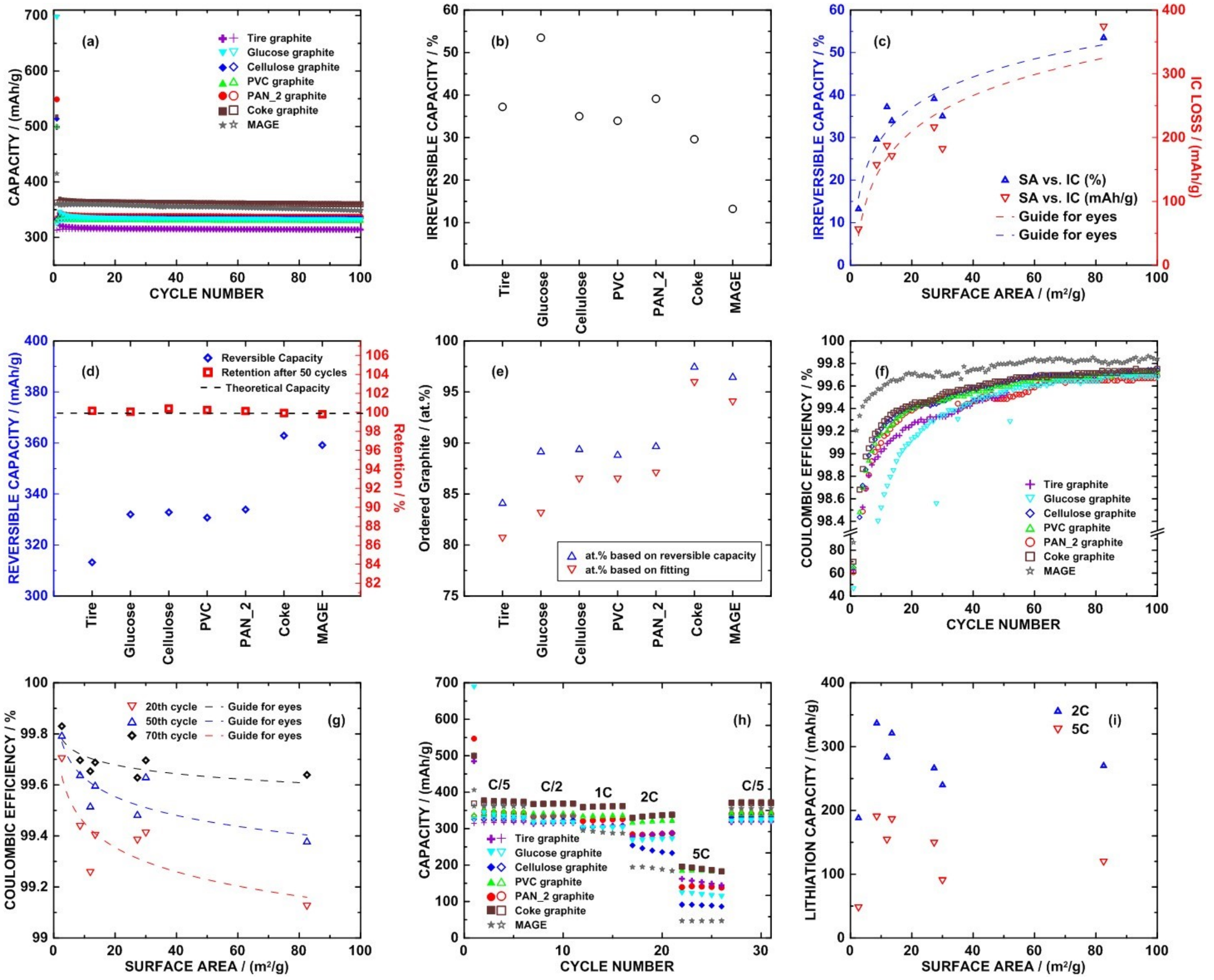

Figure 5.11 Electrochemical performance of MAGE and highly ordered catalytic graphites: (a) cycling performance at C/5, (b) irreversible capacity, (c) irreversible capacity (IC) and IC loss vs. surface area (SA), (d) reversible capacity and retention after 100 cycles, (e) comparison of ordered graphite content determined by reversible capacity and pseudo-Voigt fitting, (f) coulombic efficiency (CE), (g) CE at 20th, 50th, and 70th cycles vs. SA, (h) cycling performance at different C-rates, and (i) lithiation capacity at 2C and 5C vs. SA.

Figure 5.11(d) shows the reversible capacity of catalytic graphites and MAGE. Coke graphite has superior reversible capacity, close to MAGE and the theoretical value of graphite. Most other graphites have capacities between 330 and 340 mAh/g. The reversible capacity is proportional to ordered graphite content, since only ordered graphite is active for Li intercalation/deintercalation, according to previous research.[146] Therefore, the ordered graphite content can be calculated by: at. % ordered graphite = reversible capacity/(372 mAh/g). The calculation results agree well with the data determined by pseudo Voigt fitting, as shown in Figure 5.11(e).

Figure 5.11(f) shows the coulombic efficiency (CE) of catalytic graphites and MAGE. The CE values of all catalytic graphites keep increasing and reach 99.65% - 99.75% at 100th cycle, but are less than MAGE in general. This is likely due to the higher surface area of catalytic graphites compared to MAGE, which would result in greater Li loss during cycling due to surface reactions with electrolyte. Glucose graphite has the highest surface area among all measured catalytic graphites in Figure 5.11(f). Its CE also increases by the slowest rate. Figure 5.11(g) shows the relationship between SA and CE at 20, 50, and 70 cycles for catalytic graphites and MAGE. In general, a high SA corresponds to a lower CE at these cycles.

Figure 5.11(h) compares the capacities of catalytic graphites and MAGE at different C-rates. Catalytic graphites have much higher capacities than MAGE at high C-rates (1C, 2C, 5C). Therefore, high-C-rate capacity is not determined by graphite crystallinity. Among all catalytic graphites, coke graphite and PVC graphite are outstanding, and their capacities still have high retention when C-rate increases from C/5 to 2C. There is no relationship between surface area and high-C-rate capacity, as shown in Figure 5.11(i). However, high C-rate capacity may be greatly influenced by graphite particle sizes. MAGE has the largest particle size (> 10 µm, Figure 5.2(i1-i3)) among all tested graphites, corresponding to its worst high-C-rate performance (Figure 5.11(h)). Glucose graphite and cellulose graphite also have large platelet particles (≥ 5 µm, Figure 5.2(f2) and ~ 5 µm, Figure 5.3(b2), respectively), corresponding to their relatively low high-C-rate capacity. In comparison, coke graphite, tire graphite, PVC graphite and PAN_2 graphite all comprise small particles (< 2 µm, Figure 5.2 and Figure 5.3), corresponding to better high-C-rate performance.

5.4 Discussion

5.4.1 Morphologies of Catalytic Graphites

Catalytic graphites with various morphologies were made by using different carbon precursors. Generally, graphites with high graphitization levels (coke graphite, PAN_2 graphite, PVC graphite, cellulose graphite, and tire graphite) are essentially all composed of compact platelets. Glucose graphite is an exception, it has a high graphitization level but is composed of porous hexagonal platelets. As the most crystalline product (95.9 at. %), coke graphite contains pristine platelets with tiny particles (< 0.2 μm) on platelet surfaces. Other graphites all contain tiny particles, which are probably composed of less ordered graphites. The tiny particles might also be one of the reasons that cause high surface area. In comparison, graphites with medium graphitization levels (PAA graphite, PVA graphite, activated carbon graphite, and PAN_1 graphite) are composed of both platelets and dense particles. Their platelets are usually in small size (1-3 μm). Activated carbon graphite also contains a small amount of large hexagonal platelets (up to 10 μm), although its main content is still dense particles and small platelets. More and larger hexagonal platelets (up to 30 μm) were observed in activated carbon graphite if the graphitization time is extended from 3h to 20h. As the lowest crystalline product (17.2 at. % ordered graphite), PR graphite is composed of only dense particles with no observable platelets. To sum up, there is a general trend of morphology change as the graphitization level increases: from dense particles, to mixtures of dense particles and small platelets, to platelets as the main content with increasing sizes, and to much pure platelets with little/no less-ordered tiny particles. Two precursors are special: glucose and activated carbon. Large hexagonal platelets were only observed in their products.

Catalytic graphites with platelet structures (or lamellar structures, flaky structures) have been observed in previous studies by using different precursors and catalysts: such as coke and Pr_6O_{11} (2800 °C) [21], and coke/pitch and La_2O_3 (2800 °C) [91]. In both cases, the graphitization temperatures are very high. In this study, graphites with many large platelets were made at only 1000 °C. A lamellar structure is also a characteristic of graphites obtained from carbon-rich iron melts.[62,182] For example, highly graphitic flaky graphite was observed from a melt of cast iron at 1600 °C by Lee *et al.*[62]

Irregularly-shaped platelets in some catalytic graphites shown in Figure 5.2 and 5.3 are better described as "dendrites" or "foliated dendrites",[132] especially in coke graphite (Figure 5.2(b2)), tire graphite (Figure 5.2(h2)), PVC graphite (Figure 5.3(d1)), PVA graphite (Figure 5.3(h2)), PAA graphite (Figure 5.3(j2)), PAN_1 graphite (Figure 5.3(l2)), and PAN_2 graphite (Figure 5.3(n2)). Graphite dendrites have been observed in previous catalytic graphitization studies. Zhai *et al.* found graphite dendrites grown from mesophase pitch by adding $ZnCl_2$, $FeCl_3$, and $NiCl_3$ at below 1000 °C.[95] However, the graphitization level of the graphite product was quite low. The product was more like a mixture of turbostratic graphite and amorphous carbon. Konno *et al.* observed a dendrite-like graphite made by catalytic graphitization of polyvinyl pyrrolidone (PVP) with a Fe_3O_4 catalyst at 1000 °C.[78] Graphite dendrites were more often observed in cast iron melts.[78,132,183–185] Figure 5.12(a-c) show some examples of dendrite-graphite grown from cast iron (a[184], b[132], c[185]). The foliated dendrites schematic model has been proposed by Saratovkin (Figure 5.12 (e-f)).[186] Stefanescu *et al.* found that adding Mg can change the morphology of graphite dendrites in cast iron, as shown in Figure 5.12(d), building clusters along c-axis.[132] Graphite clusters grown along c-axis were also observed here in Mg-catalyzed graphite (Figure 5.3(b3)). Stefanescu *et al.* also pointed out that Mg favors the formation of more compact graphite and spheroidal graphite.[132] This is consistent with the finding in this study that Mg-catalytic graphites with higher crystallinity level are composed of more compact platelets. This is also consistent with the spheroidal graphite structure reported in Chapter 3 and 4. Although graphite dendrites or lamellar graphite were observed in cast iron, one should be aware that graphites found in cast iron are present in small amounts because carbon is a minor component in cast irons. In addition, graphites grown in cast iron are very difficult to isolate. In this study, catalytic graphites with special morphology were made in bulk and easily isolated from non-carbon components.

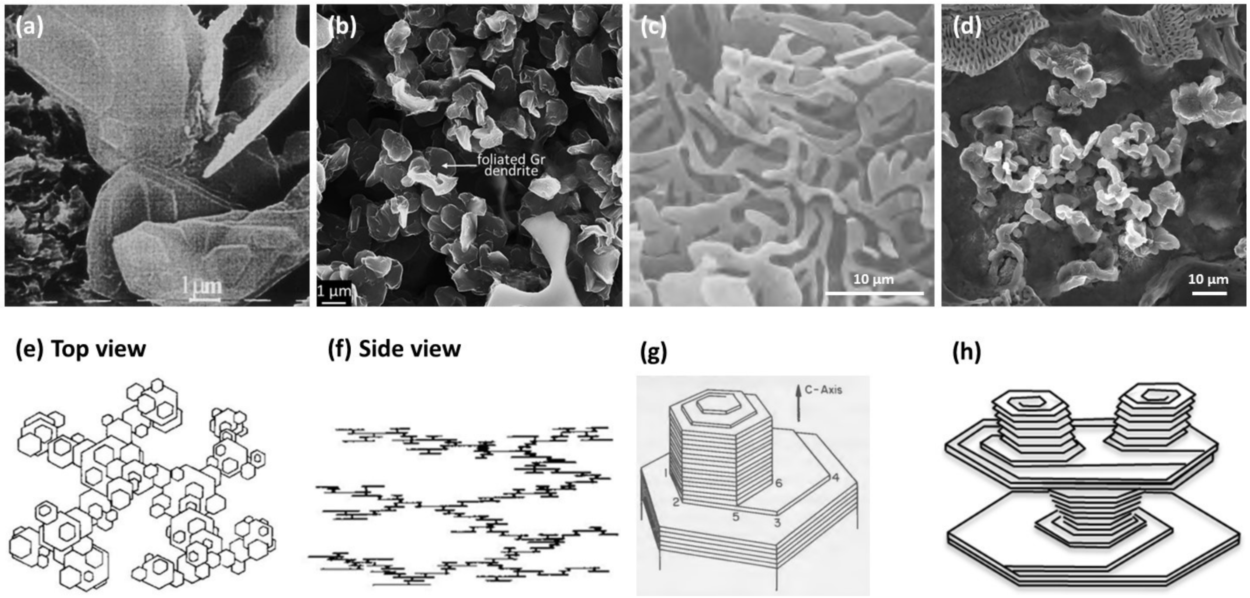

Figure 5.12 (a-d) SEM images of dendrite graphites from other studies. Models of (e-f) dendrites, (g) block-like particles, and (h) protuberances. Corresponding references are shown in text. Reproduced with permission from Reference [132,184–186].

Glucose graphite is composed of special large hexagonal platelets with random orientations with respect to each other. This has been introduced in Chapter 3 and 4. Activated carbon derived graphite also contains large hexagonal platelets. Big graphite platelets were observed in some cast irons.[137] However, well-defined hexagonal platelets in such large amounts and in such large sizes (up to 30 μm) were never reported before in catalytic graphites to the author's knowledge.

In short, catalytic graphites shown in this study contain various morphologies. Main types include platelets and spheroids. Platelets also include degenerate forms, like dendrites composed of irregularly-shaped platelets, and hexagonal platelets with random orientations. Less graphitized particles usually contain dense particles. Some of these dense particles are composed of very small platelets.

5.4.2 Crystallinity Levels of Catalytic Graphites

It must be clarified that even the least crystalline PR graphite in this study is of higher graphitization level than most other catalytic graphites reported in previous studies.[15] Although

PR graphite contains large amounts of turbostratic graphite, it is a highly graphitic material which is essentially all composed of graphitic components.

Generally, non-polymers precursors tend to form highly ordered graphites (higher ordered graphite at. %, higher L_a and L_c, lower P_r as shown in Figure 5.9), while polymer precursors tend to form less ordered graphites. On the other hand, highly ordered catalytic graphites contains more 3R graphite content, much more than MAGE.

By using different pre-heating methods, the same precursor can be made into graphites with different crystallinity levels. PAN_1 was only carbonized under Ar (Table 5.1) before graphitization. PAN_1 graphite contains a significant amount (54.5 at. %) of turbostratic graphite. PAN_2 was stabilized in air first, and then carbonized under Ar before graphitization. PAN_2 graphite is essentially all composed of ordered graphite (87.0 at. %). The stabilization process has been briefly described in the Introduction. After stabilization at lower temperatures (200 – 300 °C) in an oxygen containing atmosphere, PAN chain structures transform into ladder structures, as shown in Figure 5.1, corresponding to the formation of black orlon.[172] During carbonization at higher temperatures (500 – 1100 °C) under Ar, ladder structures combine with each other, forming larger aromatic structures through denitrogenating and dehydrogenization processes. The aromatic structures are more easily graphitized and thus PAN_2 has a higher graphitization level. On the other hand, PAN_3 was also stabilized and carbonized. However, PAN_3 graphite only contains ~20 at. % ordered graphite. This is because the final carbonization temperature of PAN_3 carbon is only 700 °C, much lower than 1100 °C. Higher temperature can improve the size of carbon unit groups, and a large carbon unit group is more easily graphitized.[14]

In short, catalytic graphites made in this study all have high crystallinity levels. For those containing significant amounts of turbostratic components, the graphitization level can be increased by modifying pre-heating methods or increasing the graphitization temperature from 1000 °C just slightly to 1100 °C or 1200 °C. As shown in Chapter 3 and 4, a slight increase in heating temperature can greatly improve the graphitization level of graphite products. This has also been confirmed in previous studies.[78,81]

5.4.3 Mechanism of Catalytic Graphitization

Three main catalytic graphitization mechanisms have been proposed, as introduced in Chapter 1. As discussed in Chapter 4, Mg catalyzed graphitization of glucose carbon might follow the third type of mechanism: carbon dissolution-precipitation and carbide formation-decomposition. Based on the three main catalytic graphitization mechanisms, many modified mechanisms have been proposed to explain the formation of various graphite morphologies (spheres, platelets, dendrites, *etc.*). Many researchers believe that a higher surface energy promotes the formation of spheroidal morphology as the system attempts to decrease its energy. [132,187] Sadocha *et al.* assumed a large number of growth steps on the spheroid surface along the a-direction, and the spheroidal structures formed due to repeated bending of the graphite sheets.[188] They suggested that the spheroidal morphology is the natural growth form of graphite in liquid metals, while flake graphite is a modified morphology. Sadocha *et al*. and Muhmond *et al.* also mentioned that trace elements can affect the growth of graphite.[188,189] Depending on the type of element, pentagonal, hexagonal and other C-rings can be present as defects in the basal plane.[189] For example, the presence of surface-active oxygen impurity might reduce the bending ability by decreasing the surface tension, so that the spherical shape is deteriorated into a platelet structure,[188] which was confirmed by Double *et al*.[190] This might explain why some graphites contain wide and thin hexagonal platelets in this study.

Based on the experimental data in this study and previous studies, a suggested mechanism for Mg-catalytic graphite growth and its modified morphologies is summarized as follows:

(1) The basic mechanism of Mg-catalytic graphite growth may be a combination of carbon dissolution-precipitation and carbide formation-decomposition (as discussed in Chapter 4): magnesium carbide forms during graphitization and decomposes into graphite; some amorphous carbon dissolves into Mg liquid, then precipitates into graphite,[19] and the precipitation/growth of graphite usually follows a lateral direction (a-direction) in the absence of impurities (Figure 4.1).[184]

(2) During the growth of Mg-catalytic graphite, various defects might appear. These defects might influence the growth rate and modify the morphologies of graphite [184] (details are described from (3) to (7) below.

(3) As graphite crystallites grow laterally, spheroidal structures (Figure 5.3) may form due to repeated bending of graphite sheets [188,191] (Figure 3.1(b,c), Figure 3.3(a,b)), probably because the system attempts to decrease its energy [132,187]. More examples of spheroidal graphite particles are introduced in Chapter 7.

(4) Rotation boundaries are a common defect in flaky type graphite [191,192] (Figure 5.2(f2)) because quasi two-dimensional crystals preferentially grow in the both 110 and 100 along the basal plane.[184]

(5) Screw-dislocations are also a common type of defect in flaky type graphite, permitting the preferential growth along the c-direction and forming block-like graphite crystals (Figure 5.3(b3) and Figure 5.12(g)), probably because the mobility in a-directions is reduced by foreign elements (impurities) [184,185].

(6) Stacking of block-like particles forms protuberances [132] (Figure 5.12(h)), and branching of protuberances forms dendrites [132,184] (Figure 5.12(e-f)).

(7) Another type of branching dendrite (Figure 5.12(c)) forms because the change of lateral growth directions rather than stacking of block-like particles or forming foliated dendrites.

5.4.4 Electrochemical Performance in Li Cells and Improvements

Catalytic graphites display good electrochemical properties in Li cells. Specially, coke graphite has excellent cycling performance and a high reversible capacity, comparable to commercial battery graphites. To the author's knowledge, few catalytic graphites made at such low temperatures have performance characteristics in Li cells that approach those observed here. Our group has previously reported a catalytic graphite made from a glucose carbon by adding a Fe catalyst, which has a high reversible capacity (~360 mAh/g).[58] However, the measured capacity corresponds to a voltage range between 0.005 – 2V. If the voltage upper limit changes to 0.9V (that used in this study), its reversible capacity is only ~340 mAh/g. Lee *et al.* made flake graphite from cast iron melts at 1600 °C.[62] The catalytic graphite has a capacity of ~ 305 mAh/g when cycled between 0.005 – 3V. Gnanaraj *et al.* synthesized carbon material from tire.[161] When used in Li cells, the tire-derived carbon display high capacity (up to 450 mAh/g at C/50). However, this carbon material has a low graphitization level, and thus a huge hysteresis and low density, similar to the first-generation Li-ion battery anode: coke, which graphite has made obsolete. Chen *et al.* also synthesized a catalytic graphitic-nano-fiber material with a high capacity in Li cells.[193] However, the graphite product had a huge hysteresis and a huge irreversible capacity. Although the reversible capacity is high (~1500 mAh/g), its low energy efficiency is an insurmountable obstacle for application as a Li-ion anode. Kakunuri *et al*. also used catalytic graphite in Li cells, but its reversible capacity was only ~200 mAh/g.[74] Therefore, it is an important advancement to synthesize catalytic graphites at such low temperatures (~1000 °C) with high reversible capacities and low hysteresis.

Although some catalytic graphites made in this study have good electrochemical performance in Li cells, they also have disadvantages. This includes huge irreversible capacities and relatively low coulombic efficiencies compared to commercial battery graphites (e.g. MAGE). Both are likely caused by the high surface areas and/or the less-ordered tiny particles on the graphite surfaces. As shown in Chapter 4, the high-surface-area problem can be solved by coating another layer of carbon, which greatly reduces the surface area and the irreversible capacity. However, this method cannot reduce the irreversible capacity to a commercial-battery-graphite level (<10%). Another direction is removing the less-ordered tiny particles, for instance by heating the catalytic graphites in air to remove these particles (since the smaller particles have a higher surface area and are less ordered, they will likely react with O_2 at lower temperatures than ordered graphite particles). Then the resulting catalytic graphites can be re-heated under inert atmosphere to reduce their oxygen content. This method will be attempted in future studies.

5.5 Summary

Mg-catalyzed graphites were made from various polymer and non-polymer precursors. All precursors were effectively converted from amorphous carbon to highly graphitic carbon after a low temperature (1000 °C) graphitization for a short time (3 h). The graphitization level of the graphite products was influenced by the precursor type. Most non-polymer precursors can be converted into highly ordered graphite, while most polymer precursors can be converted into a mixture of ordered graphite and turbostratic graphite.

Catalytic graphites are composed of particles with various morphologies. Generally, as the graphitization level increases, graphite composition changes from dense particles, to small platelets, to large platelets with tiny particles, to pure large platelets. By comparing the morphologies of Mg-catalytic graphite, it was found that they were more like graphite made from cast iron melts.

Changing the pre-heating process (carbonization) can greatly influence the final graphitization level. PAN precursors with different pre-heating methods result in quite different graphite products. This is probably because different pre-heating processes yield amorphous carbon with different unit groups (some of them are more easily graphitized and others are not), and with different types or amounts of non-carbon elements.

Some highly ordered catalytic graphites were cycled in Li cells. Most of them have excellent cycling stability and high reversible capacity. However, these catalytic graphites also have high irreversible capacity, probably due to their high surface area and the existence of less ordered particles on graphite surfaces. Possible methods to solve this problem are briefly discussed in Chapter 8.

Chapter 6 Lithium as a Graphitization Catalyst

6.1 Introduction

Compared to magnesium, lithium's melting point is lower (180.5 °C < 650 °C), and lithium can also form carbides (*e.g.* Li_2C_2). Lithium has not been previously reported as an effective graphitization catalyst. This chapter introduces a method for using lithium as a graphitization catalyst. The experimental method in this chapter is similar to that described in Chapter 4, except that lithium is used in the place of magnesium. The influence of the Li:C ratio and heat-treatment conditions were studied and analyzed. Osetzky found that LiCl might enhance the graphitization process in an earlier study.[194] Therefore, LiCl was also used as an additive here.

6.2 Experimental

6.2.1 Synthesis of lithium catalyzed graphites (LCGs)

Activated carbon (Nuchar activated carbon, 1526-R-05) was first heated under an Ar flow at 120 °C for 5 h and 600 °C for 5 h to remove impurities (H_2O, O_2, *etc.*). The heated carbon was then combined with small pieces of lithium ribbon (99.9% Aldrich) and optionally LiCl (powder, ≥99.99%, Sigma-Aldrich) in different Li:C or Li:C:LiCl molar ratios in a 65 mL hardened steel vial containing 115 g stainless-steel balls (4.76 mm in diameter) under an Ar atmosphere for 2 h by high-energy mechanical milling (HEMM) with a SPEX mill (Model 8000-D, SPEX CertiPrep, Metuchen, NJ). The resulting carbon-Li alloys were heated in sealed stainless-steel tubes filled with Ar at 900/1000/1100 °C for 3/20 h. To remove the Li catalyst after heat-treatment, ~2 g of the graphite-Li product was placed in a solution of 100 mL of 2 M HCl (prepared from concentrated HCl, Aldrich) and ~2 mL of ethanol (98%, Aldrich) for 12 h with stirring. After reacting with HCl, the products were transferred into a Büchner funnel (with a Whatman circle filter paper, qualitative, 44.25 mm in diameter) and were washed with 2 M HCl five times and then washed repeatedly with distilled water until the pH of the supernatant was about seven. Finally, the products were dried in air for 3 h at 120 °C. Hereafter, the lithium catalyzed graphite is termed as LCG. The Li:C ratio of the heated hard carbon/Li alloy and its heat-treatment conditions are labeled in parentheses. For example: LCG (Li_1C_6, 900 °C, 3 h) indicates LCG made by heating at 900 °C for 3 h from a carbon/Li alloy in a molar ratio of Li:C = 1:6.

6.2.2 Characterization

LCGs were characterized by using many techniques: scanning electron microscopy (SEM), X-ray diffraction (XRD), and pycnometry (details are introduced in Chapter 2). Electrochemical measurements in Li half-cells were performed. Details of slurry making, cell assembly, and cycling are described in Chapter 2.

To determine the graphitic and amorphous carbon contents, XRD patterns of graphite products were fit with pseudo-Voigt functions between 20° - 30°. Three pseudo-Voigt peaks were included in each fit, representing amorphous carbon, turbostratic graphite, and ordered graphite. More details regarding the pseudo-Voigt fitting procedure are described in Chapter 2. The CARBONXS program (one-layer model) was also used to fit the XRD pattern of LCG (Li_1C_6, 900 °C, 3 h) (details of the fitting procedure are in Chapter 2).

6.3 Results and Discussion

Figure 6.1 shows SEM images of the carbon precursor and LCGs. As with activated carbon, the carbon precursor is very porous (Figure 6.1(a)). LCG particles range from 5 µm to 20 µm (Figure 6.1(b)). Most particles are aggregated particles composed of primary particles (Figure 6.1(c)). LCGs made from high Li:C-ratio precursors also contain a very small fraction of particles with different structures (Figure 6.1(d-f)), e.g. small-sized compact platelets (<5 µm).

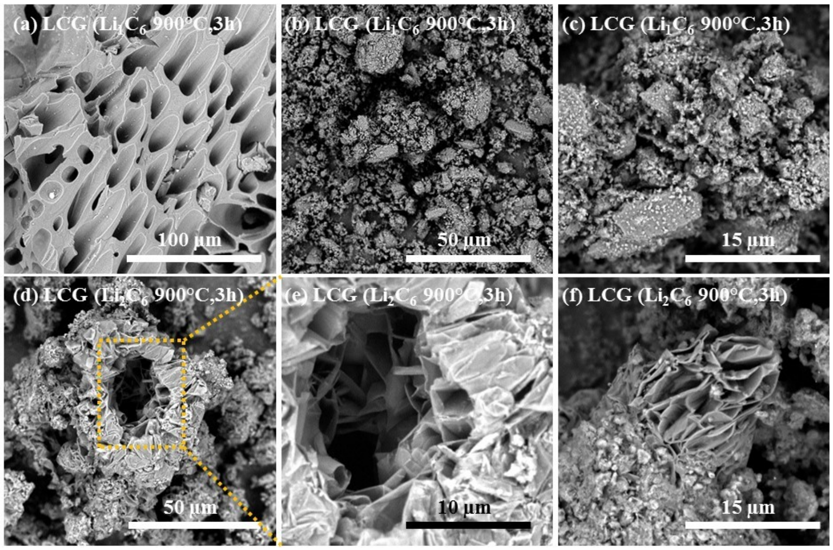

Figure 6.1 SEM images of (a) the carbon precursor, (b-c) LCG (Li_1C_6 900 °C, 3 h), and (d-f) LCG (Li_2C_6 900 °C, 3 h).

The XRD pattern of the carbon precursor is typical of a disordered hard carbon with two broad peaks (Figure 6.2(a)). After combining C with Li by HEMM, the XRD pattern of the C-Li alloy does not change (Figure 6.2(b)). All C-Li alloys had similar XRD patterns regardless of their Li:C ratios.

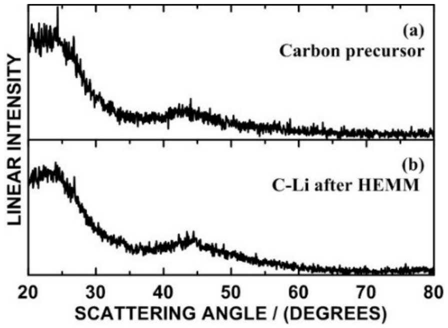

Figure 6.2 XRD patterns of (a) the carbon precursor and (b) C-Li (Li:C = 1:1) after HEMM.

Figure 6.3(a) shows XRD patterns of LCG-Li made from Li_1C_6 after different heat-treatments and prior to Li removal with HCl. All XRD patterns have sharp 002 peaks, indicating that Li is an effective graphitization catalyst at low temperatures. Li_2O peaks are also visible, which presumably arise because of the reaction between Li and metal oxide on the inner surface of the stainless-steel reaction tubes.

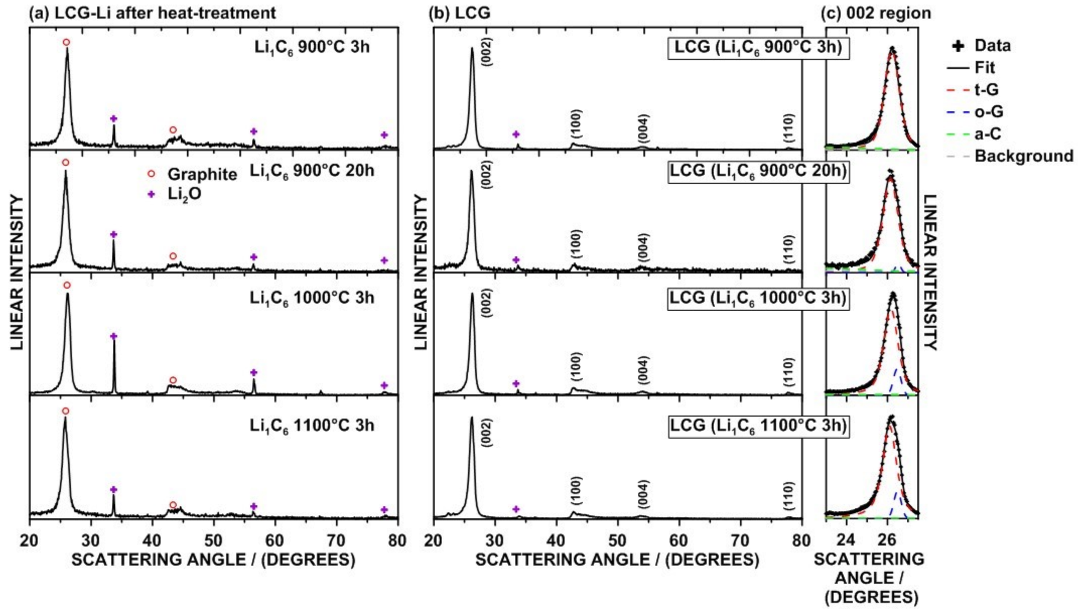

Figure 6.3 XRD patterns of (a) LCG-Li after heating, (b) LCGs and (c) the 002-peak region of (b).

The main component of LCGs (Li_1C_6) is graphite (Figure 6.3(b)). Li_2O is not completely removed after reacting with HCl (Figure 6.3(b)), possibly because some Li_2O particles are trapped in porous structures. Based on the fitting results, the primary component is turbostratic graphite (Figure 6.3(c)). Table 6.1 lists the content of different carbon components of LCGs. Increasing the heating temperature only slightly improves the graphitization level and extending the heating time also has little effect the graphitization level.

Table 6.1 Properties of LCGs made in different conditions.

Li:C (:LiCl) molar ratio	Synthesis °C	hour	Amorphous at.%	Ordered at.%	Turbostratic at.%
1: 6	900	3	10.0(7)	0.0(0)	89.9(7)
1: 6	900	20	17.0(7)	2.1(7)	80.8(7)
1: 6	1000	3	11.3(7)	9.0(7)	79.5(7)
1: 6	1100	3	9.4(7)	10.0(7)	80.5(7)
1.5: 6	900	3	13.3(7)	5.6(7)	81.1(7)
2: 6	900	3	12.8(7)	9.2(7)	78.0(7)
1: 6 (: 0.2)	1000	3	0.0	0	100

XRD patterns of LCGs made from Li-C with different Li:C ratios are compared in Figure 6.4(a). Li does not work effectively as a graphitization catalyst if its fraction is low (e.g. Li:C = 0.5:6). When the Li fraction is high (Li:C = 2:6), a Li_2C_2 impurity appears after heating, which is completely removed after reacting with HCl. Increasing the Li fraction slightly improves the ordered graphite content. However, when a high fraction of Li is added, the product is very sticky after ball milling, making it difficult to separate the product from the milling balls.

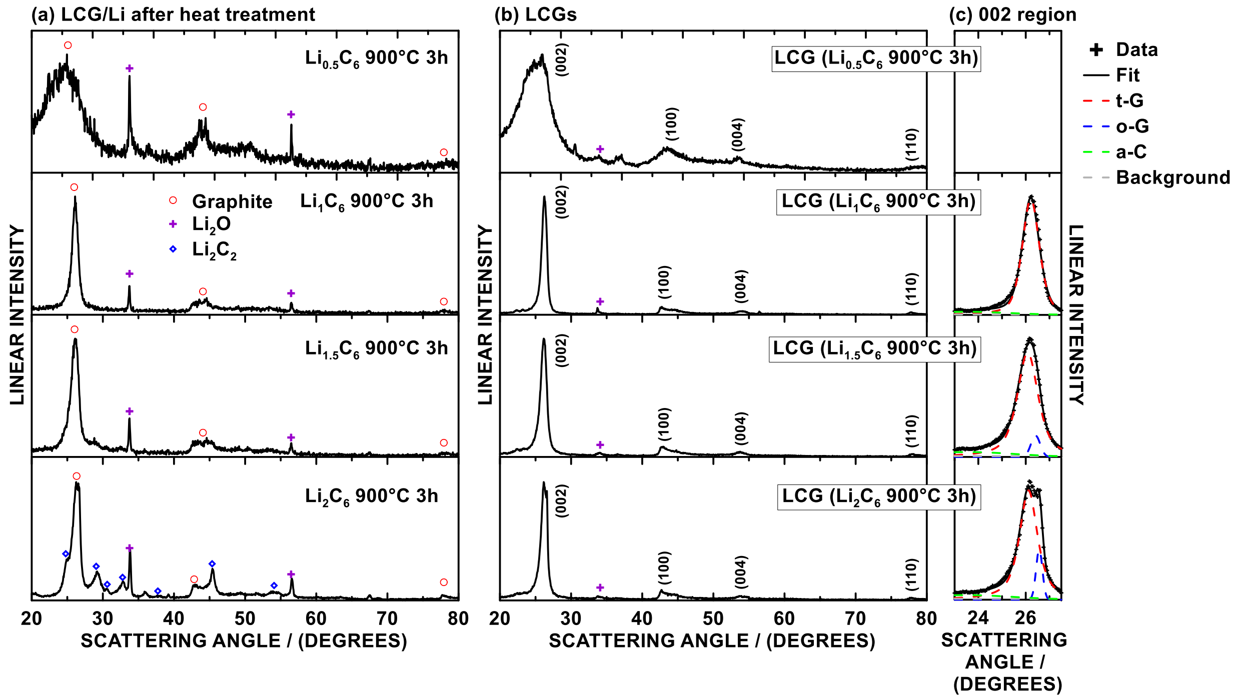

Figure 6.4 XRD patterns of (a) the LCG/Li mixtures after a heat-treatment of 900°C, 3h from Li-C in different ratios, (b) LCGs and (c) the 002-peak region in (b). The pseudo-Voigt fitting results of the 002 regions are also shown in (c).

A Li_2C_2 impurity is present after heating if LiCl is added (Figure 6.5(a)), indicating LiCl accelerates the formation of Li_2C_2. In the final product, LiCl cannot be completely removed after reacting with HCl (Figure 6.5(b)). Based on the XRD fitting data, adding LiCl facilitates the transition from amorphous carbon to graphitic carbon; however, it hinders the transition from the turbostratic graphite phase to the ordered graphite phase.

Figure 6.6 shows the voltage profiles and differential capacity curves of LCGs. LCG (Li_1C_6, 900 °C 3 h) exhibits no staging phenomena (Figure 6.6(a-b)), consistent with a highly turbostratic graphite,[105] as indicated from the XRD data. LCG (Li_2C_6, 900 °C 3 h) shows clear staging phenomena (plateaus in Figure 6.6(c) and sharp peaks in Figure 6.6(d)), consistent with its higher ordered graphite content.

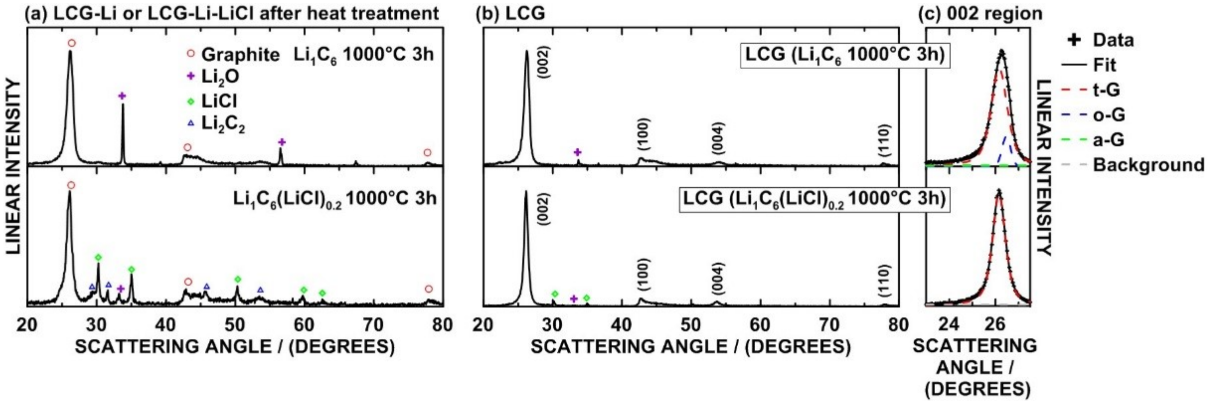

Figure 6.5 XRD patterns of (a) LCG/Li and LCG/Li/LiCl mixtures from Li_1C_6 and $Li_1C_6(LiCl)_{0.2}$ after being heated at 1000 °C for 3 h, (b) LCGs and (c) the 002-peak region in (b). The pseudo-Voigt fitting results of the 002 regions are also shown in (c).

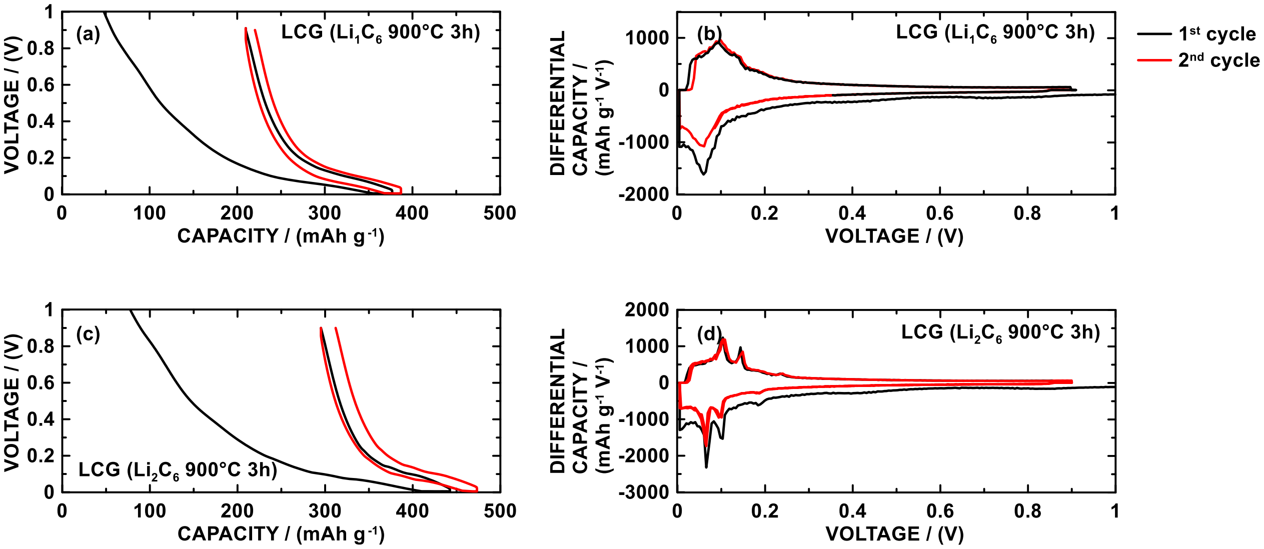

Figure 6.6 (a, c) Voltage profile and (b, d) differential capacity curve of LCG (Li_1C_6, 900 °C, 3 h) and LCG (Li_2C_6, 900 °C, 3 h), respectively.

6.4 Summary

Li is an effective graphitization catalyst. However, Li has a lower graphitization catalysis efficiency compared to Mg, even though its melting point is lower. For example, amorphous carbon is not completely converted into graphitic carbon in most LCGs, and the ordered graphite content of LCGs is very low. Increasing the graphitization temperature or increasing the Li fraction only slightly improves the graphitization efficiency. Adding LiCl facilitates the transition from amorphous carbon to graphitic carbon, but it hinders the transition from turbostratic graphite to ordered graphite. The resulting low level of graphitization of LCGs result in poor electrochemical performance in Li-ion cells. For these reasons this project was not pursued further.

Chapter 7 Additives for Mg Catalyzed Graphitization

7.1 Introduction

A number of studies have investigated the use of chlorides in catalytic graphitization.[33,52,195–197] Otani and Ōya showed that $FeCl_3$ and $AlCl_3$ had catalytic effects on the graphitization of coal tar pitch.[195,196] Zhang *et al.* showed that $AlCl_3$ and $ZrCl_4$ had catalytic effects on the graphitization of anthracene at high temperatures (~2800 °C).[52] Hatori *et al.* added $NiCl_2$ during carbonization/graphitization of polyamic acid.[197] However, adding $NiCl_2$ did not improve the carbonization/graphitization efficiency. Peng *et al.* synthesized graphitic carbon from carbon black at ~800 °C by using cathodic polarization in molten $CaCl_2$.[33]

Osetzky studied the carbon formed from the decomposition of magnesium carbide, and found the carbon product was highly graphitic.[147] This work might be one of the earliest studies showing that highly graphitic platelets (up to 10 μm) can be made from the decomposition of magnesium carbide at ~1000 °C. Osetzky also suggested that $MgCl_2$ might be a good carbide carrier, which "provides a favorable environment for the formation and unhindered growth of the carbon units".[147] However, there is no direct evidence for this. $MgCl_2$ has also been evaluated as a graphitization catalyst by itself, but it was found to have no catalytic effect.[198]

NaCl has often been used as a catalyst support in making nanocarbon materials.[93,199] Yang *et al.* synthesized graphitic nanocarbon materials with an iron catalyst supported on NaCl. They found that iron nanoparticles had a high mobility on the surface of NaCl.[93] Shi *et al.* used NaCl as a template in catalytic graphitization.[199] They also found NaCl improved catalytic efficiency.

Kamali and Fray produced graphitic carbon nanomaterials by the electrochemical erosion of graphite cathodes in molten LiCl.[200] The graphitic structure of the cathodes was greatly modified, and the following mechanism was suggested: LiCl reacts with graphite, forming Li_2C_2, which subsequently decomposes into graphite.[200] Osetzky also found LiCl additions during graphitization modified graphite morphology.[147]

As shown in previous studies, aluminum also influences the graphitization process.[41,185,201] Murty *et al.* found aluminum is an effective graphitization catalyst at ~2000 °C.[41] However, Sherby *et al*. used aluminum to stabilize iron carbide against graphitization in steel production.[201] Lux *et al*. found aluminum modified graphite growth routes, probably because Al blocked the growth of graphite parallel to the basal plane, and forced the spiral growth of graphite perpendicular to the basal plane, resulting in the formation of thicker particles.[185]

Many graphites made by the Mg catalyzed graphitization method have high specific surface area (Table 5.2), especially those made from glucose and activated carbon. Graphites with high surface areas usually have a high irreversible capacity in Li cells. Carbon-coating proved to be an effective method to reduce the surface area of graphite (Chapter 5). Another method used here to lower surface area is to use morphology modifying additives, like Al.[185]

In this chapter, $MgCl_2$, LiCl, NaCl, and Al were evaluated as additives for Mg catalyzed graphitization. Their influence on graphitization level, particle morphology, and electrochemistry was examined.

7.2 Experimental

7.2.1 Synthesis of catalytic graphites

Three carbon precursors were used: glucose (96%, Aldrich), coke (Asbury, Needle coke, Grade 4491) and activated carbon (Nuchar WV-B 10*25 mesh). Carbonization and degassing details are described in the experimental section of Chapter 5. The as-prepared amorphous carbons were combined with magnesium powder (HART METALS, INC., -325 mesh) and, optionally, $MgCl_2$ powder (anhydrous, >98%, Sigma Aldrich) or LiCl powder (>99.98%, Sigma Aldrich) or NaCl powder (>99.5%, Sigma Aldrich) or Al powder (99.97%, -325 mesh, Alfa) by high energy mechanical milling (HEMM, with SPEX Model 8000-D, SPEX CertiPrep, Metuchen, NJ) or planetary milling (Retsch PM 200). For HEMM samples, precursors were added to a 65 mL hardened steel vial and milled for 2 h with ~115 g of 4.76 mm stainless steel balls or 0.5 h with ~45 g of 1.11 mm stainless steel balls under an argon atmosphere. For samples prepared by planetary milling, precursors were combined at 100 rpm for 1 h with four WC balls (11 mm in diameter) under an argon atmosphere. Table 7.1 summarizes the different materials prepared in this study and the corresponding methods used for combining their precursors. Here, SC refers to sugar carbon, indicating amorphous carbon made from glucose, and AC refers to activated carbon. Some C-Mg-chloride materials were combined in one step, while others were combined in two steps, as indicated.

Table 7.1 Blending methods used for different C-Mg or C-Mg-chloride materials. *SC = sugar (glucose) carbon, AC = activated carbon, subscripts indicate the stoichiometric ratios. The suffix "S" indicates a one-step milling process by HEMM using a SPEX mill, while the suffixes "S+S" and "S+P" indicate a two-step combining process by HEMM or planetary milling.

Symbol*	2-Step		1-Step
	C + Mg	C-Mg + chloride	C + Mg + chloride
$SC_{50}Mg_{50}$	SPEX 115g 2h		
$SC_{50}Mg_{50}(MgCl_2)_5$_S			SPEX 115g 2h
$SC_{50}Mg_{50}(MgCl_2)_{10}$_S			SPEX 115g 2h
$SC_{50}Mg_{50}(MgCl_2)_5$_S+P	SPEX 115g 2h	Planetary 1h	
$SC_{50}Mg_{50}(MgCl_2)_{10}$_S+S	SPEX 115g 2h	SPEX 45g 0.5h	
$SC_{50}Mg_{50}Al_{2.5}$_S			SPEX 115g 2h
$SC_{50}Mg_{50}Al_{10}$_S+S	SPEX 115g 2h	SPEX 45g 0.5h	
$SC_{70}Mg_{30}$	SPEX 115g 2h		
$SC_{70}Mg_{30}(MgCl_2)_{10}$_S			SPEX 115g 2h
$SC_{70}Mg_{30}(MgCl_2)_{10}$_S+P	SPEX 115g 2h	Planetary 1h	
$SC_{70}Mg_{30}(MgCl_2)_{10}$_S+S	SPEX 115g 2h	SPEX 45g 0.5h	
$SC_{70}Mg_{30}Al_{10}$_S+S	SPEX 115g 2h	SPEX 45g 0.5h	
$SC_{70}Mg_{30}(MgCl_2)_{10}Al_{10}$_S+S	SPEX 115g 2h	SPEX 45g 0.5h	
$SC_{90}Mg_{10}$	SPEX 115g 2h		
$SC_{90}Mg_{10}(MgCl_2)_{10}$_S+S	SPEX 115g 2h	SPEX 45g 0.5h	
$SC_{90}Mg_{10}(MgCl_2)_{20}$_S+S	SPEX 115g 2h	SPEX 45g 0.5h	
$Coke_{50}Mg_{50}$	SPEX 115g 2h		
$Coke_{50}Mg_{50}Al_{2.5}$_S+S	SPEX 115g 2h	SPEX 45g 0.5h	
$Coke_{70}Mg_{30}$	SPEX 115g 2h		
$Coke_{70}Mg_{30}(MgCl_2)_{10}$_S			SPEX 115g 2h
$Coke_{70}Mg_{30}(MgCl_2)_{10}$_S+S	SPEX 115g 2h	SPEX 45g 0.5h	
$Coke_{90}Mg_{10}$	SPEX 115g 2h		
$Coke_{90}Mg_{10}(MgCl_2)_5$_S			SPEX 115g 2h
$Coke_{90}Mg_{10}(MgCl_2)_{20}$_S	SPEX 115g 2h	SPEX 45g 0.5h	
$AC_{50}Mg_{50}$	SPEX 115g 2h		
$AC_{50}Mg_{50}(MgCl_2)_{10}$_S+S	SPEX 115g 2h	SPEX 45g 0.5h	SPEX 115g 2h
$SC_{70}Mg_{30}(LiCl)_{10}$_S+S	SPEX 115g 2h	SPEX 45g 0.5h	

Symbol*	2-Step		1-Step
	C + Mg	C-Mg + chloride	C + Mg + chloride
$SC_{70}Mg_{30}(NaCl)_{10}$_S+S	SPEX 115g 2h	SPEX 45g 0.5h	
$SC_{90}Mg_{10}(NaCl)_{10}(MgCl_2)_{10}$_S+S	SPEX 115g 2h	SPEX 45g 0.5h	
$SC_{90}Mg_{10}(NaCl)_{10}(MgCl_2)_{10}$_S+S	SPEX 115g 2h	SPEX 45g 0.5h	

After milling, C-Mg, C-Mg-Al or C-Mg-chloride(s) were heated in an argon-filled stainless-steel tube (100-200 mm, OD 12.70 mm, ID 9.40 mm, sealed with Parker-A-lok caps) at 1000 °C for 3 h (unless specified otherwise), resulting in the formation of graphite-Mg, graphite-Al or graphite-Mg-chloride. Then ~2 g of the graphite-Mg, graphite-Al or graphite-Mg-chloride materials were placed in a solution of 100 mL of 2 M HCl (prepared from 37 wt. % HCl, Aldrich) and 2 mL of ethanol (98%, Aldrich) for 12 h with stirring. The products were transferred to a Büchner funnel (Whatman filter paper, qualitative) and were washed with 2 M HCl five times and then washed with distilled water repeatedly until the pH of the supernatant was about 7. Finally, the products were dried in air at 120 °C for 3 h. Some C-Mg or C-Mg-$MgCl_2$ samples were heated under low pressure (< 20 Pa) at 900 °C for 5 h to remove impurities.

Degassed coke and $MgCl_2$ powders (Coke: $MgCl_2$ = 80: 20 by mole) were ground for 5 minutes by hand in an Ar-filled glove box. The coke-$MgCl_2$ mixture was graphitized using the same method described above to test if $MgCl_2$ is an effective catalyst alone.

7.2.2 Materials characterization

Graphite products were characterized by using many techniques: scanning electron microscopy (SEM), energy dispersive X-ray spectroscopy (EDS), transition electron microscopy (TEM), X-ray diffraction (XRD), Brunauer-Emmett-Teller (BET) surface analysis, and pycnometry. Some $MgCl_2$ containing graphites were milled by HEMM (SPEX Model 8000-D, SPEX CertiPrep, Metuchen, NJ) in a 65 mL hardened steel vial under an argon atmosphere containing stainless-steel balls (~115 g of 4.76 mm balls) for 1 h. The $MgCl_2$ contents of milled graphites were determined by inductively coupled plasma-optical emission spectroscopy (ICP-OES). Details of these techniques and characterization methods are described in Chapter 2. Electrochemical measurements of catalytic graphites as working electrodes in Li-half cells were performed. Details of slurry making, cell assembling and cycling are described in Chapter 2.

Pseudo-Voigt profiles were used to fit the 002-peak region (between 24° - 28°) of each catalytic graphite XRD pattern. Depending on the graphitization level, a combination of a turbostratic 002 peak and an ordered graphite 002 peak (both between 26° - 27°) or a combination of an amorphous carbon peak (~22°) and a turbostratic peak (between 26° - 27°) were applied for each fit. The detailed fitting procedure can be found in Chapter 2.

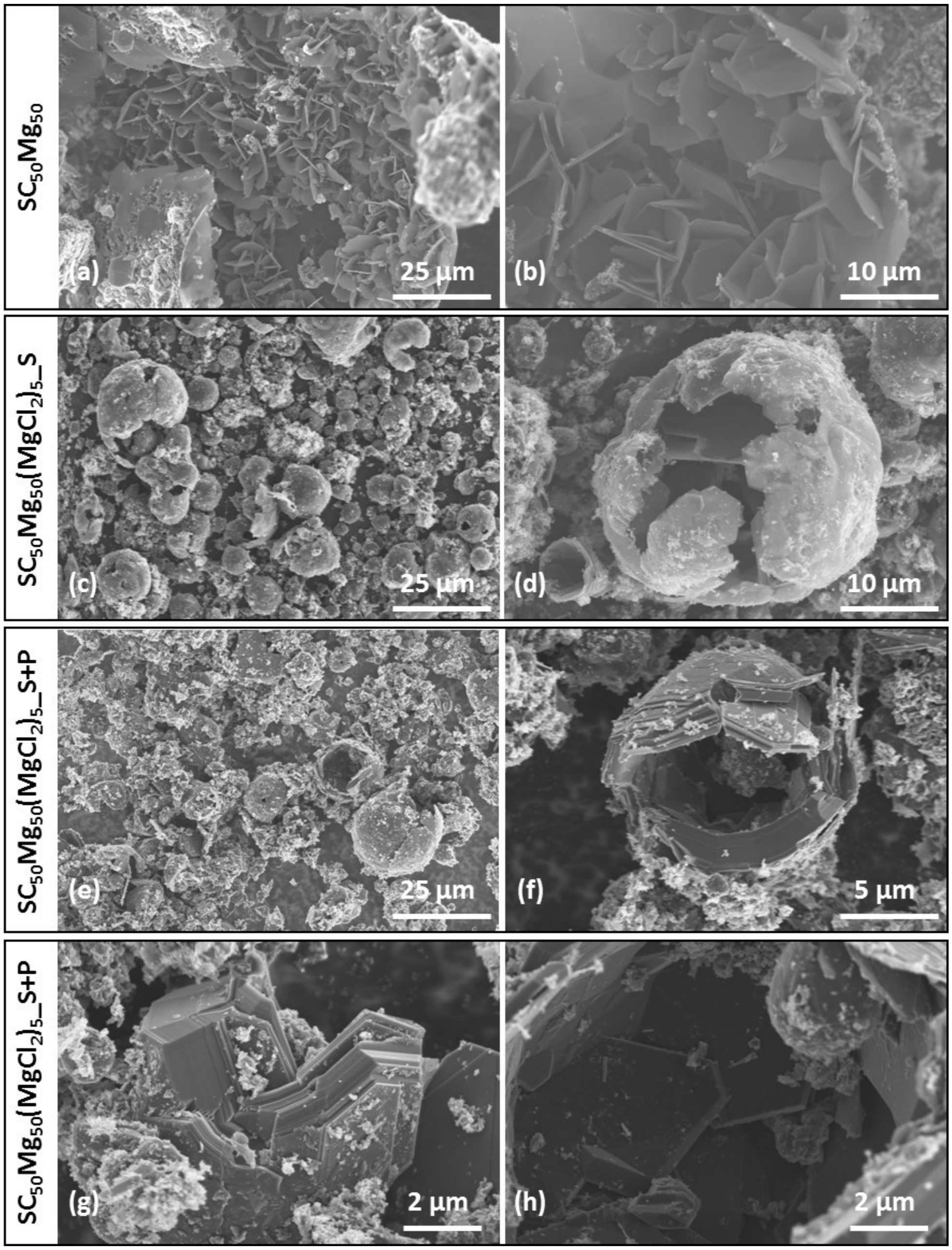

Figure 7.1 SEM images of graphites made from (a,b) $SC_{50}Mg_{50}$, (c,d) $SC_{50}Mg_{50}(MgCl_2)_5$_S, and (e-h) $SC_{50}Mg_{50}(MgCl_2)_5$_S+P.

7.3 Results

7.3.1 $MgCl_2$ additive: structural and morphological characterization

Figure 7.1 compares the morphology of the graphites made from $SC_{50}Mg_{50}$ without and with 5 at. % $MgCl_2$. The graphite made without adding $MgCl_2$ is mainly composed of hexagonal platelets (Figure 7.1(a,b)). Its structure has been discussed in Chapters 4 and 5. Adding $MgCl_2$ greatly changes the particle and crystallite morphology (Figure 7.1 (c-h)). These samples contain particles which are mainly composed of spheroidal structures. Most of the spheroidal structures are hollow, while some contain platelets inside. There are also many tiny particles on the surface of the spheroidal structures, which are probably less-ordered graphite. The $SC_{50}Mg_{50}(MgCl_2)_5$_S derived graphite particles are composed of thinner spheroidal shells (< 0.5 μm, Figure 7.1(d)), while the $SC_{50}Mg_{50}(MgCl_2)_5$_S+P derived graphite contains particles with thicker shells (up to 3 μm thick, Figure 7.1(f,g)), which are composed of multiplayer-platelets. These morphological changes greatly reduce the specific surface area from 82.5 m^2 g^{-1} ($SC_{50}Mg_{50}$ derived) to 22.2 m^2 g^{-1} ($SC_{50}Mg_{50}(MgCl_2)_5$_S derived).

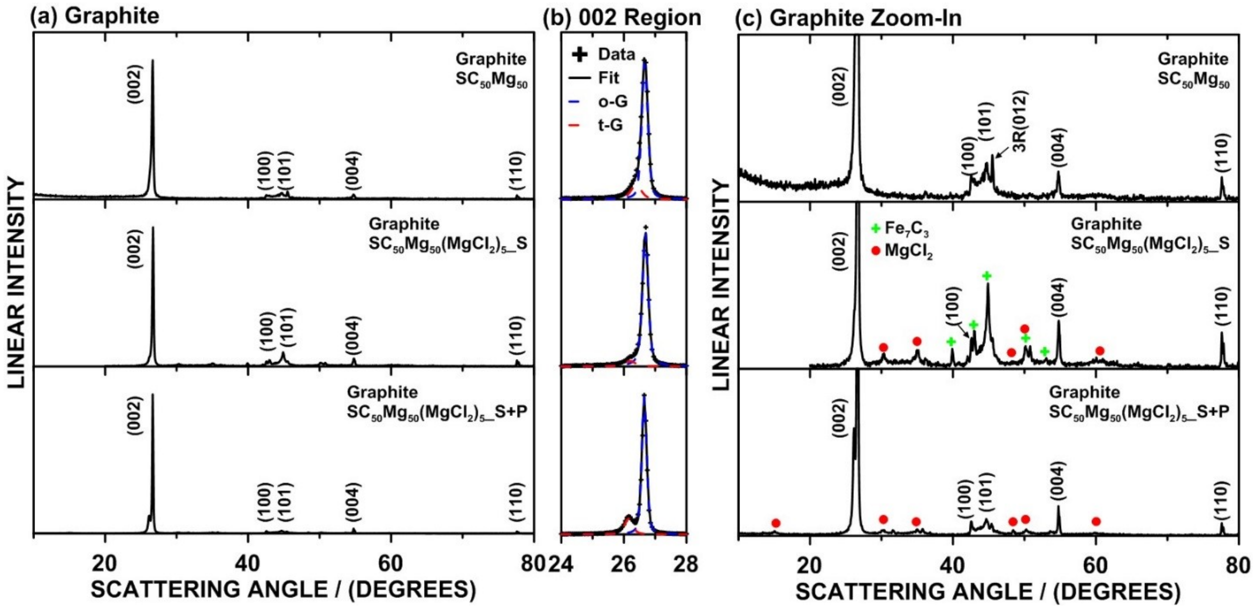

Figure 7.2 (a) XRD patterns of graphites made from glucose. Molar ratios and combination methods indicated in each figure. (b) 002 peak regions and (c) enlarged version of each XRD pattern.

Table 7.2 Structural data of catalytic graphites obtained by pseudo-Voigt fitting.

Symbols	Temperature/°C	002	d$_{002}$/Å	L$_c$/Å	at. %*
SC$_{50}$Mg$_{50}$	1000	O	3.343(4)	357(5)	83.1
SC$_{50}$Mg$_{50}$(MgCl$_2$)$_5$_S	1000	O	3.341(4)	371(5)	92.4
SC$_{50}$Mg$_{50}$(MgCl$_2$)$_5$_S+P	1000	O	3.345(4)	427(5)	83.6
		T	3.408(4)	-	
SC$_{70}$Mg$_{30}$	1000	O	3.345(4)	335(5)	12.7
		T	3.386(4)	150(5)	
SC$_{70}$Mg$_{30}$(MgCl$_2$)$_{10}$_S	1000	O	3.340(4)	328(5)	51.6
		T	3.399(4)	186(5)	
SC$_{70}$Mg$_{30}$(MgCl$_2$)$_{10}$_S+P	1000	O	3.346(4)	393(5)	65.0
SC$_{70}$Mg$_{30}$(MgCl$_2$)$_{10}$_S+S	1000	O	3.345(4)	380(5)	91.9
SC$_{90}$Mg$_{10}$	1000	T	3.401(4)	75(5)	-
SC$_{90}$Mg$_{10}$(MgCl$_2$)$_{10}$_S+S	1000	O	3.343(4)	263(5)	20.4
		T	3.400(4)	177(5)	
SC$_{90}$Mg$_{10}$(MgCl$_2$)$_{20}$_S+S	1000	O	3.348(4)	242(5)	35.3
		T	3.400(4)	165(5)	
SC$_{50}$Mg$_{50}$	900	O	3.348(4)	288(5)	32.9
		T	3.392(4)	178(5)	
SC$_{50}$Mg$_{50}$(MgCl$_2$)$_{10}$_S	900	O	3.363(4)	291(5)	68.8
SC$_{50}$Mg$_{50}$(MgCl$_2$)$_{10}$_S+S	900	O	3.347(4)	322(5)	80.9
SC$_{50}$Mg$_{50}$	800	T	3.401(4)	179(5)	-
SC$_{50}$Mg$_{50}$(MgCl$_2$)$_{10}$_S	800	O	3.370(4)	185(5)	11.7
		T	3.427(4)	79(5)	
SC$_{50}$Mg$_{50}$(MgCl$_2$)$_{10}$_S+S	800	O	3.351(4)	196(5)	18.7
		T	3.401(4)	86(5)	
Coke$_{70}$Mg$_{30}$	1000	O	3.350(4)	368(5)	17.1
		T	3.396(4)	144(5)	
Coke$_{70}$Mg$_{30}$(MgCl$_2$)$_{10}$_S	1000	O	3.341(4)	382(5)	34.1
		T	3.401(4)	210(5)	
Coke$_{70}$Mg$_{30}$(MgCl$_2$)$_{10}$_S+S	1000	O	3.344(4)	331(5)	80.0
		T	3.399(4)	157(5)	
Coke$_{90}$Mg$_{10}$	1000	T	3.424(4)	57(5)	-
Coke$_{90}$Mg$_{10}$(MgCl$_2$)$_5$_S	1000	O	3.350(4)	207(5)	13.4
		T	3.410(4)	202(5)	

Symbols	Temperature/°C	002	d_{002}/Å	L_c/Å	at. %*
$Coke_{90}Mg_{10}(MgCl_2)_{20}$_S	1000	O	3.351(4)	277(5)	35.9
		T	3.401(4)	198(5)	
$SC_{70}Mg_{30}(LiCl)_{10}$_S+S	1000	O	3.342(4)	373(5)	33.6
		T	3.400(4)	137(5)	
$SC_{70}Mg_{30}(NaCl)_{10}$_S+S	1000	O	3.346(4)	374(5)	26.3
		T	3.414(4)	164(5)	
$SC_{90}Mg_{10}(LiCl)_{10}(MgCl_2)_{10}$_S+S	1000	O	3.348(4)	303(5)	15.9
		T	3.403(4)	207(5)	
$SC_{90}Mg_{10}(NaCl)_{10}(MgCl_2)_{10}$_S+S	1000	O	3.347(4)	342(5)	26.2
		T	3.408(4)	218(5)	

* at. % indicates ordered graphite atomic percent.

Figure 7.2 compares the XRD patterns of the graphites made from $SC_{50}Mg_{50}$ without and with 5 at. % $MgCl_2$. All graphites are highly graphitic (Figure 7.2 (a)). The $SC_{50}Mg_{50}$ derived product is composed of 83.1 at. % ordered graphite. Adding $MgCl_2$ further improves the graphitization level to 92.4 at. % (Table 7.2). However, the $SC_{50}Mg_{50}(MgCl_2)_5$_S derived graphite also contains $MgCl_2$ and Fe_7C_3 peaks (Figure 7.2(c)). $MgCl_2$ has a high water-solubility. However, $MgCl_2$ was not completely removed even after reacting with water for an additional 12 hours (stirring) and repeated washings with water. In addition, no magnesium chloride hydrates were detected by XRD from these graphites. Since $MgCl_2$ is highly hygroscopic and absorbs water quickly to form magnesium chloride hydrates in air, this suggests that the $MgCl_2$ detected by XRD is neither accessible by air or water, which might be trapped in voids within graphite particles. The Fe_7C_3 is likely a consequence of Fe contamination during HEMM. Similar Fe_7C_3 peaks were found for some of the graphites mentioned in Chapter 5. This contamination might be avoided if HEMM is conducted with ceramic vessels/milling media. When using the one-step combination method (carbon + Mg + $MgCl_2$, 2h HEMM), Fe_7C_3 XRD peaks were always detected in the products. The Fe_7C_3 is problematic, since the Fe_7C_3 XRD peaks influence CARBONXS fitting because some Fe_7C_3 peaks overlap with graphite peaks (100 and 101). If the Fe_7C_3 peaks are strong, CARBONXS fitting results are not trustworthy. Therefore, CARBONXS fitting was not used in this chapter. In addition, if there are Fe_7C_3 XRD peaks, the contribution of Fe to the catalytic graphitization may not be insignificant. The two-step combination method, in comparison, effectively suppresses Fe contamination (Figure 7.2(c)). In this method, carbon and magnesium were first milled by 2h HEMM, and then $MgCl_2$ was added by a low-energy method, such as planetary milling or 0.5h HEMM. No Fe_7C_3 XRD peaks were detected for the graphites made by using the two-step combination method.

Figure 7.3 compares the morphology of the graphites made from $SC_{70}Mg_{30}$ without and with 10 at. % $MgCl_2$. Reducing the Mg content from 50 at. % to 30 at. % greatly influences the particle morphology and the graphitization efficiency. As shown in Figure 7.3 (a,b), the $SC_{70}Mg_{30}$ derived graphite is mainly composed of densely packed fine particles, with some aggregated hexagonal platelets. Densely packed fine particles indicate a lower graphitization level, as demonstrated in Chapter 5. After adding $MgCl_2$, the graphite products mainly contain spheroidal structures (5 - 20 µm, Figure 7.3 (c-h)), which are composed of bent polygonal platelets (Figure 7.3(d,e,g,h). The surface area of the graphite products decreases from 87.7 m^2 g^{-1} ($SC_{70}Mg_{30}$ derived) to 29.6 m^2 g^{-1} ($SC_{70}Mg_{30}(MgCl_2)_{10}$_S+S derived) due to these morphological changes. Graphites made from $SC_{70}Mg_{30}(MgCl_2)_{10}$_S+P and $SC_{70}Mg_{30}(MgCl_2)_{10}$_S+S also contain many tiny particles on the spheroid surfaces, which are probably composed of less ordered graphite.

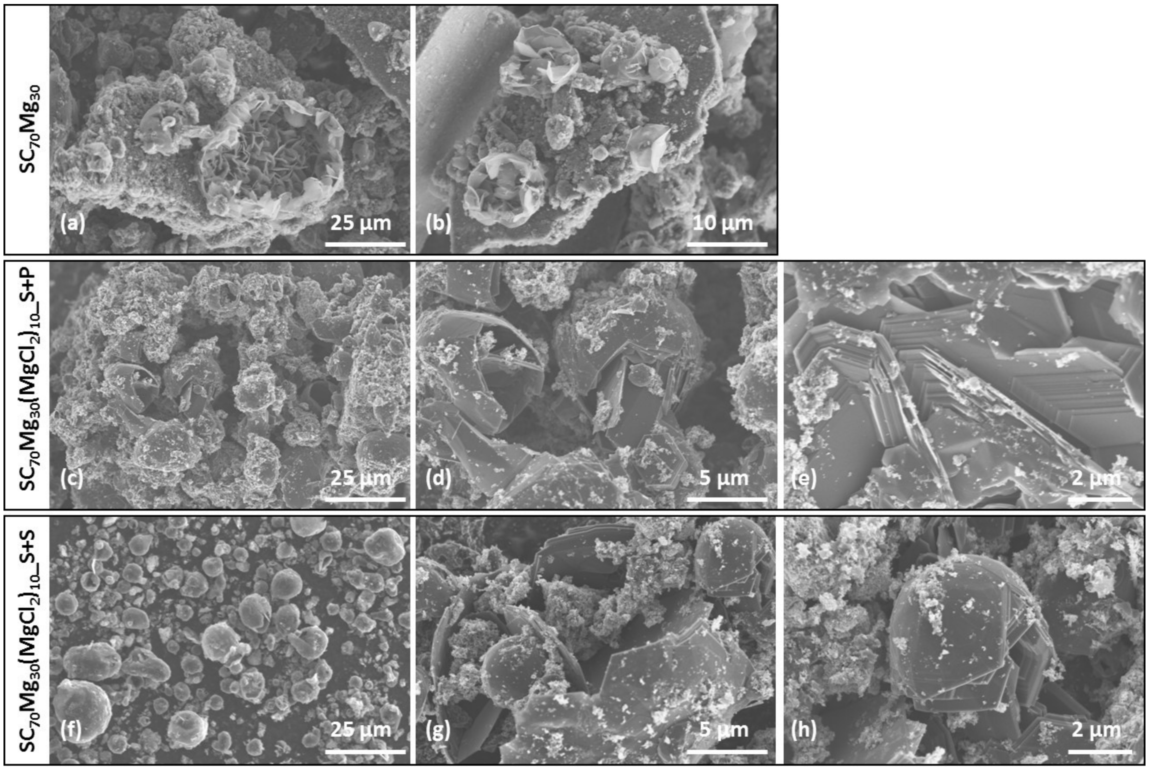

Figure 7.3 SEM images of graphites made from (a,b) $SC_{70}Mg_{30}$, (c,d,e) $SC_{70}Mg_{30}(MgCl_2)_{10}$_S+P, and (f,g,h) $SC_{70}Mg_{30}(MgCl_2)_{10}$_S+S.

Figure 7.4(a) shows XRD patterns of SC-Mg and SC-Mg-$MgCl_2$ after milling. All the XRD patterns contain sharp Mg peaks, indicating a crystalline Mg structure. The $SC_{70}Mg_{30}(MgCl_2)_{10}$_S XRD pattern has no $MgCl_2$ peaks, probably because the grain size of $MgCl_2$ is too small to be detected after 2h HEMM. In comparison, the XRD patterns of $SC_{70}Mg_{30}(MgCl_2)_{10}$_S+P and $SC_{70}Mg_{30}(MgCl_2)_{10}$_S+S have $MgCl_2$ peaks, because the crystalline structure of $MgCl_2$ was not destroyed in the low-energy combination step. An Fe peak was also detected for $SC_{70}Mg_{30}(MgCl_2)_{10}$_S, confirming that Fe contaminant is more easily induced by using the one-step combination method than the two-step method.

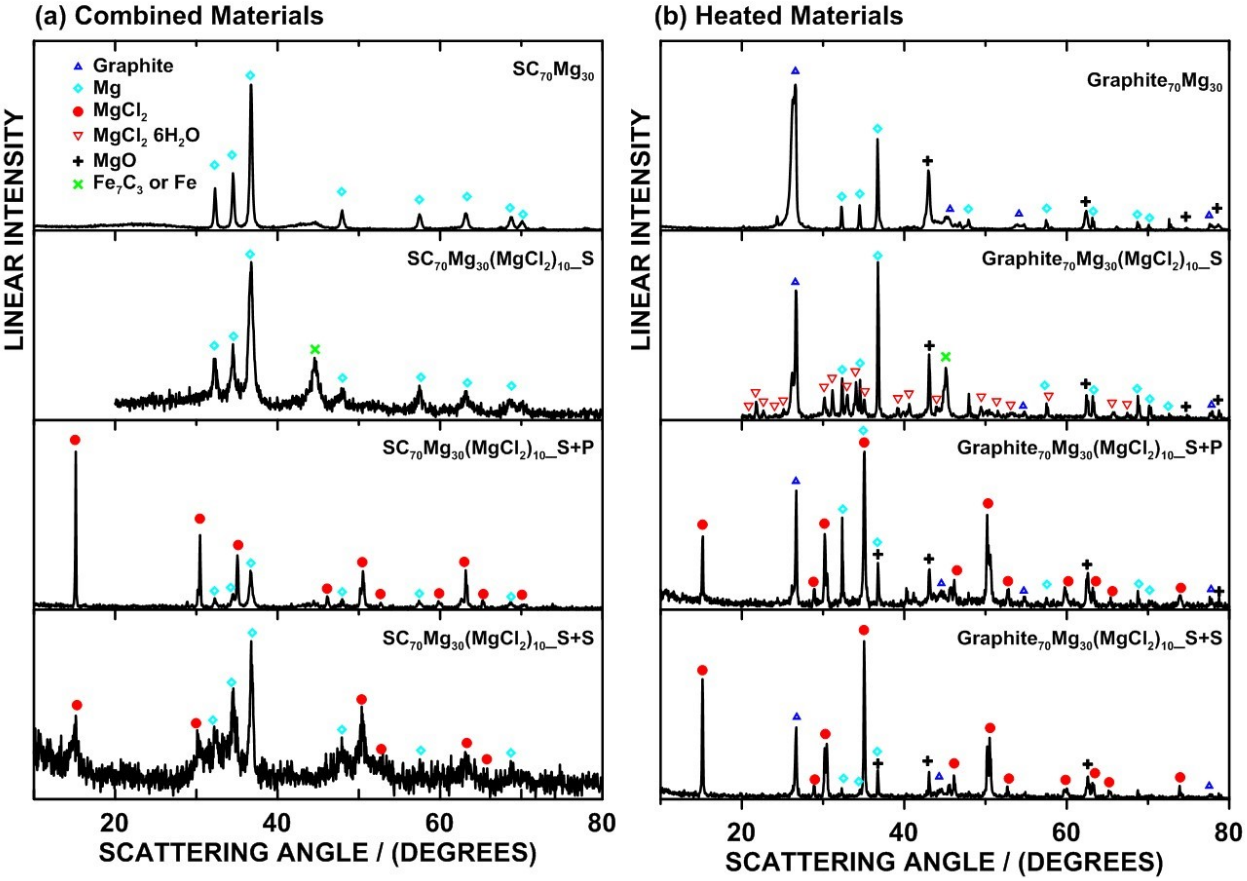

Figure 7.4 XRD of (a) combined C-Mg or C-Mg-$MgCl_2$ materials before heating, and (b) corresponding heated graphite-Mg or graphite-Mg-$MgCl_2$ materials.

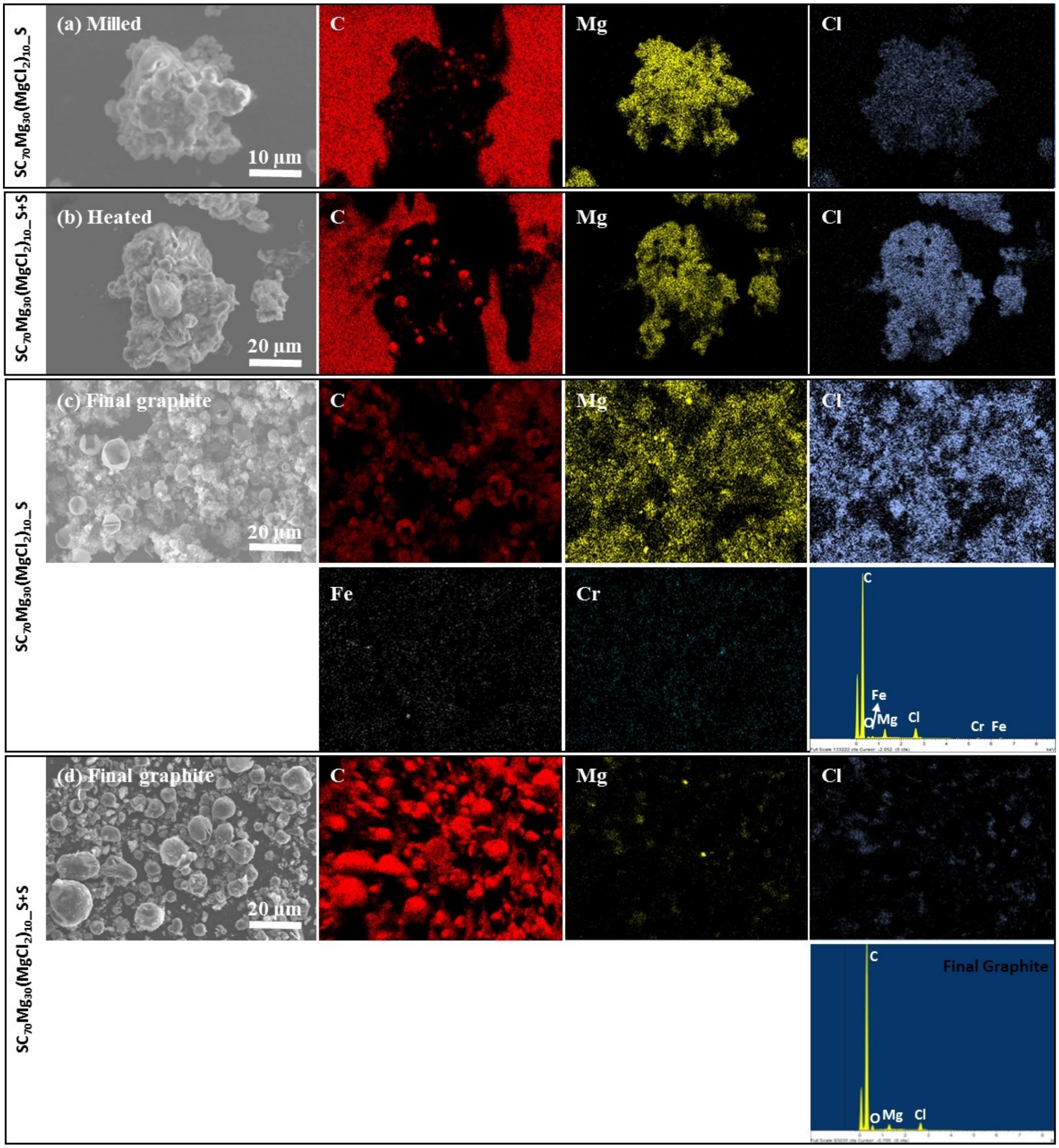

Figure 7.5 SEM images of graphites made from glucose with different precursor stoichiometries and different combination methods as indicated, and their corresponding EDS elemental mapping images and spectra.

Figure 7.5(a) shows an SEM image and corresponding elemental mapping images of $SC_{70}Mg_{30}(MgCl_2)_{10}$_S after milling. The particle in Figure 7.5(a) is an aggregate of primary particles. Carbon signals from this particle are weak while Mg signals are strong, indicating the particle is covered by Mg. Cl signals are evenly distributed, indicating a homogeneous distribution of $MgCl_2$. The SEM and EDS results for $SC_{70}Mg_{30}(MgCl_2)_{10}$_S+P and $SC_{70}Mg_{30}(MgCl_2)_{10}$_S+S after milling are similar (not shown).

Figure 7.4(b) shows XRD patterns of SC-Mg and SC-Mg-$MgCl_2$ after heating. The $MgCl_2$-free sample has sharp graphite peaks, Mg peaks, and MgO peaks. MgO may have formed due to an oxygen impurity in the carbon precursor or introduced as oxides on the inner surfaces of the stainless-steel reaction tube. $Graphite_{70}Mg_{30}(MgCl_2)_{10}$_S also has $MgCl_2{\cdot}6H_2O$ and Fe_7C_3 peaks. $MgCl_2{\cdot}6H_2O$ formed because this sample was accidentally exposed to air after heating and the $MgCl_2$ immediately reacted with water. In comparison, $Graphite_{70}Mg_{30}(MgCl_2)_{10}$_S+P and $Graphite_{70}Mg_{30}(MgCl_2)_{10}$_S+S do not have Fe or Fe_7C_3 peaks.

Figure 7.5(b) shows an SEM image and corresponding elemental mapping images of $SC_{70}Mg_{30}(MgCl_2)_{10}$_S+S after heating. The aggregate contains spherical structures, on which C signals are strong while Mg/Cl signals are weak. This suggests C, Mg and $MgCl_2$ have re-distributed after graphitization. $SC_{70}Mg_{30}(MgCl_2)_{10}$_S+P and $SC_{70}Mg_{30}(MgCl_2)_{10}$_S have similar particle morphologies and elemental distributions after heating (not shown).

Figure 7.6 shows XRD patterns of the graphites made from $SC_{70}Mg_{30}$ with optional $MgCl_2$. Although the graphite made from $SC_{70}Mg_{30}$ is essentially all composed of graphitic carbon, is highly turbostratically disordered, with an ordered graphite content of only 12.7 at. %. Adding $MgCl_2$ greatly increases the ordered graphite content to 51.6 at. % ($SC_{70}Mg_{30}(MgCl_2)_5$_S derived), 65.0 at. % ($SC_{70}Mg_{30}(MgCl_2)_{10}$_S+P derived) and 91.9 at. % ($SC_{70}Mg_{30}(MgCl_2)_{10}$_S+S derived) (Table 7.2). However, adding $MgCl_2$ results in an $MgCl_2$ residue, which is not accessible by water or air, as discussed above. The graphite made by the one-step combination method also contains Fe_7C_3, which is not detected for the graphite made by the two-step combination method.

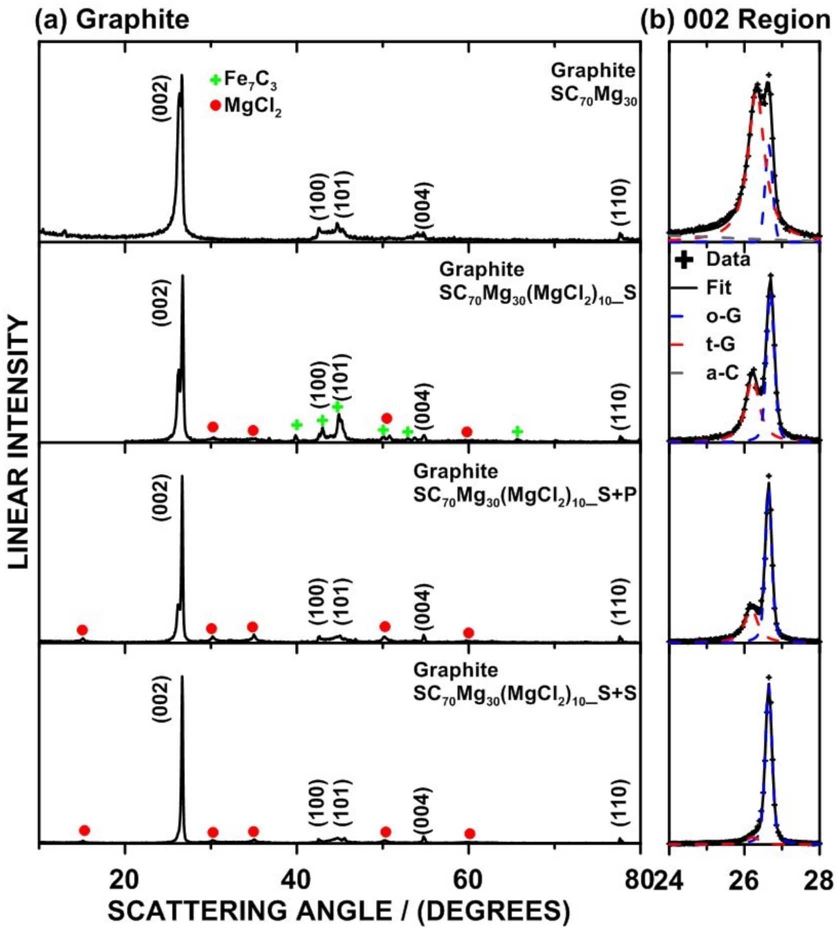

Figure 7.6 (a) XRD patterns of graphites made from SC$_{70}$Mg$_{30}$ with and without MgCl$_2$ and (b) their corresponding 002 peak regions.

Figure 7.5(c,d) show SEM images, corresponding elemental mapping images, and EDS spectra of the graphites made from SC$_{70}$Mg$_{30}$(MgCl$_2$)$_5$_S and SC$_{70}$Mg$_{30}$(MgCl$_2$)$_{10}$_S+S. All Mg signals should come from MgCl$_2$ because the atomic ratio of detected Mg and Cl is very close to 1:2. Strong and evenly distributed Mg and Cl signals were detected from the SC$_{70}$Mg$_{30}$(MgCl$_2$)$_5$_S derived graphite, while weak and sporadic Mg and Cl signals were detected from the SC$_{70}$Mg$_{30}$(MgCl$_2$)$_{10}$_S+S graphite during the same data collecting time, probably because the latter contains less MgCl$_2$ residues. Fe was identified from the SC$_{70}$Mg$_{30}$(MgCl$_2$)$_5$_S derived graphite by EDS, but not detected for the SC$_{70}$Mg$_{30}$(MgCl$_2$)$_{10}$_S+S derived graphite, consistent with XRD data.

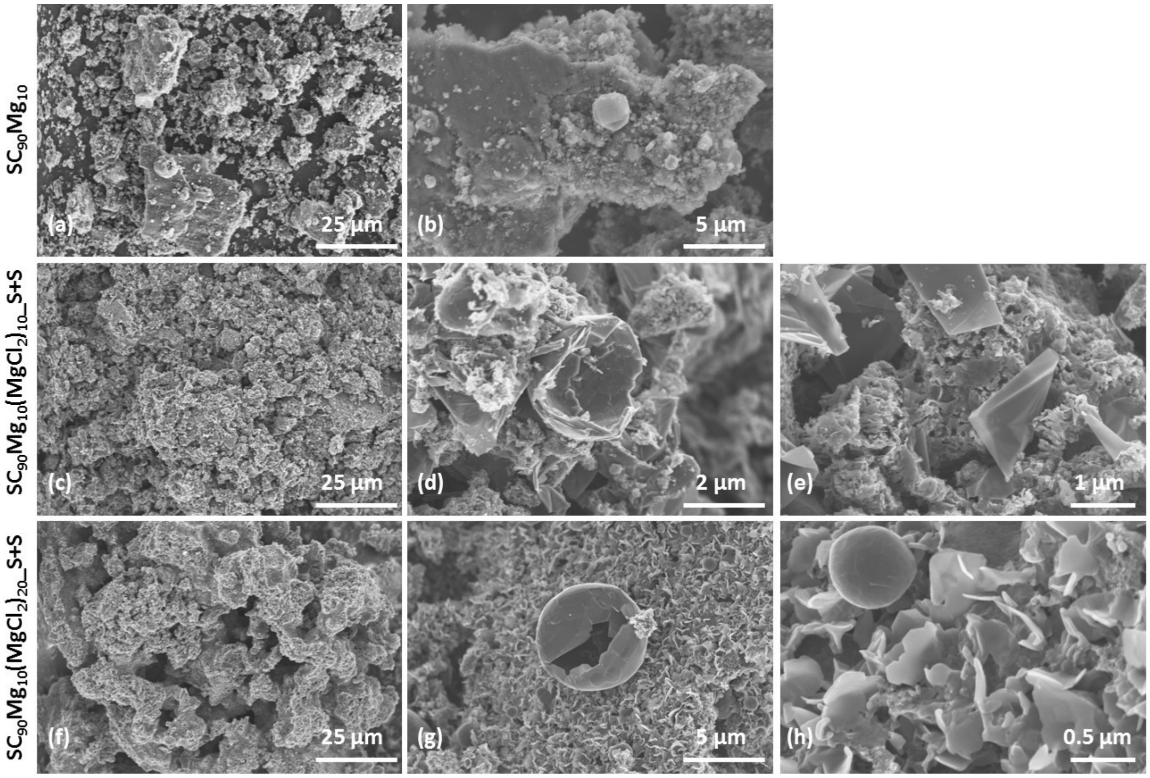

Figure 7.7 SEM images of graphites made from (a,b) $SC_{90}Mg_{10}$, (c,d,e) $SC_{90}Mg_{10}(MgCl_2)_{10}$_S+S, and (f,g,h) $SC_{90}Mg_{10}(MgCl_2)_{20}$_S+S.

Figure 7.7 and 7.8 show SEM images and XRD patterns of the graphites made from $SC_{90}Mg_{10}$ without and with 10 or 20 at. % extra $MgCl_2$. The $SC_{90}Mg_{10}$ derived graphite is essentially all composed of densely packed fine particles, without any platelet structures (Figure 7.7 (a,b)), and is composed of turbostratic graphite and amorphous carbon (Figure 7.8). In comparison, the $SC_{90}Mg_{10}$-$MgCl_2$ derived graphites are composed of tiny platelets (< 0.5 µm, Figure 7.7 (h)), with a few spheroidal structures (Figure 7.7 (d,g,h)). Adding $MgCl_2$ improves the graphitization efficiency, and more $MgCl_2$ results in higher graphitization levels (Figure 7.8 and Table 7.2).

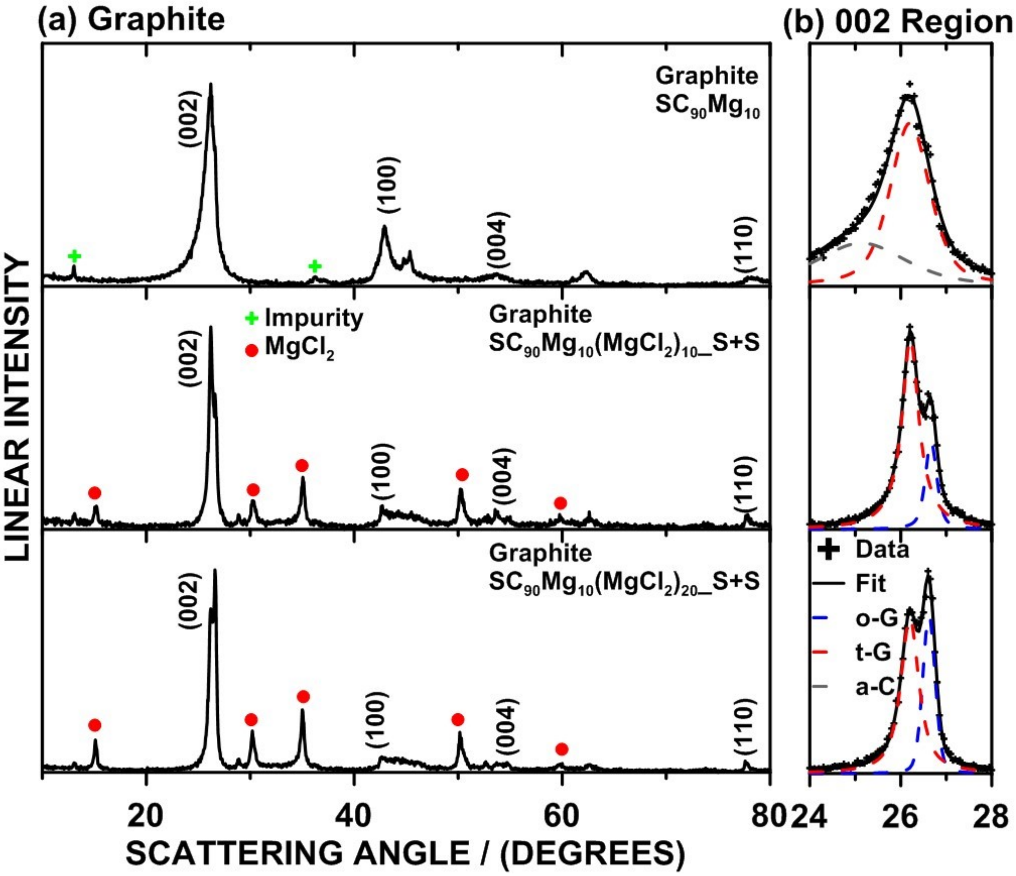

Figure 7.8 (a) XRD patterns of graphites made from $SC_{90}Mg_{10}$ without and with $MgCl_2$. Precursor stoichiometries and blending methods are indicated. (b) 002 peak regions of each XRD pattern.

By comparing Figure 7.2(a), Figure 7.6(a) and Figure 7.8(a), it is noteworthy that the graphites made from $SC_{50}Mg_{50}(MgCl_2)_{10}$_S and $SC_{70}Mg_{30}(MgCl_2)_{10}$_S+S, which have a high graphitization level, have weaker $MgCl_2$ peaks than the graphite made from $SC_{90}Mg_{10}(MgCl_2)_{10}$_S+S, which has a low graphitization efficiency. The $MgCl_2$ contents of these graphites were determined to be 0.52 wt. %, 1.94 wt. %, and 6.88 wt. %, respectively, by ICP-OES. In other words, a higher graphitization level corresponds to a lower $MgCl_2$ content in the final graphite. This may indicate that the more highly graphitized samples have fewer void spaces in which $MgCl_2$ can become trapped and inaccessible to washing.

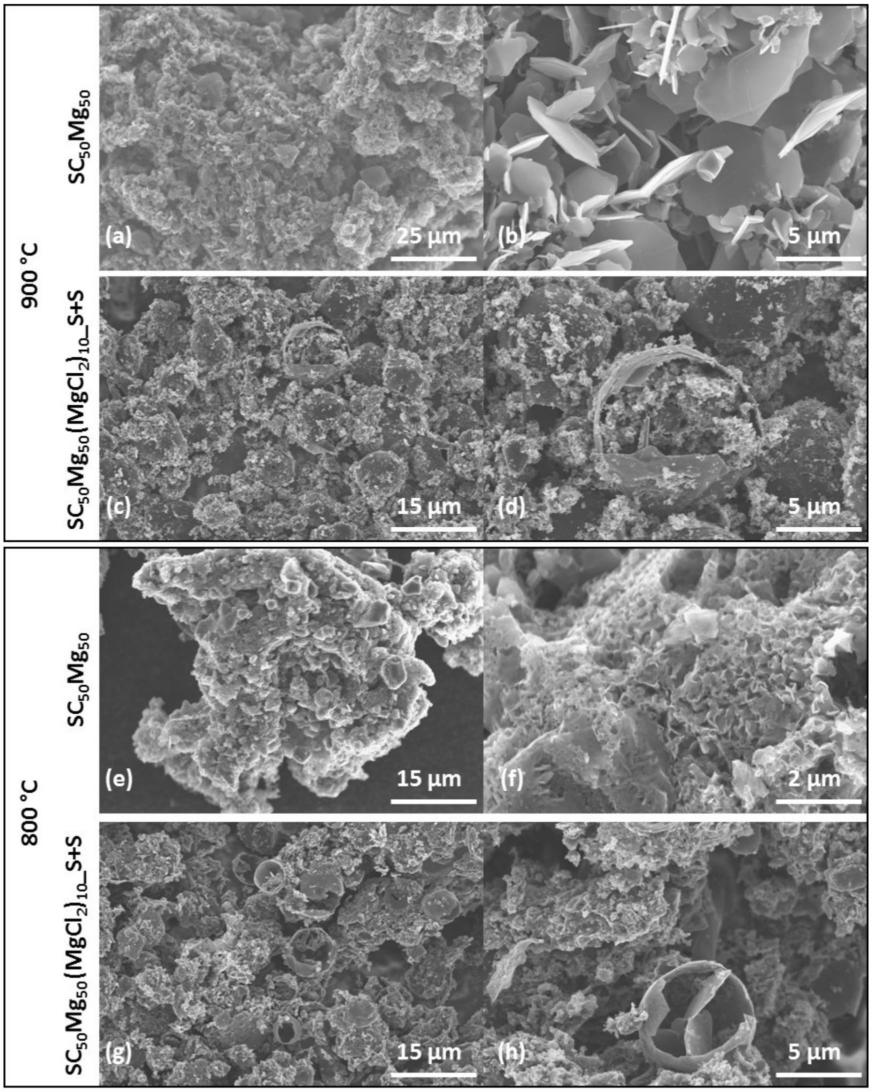

Figure 7.9 SEM images of graphites made from (a,b) $SC_{50}Mg_{50}$, (c,d) $SC_{50}Mg_{50}(MgCl_2)_{10}$_S+S at 900 °C, and (e,f) $SC_{50}Mg_{50}$, (g,h) $SC_{50}Mg_{50}(MgCl_2)_{10}$_S+S at 800 °C.

Figure 7.9 shows SEM images of the graphites made at lower temperatures (900 and 800 °C) from $SC_{50}Mg_{50}$ without and with $MgCl_2$. The graphite made from $SC_{50}Mg_{50}$ at 900 °C is essentially all composed of small platelets (<5 µm, Figure 7.9 (a,b)), while the graphite made at 800 °C is mainly composed of densely packed fine particles, with a small amount of tiny platelets (<0.5 µm, Figure 7.9 (c,d)). After adding $MgCl_2$, the $SC_{50}Mg_{50}$-$MgCl_2$ derived graphite (900 °C) is mainly composed of spheroidal particles with tiny particles on surface (Figure 7.9 (c,d)), while the $SC_{50}Mg_{50}$-$MgCl_2$ derived graphite (800 °C) is composed of dense particles (major component) and spheroidal particles. Figure 7.10 shows XRD patterns of the graphites made at lower temperatures from $SC_{50}Mg_{50}$ without and with $MgCl_2$. Similar phenomenon can also be observed here: (1) adding $MgCl_2$ greatly increases the graphitization level at 900 and 800 °C (Table 7.2); (2) combining C, Mg and $MgCl_2$ together by 2h HEMM increases the graphitization level, but also induces Fe_7C_3 contaminants (3) combining C-Mg with $MgCl_2$ by a milder method prevents inducing Fe_7C_3 contaminants and further increases the graphitization level; (4) graphites of higher crystallinity contain less amounts of $MgCl_2$ residue.

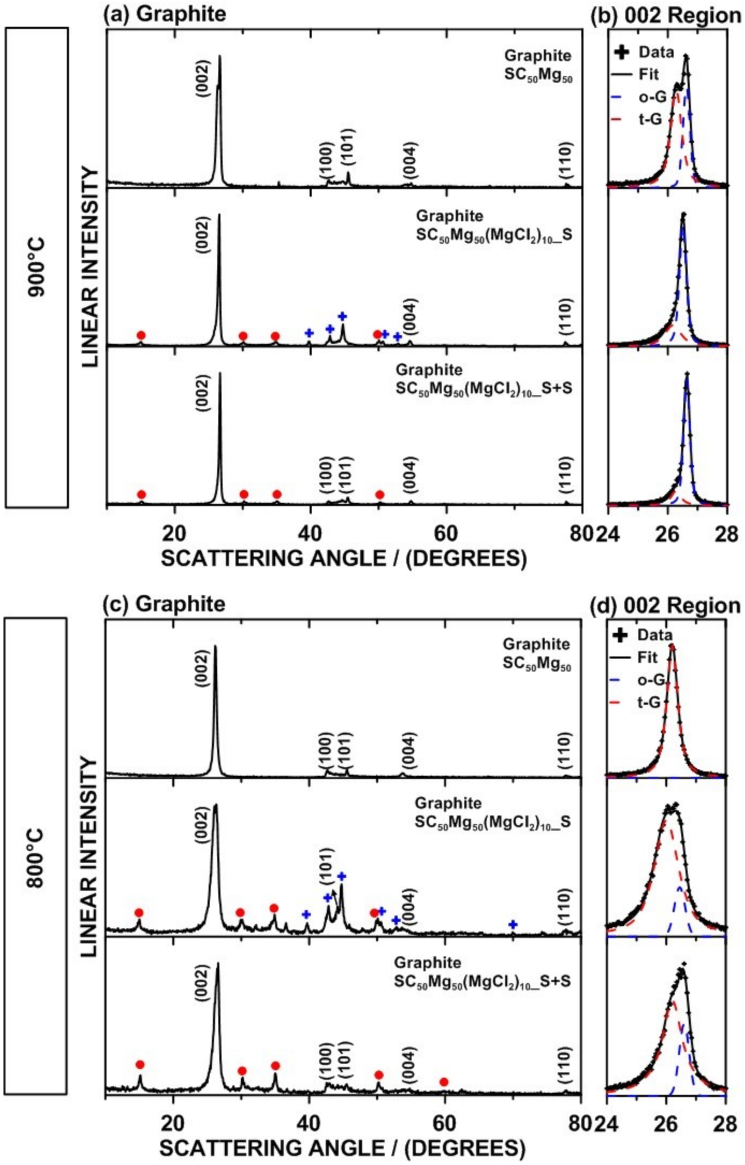

Figure 7.10 XRD patterns of graphites made from $SC_{50}Mg_{50}$, $SC_{50}Mg_{50}(MgCl_2)_{10}$_S, and $SC_{50}Mg_{50}(MgCl_2)_{10}$_S+S (a) at 900 °C and (c) at 800 °C, and (b,d) corresponding 002 peak regions.

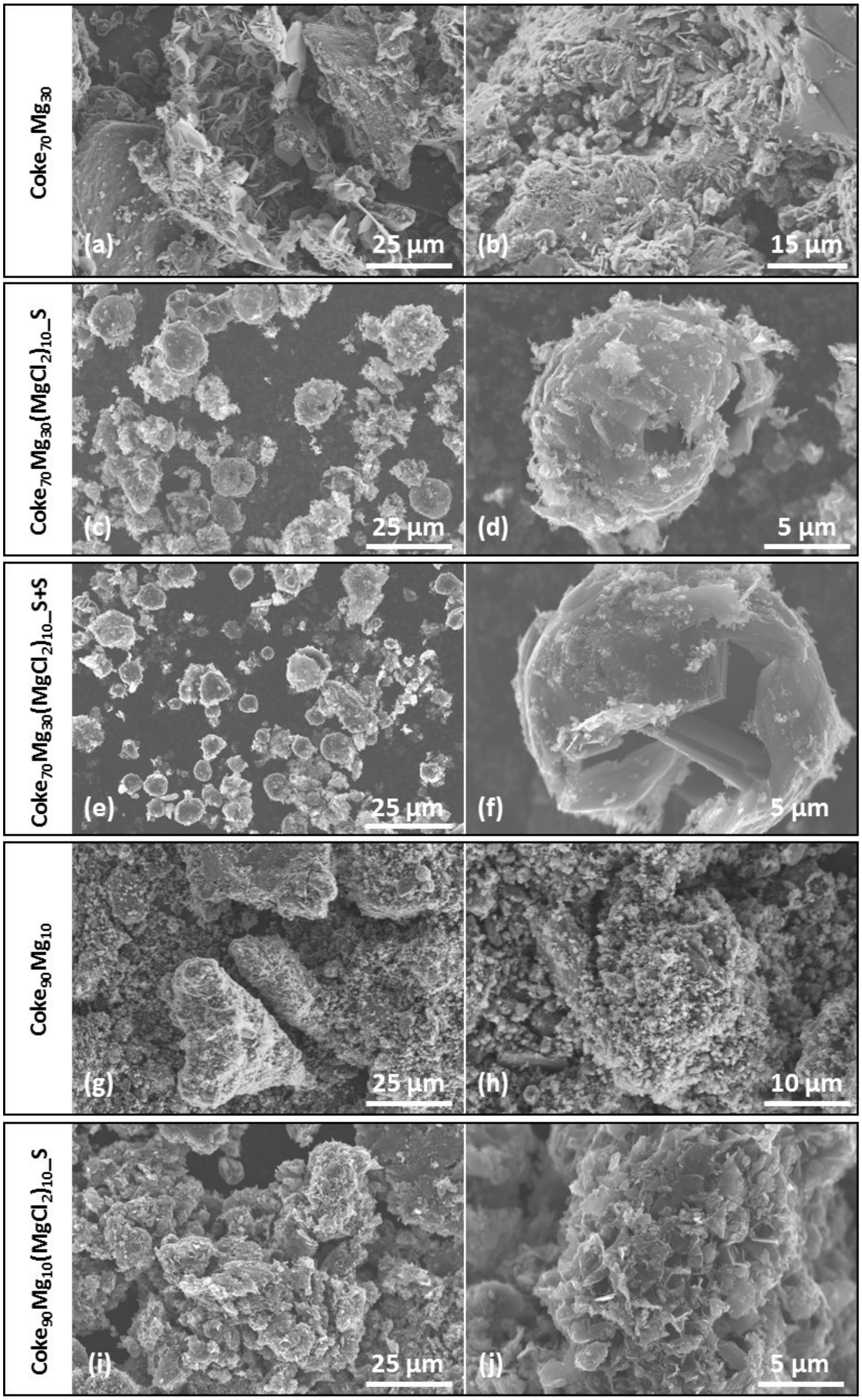

Figure 7.11 SEM images of graphites made from Coke-Mg without and with $MgCl_2$. Precursors are labelled on the left.

The $Coke_{70}Mg_{30}$ derived graphite is composed of platelets and densely packed fine particles (Figure 7.11(a,b)). Adding $MgCl_2$ changes the particle morphology from platelets to spheroidal structures (Figure 7.11(c-f)) and improves the graphitization efficiency (Figure 7.12(a,b)). This suggests adding $MgCl_2$ changes the graphite morphology and improves the graphitization efficiency regardless of the precursor type. The $Coke_{90}Mg_{10}$ derived graphite is essentially all composed of dense particles (Figure 7.11(g,h)). In comparison, the $Coke_{90}Mg_{10}$-$MgCl_2$ derived graphite contains small platelets (Figure 7.11(i,j)), indicating an improvement in graphitization level (Figure 7.12(c,d)).

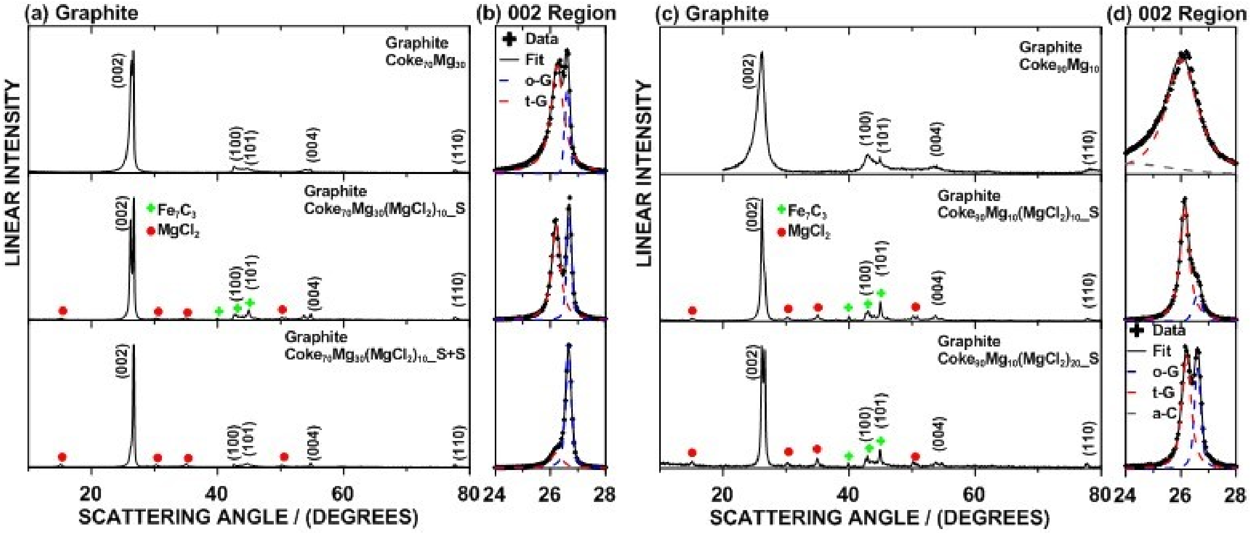

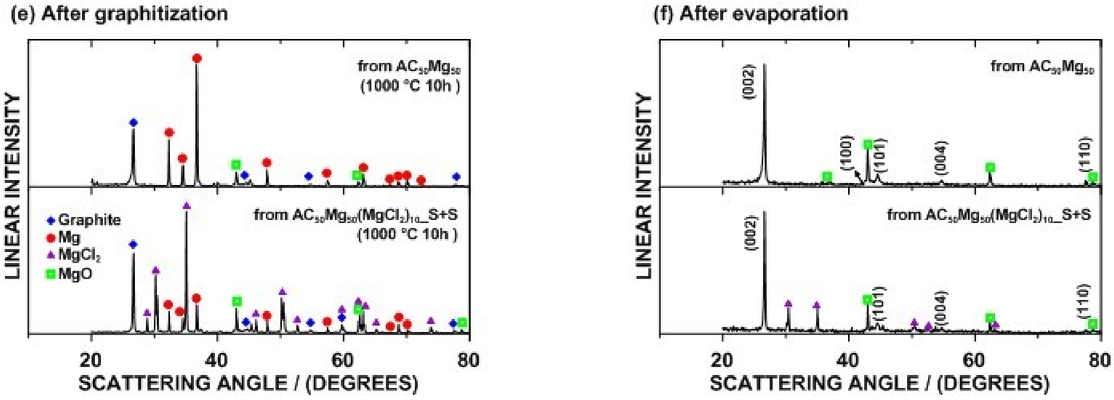

Figure 7.12 (a-d) XRD patterns of graphite made from Coke-Mg without and with $MgCl_2$. XRD patterns of (e) graphite-impurity mixtures after graphitization and (f) corresponding graphite products after low-pressure heating (900 °C, 5h).

The low-pressure evaporation method (introduced in Chapter 4) was also used here. After graphitization, the products are mixtures of graphite, Mg, MgO and $MgCl_2$ (Figure 7.12(e)). After heating under low-pressure, Mg was completely removed (Figure 7.12(f)) while MgO remains. As explained in Chapter 4, this is because Mg easily evaporates at 900 °C under low pressure while MgO does not. For the $MgCl_2$-containing sample, $MgCl_2$ was not completely removed after low-pressure heating. But the $MgCl_2$ peaks become much weaker, indicating some $MgCl_2$ has been removed.

To test if $MgCl_2$ is an effective graphitization catalyst by itself, $MgCl_2$ was combined with coke without Mg. Figure 7.13 compares the XRD patterns of heated coke-$MgCl_2$ (1000 °C, 3h) and coke. The carbon structure almost does not change before and after heating, suggesting $MgCl_2$ is not an effective catalyst. This is consistent with previous studies.[198]

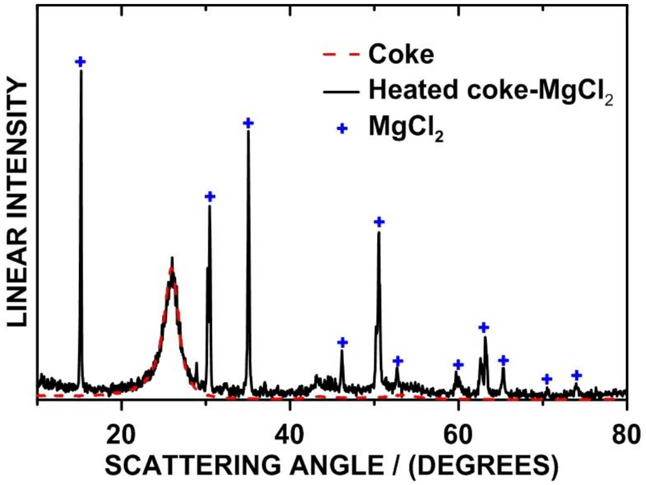

Figure 7.13 XRD patterns comparing coke with heated coke-$MgCl_2$.

7.3.2 $MgCl_2$ additive: electrochemical characterization

Figure 7.14 shows the electrochemical performance of the graphites made from SC-Mg without and with $MgCl_2$. The graphites made from $SC_{70}Mg_{30}(MgCl_2)_{10}$_S+S (1000 °C) and $SC_{50}Mg_{50}(MgCl_2)_{10}$_S+S (900 °C) have well defined staging phenomena (Figure 7.14(a-d)), corresponding to their highly graphitic structures. The reversible capacity and columbic efficiency of these graphites were greatly improved compared to the graphites made without adding $MgCl_2$ (Figure 7.14(e-f)). However, the irreversible capacities of these graphites were still very high (~50%), similar to that of graphites made without adding $MgCl_2$, although their surface areas were much smaller (~ 30 m^2 g^{-1} vs. ~ 80 m^2 g^{-1}). It has been shown that the irreversible capacity of graphite increased proportionally to its specific surface area.[202,203] However, the irreversible capacity is not only determined by the surface area of graphite, but also by many other factors, such as particle size and morphology. [204,205] For the graphites made from C-Mg-$MgCl_2$, there are not insignificant amounts of voids within graphite particles, as shown indirectly by the trapped $MgCl_2$. Li species may become trapped in these voids , contributing to the irreversible capacity.[206] In addition, there are many tiny particles on the graphite surfaces, which may significantly contribute to the irreversible capacity. Removal of these tiny particles, for example by mild oxidation, may improve performance further.

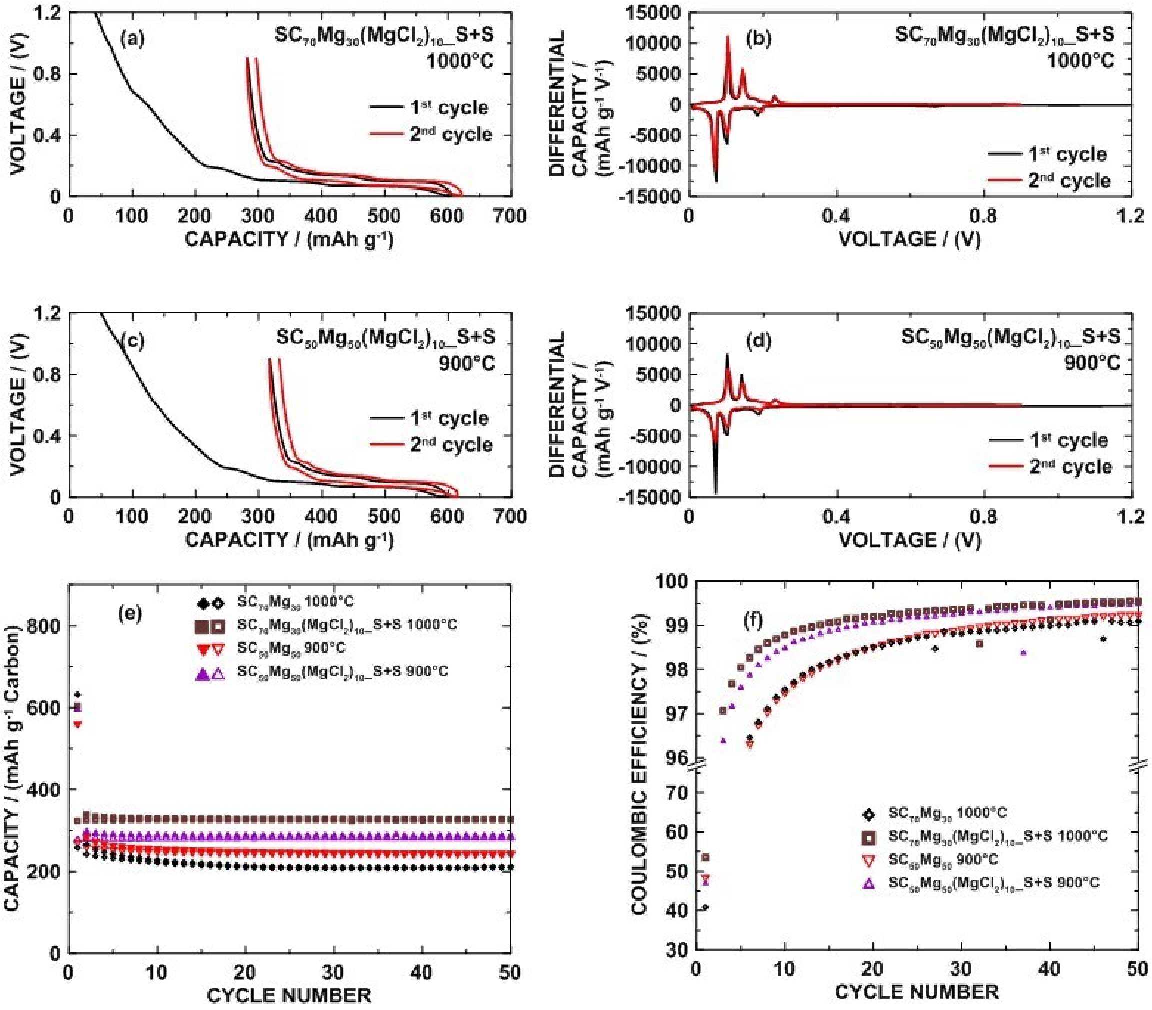

Figure 7.14 (a-b) Voltage profiles and (c-d) differential capacity curves of graphite made from SC-Mg-$MgCl_2$. (e) Cycling performance and (f) coulombic efficiency of graphites made from SC-Mg without and with $MgCl_2$ as labelled.

7.3.3 LiCl and NaCl additives: structural and morphological characterization

Figure 7.15(a-f) show the SEM images of the graphites made from $SC_{70}Mg_{30}$ with LiCl or NaCl. Adding LiCl/NaCl changes the morphology of graphites, and LiCl and NaCl have similar effects. Both of the graphites made from $SC_{70}Mg_{30}(LiCl)_{10}$ and $SC_{70}Mg_{30}(NaCl)_{10}$ are composed of two main components: well-defined small spheroids (1-5 μm) and tiny platelets (< 0.5 μm). The spheroidal structures are more complete and smoother, compared to those observed in the graphites made from SC-Mg-$MgCl_2$. Similar to $MgCl_2$, LiCl and NaCl residues cannot be completely removed from the final products (Figure 7.16(a)), probably again due to NaCl/LiCl trapped within voids in the graphite particles that are not accessible by water/air. NaCl residues are evenly distributed on the product surface (Figure 7.15(g)). Adding LiCl/NaCl also increases the graphitization level (Figure 7.16(a)), but not as drastically as adding $MgCl_2$ (Table 7.2). Osetzky found that carbon with a higher graphitization level can be made by adding $MgCl_2$ and LiCl/NaCl, compared to only adding $MgCl_2$.[147] However, the result in this work is contradictory to Osetzky's study (Figure 7.16(c,d) and Table 7.2).[147]

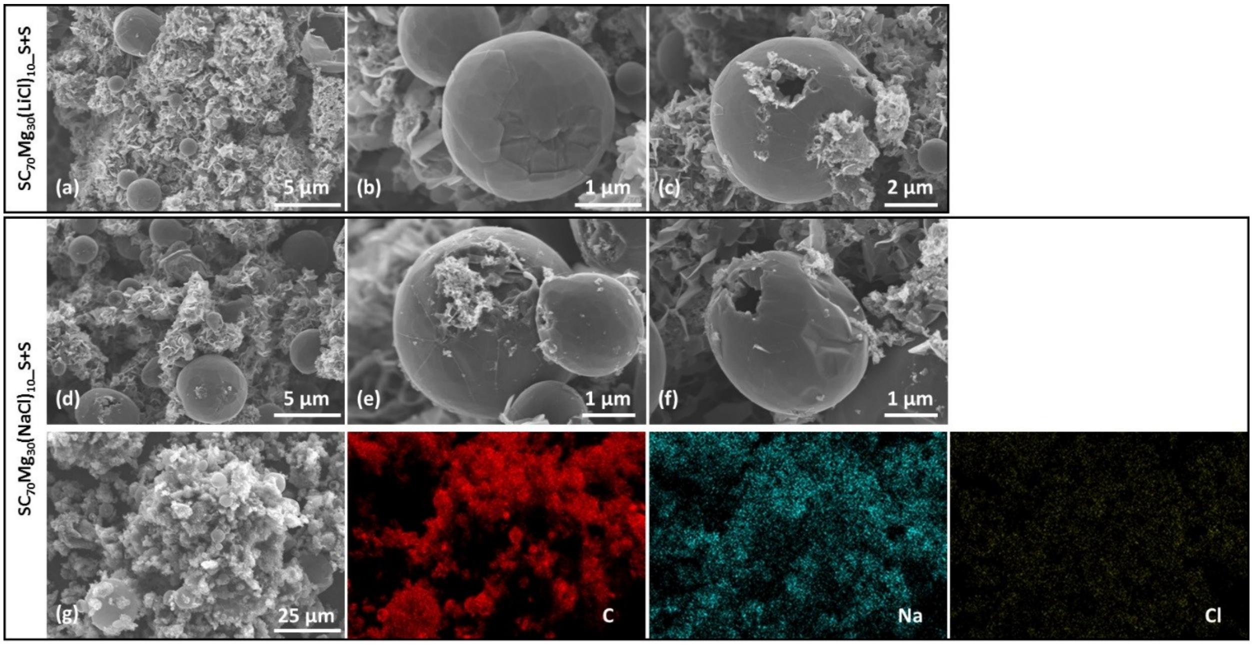

Figure 7.15 SEM images of graphites made from (a,b,c) $SC_{70}Mg_{30}(LiCl)_{10}$_S+S and (d,e,f) $SC_{70}Mg_{30}(NaCl)_{10}$_S+S. (g) An SEM image of graphite made from $SC_{70}Mg_{30}(NaCl)_{10}$_S+S and corresponding elemental mappings.

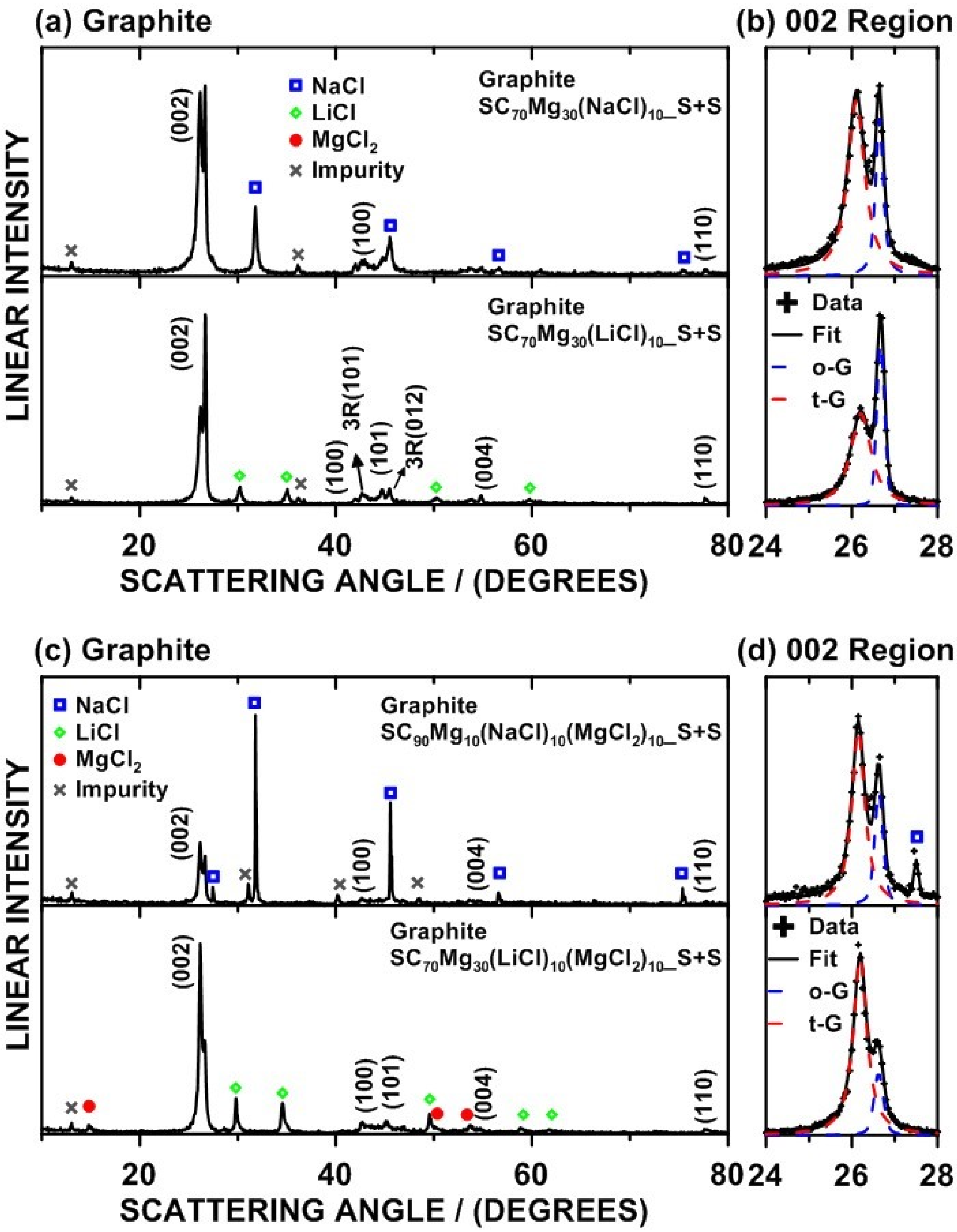

Figure 7.16 XRD patterns of graphites made from (a) SC$_{70}$Mg$_{30}$(NaCl)$_{10}$_S+S and SC$_{70}$Mg$_{30}$(LiCl)$_{10}$_S+S, and (b) corresponding 002 peak regions. XRD patterns of graphites made from (c) SC$_{90}$Mg$_{10}$(NaCl)$_{10}$(MgCl$_2$)$_{10}$_S+S and SC$_{90}$Mg$_{10}$(NaCl)$_{10}$(MgCl$_2$)$_{10}$_S+S, and (d) corresponding 002 peak regions.

7.3.4 Aluminum additive

Adding Al as an additive greatly changes the morphology of graphite particles (Figure 7.17(a-c)), which are essentially all composed of crystalline branches. These crystal branches do not remain planar, but curve quite freely (Figure 7.17(c)).

When both Al and $MgCl_2$ were added, another type of particle morphology was observed (Figure 7.17(d-i)). The graphite grown from SC-Mg-Al-$MgCl_2$ is mainly composed of spheroidal particles. Most of the spheroidal particles are filled with bent crystalline platelets (Figure 7.17(e,g)). This is different from the graphite particles made from C-Mg-$MgCl_2$ (Figure 7.1(c-f)), which are mainly hollow spheroids, or C-Mg-Al (Figure 7.17(a-c)), which are crystalline branches.

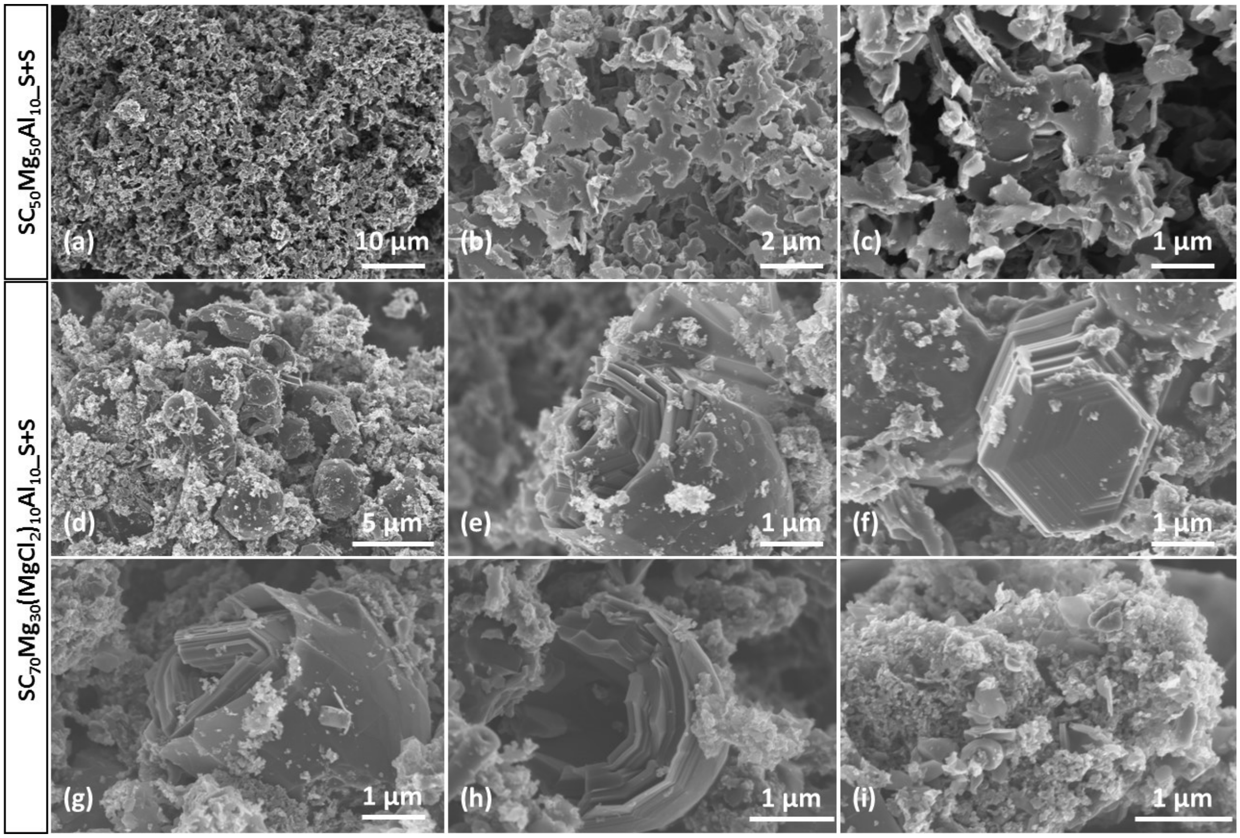

Figure 7.17 SEM images of graphites made from SC-Mg with aluminum and optional $MgCl_2$.

Graphite specific surface areas (SSA) were also greatly reduced after adding Al due to the change in morphology. For example, SSA of the graphites made from $SC_{50}Mg_{50}Al_{10}$ and $SC_{70}Mg_{30}Al_{10}(MgCl_2)_{10}$ are only ~40 $m^2\ g^{-1}$ and ~20 $m^2\ g^{-1}$, respectively. In comparison, SSA of the graphites made from $SC_{50}Mg_{50}$ and $SC_{70}Mg_{30}$ are ~80 $m^2\ g^{-1}$.

Figure 7.18(a-b) show XRD patterns of the graphites made from $SC_{50}Mg_{50}$ and $SC_{50}Mg_{50}Al$. All products are highly ordered graphites. Adding Al does not change the graphitization level greatly. However, an impurity ($Al_{0.4}Fe_{0.6}$) was induced to the final product when SC, Mg and Al were combined together by a one-step 2h HEMM. The induction of $Al_{0.4}Fe_{0.6}$ can be avoided by combining SC with Mg first, then combining SC-Mg with Al by 0.5h HEMM. Figure 7.18(c-d) show XRD patterns of the graphites made from $SC_{70}Mg_{30}$, $SC_{70}Mg_{30}Al_{10}$ and $SC_{70}Mg_{30}Al_{10}(MgCl_2)_{10}$. As above, adding the Al additive does not change the graphitization level. However, adding $MgCl_2$ greatly improved the graphitization efficiency.

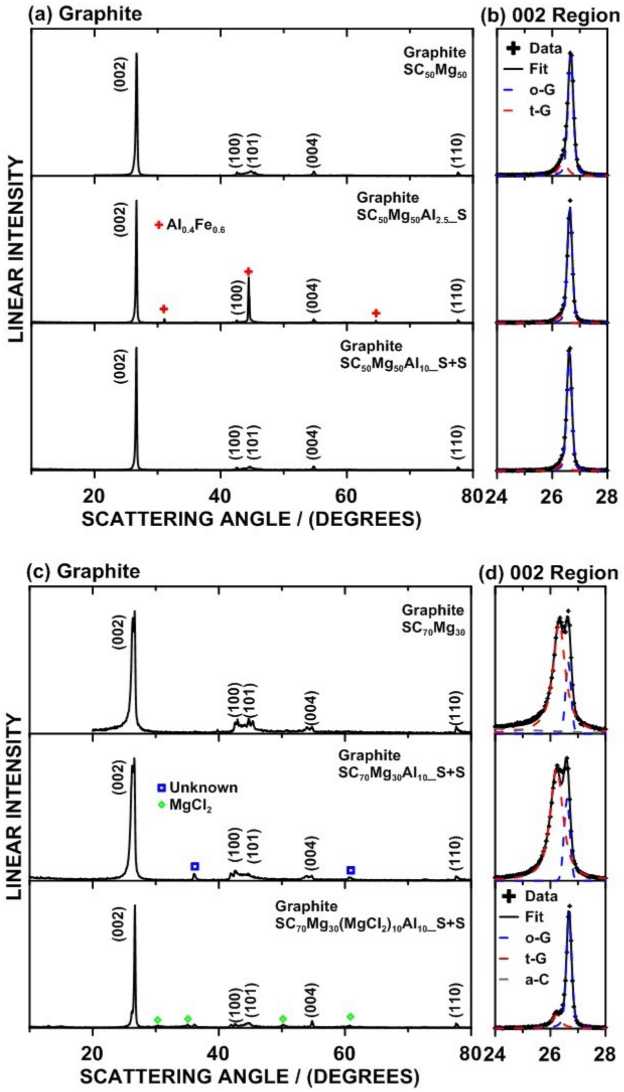

Figure 7.18 (a, c) XRD patterns of graphites made from SC-Mg with optional Al and optional $MgCl_2$ as additives, and (b, d) corresponding enlarged 002-regions.

Adding Al also changes the graphite morphology when using coke as the precursor. The graphite made from Coke$_{50}$Mg$_{50}$Al$_{2.5}$ is composed of small curly platelets and large block-like particles, as shown in Figure 7.19. However, adding Al reduces the catalytic graphitization efficiency and adding more Al results in a lower graphitization level (Figure 7.20). This is very different from using a glucose precursor.

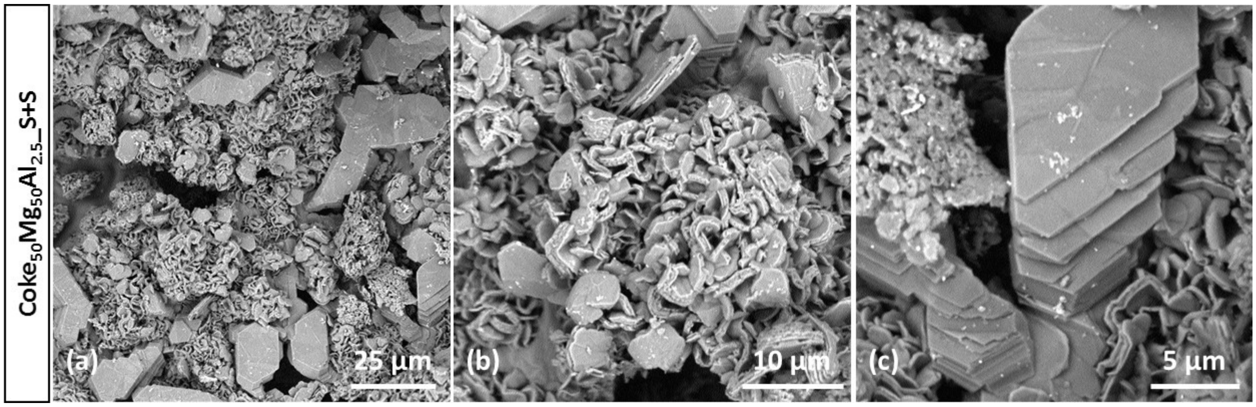

Figure 7.19 SEM images of the graphite made from Coke$_{50}$Mg$_{50}$Al$_{2.5}$_S+S.

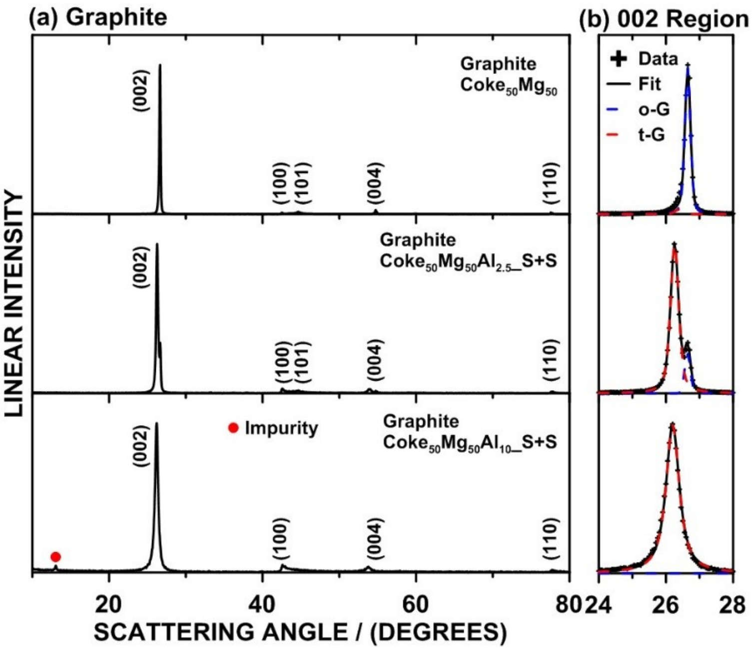

Figure 7.20 XRD patterns of graphites made from coke-Mg with optional Al.

7.4 Discussions

7.4.1 $MgCl_2$: morphology modification, graphitization efficiency and mechanism

The graphites made from C-Mg without $MgCl_2$ are mainly composed of platelets and dendrites, and very small amounts of spheroidal structures are also found in the graphite made from ground SC-Mg (Chapter 3). Adding $MgCl_2$ greatly modifies the particle morphology. The SC-Mg-$MgCl_2$ derived graphites are essentially all composed of spheroidal particles (Figure 7.1(c), Figure 7.3(f), Figure 7.9(c), Figure 7.11(c-f)), regardless of the precursor type.

The growth of spheroidal graphite from metal melts have been intensively studied and various models have been proposed.[137,207–209] It was suggested that an increase in cooling rate favors a graphite morphology change from flakes to spheres in metal-carbon melt systems.[137,209–211] But the cooling rates of C-Mg and C-Mg-$MgCl_2$ are almost the same in this study, and therefore should not be a factor influencing the formation of the spheroidal morphology. Amini *et al.* pointed out that the cooling rate of metal-carbon melts influenced the growth rate of graphite, and further influenced graphite morphology.[137] In other words, graphite morphology is kinetically dependent, and is affected by the crystal growth rate. In this study, the $MgCl_2$ additive may be a good carrier for carbides, as suggested by Osetzky, and may kinetically improve the catalytic graphitization process somehow.[147] However, Boehm disagreed with Osetzky's assumption and pointed out that alkaline earth metals are soluble in the corresponding molten metal chlorides,[212] and are highly reactive in this form.[150] Therefore, the Mg dissolved in $MgCl_2$ are more reactive during catalytic graphitization and thus cause graphite crystals to grow faster compared to that without $MgCl_2$. At low growth rates, graphite crystals grow normal to basal planes (*e.g.* 002) and prismatic planes (*e.g.* 101), following a continuous growth mechanism.[137,213–215] At intermediate growth rates, solid-liquid interfaces between graphite prismatic planes (*e.g.* 101) and liquid become rough and prismatic planes grow faster than basal planes, and thus the formation of flakes is favored, following a lateral growth mechanism, such as the growth of graphitic platelets from C-Mg.[137,213–215] At high growth rates, interfaces of both basal planes and prismatic planes become rough and grow faster; and particle bending appears, resulting in bulky spheroidal morphology, such as the growth of graphite from C-Mg-$MgCl_2$.[137,188,213–215] This also explains why some spheroidal particles have thick shells (Figure 7.1(f,g), Figure 7.3(h)). Because of repeated bending of graphite platelets, spheroidal particles usually contain a higher amount of structural defects, such as rotation defects (Figure 7.3(e,h)) and vacancies.[188]

The formation of spheroidal structures might also be explained by other reasons. Sadocha *et al*. and Muhmond *et al.* suggested that foreign elements can affect the growth of graphite crystals.[188,189] For example, the presence a surface oxygen impurity might reduce the bending ability of platelets by decreasing their surface tension, so that the spherical shape deteriorates into a platelet structure.[188] In this study, $MgCl_2$ may affect the growth of graphite in an opposite way: it may improve the bending ability possibly by increasing the platelet surface tension and surface energy, so that the system attempts to decrease its energy by forming spheroidal structures.[132,187] Muhmond *et al.* also demonstrated that some foreign elements (*e.g.* H, F) might favor the formation of pentagonal rings of C atoms instead of hexagonal rings, by forming chemical bonds between foreign elements and pentagonal rings. Pentagonal C rings create curvature in the basal plane and cause spheroidal growth of graphite.[189] It is possible that Cl forms chemical bonds with pentagonal C rings, or $MgCl_2$ may favor the formation of chemical bonds between pentagonal C rings and other foreign elements. Similar phenomena were found in cast irons where some elements indirectly assisted sphere growth.[137]

Adding $MgCl_2$ also improves the catalytic graphitization efficiency, even at lower temperatures (900 and 800 °C) or when using a lower amount of Mg catalyst (30 at. % and 10 at. %), regardless of precursor types. This is likely because $MgCl_2$ is a good carrier for carbides or Mg is more reactive in the Mg-$MgCl_2$ system, as explained above, and thus the catalytic graphitization process is accelerated.[147,150] However, $MgCl_2$ alone is not an effective catalyst (Figure 7.13).

7.4.2 $MgCl_2$: combination methods and impurities

Fe contamination is an inherent drawback of HEMM with stainless steel vials and balls.[180] $MgCl_2$ further enhances the possibility of Fe contamination during HEMM.[180] A proper combination method is crucial in this study, which greatly influences the purity and graphitization level of the final products: if the energy is too high (2h HEMM with ~115g balls) when adding $MgCl_2$, significant amounts of Fe contaminant is induced, while if the energy is too low (1h planetary milling), the graphitization efficiency is limited. Only a proper combination method

(0.5h HEMM with ~45g balls) can avoid the formation of Fe-C compounds and lead to a high graphitization level.

The graphites made from C-Mg-$MgCl_2$ contain $MgCl_2$ residues, which are not water or air accessible. As explained above, spheroidal graphite particles contain many defects such as voids, where $MgCl_2$ may be trapped.[188] These voids are within the graphite particles and thus are not accessible by water or air, unless the graphite structure is destroyed. Therefore, some $MgCl_2$-containing graphites were ball milled by HEMM to destroy their graphite structures, so that $MgCl_2$ could be dissolved in acid for ICP-OES measurements. The ICP-OES results prove that a higher graphitization level corresponds to a lower $MgCl_2$ content, probably because the more ordered graphites contain less voids and thus less amounts of trapped $MgCl_2$.

7.4.3 LiCl and NaCl

Adding LiCl or NaCl also greatly modifies graphite morphology, resulting in a mixture of spheroidal particles and tiny platelets (< 0.5 μm). The spheroidal structures are more complete, smoother, and smaller compared to those found in the graphite made from C-Mg-$MgCl_2$. Spheroidal particles form probably also because LiCl and NaCl make magnesium carbon formation and decompositions kinetically favorable.[147] However, the graphitization enhancement resulting from LiCl or NaCl is much less dramatic than $MgCl_2$, and therefore a significant amount of small platelets (probably of low-graphitization level) exist in these samples.

7.4.4 Al

Adding Al greatly changes the morphology of graphite particles (Figure 7.17(a-c)), which are essentially all composed of crystalline branches. This type of crystal growth is usually called "dendric branching growth", which occurs when a solute impurity is present in a carbon-catalyst solution.[185] Similar crystal branches were observed in graphite grown from a C-Ni-B solution (Figure 7.21(a)) [185]. In comparison, the way hexagonal graphitic platelets (Figure 4.1(e-h)) grow from C-Mg melts is usually called "single crystal growth", which is common for graphite grown from carbon-catalyst solutions with little impurities.[185]

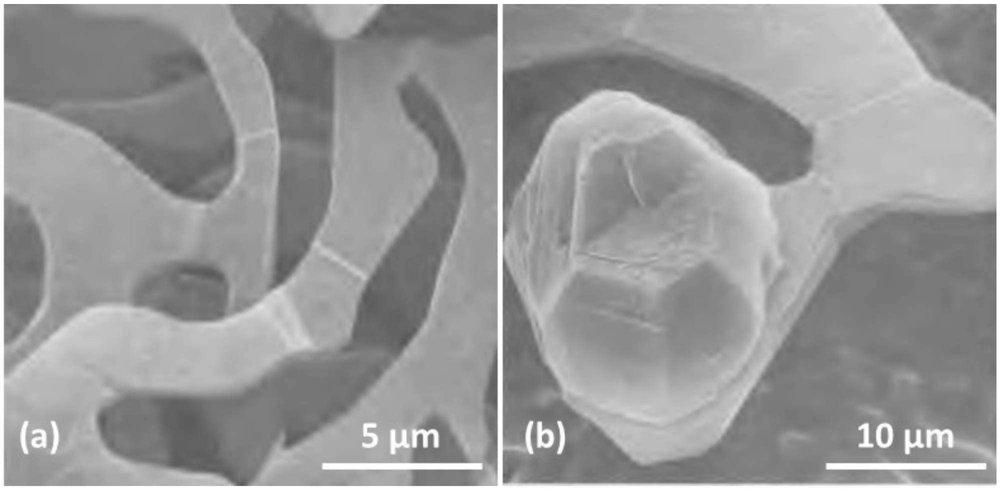

Figure 7.21 A graphite particle formed due to the existence of Al during graphitization of Ni-C. Reproduced from [185] with permission.

Block-like graphite crystals were observed in graphite made from C-Mg-Al (Figure 7.17(f)), which formed probably because Al particles blocked the original growth routes of graphite, forcing the crystal to grow along the 001 direction. A similar phenomenon was observed in the graphite grown from a C-Ni-Al solution, (Figure 7.21(b)) [185].

The graphite made from C-Mg-$MgCl_2$-Al has a modified morphology and an improved graphitization level. Al and $MgCl_2$ apparently work independently: $MgCl_2$ improves the graphitization efficiency, while Al alters crystal growth routes and modifies particle morphologies in the way explained above.

Adding Al also modifies the morphology of graphite made from coke (Figure 7.19), which is, however, quite different from the morphology of graphite made from SC. Moreover, adding Al greatly reduces the graphitization efficiency of coke, while it is not the case when using SC as the precursor. The reason is not fully understood yet.

7.5 Summary

Adding chlorides ($MgCl_2$, LiCl, and NaCl) greatly changes the morphology of graphite particles during the Mg-catalyzed graphitization process regardless of the precursor type. Spheroidal particles rather than platelets dominate the graphite products. This is probably because these chlorides increase the growth rate of graphite particles and thus particle bending appears. Adding chlorides greatly improves the Mg catalyzed graphitization efficiency. Among all three chlorides, $MgCl_2$ works the best. It effectively improves the graphitization level even at relatively low temperatures (800 and 900 °C) or when less Mg catalyst (10 and 30 at. %) is used. The chloride residues cannot be completely removed by reacting with acid/water. These chlorides are not accessible by neither air nor water, probably because they are trapped in voids within graphite particles. The voids may be formed during the formation of the spheroidal structures. A higher graphitization level leads to a lower $MgCl_2$ content, due to a lower void content.

Adding Al also changes the morphology of graphite particles. However, for different precursors, different graphite morphologies were observed. It was expected that Al blocked the original growth routes parallel to the basal plane, forcing the crystal to grow perpendicularly in a spiral way. Interestingly, the graphitization efficiency for a coke precursor is significantly suppressed after adding Al, while it is almost not influenced when using a SC precursor. This is not fully understood yet. When both Al and $MgCl_2$ are added, the graphite product has a modified morphology and an improved graphitization level, probably in a way that Al and $MgCl_2$ work independently.

The method used to combine precursors played an important role in this study, as it greatly influences the product purity and the graphitization efficiency. If C, Mg and additives are combined with one-step HEMM, Fe contaminants are induced. If C and Mg are combined first by HEMM and then additives are added using a low energy process (1h planetary milling), the graphitization efficiency is limited. Only a proper combination method can avoid the formation of iron carbides and meanwhile lead to a high graphitization level. Switching to ceramic milling containers and media may eliminate this source of contamination.

Chapter 8 Conclusion

8.1 Summary

In this thesis, the catalytic effects of Mg and Li on the graphitization process and the effects of precursors, mixing/heating conditions, and additives on the graphitization rate and the final graphite morphology were studied using a variety of techniques. Many interesting chemistries were discovered and discussed. These findings could guide to further understanding of the catalytic graphitization process and the resulting products.

In Chapter 3, Voronoi-tessellated graphites (VTGs) were made by heat-treatment of hard carbon at 800 - 1000 °C for 1 - 3 h with a Mg catalyst. The magnesium and carbon precursors were combined together by hand grinding. The temperatures at which graphitization was achieved (≤ 1000 °C) were far below that conventionally used for artificial graphites (~3000 °C) and the graphitization level of some the resulting graphites was high (~99 at. % graphitic carbon), suggesting that this method may lead to less energy intensive graphite synthesis methods. To the authors' knowledge, this is the first time that Mg has been shown to be an effective and efficient graphitization catalyst that works at ~1000 °C. The microstructure of VTGs is quite interesting, indicating that the graphite grows as sheets outward from Mg spheroidal centers to form Voronoi-tessellated regions. Unlike transition metal catalysts (Fe, Co, Ni), Mg was easily removed by reacting with acid. The purity of the VTGs were very high, as confirmed by using ICP-OES, fulfilling an initial goal of achieving effective graphitization using a catalyst that can be easily removed from the graphite products. However, VTGs made by the grinding method comprise significant amounts of turbostratic graphite. It was also shown that the Mg vapor is not an effective graphitization catalyst.

In Chapter 4, hexagonal platelet graphite (HPG) crystals were grown from milled hard carbon/Mg alloys at 800 - 1000 °C in 3 - 20 h. Compared to the grinding method introduced in Chapter 3, the milling method worked much more efficiently at the same graphitization conditions. Some HPGs are highly crystalline, and are more ordered than some artificial graphites made at 2850 °C. When cycled in Li half-cells, the HPGs made at 1000 °C have the best performance reported thus far for graphites made at such low temperatures, with characteristics similar to that of commercial artificial graphites made at much higher temperatures (~ 3000 °C). However, HPGs contain hexagonal platelets and some graphene particles. The special microstructure results in high specific surface area (~80 $m^2 g^{-1}$), leading to high irreversible capacity in Li half-cells. Carbon coating greatly reduced the irreversible capacity and increased the coulombic efficiency (CE) of HPGs during cycling. However, the reversible capacity of carbon-coated HPGs was slightly reduced due to the added amorphous carbon content. Mg catalyzed graphitization may be a convenient route to synthesizing high purity bulk graphite with unique microstructures. Such highly graphitized, but high surface area carbons in this study may be desirable in applications such as supports for catalysts used in chemical synthesis or in fuel cells. The low-pressure evaporation method was shown to be an effective way to remove Mg, although MgO impurities remain in the product. By a proper design of the furnace and tubes, it is possible to recover the Mg catalyst.

In Chapter 5, Mg catalyzed graphites were made from various precursors, including polymer, composite and carbohydrate precursors. All precursors were effectively converted from amorphous carbon to highly graphitic carbon after a low temperature (1000 °C) and a short duration (3 h) graphitization process. The graphitization level of the graphite products was greatly influenced by the precursor types. Most non-polymer precursors can be converted into highly ordered graphite, while most polymer precursors can be converted into a mixture of ordered graphite and turbostratic graphite. Catalytic graphites are composed of particles with various morphologies. Generally, as the graphitization level increases, the graphite morphology changes from dense particles, to small platelets, to large platelets with tiny particles, to pure large platelets. The graphitization level is also greatly affected by the pre-heating process (carbonization). This is probably because different pre-heating processes yield amorphous carbons with different structures (e.g. cross-linking, aromatic structure, parallel-layer groups), and with different types or amounts of non-carbon elements. Some highly ordered catalytic graphites have excellent cycling stability and high reversible capacity in Li half-cells. However, most of the catalytic graphites have high irreversible capacity, probably due to their high surface areas and the existence of less ordered particles on the graphite particle surfaces.

In Chapter 6, Li was shown to be an effective graphitization catalyst. However, Li has a lower catalysis efficiency compared to Mg. Most of the lithium catalyzed graphites (LCGs) comprise amorphous carbon, and only comprise small amounts of ordered graphite.

In Chapter 7, chlorides ($MgCl_2$, LiCl, and NaCl) were used as additives in Mg catalyzed graphitization, which greatly changed the morphology of graphite particles regardless of the precursor type. After adding these chloride additives, spheroidal particles dominated in graphite products rather than platelets. This is probably because chlorides increase the growth rate of graphite, resulting in particle bending. Adding chlorides also improved the graphitization efficiency, among which $MgCl_2$ worked the best. Although $MgCl_2$ is not an effective catalyst by itself, adding $MgCl_2$ improved the graphitization efficiency at relatively low temperatures (800 and 900 °C) or when using a lower amount of Mg catalyst (10 and 30 at. %). However, chloride residues in graphite products cannot be completely removed by reacting with acid/water, and are not accessible by air, probably because they are trapped in voids within the graphite particles. A higher graphitization level leads to a lower $MgCl_2$ residue content, perhaps due to a higher structural order and a lower void content. The method in which the precursors, catalyst and additives are combined plays an important role. A proper combination method can avoid inducing impurities and improve graphitization efficiency. The low-pressure evaporation method was effective in removing $MgCl_2$, though it was less efficient compared to reacting with acid. Al was also used as an additive in Mg catalyzed graphitization, which changed the graphite morphology and reduced the graphite surface area.

8.2 Future Work

8.2.1 Surface treatment and refining of catalytic graphite particles

Most catalytic graphites in this study have high specific surface area (> 30 m^2 g^{-1}), leading to high irreversible capacity and relatively low CE during Li cell cycling, as shown in Chapter 4 and 5. Some relatively-low-surface-area graphites (e.g. coke graphite and tire graphite, ~ 10 m^2 g^{-1}) also have higher irreversible capacity than battery-grade commercial graphites (e.g. MAGE). The carbon-coating method introduced in Chapter 4 is an effective method to reduce the graphite surface area and improve initial CE. However, the resulting initial CE is still not high enough (should be > 90% or even > 95%), perhaps because the surface area of the carbon-coated graphite is still high (~20 m^2 g^{-1}). A better particle refinement or surface treatment method is required to reduce the irreversible capacity and improve the CE of catalytic graphites in Li cells.

Particle refinement and surface treatment processes are always required in battery-grade anode graphite production in industry. For synthetic anode graphite made by the Acheson process, particle refinement is conducted by grinding, classifying and coating to optimize graphite particle design.[216] Natural graphite flakes are treated by sophisticated mechanical milling techniques (via micronization and spheroidization) to obtain spherical particles for better cycling performance.[216,217] A wet-chemical and/or a thermal purification process is also conducted to decrease the impurity content in natural graphite.[216] Although it is difficult to get detailed information of these processes from manufacturers, many inspiring methods have been described in publications, such as mechanical milling,[216,218] carbon coating,[218–221] and oxidization.[205] For different graphite products made from various precursors, different methods should be applied due to their difference in particle morphology and impurity types and contents.

8.2.1.1 Graphite particle morphology

Changing particle morphology is an effective way to reduce the surface area of graphite.[216] The reduced surface area results in a low irreversible capacity and high CE. Yoshio et al. described a method of making spherical graphite from flaky graphite by impact milling, which greatly changes the particle morphology and reduces the surface area.[218] A proper method is required to convert catalytic graphite platelets into low-surface area particles (e.g. spheres).[222,223] This is important in future work if catalytic graphites were to be applied in Li batteries.

8.2.1.2 Carbon coating

Carbon coating is a vital step to ensure the good electrochemical performance of graphite,[216] probably because: (1) the SEI film formed on carbon-coated graphite is more compact and much thinner than that on bare graphite;[219–221] (2) the coated carbon layer suppresses many side reactions such as graphite exfoliation, electrolyte decomposition, and reduction of functional groups on graphite surface.[219] Therefore, it is important to apply a proper carbon-coating process to improve the electrochemical characteristics of catalytic graphites. For example, chemical and thermal vapor decomposition (CVD and TVD) may be promising methods as they have been the most widely used methods for carbon-coating on graphite.[218,220]

8.2.1.3 Mild oxidation

Catalytic graphites in this study were made at ~ 1000 °C. Carbon materials heated at ~ 1000 °C usually comprise non-negligible amounts of hydrogen.[224] During the lithiation process, Li can bind with H in an activated process, which causes hysteresis during cycling.[146] These Li-

H bonds are quasi-reversible and some of the bonds would not reform during the delithiation process, resulting in low CE.[146,224] A mild oxidation (e.g. burning in air) of graphite was found to reduce the irreversible capacity of graphite in Li cells.[205] During the mild oxidation process, C-H can be converted into COOH, C=O or C-OH, which irreversibly form COOLi or C-OLi during the lithiation process, becoming part of the solid electrolyte interphase (SEI) layer.[205] In this way, electrolyte decomposition is inhibited to some degree and the irreversible capacity is reduced.[205] In addition, some catalytic graphites comprise tiny particles on the graphite surface, which are less graphitic carbon. These tiny particles may significantly contribute to the irreversible capacity and reduce the reversible capacity in Li cell cycling. The less graphitic components have a lower burning point in air than the ordered graphite as been confirmed by the thermal gravimetric analysis. Therefore, a mild oxidation process may be a promising method to reduce irreversible capacity of catalytic graphites in future work. In the oxidation process, a proper temperature should be applied, or the irreversible capacity would be increased [204].

8.2.2 Reducing Mg amount

To make highly ordered graphite products, 50 at. % Mg was used in graphitization as introduced in Chapter 3 – 5. After adding a proper additive (e.g. $MgCl_2$), highly ordered graphite products were made with 30 at. % Mg. However, 30 at. % Mg is still too much. It is desirable to use less Mg (e.g. < 10 at. % or even < 5 at. %) in catalytic graphitization. This is a kinetic problem considering that highly ordered graphite can be made at 1000 °C, rather than a thermodynamic problem. Therefore, one should find a way to increase the reaction rate of the catalytic graphitization. Possible solutions include increasing the heating temperature (from 1000 °C to 1100 °C, 1200 °C or even higher) and extending heating duration (from 3 h to 5h, 10h or even longer). This has been shown to be effective in improving the graphitization level in Chapter 3 and 4. In addition, proper additives (e.g. $MgCl_2$) should also be used.

8.2.3 Other additives for Mg-catalyzed graphitization

Additives play an important role in influencing the catalytic graphitization mechanism, improving/reducing catalytic graphitization efficiency and modifying graphite particle morphology. Besides $MgCl_2$, LiCl, NaCl, and Al introduced in Chapter 7 and 8, other additives may also be useful. For example, Fitzer et al. found that natural graphite as an additive has a catalyzing effect on the crystalline ordering of the glasslike disordered carbon.[225] Stefanescu et al. found that Ca, Y and Lanthanides (Ce, La) favored the formation of spherical graphite particles.[132]

8.2.4 Materials recycling by catalytic graphitization

Human society produces a lot of carbon-containing solid waste. For example, millions of tires are discarded around the globe every year.[160] It is desirable to find a good way to recycle these materials, such as converting them into graphite. Various materials have been used as precursors in Mg catalyzed graphitization as described in Chapter 5, and many of them have been made into highly ordered graphite. However, there are many problems to overcome in order to make the catalytic graphitization applicable to the recycling process. Here only chemical processing will be considered. The first problem, as mentioned above, is that too much Mg was used in catalytic graphitization. A lower amount of Mg should be used to make the process scalable. The second problem is the low graphitization efficiency of some precursors. A better carbonization process is a possible solution to increase the graphitization efficiency of some precursors, as discussed in Chapter 5. For example, polyvinyl alcohol (PVA) is a graphitizable polymer. Highly ordered graphite has been made from a PVA/metal oxide mixture at 1200 °C.[81] It is possible that highly ordered graphite can be made from PVA by applying the Mg-catalyzed graphitization process with a modified carbonization method. A good carbonization method for PVA (or other precursors) is to convert it into a carbon comprising a high fraction of aromatic structures and parallel-layer groups. Methods that have been used to improve the carbonization process include using mixed precursors. For instance, in the industrial graphite synthesis process, coal tar pitch is used as a filler for petroleum coke during the carbonization process to densify the graphite product.[151] Sugii et al. also found that adding PVA to a carbonaceous gel improved the graphitization efficiency of the latter material.[226]

8.2.5 Mechanism of Mg catalyzed graphitization

In this work, it is believed that the mechanism of the Mg catalyzed graphitization is a combination of the dissolution-precipitation of carbon and the formation-decomposition of carbide. However, there is no direct evidence confirming the formation of magnesium carbide. Further work should be done to confirm the mechanism, for example, using in-situ XRD.

8.2.6 Oxygen content in carbon precursors

MgO impurities have been observed in many graphite/Mg mixtures after graphitization. There are two assumptions for the source of oxygen: oxygen impurity in carbon precursors and metal oxides in the inner surface of the heating tubes. Further work should be done to confirm the oxygen content in carbon precursors. This is very important because if carbon precursors still contain significant amounts of oxygen, Mg may preferentially react with the oxygen impurity, forming MgO and reducing the amount of effective Mg catalyst, leading to the reduction of graphitization efficiency.

8.2.7 Fe contamination

As is shown in Chapter 5, iron contaminants were detected by XRD in some catalytic graphites. Because iron is also an effective catalyst for graphitization, it is important to determine the Fe contamination content in the milled C/Mg before graphitization to estimate how much Fe contributes to the catalyzed graphitization process. It is also important to determine the Fe amount in the final graphite products.

8.2.8 Other Catalysts

Many other alkali metal and alkali earth metal elements were previously thought to be ineffective or inefficient graphitization catalysts. Using the Mg-catalyzed graphitization method introduced in this thesis, these elements (e.g. Na, Ca, Al) were found to be effective or highly-efficient graphitization catalysts.

8.3 Concluding remarks

Mg-catalyzed graphitization is a new method to make graphites from a variety of precursors. Many more graphites are likely to be discovered than shown in this thesis. Many more applications other than Li-ion batteries may be possible. This is a highly promising field for future work.

Reference

1. Hammond, C. R. Properties of the Elements and Inorganic Compounds. in *Handbook of Chemistry and Physics* (ed. Haynes, W. M.) 4–7 (CRC Press, 2014).
2. McEnaney, B. Structure and Bonding in Carbon Materials. in *Carbon Materials for Advanced Technologies* (ed. Burchell, T. D.) 1–34 (Elsevier, 1999).
3. Pierson, H. O. *Handbook of Carbon, Graphite, Diamond and Fullerenes: Properties, Processing and Applications*. (William Andrew, 1993).
4. Zondlo, J. W. Graphite: Structure, Properties, and Applications. in *Graphite, graphene and their polymer nanocomposites* (eds. Mukhopadhyay, P. & Gupta, R. K.) 2–56 (CRC Press, 2012).
5. Delhaes, P. Polymophism of Carbon. in *Graphite and Precursors* (ed. Delhaes, P.) 1–24 (Gordon and Breach Science Publishers, 2001).
6. Wyckoff, R. W. G. Structures of the Elements. in *Crystal Structures Volume I* (ed. Wyckoff, R. W. G.) 26–28 (Robert E. Krieger Publishing Company, Malabar, Florida, 1982).
7. Acheson, E. G. Manufacture of graphite. US Patent 568323. (1896).
8. Acheson, E. G. Method of Manufacturing Graphite Articles. US Patent 617979A. (1899).
9. Acheson, E. G. Process of making graphite. US Patent 711031A. (1902).
10. Nemeth, N. N. & Bratton, R. L. Statistical Models of Fracture Relevant to Nuclear-Grade Graphite: Review and Recommendations. (2011).
11. Oberlin, A. Carbonization and graphitization. *Carbon* **22**, 521–541 (1984).
12. Jenkins, G. & Kawamura, K. *Polymeric carbons carbon fibre, glass and char*. (Cambridge University Press, 1976).
13. Lewis, I. C. Chemistry of carbonization. *Carbon* **20**, 519–529 (1982).
14. Franklin, R. E. Crystallite growth in graphitizing and non-graphitizing carbons. *Proc. R. Soc. A* **209**, 196–218 (1951).
15. Oya, A. & Marsh, H. Phenomena of catalytic graphitization. *J. Mater. Sci.* **17**, 309–322 (1982).
16. Dahn, J. R., Xing, W. & Gao, Y. The ‘falling cards model’ for the structure of microporous carbons. *Carbon* **35**, 825–830 (1997).
17. Li, Z. Q., Lu, C. J., Xia, Z. P., Zhou, Y. & Luo, Z. X-ray diffraction patterns of graphite and turbostratic carbon. *Carbon* **45**, 1686–1695 (2007).
18. Marsh, H. & Warburton, A. P. Catalysis of graphitisation. *J. Chem. Technol. Biotechnol.* **20**, 133–142 (1970).

19. Fitzer, E. & Kegel, B. Reaktionen von Kohlenstoffgesättigter Vanadiumcarbidschmelze mit ungeordnetem Kohlenstoff (Beitrag zur katalytischen Graphitierung). *Carbon* **6**, 433–436 (1968).

20. Liu, Y. *et al.* Highly porous graphitic materials prepared by catalytic graphitization. *Carbon* **64**, 132–140 (2013).

21. Wang, R. *et al.* Catalytic effect of praseodymium oxide additive on the microstructure and electrical property of graphite anode. *Carbon* **95**, 940–948 (2015).

22. Niu, Y. *et al.* Catalytic and enhanced effects of silicon carbide nanoparticles on carbonization and graphitization of polyimide films. *RSC Adv.* **4**, 42569–42576 (2014).

23. Lin, Q., Feng, Z., Liu, Z., Guo, Q. & Hu, Z. Atomic scale investigations of catalyst and catalytic graphitization in a silicon and titanium doped graphite. *Carbon* **88**, 252–261 (2015).

24. Qiu, H., Song, Y., Liu, L., Zhai, G. & Shi, J. Thermal conductivity and microstructure of Ti-doped graphite. *Carbon* **41**, 973–978 (2003).

25. Oya, A. & Marsh, H. Phenomena of catalytic graphitization. *J. Mater. Sci.* **17**, 309–322 (1982).

26. Wang, X. *et al.* Graphitization of glassy carbon prepared under high temperatures and high pressures. *Carbon* **41**, 188–191 (2003).

27. Zhao, J. G., Li, F. Y. & Jin, C. Q. Graphitization of activated carbon under high pressures and high temperatures. *Solid State Commun.* **149**, 818–821 (2009).

28. Loh, G. C. & Baillargeat, D. Graphitization of amorphous carbon and its transformation pathways. *J. Appl. Phys.* **114**, 33534 (2013).

29. Ci, L. *et al.* Crystallization behavior of the amorphous carbon nanotubes prepared by the CVD method. *J. Cryst. Growth* **233**, 823–828 (2001).

30. Yoon, S. H. *et al.* Novel carbon nanofibers of high graphitization as anodic materials for lithium ion secondary batteries. *Carbon* **42**, 21–32 (2004).

31. Kim, T. *et al.* Facile conversion of activated carbon to battery anode material using microwave graphitization. *Carbon* **104**, 106–111 (2016).

32. Yang, K. S., Yoon, Y. J., Lee, M. S., Lee, W. J. & Kim, J. H. Further carbonization of anisotropic and isotropic pitch-based carbons by microwave irradiation. *Carbon* **40**, 897–903 (2002).

33. Peng, J. *et al.* Electrochemically Driven Transformation of Amorphous Carbons to Crystalline Graphite Nanoflakes : A Facile and Mild Graphitization Method. *Angew. Chem. Int. Ed.* **129**, 1777–1781 (2017).

34. Oya, A. & Otani, S. Catalytic of Carbons By Various Metals. *Carbon* **17**, 131–137 (1979).

35. Ishikawa, T., Magari, S., Mizutani, Y. & Yoshizawa, S. Catalyst on graphitization of Carbon (II). *TANSO* **42**, 7–12 (1965).

36. Xu, Z. *et al.* Graphitization of aerogel-like carbons in molten sodium metal. *Carbon* **49**, 3385–3387 (2011).

37. Xu, L., Wu, J. & Bai, S. Fabrication and microstructure of boron-doped isotropic pyrolytic carbon. *Carbon* **50**, 4705–4710 (2012).

38. Niu, Y., Zhang, X., Wu, J., Zhao, J. & Li, Y. Catalytic and enhanced effects of silicon carbide nanoparticles on carbonization and graphitization of polyimide films. *RSC Adv.* **4**, 42569–42576 (2014).

39. Nishimiya, K., Hata, T. & Kikuchi, H. Effect of aluminum compound addition on graphitization of wood charcoal by direct electric pulse heating method. 177–181 (2004). doi:10.1007/s10086-003-0532-z

40. Yang, G., Han, H., Li, T. & Du, C. Synthesis of nitrogen-doped porous graphitic carbons using nano-CaCO3 as template, graphitization catalyst, and activating agent. *Carbon* **50**, 3753–3765 (2012).

41. Murty, H. N., Biederman, D. L. & Heintz, E. A. Catalytic graphitization of model compound chars by aluminum and beryllium. *Carbon* **11**, 163–169 (1973).

42. Jones, L. E. & Thrower, P. A. Influence of boron on carbon fiber microstructure, physical properties, and oxidation behavior. *Carbon* **29**, 251–269 (1991).

43. Wen, Y., Lu, Y., Xiao, H. & Qin, X. Further investigation on boric acid catalytic graphitization of polyacrylonitrile carbon fibers: Mechanism and mechanical properties. *Mater. Des.* **36**, 728–734 (2012).

44. Xu, Z., Cai, D., Hu, Z., Wang, F. & Gan, L. The structural optimization and high electrochemical behavior of porous carbons by graphitization in molten sodium metals. *Electrochim. Acta* **117**, 486–491 (2014).

45. Lee, Y., Mori, T., Yamamoto, S. & Kawano, Y. Influences of Mg, S and Graphitization Rate on the Spheroidization of Graphite. *J. Jpn. Inst. Met.* **48**, 1047–1052 (1984).

46. Okamoto, T., Huang, X. & Kagawa, A. Graphite nodularization and graphitization of magnesium treated cast irons solidified under argon atmosphere pressure up to 145 atm. *Met. Sci.* **18**, 169–176 (1984).

47. Minrale, L. D. P., Cnrs, U. R. A., Claude, U., Lyon, B. & Cedex, V. Effect of magnesium on the composition , microstructure and mechanical properties of carbon fibres. *J. Mater. Sci.* **26**, 4977–4984 (1991).

48. Qiu, H., Han, L. & Liu, L. Properties and microstructure of graphitised ZrC/C or SiC/C composites. *Carbon* **43**, 1021–1025 (2005).

49. Imamura, R., Matsui, K., Takeda, S., Ozaki, J. & Oya, a. A new role for phosphorus in graphitization of phenolic resin. *Carbon* **37**, 261–267 (1999).

50. Sugimoto, Y., Derbyshire, F. J. & Scaroni, A. W. The effect of sulfur evolution on the properties of high-temperature carbons—I. Thianthrene and thianthrene-anthracene precursors. *Carbon* **23**, 411–416 (1985).

51. Rümmeli, M. H. *et al.* On the graphitization nature of oxides for the formation of carbon nanostructures. *Chem. Mater.* **19**, 4105–4107 (2007).

52. Zhang, B. *et al.* Transformation of Lewis acid during the carbonization and graphitization of mesophase pitches. *J. Anal. Appl. Pyrolysis* **104**, 433–440 (2013).

53. Hu, X. Bin, Cheng, G., Zhao, B. Y., Wang, H. M. & Hu, K. A. Catalytic effect of dopants on microstructure and performance of MCMB-derived carbon laminations. *Carbon* **42**, 381–386 (2004).

54. Tang, K. *et al.* Integrated electrospun carbon nanofibers with vanadium and single-walled carbon nanotubes through covalent bonds for high-performance supercapacitors. *RSC Adv.* **5**, 40163–40172 (2015).

55. Sinclair, R., Itoh, T. & Chin, R. In situ TEM studies of metal–carbon reactions. Microscopy and Microanalysis. *Microsc. Microanal.* **8**, 288–304 (2002).

56. Sevilla, M. & Fuertes, A. B. Catalytic graphitization of templated mesoporous carbons. *Carbon* **44**, 468–474 (2006).

57. Zhao, X., Yao, Y., George, A. E., Dunlap, R. A. & Obrovac, M. N. Electrochemistry of Catalytically Graphitized Ball Milled Carbon in Li Batteries. *J. Electrochem. Soc.* **163**, A858–A866 (2016).

58. Obrovac, M. N., Zhao, X., Burke, L. T. & Dunlap, R. A. Reversible lithium insertion in catalytically graphitized sugar carbon. *Electrochem. Commun.* **60**, 221–224 (2015).

59. Skowroński, J. M. & Knofczyński, K. Catalytically graphitized glass-like carbon examined as anode for lithium-ion cell performing at high charge/discharge rates. *J. Power Sources* **194**, 81–87 (2009).

60. Skowroński, J. M., Knofczyński, K. & Inagaki, M. Changes in electrochemical insertion of lithium into glass-like carbon affected by catalytic graphitization at 1000 °C. *Solid State Ionics* **178**, 137–144 (2007).

61. Skowroński, J. M. & Knofczyński, K. New anode material for lithium-ion cells produced by catalytic graphitization of glassy carbon at 1000°C. *J. New Mater. Electrochem. Syst.* **9**, 359–365 (2006).

62. Lee, Y. H. *et al.* Graphite with fullerene and filamentous carbon structures formed from iron melt as a lithium-intercalating anode. *Mater. Lett.* **57**, 1113–1119 (2003).

63. Sajitha, E. P. *et al.* Synthesis and characteristics of iron nanoparticles in a carbon matrix along with the catalytic graphitization of amorphous carbon. *Carbon* **42**, 2815–2820 (2004).

64. Marshall, C. P. & Wilson, M. A. Ball milling and annealing graphite in the presence of cobalt. *Carbon* **42**, 2179–2186 (2004).

65. Iwazaki, T. *et al.* Catalytic Excavation and Graphitization of Activated Carbon by Cobalt Nanoparticles. *Chem. Lett.* **37**, 1194–1195 (2008).

66. Narkiewicz, U., Podsiadły, M., Jędrzejewski, R. & Pełech, I. Catalytic decomposition of hydrocarbons on cobalt, nickel and iron catalysts to obtain carbon nanomaterials. *Appl. Catal., A* **384**, 27–35 (2010).

67. Kodama, Y. *et al.* Electron microscope study of the formation of graphitic nanostructures in nickel-loaded wood char. *Carbon* **50**, 3486–3496 (2012).

68. Lamber, R., Jaeger, N. & Schulz-Ekloff, G. Electron microscopy study of the interaction of Ni, Pd and Pt with carbon. I. Nickel catalyzed graphitization of amorphous carbon. *Surf. Sci.* **197**, 402–414 (1988).

69. Wang, L., Yue, X., Zhang, F. & Zhang, R. Effect of additional nickel on crystallization degree evolution of expanded graphite during ball-milling and annealing. *J. Alloy. Compd.* **497**, 344–348 (2010).

70. Khosh, M. S., Xu, X. & Trumbore, S. E. Nuclear Instruments and Methods in Physics Research B Small-mass graphite preparation by sealed tube zinc reduction method for AMS 14 C measurements. *Nucl. Inst. Methods Phys. Res. B* **268**, 927–930 (2010).

71. Tang, J. *et al.* Effect of transition metal on catalytic graphitization of ordered mesoporous carbon and Pt/metal oxide synergistic electrocatalytic performance. *Microporous Mesoporous Mater.* **177**, 105–112 (2013).

72. Yan, Z., Zhang, M., Xie, J. & Shen, P. K. Vanadium carbide and graphite promoted Pd electrocatalyst for ethanol oxidation in alkaline media. *J. Power Sources* **243**, 336–342 (2013).

73. Maldonado-Hódar, F. J., Moreno-Castilla, C., Rivera-Utrilla, J., Hanzawa, Y. & Yamada, Y. Catalytic graphitization of carbon aerogels by transition metals. *Langmuir* **16**, 4367–4373 (2000).

74. Kakunuri, M., Kali, S. & Sharma, C. S. Catalytic graphitization of resorcinol-formaldehyde xerogel and its effect on lithium ion intercalation. *J. Anal. Appl. Pyrolysis* **117**, 317–324 (2016).

75. Wu, F., Huang, R., Mu, D., Wu, B. & Chen, Y. Controlled synthesis of graphitic carbon-encapsulated α-Fe 2 O 3 nanocomposite via low-temperature catalytic graphitization of biomass and its lithium storage property. *Electrochim. Acta* **187**, 508–516 (2016).

76. Nettelroth, D., Schwarz, H. C., Burblies, N., Guschanski, N. & Behrens, P. Catalytic graphitization of ordered mesoporous carbon CMK-3 with iron oxide catalysts: Evaluation of different synthesis pathways. *Phys. Status Solidi A* **213**, 1395–1402 (2016).

77. Zhao, M. & Song, H. Catalytic Graphitization of Phenolic Resin. *J. Mater. Sci. Technol.* **27**, 266–270 (2011).

78. Konno, H., Fujita, K., Habazaki, H. & Inagaki, M. Graphite Formation at 1150-1200° C from Hard-carbon Precursors and Magnetite. *tanso* **203**, 113–116 (2002).

79. Wang, Y. G. *et al.* Modification of synthetic mesophase pitch with iron oxide, Fe2O3. *Carbon* **39**, 1627–1634 (2001).

80. Kim, J., Lee, J., Choi, Y. & Jo, C. Synthesis of hierarchical linearly assembled graphitic carbon nanoparticles via catalytic graphitization in SBA-15. *Carbon* **75**, 95–103 (2014).

81. Inagaki, M. *et al.* Formation of graphite crystals at 1000–1200 C from mixtures of vinyl polymers with metal oxides. *Carbon* **39**, 921–929 (2001).

82. Käärik, M., Arulepp, M., Karelson, M. & Leis, J. The effect of graphitization catalyst on the structure and porosity of SiC derived carbons. *Carbon* **46**, 1579–1587 (2008).

83. Sevilla, M. & Fuertes, A. B. Graphitic carbon nanostructures from cellulose. *Chem. Phys. Lett.* **490**, 63–68 (2010).

84. Tang, J. *et al.* Bimetallic Metal-Organic Frameworks for Controlled Catalytic Graphitization of Nanoporous Carbons. *Sci. Rep.* **6**, 30295 (2016).

85. Li, W. Q., Zhang, H. B., Xiong, X. & Xiao, F. Effect of zirconium addition on the microstructure and performance of carbon foam. *Mater. Sci. Eng. A* **527**, 2993–2997 (2010).

86. Xue, G. & Structures, C. SERS studies of polymers on metal surfaces. 4. Cyclization and graphitization of polyacrylonitrile on rough silver surfaces. *Macromolecules* **25**, 5855–5857 (1992).

87. Chen, Z., Wu, W., Chen, Z., Cong, X. & Qiu, J. Microstructural characterization on ZrC doped carbon/carbon composites. *Ceram. Int.* **38**, 761–767 (2012).

88. Liu, M. *et al.* A facile synthesis of highly compacted , molybdenum-embedded , ordered , mesoporous , protective carbon films of graphitic structure. *Corros. Sci.* **87**, 297–305 (2014).

89. Wang, R., Lu, G., Zhuang, H. & Yu, J. Synergistic catalytic effect of light rare earth element and other additives on the degree of graphitization and properties of graphite. *J. Mater. Sci.* **52**, 663–673 (2017).

90. YI, S., CHEN, J., XIAO, X., LIU, L. & FAN, Z. Effect of praseodymium on catalytic graphitization of furan resin carbon. *J. Rare Earths* **28**, 69–71 (2010).

91. Zhang, C., Lu, G., Sun, Z. & Yu, J. Catalytic graphitization of carbon / carbon composites by lanthanum oxide. *J Rare Earths* **30**, 128–132 (2012).

92. Zhou, H. H. *et al.* Catalytic graphitization of PAN-based carbon fibers with electrodeposited Ni-Fe alloy. *Trans. Nonferrous Met. Soc. China* **21**, 581–587 (2011).

93. Yang, Y., Liu, X., Guo, X., Wen, H. & Xu, B. Synthesis of nano onion-like fullerenes by chemical vapor deposition using an iron catalyst supported on sodium chloride. *J. Nanoparticle Res.* **13**, 1979–1986 (2011).

94. Xu, Z., Cai, D., Hu, Z. & Gan, L. A combination of porous and crystalline characters in carbon aerogels by a synergistic graphitization. *Microporous Mesoporous Mater.* **195**, 36–42 (2014).

95. Zhai, D., Du, H., Li, B., Zhu, Y. & Kang, F. Porous graphitic carbons prepared by combining chemical activation with catalytic graphitization. *Carbon* **49**, 725–729 (2011).

96. Avdeeva, L. B. *et al.* Coprecipitated Ni-alumina and Ni-Cu-alumina catalysts of methane decomposition and carbon deposition. II. Evolution of the catalysts in reaction. *Appl. Catal. A Gen.* **141**, 117–129 (1996).

97. Tzeng, S. Catalytic graphitization of electroless Ni – P coated PAN-based carbon fibers. *Carbon* **44**, 1986–1993 (2006).

98. Yoshio, M., Brodd, R. J. & Kozawa, A. *Lithium-ion batteries*. (Springer, 2009).

99. Yoshino, A. Development of the Lithium-Ion Battery and Recent Technological Trends. in *Lithium-ion batteries: advances and applications* (ed. Pistoia, G.) 2–19 (Newnes, 2013).

100. Obrovac, M. N. & Chevrier, V. L. Alloy negative electrodes for Li-ion batteries. *Chem. Rev.* **114**, 11444–11502 (2014).

101. Dresselhaus, M. & Dresselhaus, G. Intercalation Compounds of Graphite. *Adv. Phys.* **30**, 139–326 (1981).

102. Kirczenow, G. Staging and Kinetics. in *Graphite Intercalation Compounds I: Structure and Dynamics* (eds. Zabel, H. & Solin, S. A.) 59–100 (Springer-Verlag Berlin Heidelberg, 1991).

103. Dahn, J. R. Phase diagram of LixC6. *Phys. Rev. B* **44**, 9170–9177 (1991).

104. Zheng, T. & Dahn, J. R. The effect of turbostratic disorder on the staging transitions in lithium intercalated graphite. *Synth. Met.* **73**, 1–7 (1995).

105. Zheng, T., Reimers, J. N. & Dahn, J. R. Effect of turbostratic disorder in graphitic carbon hosts on the intercalation of lithium. *Phys. Rev. B* **51**, 734–741 (1995).

106. Weisweiler, W., Subramanian, N. & Terwiesch, B. Catalytic influence of metal melts on the graphitization of monolithic glasslike carbon. *Carbon* **9**, (1971).

107. Cullity, B. D. *Elements of X-ray Diffraction*. (Addison-Wesley Publishing, 1956).

108. Warren, B. E. *X-ray diffraction*. (Courier Corporation, 1969).

109. Waseda, Y., Matsubara, E. & Shinoda, K. *X-Ray Diffraction Crystallography Introduction, Examples and Solved Problems*. (Springer Science & Business Media, 2011).

110. Fujimoto, H. Theoretical X-ray scattering intensity of carbons with turbostratic stacking and AB stacking structures. *Carbon* **41**, 1585–1592 (2003).

111. Shi, H. Disordered carbons and battery applications. (Simon Fraser University, 1993).

112. Shi, H., Reimers, J. N. & Dahn, J. R. Structure-refinement program for disordered carbons. *J. Appl. Crystallogr.* **26**, 827–836 (1993).

113. Reichelt, R. Scanning electron microscopy. in *Science of microscopy* 133–272 (Springer New York, 2007).

114. Reimer, L. *Scanning Electron Microscopy: Physics of Image Formation*. (Springer, 1998).

115. Brundle, C. R. & Evans, C. A. *Encyclopedia of materials characterization: surfaces, interfaces, thin films*. (Gulf Professional Publishing, 1992).

116. Bell, D. C. & Garratt-Reed, A. J. *Energy-Dispersive X-Ray Analysis in the Electron Microscope*. **49**, (Garland Science, 2003).

117. *Introduction to focused ion beams: instrumentation, theory, techniques and practice*. (Springer Science & Business Media, 2006).

118. Reimer, L. *Transmission electron microscopy: physics of image formation and microanalysis*. **36**, (Springer, 2013).

119. Long, D. A. *The Raman effect: a unified treatment of the theory of Raman scattering by molecules*. (West Sussex, 2002). doi:10.1002/0470845767

120. Ferrari, A. C. Raman spectroscopy of graphene and graphite: Disorder, electron-phonon coupling, doping and nonadiabatic effects. *Solid State Commun.* **143**, 47–57 (2007).

121. Dean, J. R. *Practical Inductively Coupled Plasma Spectroscopy Analytical Techniques*. (John Wiley & Sons, 2005).

122. Boss, C. B. & Fredeen, K. J. *Concepts, instrumentation and techniques in inductively coupled plasma optical emission spectrometry*. (Norwalk: Perkin Elmer, 1999).

123. *Progress in filtration and separation*. (Academic Press, 2014).

124. Fagerlund, G. Determination of specific surface by the BET method. *Mater. Struct.* **6**, 239–245 (1973).

125. Marks, T., Trussler, S., Smith, A. J., Xiong, D. & Dahn, J. R. A Guide to Li-Ion Coin-Cell Electrode Making for Academic Researchers. *J. Electrochem. Soc.* **158**, A51 (2011).

126. Double, D. D. & Hellawell, A. The structure of flake graphite in Ni-C eutectic alloy. *Acta Metall.* **17**, 1071–1083 (1969).

127. Reich, S. & Thomsen, C. Raman spectroscopy of graphite. *Philos. Trans. R. Soc. A Math. Phys. Eng. Sci.* **362**, 2271–2288 (2004).

128. Wang, Y., Alsmeyer, D. C. & Mccreery, R. L. Raman Spectroscopy of Carbon Materials: Structural Basis of Observed Spectra. *Carbon* 557–563 (1990). doi:10.1021/cm00011a018

129. Tuinstra, F. & Koenig, J. L. Raman Spectrum of Graphite. *J. Chem. Phys.* **53**, 1126–1130 (1970).

130. Velichko, A., Holzapfel, C., Siefers, A., Schladitz, K. & Mücklich, F. Unambiguous classification of complex microstructures by their three-dimensional parameters applied to graphite in cast iron. *Acta Mater.* **56**, 1981–1990 (2008).

131. Theuwissen, K., Lacaze, J. & Laffont, L. Structure of graphite precipitates in cast iron. *Carbon* **96**, 1120–1128 (2016).

132. Stefanescu, D. M., Alonso, G., Larrañaga, P., De La Fuente, E. & Suarez, R. On the crystallization of graphite from liquid iron-carbon-silicon melts. *Acta Mater.* **107**, 102–126 (2016).

133. Oberlin, A. & Rouchy, J. P. Transformation des carbones non graphitables par traitement thermique en presence de fer. *Carbon* **9**, (1971).

134. Gornostayev, S. S. & Härkki, J. J. Graphite crystals in blast furnace coke. *Carbon* **45**, 1145–1151 (2007).

135. Zhao, L. *et al.* Voronoi-Tessellated Graphite Produced by Low-Temperature Catalytic Graphitization from Renewable Resources. *ChemSusChem* **10**, 1–11 (2017).

136. Zhang, H. L., Li, F., Liu, C. & Cheng, H. M. Poly (vinyl chloride)(PVC) coated idea revisited: Influence of carbonization procedures on PVC-coated natural graphite as anode materials for lithium ion batteries. *J. Phys. Chem. C* **112**, 7767–7772 (2008).

137. Amini, S. & Abbaschian, R. Nucleation and growth kinetics of graphene layers from a molten phase. *Carbon* **51**, 110–123 (2013).

138. Zaghib, K., Nadeau, G. & Kinoshita, K. Effect of Graphite Particle Size on Irreversible Capacity Loss. *J. Electrochem. Soc.* **147**, 2110–2115 (2000).

139. Chung, G., Jun, S., Lee, K. & Kim, M. Effect of surface structure on the irreversible capacity of various graphitic carbon electrodes. *J. Electrochem. Soc.* **146**, 1664–1671 (1999).

140. Shornikova, O. N., Kogan, E. V., Sorokina, N. E. & Avdeev, V. V. The specific surface area and porous structure of graphite materials. *Russ. J. Phys. Chem. A* **83**, 1022–1025 (2009).

141. Zheng, T. & Dahn, J. Effect of turbostratic disorder on the staging phase diagram of lithium-intercalated graphitic carbon hosts. *Phys. Rev. B* **53**, 3061–3071 (1996).

142. Cuesta, A., Dhamelincourt, P., Laureyns, J., Martínez-Alonso, A. & Tascón, J. M. D. Raman microprobe studies on carbon materials. *Carbon* **32**, 1523–1532 (1994).

143. Dahn, J. R. *et al.* Dependence of the electrochemical intercalation of lithium in carbons on the crystal structure of the carbon. *Electrochim. Acta* **38**, 1179–1191 (1993).

144. Zheng, T. *et al.* Lithium Insertion in High Capacity Carbonaceous Materials. **142**, (1995).

145. Dahn, J. R., Fong, R. & Spoon, M. J. Suppression of staging in lithium-intercalated carbon by disorder in the host. *Phys. Rev. B* **42**, 6424–6432 (1990).

146. Dahn, J. R., Zheng, T., Liu, Y. & Xue, J. S. Mechanisms for Lithium Insertion in Carbonaceous Materials. *Science (80-.).* **270**, 590–593 (1995).

147. Osetzky, D. Macrocrystalline graphite from magnesium carbide. *Carbon* **12**, 517–523 (1974).

148. Chen, H., Li, N. & Schmid-fetzer, R. Measurement of carbon solubility in magnesium alloys using GD-OES. *J. Anal. At. Spectrom.* **26**, 2189–2196 (2011).

149. Chen, H.-L. & Schmid-fetzer, R. The Mg–C phase equilibria and their thermodynamic basis. *Int. J. Mater. Res.* **103**, 1294–1301 (2012).

150. Boehm, H. P. Formation of well-crystallized graphite in the calcium cyanamide process. *Carbon* **16**, 385–387 (1978).

151. Pierson, H. O. *Handbook of carbon, graphite, diamonds and fullerenes: processing, properties and applications*. (William Andrew, 2012).

152. Engle, G. B. Low-temperature graphitization of cokes and binder-filler artifacts. *Carbon* **10**, 409–415 (1972).

153. Parker, W. E., Marek, R. W. & Woodruff, E. M. Use of additives for graphite densification and improved neutron radiation stability. *Carbon* **2**, 395–406 (1965).

154. Liu, L. *et al.* A facile novel preparation of three-dimensional Ni@graphene by catalyzed glucose blowing for high-performance supercapacitor electrodes. *RSC Adv.* **5**, 74463–74466 (2015).

155. Lei, H. *et al.* Graphene-like carbon nanosheets prepared by a Fe-catalyzed glucose-blowing method for capacitive deionization. *J. Mater. Chem. A* **3**, 5934–5941 (2015).

156. Zhao, L., Bennett, J. C. & Obrovac, M. N. Hexagonal platelet graphite and its application in Li-ion batteries. *Carbon* **134**, 507–518 (2018).

157. Zhao, X., Yao, Y., George, A. E., Dunlap, R. A. & Obrovac, M. N. Electrochemistry of Catalytically Graphitized Ball Milled Carbon in Li Batteries. *J. Electrochem. Soc.* **163**, A858–A866 (2016).

158. Ramarad, S., Khalid, M., Ratnam, C. T., Chuah, A. L. & Rashmi, W. Waste tire rubber in polymer blends: A review on the evolution, properties and future. *Prog. Mater. Sci.* **72**, 100–140 (2015).

159. Konar, B. B., Roy, S. K. & Pariya, T. K. Study on the effect of nano and active particles of alumina on natural rubber-alumina composites in the presence of epoxidized natural rubber as compatibilizer. *J. Macromol. Sci. Part A Pure Appl. Chem.* **47**, 416–422 (2010).

160. Van Beukering, P. J. H. & Janssen, M. A. Trade and recycling of used tyres in Western and Eastern Europe. *Resour. Conserv. Recycl.* **33**, 235–265 (2001).

161. Gnanaraj, J. *et al.* Sustainable Waste Tire Derived Carbon Material as a Potential Anode for Lithium-Ion Batteries. *Sustainability* **10**, 2840 (2018).

162. Aykut, Y., Pourdeyhimi, B. & Khan, S. A. Catalytic graphitization and formation of macroporous-activated carbon nanofibers from salt-induced and H2S-treated polyacrylonitrile. *J. Mater. Sci.* **48**, 7783–7790 (2013).

163. Dumanli, A. G. & Windle, A. H. Carbon fibres from cellulosic precursors: A review. *J. Mater. Sci.* **47**, 4236–4250 (2012).

164. Wu, F., Huang, R., Mu, D., Wu, B. & Chen, Y. Controlled synthesis of graphitic carbon-encapsulated α-Fe2O3nanocomposite via low-temperature catalytic graphitization of biomass and its lithium storage property. *Electrochim. Acta* **187**, 508–516 (2016).

165. Kim, D.-Y., Nishiyama, Y., Wada, M. & Kuga, S. Graphitization of highly crystalline cellulose. *Carbon* **39**, 1051–1056 (2001).

166. Sevilla, M. & Fuertes, A. B. Graphitic carbon nanostructures from cellulose. *Chem. Phys. Lett.* **490**, 63–68 (2010).

167. Inagaki, M., Okada, Y., Miura, H. & Konno, H. Preparation of carbon-coated transition metal particles from mixtures of metal oxide and polyvinylchloride. *Carbon* **37**, 329–334 (1999).

168. Ōya, A. & Ōtani, S. Influences of particle size of metal on catalytic graphitization of non-graphitizing carbons. *Carbon* **19**, 391–400 (1981).

169. Zhao, M. & Song, H. Catalytic Graphitization of Phenolic Resin. *J. Mater. Sci. Technol.* **27**, 266–270 (2011).

170. Zhao, M., Song, H., Chen, X. & Lian, W. Large-scale synthesis of onion-like carbon nanoparticles by carbonization of phenolic resin. *Acta Mater.* **55**, 6144–6150 (2007).

171. Zhen-hua, H., Hai-hui, Z. & Qi-ling, P. Catalytic graphitization of polyacrylonitrile (PAN) -based carbon fibers with. *Trans. Nonferrous Met. Soc. China* **20**, 1418–1423 (2009).

172. Rahaman, M. S. A., Ismail, A. F. & Mustafa, A. A review of heat treatment on polyacrylonitrile fiber. *Polym. Degrad. Stab.* **92**, 1421–1432 (2007).

173. Nataraj, S. K., Yang, K. S. & Aminabhavi, T. M. Polyacrylonitrile-based nanofibers - A state-of-the-art review. *Prog. Polym. Sci.* **37**, 487–513 (2012).

174. Singh, S., Wu, C. & Williams, P. T. Pyrolysis of waste materials using TGA-MS and TGA-FTIR as complementary characterisation techniques. *J. Anal. Appl. Pyrolysis* **94**, 99–107 (2012).

175. Lin, J. M. & Ma, C. C. M. Thermal degradation of phenolic resin/silica hybrid ceramers. *Polym. Degrad. Stab.* **69**, 229–235 (2000).

176. Peng, Z. & Kong, L. X. A thermal degradation mechanism of polyvinyl alcohol/silica nanocomposites. *Polym. Degrad. Stab.* **92**, 1061–1071 (2007).

177. Dubinsky, S., Grader, G. S., Shter, G. E. & Silverstein, M. S. Thermal degradation of poly(acrylic acid) containing copper nitrate. *Polym. Degrad. Stab.* **86**, 171–178 (2004).

178. Ge, J. J. *et al.* Assembly of well-aligned multiwalled carbon nanotubes in confined polyacrylonitrile environments: Electrospun composite nanofiber sheets. *J. Am. Chem. Soc.* **126**, 15754–15761 (2004).

179. Donnet, J.-B. Black and White Fillers and Tire Compound. *Rubber Chem. Technol.* **71**, 323–341 (1998).

180. Suryanarayana, C. Mechanical alloying and milling. *Prog. Mater. Sci.* **46**, 1–184 (2001).

181. Coronado, J. J. Effect of (Fe,Cr)7C3 carbide orientation on abrasion wear resistance and fracture toughness. *Wear* **270**, 287–293 (2011).

182. Liu, S. & Loper, C. R. Kish, a source of crystalline graphite. *Carbon* **29**, 1119–1124 (1991).

183. Stefanescu, D. M., Alonso, G., Larrañaga, P. & Suarez, R. On the stable eutectic solidification of iron-carbon-silicon alloys. *Acta Mater.* **103**, 103–114 (2016).

184. Roviglione, A. N. & Hermida, J. D. From flake to nodular: A new theory of morphological modification in gray cast iron. *Metall. Mater. Trans. B Process Metall. Mater. Process. Sci.* **35**, 313–330 (2004).

185. Lux, B., Minkoff, F. & Thury, E. Branching of graphite crystals growing from a metallic solution. in *Proceedings of the second international symposium on the metallurgy of cast iron* (eds. Lux, B., Minkoff, I. & Mollard, F.) 495–508 (Georgi Publishing, Switzerland, 1976).

186. Saratovkin, D. D. *Dendritic Crystallization*. (Consultants Bureau, New York, 1959).

187. McSwain, R. H. & Bates, C. E. Surface and interfacial energy relationships controlling graphite formation. in *The Metallurgy of Cast Iron* (eds. Lux, B., Minkoff, I. & Mollard, F.) 423–442 (Georgi Publishing Co., St Saphorin, Switzerland, 1976).

188. Sodocha, J. P. & Gruzleski, J. E. The mechanism of graphite spheroid formation in pure Fe-C-Si alloys, in: B. Lux, I. Minkoff, F. Mollard (Eds.), The Metallurgy of Cast Iron, Georgi Publishing Co., St. Saphorin, Switzerland, 1974, pp. pp.443e459. in *The Metallurgy of Cast Iron* (eds. Lux, B., Minkoff, I. & Mollard, F.) 443–459 (Georgi Publishing Co., St Saphorin, Switzerland, 1976).

189. Muhmond, H. M. & Fredriksson, H. Relationship Between the Trace Elements and Graphite Growth Morphologies in Cast Iron. *Metall. Mater. Trans. A Phys. Metall. Mater. Sci.* **45**, 6187–6199 (2014).

190. Double, D. D. & Hellawell, A. The Nucleation and Growth of Graphite - The Modification of Cast Iron. *Acta Metall. Mater.* **43**, 2435–2442 (1995).

191. Double, D. D. & Hellawell, A. Growth structure of vatious forms of graphite. in *The Metallurgy of Cast Iron* (eds. Lux, B., Minkoff, I. & Mollard, F.) 509–528 (Georgi Publishing Co., St Saphorin, Switzerland, 1975).

192. Bollmann, W. & Lux, B. Grain boundaries in graphite. in *The Metallurgy of Cast Iron* (eds. Lux, B., Minkoff, I. & Mollard, F.) 461–470 (Georgi Publishing Co., St Saphorin, Switzerland, 1975).

193. Chen, Y. *et al.* Hollow-tunneled graphitic carbon nanofibers through Ni-diffusion-induced graphitization as high-performance anode materials. *Energy Environ. Sci.* 2689–2696 (2014). doi:10.1039/c4ee00148f

194. Osetzky, D. Macrocrystalline graphite from magnesium carbide. *Carbon* **12**, 517–523 (1974).

195. Otani, S. & Oya, A. Effects of FeCl3 on the Graphitizability of Coal Tar Pitch. *Bull. Chem. Soc. Jpn.* **45**, 623–624 (1972).

196. Otani, S. & Oya, A. Effect of AlCl3 on graphitizability. 1. Effect of AlCl3 on graphitibility of coal tar pitch. *Kog Kagaku Zasshi* **73**, 1110 (1970).

197. Hatori, H. *et al.* Carbonization behavior of polyimide containing nickel compounds. *Tanso* **189**, 165–170 (1999).

198. Rufford, T. E., Hulicova-Jurcakova, D., Zhu, Z. & Lu, G. Q. A comparative study of chemical treatment by FeCl3, MgCl 2, and ZnCl2on microstructure, surface chemistry, and double-layer capacitance of carbons from waste biomass. *J. Mater. Res.* **25**, 1451–1459 (2010).

199. Shi, R. *et al.* NaCl-templated synthesis of hierarchical porous carbon with extremely large specific surface area and improved graphitization degree for high energy density lithium ion capacitors. *J. Mater. Chem. A* (2018). doi:10.1039/C8TA05853A

200. Kamali, A. R. & Fray, D. J. Towards large scale preparation of carbon nanostructures in molten LiCl. *Carbon* **77**, 835–845 (2014).

201. Sherby, O. D., Kum, D. W., Oyama, T. & Wadsworth, J. Ultrahigh carbon steels containing aluminum. (1988).

202. R. & Fong, J. R. D. Studies of Lithium Intercalation into Carbons Using Nonaqueous Electrochemical Cells. *J. Electrochem. Soc.* **137**, 2009–2013 (1990).

203. Winter, M., Novák, P. & Monnier, A. Graphites for Lithium-Ion Cells: The Correlation of the First-Cycle Charge Loss with the Brunauer-Emmett-Teller Surface Area. *J. Electrochem. Soc.* **145**, 428–436 (1998).

204. Suzuki, K. Effect of Graphite Surface Structure on Initial Irreversible Reaction in Graphite Anodes. *J. Electrochem. Soc.* **146**, 890 (1999).

205. Peled, E. Improved Graphite Anode for Lithium-Ion Batteries Chemically. *J. Electrochem. Soc.* **143**, L4 (1996).

206. Fujimoto, H., Mabuchi, A., Tokumitsu, K. & Kasuh, T. Irreversible capacity of lithium secondary battery using meso-carbon micro beads as anode material. *J. Power Sources* **54**, 440–443 (1995).

207. Venugopalan, D. A kinetic model of the γ→ α+ Gr eutectoid transformation in spheroidal graphite cast irons. *Metall. Trans. A* **21**, 913–918 (1990).

208. Monchoux, J., Verdu, C., Thollet, G., Fouge, R. & Reynaud, A. Morphological changes of graphite spheroids during heat treatment of ductile cast irons. *Acta Mater.* **49**, 4355–4362 (2001).

209. Hunter, M. J. & Chadwick, G. Nucleation and growth of spheroidal graphite alloys. *J. Iron Steel Inst.* **210**, 707–717 (1972).

210. Hellawell, A. & Wilkinson, M. P. Directional Freezing of Eutectic Alloys Containing Graphite. *J. Iron Steel Insts* **203**, 834–835 (1965).

211. Banerjee, S. A review of the formation of spheroidal graphite in cast iron. *BRIT Foundrym.* **58**, 344–353 (1965).

212. Sundermeyer, W. Fused salts and their use as reaction media. *Angew. Chemie Int. Ed. English* **4**, 222–238 (1965).

213. Peteves, S. D. & Abbaschian, R. Growth kinetics of solid-liquid Ga interfaces: Part I. Experimental. *Metall. Trans. A* **22**, 1259–1270 (1991).

214. Peteves, S. D. & Abbaschian, R. Growth kinetics of solid-liquid Ga interfaces: Part II. Theoretical. *Metall. Trans. A* **22**, 1271–1286 (1991).

215. Abbaschian, R. & Reed-Hill, R. E. *Physical metallurgy principles*. (Cengage Learning, 2008).

216. Schmuch, R., Wagner, R., Hörpel, G., Placke, T. & Winter, M. Performance and cost of materials for lithium-based rechargeable automotive batteries. *Nat. Energy* **3**, 267–278 (2018).

217. Lämmerer, W. & Flachberger, H. Wissenswertes zur Charakterisierung und Aufbereitung von Rohgrafiten. *BHM Berg- und Hüttenmännische Monatshefte* **162**, 336–344 (2017).

218. Yoshio, M. *et al.* Improvement of natural graphite as a lithium-ion battery anode material, from raw flake to carbon-coated sphereElectronic supplementary information (ESI) available: colour versions of Figs. 6, 8 and 9. See http://www.rsc.org/suppdata/jm/b3/b316702j/. *J. Mater. Chem.* **14**, 1754 (2004).

219. Li, H. & Zhou, H. Enhancing the performances of Li-ion batteries by carbon-coating: Present and future. *Chem. Commun.* **48**, 1201–1217 (2012).

220. Natarajan, C., Fujimoto, H., Tokumitsu, K., Mabuchi, A. & Kasuh, T. Reduction of the irreversible capacity of a graphite anode by the CVD process. *Carbon* **39**, 1409–1413 (2001).

221. Zhang, H. L. *et al.* Electrochemical performance of pyrolytic carbon-coated natural graphite spheres. *Carbon* **44**, 2212–2218 (2006).

222. Kim, H. W., Kim, E. K. & Shin, S. Y. Negative electrode active material and negative electrode including the same. US Patent 20180069266A1. (2018).

223. Kim, H. W., Kim, E. K. & Shin, S. Y. Negative electrode active material and method of preparing the same. US 20180040875A1. (2018).

224. Zheng, T., Xue, J. S. & Dahn, J. R. Lithium insertion in hydrogen-containing carbonaceous materials. *Chem. Mater.* **8**, 389–393 (1996).

225. Fitzer, E. & Schaefer, W. The formation of glasslike carbon by pyrolysis of polyfurfuryl and phenolic resin carbon alcohol. *Carbon* **7**, 643–648 (1969).

226. Sugii, H., Esumi, K., Honda, H. & Oda, H. Characterization of carbonaceous gel beads prepared in presence of polymer using water-in-oil emulsion. *Carbon* **33**, 821–825 (1995).